Lifetime Image Reconstruction Super Resolution Microscopy: Principles, Applications and Underlying Photophysics

Siân Culley

A thesis submitted to
University College London
for the degree of
Doctor of Philosophy

Centre for Mathematics and Physics in Life Sciences and Experimental Biology
&
Department of Physics and Astronomy

I, Siân Culley, confirm that the work presented in this thesis is my own. Where information has been derived from other sources, I confirm that this has been indicated in the thesis.

February 14, 2015

Abstract

Many biological structures exist on a scale smaller than can be resolved by conventional fluorescence microscopy, which has limited the study of cellular processes. For this reason, there has been a large amount of research over the past decade dedicated to the development of super resolution microscopy techniques, which allow optical imaging of structures below the so-called resolution limit. In particular there has been much interest in developing super resolution microscopy techniques capable of non-destructive imaging of living samples.

A novel super resolution microscopy technique, lifetime image reconstruction super resolution (LIR-SR), is presented here; this uses continuous wave stimulated emission depletion (CW STED) to shorten the fluorescence lifetimes of fluorophores within a labelled sample. Differential lifetime shortening across the area of a scanning laser beam pair in the microscope results in spatial variation in the distribution of detected fluorescence on a nanosecond timescale, which can be subsequently used to reconstruct a super resolution image. Detailed theory of LIR-SR is explained, as well as the microscope hardware and computational methods used for its implementation. The technique is then tested on structures of known size and shape to gauge performance, and future directions for the technique are discussed.

Spectroscopic studies of CW STED are also undertaken to better understand the underlying photophysics of the process. The effects of solvent viscosity on CW STED are investigated and analysed, and a mathematical model of CW STED is presented. Further investigations are then undertaken which address a wide range of factors which could affect CW STED, including out-of-focus fluorescence and involvement of the triplet state, and possible refinements to the model of CW STED are suggested in light of the experimental results.

Acknowledgements

Okay, so there is absolutely no way that I'd have ever been able to survive the last three years on my own. Without the help, guidance, sympathy and tea-making skills of the following people I'd probably be curled up in the foetal position underneath an optical bench, weeping.

Firstly, I must of course thank my supervisors. Angus, thank you for faith in letting an ostensible cell biologist loose on hundreds of thousands of pounds worth of lasers. I didn't break anything! Too expensive. I hope. I never thought that I'd ever care so much about 2'7'-dichlorofluorescein before joining your group, so thank you again for your support and guidance. Jonathan, I am eternally grateful for your support and assistance in getting me to leave the basement once in a while to present my work and meet others in the field. Although, it must be admitted that standing barefoot in my pyjamas in Manchester rain in a Travelodge car park at 2am on the morning of the 15th European Microscopy Congress was a low point.

Next, the Bain group. Richard, did you ever know that you're my hero, and everything I would like to be? Seriously, to say that you've taught me everything I know is just a complete understatement. From tuning lasers to plant husbandry to soldering to the correct positioning of cycle lanes to cleaning teeny tiny mirrors to Mathematica to the benefits of casein to spherical harmonics and everything in-between. Thank you so much, without you this thesis would probably consist of a tea stain and a drawing of a cat. Tom bloody Blacker. Thanks for the tea (once you finally admitted that you like it), the cells, the proofreading and of course the Matt Berry interludes. Elly, your sardonic wit has made me laugh so many times when I have been spectacularly grumpy, you're a star. Nick and Dav, cheers for the moonlighting, innuendos and Sporcle. One day I WILL win fantasy football, and Fernando and Alastair WILL be mine.

I am fully aware that at this rate, the content of my Acknowledgements is soon going to outstrip that of the actual thesis, so although I could write reams of gratitude about the following...to be honest, I can't afford the extra printing cost. So, an additional thank you to: everyone at CoMPLEX who has supported me - Guy, Lewis, Geraint, Chris, Abi, Gemma, Laura and many more, Sonja, Nicky, Piotr, Alice, Gareth, all the Pedros in the Henriques group, Ben, my lovely friends from back home (I can be slightly less antisocial from now on!) and all of my awesome teammates at HCC.

Finally, I need to thank my mum and dad for having to answer a further three years of “So what’s Siân doing now?” with “She’s *still* a student”. I’m done now! I promise! Thank you for not having any idea what I’m doing, but still not disowning me and loving me nonetheless. Thank you Sox for sitting on my notes and laptop at the most inconvenient moments during thesis writing. Actually, that was really annoying. Screw you. Last but definitely not least, thank you Tomo for putting up with me. You’re the best.

‘But I tried though,’ he says. ‘Goddammit, I sure as hell did that much, now, didn’t I?’
- R.P. McMurphy, One Flew Over The Cuckoo’s Nest.

Contents

List of Figures

List of Tables

List of Abbreviations

ADC - analog to digital converter
ATP - adenosine triphosphate
CCD - charge coupled device
CFD - constant fraction discriminator
CW - continuous wave
DNA - deoxyribonucleic acid
DPSS - diode pumped solid state
EGFP - enhanced green fluorescent protein
FCS - fluorescence correlation spectroscopy
Fd - fractional depletion
FLIM - fluorescence lifetime imaging microscopy
FP - fluorescent protein
FRET - Förster Resonance Energy Transfer
FWHM - full width at half maximum
GFP - green fluorescent protein
GM - Goeppert-Mayer
HEK - human embryonic kidney
HOMO - highest occupied molecular orbital
HyD - hybrid PMT detector
IR - infra-red
IRF - instrument response function
LIR-SR - lifetime image reconstruction super resolution
LUMO - lowest unoccupied molecular orbital
MCS - multi-channel scaling
NA - numerical aperture
OPA - optical parametric amplifier
OPO - optical parametric oscillator
PALM - photoactivated light microscopy
PMT - photomultiplier tube
PSF - point spread function
$\mathbf{S}_0$ - ground singlet state
$\mathbf{S}_1$ - first excited singlet state
SIM - structured illumination microscopy

SPAD - single photon avalanche diode
STED - stimulated emission depletion
STORM - stochastic optical reconstruction microscopy
TAC - time to amplitude converter
TCSPC - time correlated single photon counting
TPE - two photon excitation
TW - time window
UV - ultraviolet
VECSEL - vertical external cavity surface emission laser

Chapter 1

Introduction

Fluorescence is an important tool which can be used for studying a vast range of physical, chemical and biological phenomena with examples of applications ranging from pH sensing to DNA sequencing [1, 2]. However, the principal application of fluorescence discussed in this thesis is its use in the labelling and imaging of biological samples to reveal structures within cells at sub-micron resolution. This chapter introduces the basic physics of fluorescence, information which can be gained through examining the time-dependence and polarisation of the detected fluorescence, and the practical translation of this into biological imaging techniques.

1.1 Fundamental principles of fluorescence

Fluorescence generally refers to the spontaneous emission of a photon resulting from a transition from a higher to a lower energy electronic configuration. Spontaneous emission is observed from the excited states of atoms, molecules and semiconductors. This thesis concerns the applications of visible (ultraviolet to near infrared) fluorescence techniques involving absorption, spontaneous emission and stimulated emission from polyatomic molecules. Molecules in which fluorescence can be excited are commonly referred to as fluorophores; in large molecules such as fluorescent proteins, fluorescence often originates from transitions localised within a specific part of the fluorophore termed the chromophore.

1.1.1 Molecular orbitals

In polyatomic molecules, the atomic valence electrons involved in the formation of chemical bonds combine to form molecular orbitals, which are occupied by pairs of electrons in accordance with the Pauli Exclusion Principle [3]. Specific electronic states of molecules are determined by the configuration, or population, of these molecular orbitals. The lowest energy configuration has all electron spins paired, with a resultant spin angular momentum of zero and is termed the singlet ground state, or S_0 [1], and this is the state in which molecules are most likely to be found

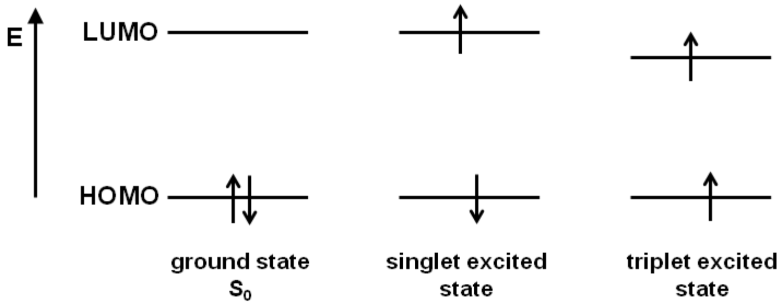

Figure 1.1: Diagram illustrating electron spins for ground, singlet excited and triplet excited states. HOMO and LUMO are indicated for the ground state, small arrows indicate electron spins. Adapted from Valeur (2001) [1].

in the absence of an external field. The next highest singlet state corresponds to the promotion of an electron from the highest occupied molecular orbital (HOMO) to the lowest unoccupied molecular orbital (LUMO). This is termed the first excited state (S_1) of the molecule, with higher energy singlet states denoted $S_2, S_3 ... S_n$.

Electronic absorption given the appropriate photon energy $E = h\nu$, where h is Planck's constant and ν is the frequency of the absorbed photon, can in principle be induced from S_0 to any of the higher singlet states. The strength of the transition is however determined by the magnitude of the transition dipole moment, which is the nearly instantaneous change in electronic charge distribution within the fluorophore created by the change in the electronic configuration [1].

In addition to the manifold of singlet states in a molecule, electronic configurations in which the electron spins are not paired are possible. In many fluorophores there is a finite probability that, once promoted to S_1, the electron spin in the now occupied LUMO can flip, leading to an electronic state with a spin angular momentum of 1 (Fig. 1.1). Such configurations are termed triplet states, denoted $T_1 ... T_n$. Figure 1.2 shows a Jablonski diagram, which is a simplified depiction of energy states in a fluorophore and the photophysical processes which can occur between these states, to be discussed later in this chapter.

1.1.2 Structure of visible fluorophores

The wavelengths of absorption and spontaneous emission in a fluorophore are governed by the HOMO-LUMO energy separation. Many fluorophores are built up from a sequence of alternating single (C-C) and double (C=C) carbon bonds over which the carbon π electrons can be delocalised. For example, the C=C bond alone absorbs ultraviolet light at 180nm, which excites an electron in the bonding π orbital into the anti-bonding $\pi*$ orbital. Fluorophore structures containing many conjugated C=C bonds have large clouds of delocalised electrons and a decreased energy gap between the bonding and anti-bonding orbitals, leading to absorption in the visible wavelength range [5]. The structures of four common fluorophores are shown in Fig.

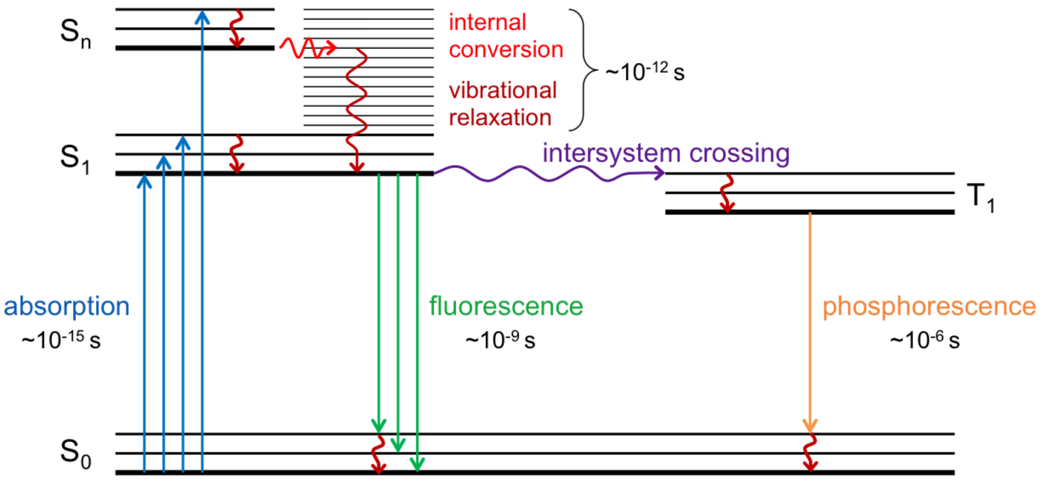

Figure 1.2: Jablonski diagram representing energy states of a fluorophore, photophysical processes and attendant timescales. Straight arrows indicate radiative transitions, wavy arrows indicate non-radiative transitions (adapted from Lichtman and Conchello (2005) [4]).

1.3a along with the wavelength ranges over which they absorb and emit (fluoresce) (Fig. 1.3b,c). Many fluorophores can be derived from common 'core' structures. For example, fluorescein and rhodamine B (Fig. 1.3a) are both based on xanthene, the three-ringed structure present in the structures of both of these fluorophores.

The absorption and emission spectra of fluorophores do not depend solely on electronic rearrangement within the molecule, but also upon the vibrational and rotational degrees of freedom of the constituent atoms and the environment of the fluorophore. This thesis is concerned with fluorophores in the condensed phase, namely in solution, and here mechanisms through which the absorption and emission spectra can be modified include solvation effects such as the formation of a solvation shell around a fluorescent molecule [1].

1.1.3 The Born-Oppenheimer approximation and the Franck-Condon principle

Two important concepts in understanding the absorption and spontaneous emission (fluorescence) spectra of molecules are the Born-Oppenheimer approximation and the Franck-Condon principle [3]. The Born-Oppenheimer approximation recognises that electronic and nuclear motions in molecules occur on very different timescales and so the kinetic energy of the much slower nuclei play little part in determining the electronic energy of (bound) states. As such, the total wavefunction for the molecule can be split into electronic and nuclear components as:

$$\Psi(r,R) = \psi_e(r;R)\chi_n(R) \tag{1.1}$$

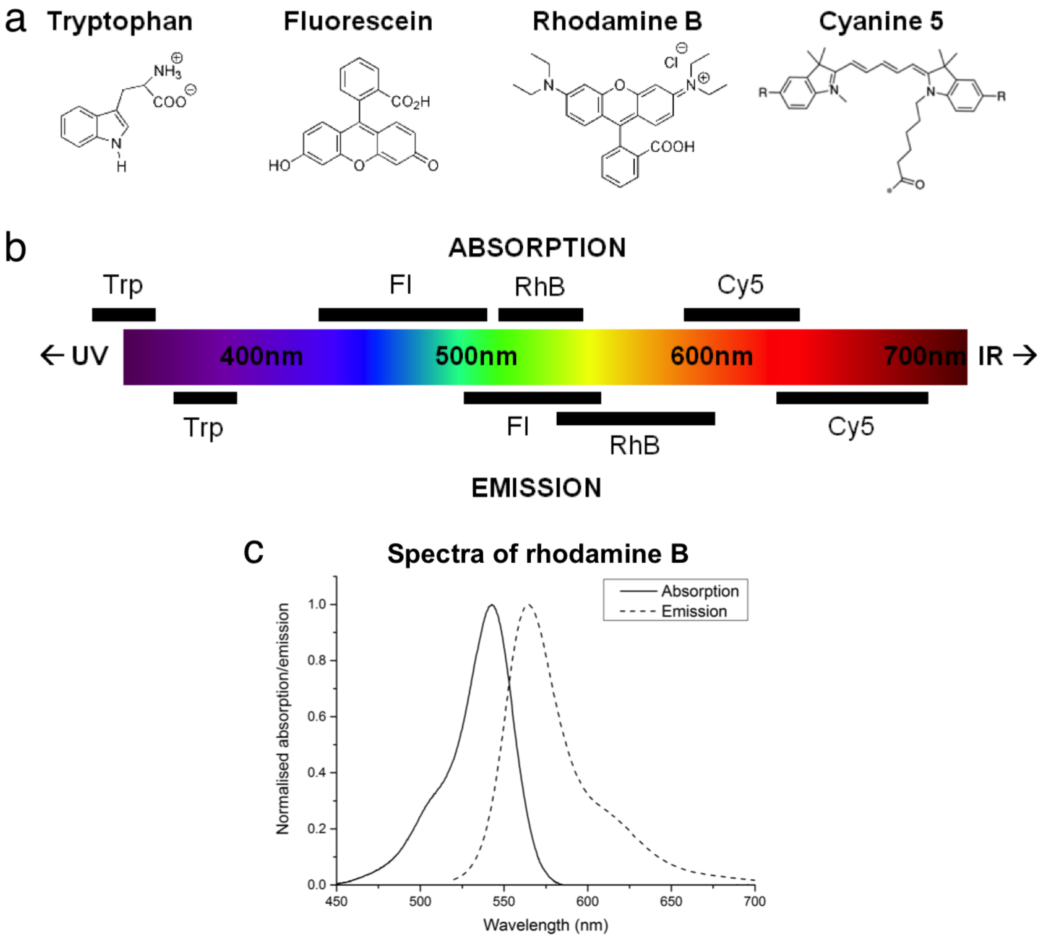

Figure 1.3: Structure of four fluorophores and the wavelengths over which they absorb and fluoresce. a) Structures of four common fluorophores. b) Absorption and emission ranges of the four fluorophores in a). c) Detailed absorption and emission spectra of rhodamine B. Abbreviations: Trp - tryptophan, Fl - fluorescein, RhB - rhodamine B, Cy5 - cyanine 5. Spectral data for tryptophan, fluorescein and rhodamine B taken from PhotoChemCAD online resource [6], spectral data for cyanine 5 taken from Jackson ImmunoResearch website [7].

where $\psi_e(r; R)$ represents the electronic wavefunction and $\chi_n(R)$ represents the nuclear wavefunction, with r denoting the electronic coordinates and R the nuclear coordinates [3]. This formulation allows for solution of the Schrödinger equation for the electronic wavefunction $\psi_e(r; R)$ for nuclei at fixed coordinates R. Solving the Schrödinger equation for many different combinations of nuclear coordinates can be used to generate a molecular potential energy curve, which describes the variation of the energy of the molecule $E_e(R)$ at different nuclear configurations [5]. The form of $E_e(R)$ for the ground and first excited states of a diatomic molecule are shown in Fig. 1.4 together with the corresponding vibrational energy levels.

The Franck-Condon principle explains the intensity of induced and spontaneous transitions between the vibrational levels of two electronic states. The timescale

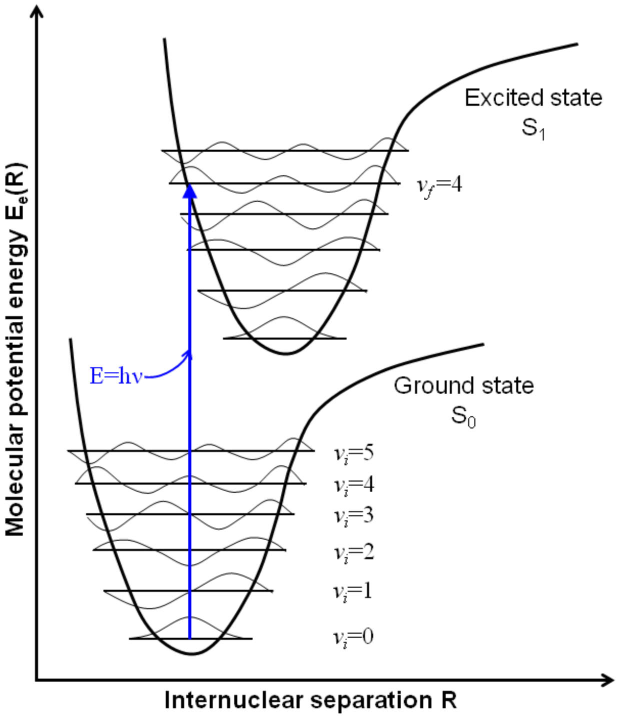

Figure 1.4: Absorption from the $v_i = 0$ vibrational level of S_0 to the $v_f = 4$ vibrational level of S_1 in a diatomic molecule upon absorption of a photon shown as a potential energy diagram (adapted from Atkins and de Paula (2006) [5]).

for electronic reorganisation resulting from the absorption or emission of a photon in molecules is on the order of 10^{-15} seconds, which is significantly shorter than vibrational periods ($\sim 10^{-12} - 10^{-10}$ seconds) [1], and as such corresponds to an instantaneous change in the potential energy surface $E_e(R)$ (Fig. 1.4). Such instantaneous transitions are referred to as vertical transitions [3]. Within each electronic state there exist many vibrational levels, as shown in Fig. 1.4, and prior to absorption the vibrational levels of the ground electronic state are populated according to the Boltzmann distribution. During absorption the molecule must be excited to an energy level in the first excited state corresponding to the same nuclear framework as in the ground state, which for a diatomic molecule as in Fig. 1.4 is equal to the internuclear separation. The case in Fig. 1.4 describes a diatomic molecule; for molecular fluorescence there exist many vibrational and rotational energy levels which are more conveniently represented in the form of a Jablonski diagram, as shown in Fig. 1.2.

The transition dipole moment is a measure of how electronic charge is displaced between initial and final states, and is described by [5]

$$\boldsymbol{\mu}_{\text{fi}} = \langle \Psi_f | \, \hat{\boldsymbol{\mu}} \, | \Psi_i \rangle \, , \tag{1.2}$$

where f and i denote the final and initial states respectively of the wavefunction of the molecule as given in Eq. 1.1. The operator $\hat{\boldsymbol{\mu}}$ is the sum over all electrons and nuclei in the molecule as defined by [5]

$$\hat{\boldsymbol{\mu}} = -e\sum_{n}\boldsymbol{r}_n + e\sum_{N} Z_N\boldsymbol{R}_N, \tag{1.3}$$

where the first term is the electronic contribution and the second term is the nuclear contribution, with e and Z_N denoting electronic and nuclear charges respectively, and $\boldsymbol{r}_n$, $\boldsymbol{R}_N$ the electronic and nuclear coordinates as in Eq. 1.1. The overall vibronic (vibrational and electronic) state of the molecule can be described as $|\varepsilon v\rangle$ according to the Born-Oppenheimer principle, where ε corresponds to the electronic wavefunction $\psi_e(r;R)$ and v corresponds to the nuclear wavefunction $\chi_n(R)$, which describes the vibrational state of the molecule [3]. Combining Eqs. 1.2 and 1.3 thus yields [5]

$$\boldsymbol{\mu}_{\text{fi}} = \boldsymbol{\mu}_{\varepsilon_f,\varepsilon_i} S(v_f, v_i) \tag{1.4}$$

where $\boldsymbol{\mu}_{\varepsilon_f,\varepsilon_i} = -e\sum_i \langle\varepsilon_f|\,\boldsymbol{r}_i\,|\varepsilon_i\rangle$ and $S(v_f, v_i) = \langle v_f|v_i\rangle$, with subscripts f and i denoting final and initial states as before. The intensity of an electronic transition can be calculated from its Franck-Condon factor, the squared modulus of the overlap integral of the two vibrational wavefunctions $|S(v_f, v_i)|^2$ [5]. Transitions are possible if the Franck-Condon factor is greater than zero and as a result, for polyatomic molecules in solution transitions can occur between the many different vibrational states of S_0 and S_1. This is shown in Fig. 1.4 for the absorption of a photon by the ground electronic state of a diatomic molecule. The vertical line indicates that there is no time for a change in internuclear separation to occur; in this schematic, the $v = 4$ vibrational wavefunction in the excited state most closely matches that of the $v = 0$ wavefunction in the ground state, and hence the Franck-Condon factor is largest for this transition [5]. Transitions to higher and lower vibrational levels of S_1 are allowed, but their transition probabilities are governed by smaller Franck-Condon factors.

1.1.4 Absorption and emission spectra

For each vibronic transition, rotational transitions also occur which are governed by angular momentum selection rules [3]. In polyatomic molecules there are numerous vibrational and rotational states at a given energy, and so the absorption (and emission) spectra are both complex and congested at room temperature. Furthermore, in liquids there are continuous interactions between a fluorescent molecule and the solvent molecules surrounding it, which can take place in a multitude of different configurations and consequently ‘blur’ vibrational and rotational transitions leading to a broadening of the spectrum [1] (e.g. spectrum of rhodamine B, Fig. 1.3c).

A notable feature of polyatomic fluorophores is a marked red shift between their absorption and emission spectra, known as the Stokes shift. The Franck-Condon factors for absorption favour transitions from the thermally populated low vibrational levels of the ground state to higher vibrational levels of the excited state; as a result, excited state molecules are vibrationally 'hot' compared to their local environment. These molecules lose energy rapidly due to sub-picosecond collisions with solvent molecules, returning the molecules back to lower vibrational levels of the excited state. This process is commonly referred to as vibrational relaxation, and is a non-radiative process (no emission of photons).

As vibrational relaxation within the excited state occurs on a significantly rapid timescale compared to spontaneous emission (Fig. 1.2), the majority of spontaneous emission consequently occurs from the lower vibrational levels of the excited state, and these downwards vertical transitions are again governed by Franck-Condon factors. The energy lost to the environment due to vibrational relaxation results in the majority of spontaneous emission transitions having lower energies than the absorption transitions. However, it can be seen in the absorption and emission spectra of rhodamine B that there is also a degree of overlap between the two spectra which arises from high energy (short wavelength) emission from higher vibrational levels of S_1 to lower vibrational levels of S_0 and conversely low energy (long wavelength) absorption from higher vibrational levels of S_0 to lower vibrational levels of S_1.

The approximate mirror symmetry often observed in the $S_0 \rightarrow S_1$ absorption and $S_1 \rightarrow S_0$ emission spectra reflects the fact that the magnitudes of Franck-Condon factors are independent of the direction of the transition. Examples of asymmetric spectra can arise when, for example, there is excitation to the second excited state S_2. When this occurs there is rapid non-radiative relaxation (internal conversion) to S_1 and so whilst the absorption spectrum describes absorption from S_0 to both S_1 and S_2, the emission spectrum still only reflects emission from S_1 to S_0 [2].

1.1.5 The single photon absorption cross-section

Laser sources provide narrow bandwidth, polarised light which is suitable for exciting fluorophores, and are used throughout the experimental chapters of this thesis for this purpose. The probability that a molecule absorbs a photon of wavelength λ is given by its absorption cross-section

$$\sigma_\lambda = \frac{2.303}{N_A}\varepsilon_\lambda = 3.83 \times 10^{-21}\mathrm{mol} \cdot \varepsilon_\lambda, \tag{1.5}$$

where N_A is Avogadro's number (mol^{-1}) and ε_λ is the molar absorption coefficient (L mol^{-1} cm^{-1}). The formulation of the absorption cross-section is derived from the Beer-Lambert Law, which describes the efficiency of light absorption as a function of fluorophore concentration and sample thickness [1].

Values of ε range from $10^4 - 10^5$ L mol^{-1}cm^{-1} for commonly used fluorophores, yielding absorption cross-sections of $10^{-17} - 10^{-16}$cm^2. For example, rhodamine B has a molar absorption coefficient of $\varepsilon \approx 105{,}000$ L mol^{-1}cm^{-1} and thus an absorption cross-section of $\sigma \approx 4 \times 10^{-16}\text{cm}^2$ [1].

1.1.6 Radiative and non-radiative decay of the excited state

The Jablonski diagram in Fig. 1.2 shows that there are many possible transitions that fluorophores in the excited state can undergo. The principal mechanism by which a fluorophore returns from S_1 to S_0 is spontaneous emission (fluorescence). Following short pulsed laser excitation ($< 10^{-9}$s pulses) the population of the excited state decays according to

$$N(t) = N_0 \exp\left(-\frac{t}{\tau_r}\right), \tag{1.6}$$

where N_0 is the initial population of the excited state and τ_r is the radiative lifetime of the excited state [1]. The radiative lifetime is the reciprocal of the Einstein A coefficient for the $S_1 \to S_0$ transition, and the Einstein A and B coefficients are related through [8]

$$A_{21} = B_{21}\frac{8\pi h\nu_{21}^3}{c^3}. \tag{1.7}$$

A_{21} is the Einstein coefficient for the rate of spontaneous emission from level 2 (here state S_1) to level 1 (here state S_0), and $B_{21} = (g_1/g_2)B_{12}$ where g_1 and g_2 are the degeneracies of levels 1 and 2 respectively and B_{12} is the Einstein coefficient for absorption. B_{21} is proportional to the overlap of levels 1 and 2, $|\boldsymbol{\mu}_{21}|^2$, and is the Einstein coefficient for stimulated emission, a mechanism by which an incident photon can stimulate radiative de-excitation from the excited state to the ground state. Stimulated emission is discussed in further detail in later chapters.

In most fluorophores, however, the lifetime of the S_1 excited state is shorter than τ_r. This is due to additional, non-radiative pathways which remove population from S_1. The excited state lifetime, or fluorescence lifetime as it will be referred to throughout this thesis, is given by

$$\tau_f = \frac{1}{k_r + k_{nr}} \tag{1.8}$$

where k_r is the radiative decay rate ($= 1/\tau_r = A_{21}$) and k_{nr} is the non-radiative decay rate, which is the sum of processes such as vibrational relaxation (as described in Section 1.1.4), intersystem crossing, internal conversion and quenching. Commonly used fluorophores typically have fluorescence lifetimes on the order of $10^{-10} - 10^{-8}$ seconds, and the population of the excited state still decays exponentially according to Eq. 1.6 but with a characteristic lifetime of τ_f rather than τ_r.

Intersystem crossing describes the crossing of fluorophores from S_1 into triplet states T_n (usually T_1). Whilst such transitions are typically forbidden by the spin selection rule (no change in overall spin), in reality spin-orbit coupling allows for these transitions to occur, albeit weakly [5]. The rate at which intersystem crossing occurs can vary depending on the fluorophore structure; for example, spin-orbit coupling scales with nuclear mass as Z^4 and hence is more probable in fluorophores containing heavy atoms [1]. Once in a triplet state, vibrational relaxation occurs as in singlet states, with the consequence that fluorophores can become trapped in lower vibrational levels of T_1 which are at lower energies than the lowest vibrational levels of S_1. Once in the lower vibrational levels of T_1, fluorophores can return to S_0 through spin-orbit coupling (again a very weak transition) and emit a photon in a radiative process termed phosphorescence. The low probability of the $T_1 \rightarrow S_0$ transition means that phosphorescence is typically emitted following triplet state lifetimes of microseconds and longer.

Internal conversion is non-radiative conversion between electronic states of the same spin multiplicity, and typically occurs when there is an intersection between two molecular potential energy curves [5]. This process is more common between the higher excited singlet states, for example $S_2 \rightarrow S_1$, as the higher excited states are more closely spaced and thus more likely to have some degree of overlap. $S_1 \rightarrow S_0$ intersystem crossing is less efficient as there is a larger energy gap between these two states [1].

The final main method through which de-excitation of excited fluorophores can occur is quenching. The term quenching covers several processes by which fluorophores can become de-excited, including collisions with molecules in the local environment, such as solvent molecules and oxygen, and energy transfer processes such as Förster Resonance Energy Transfer (FRET). During collisional quenching the fluorophore is either returned to the ground state or rendered incapable of fluorescence through chemical modifications such as proton and electron transfer, or formation of complexes [1]. Collisions between singlet and triplet fluorophores can also quench fluorescence, and the interaction of oxygen with triplet state fluorophores in particular can lead to destruction of the fluorophore (a process often referred to as photobleaching). These latter quenching processes are discussed in further detail in Chapter 5.

FRET is the process by which electronic energy is transferred from an excited electronic state of a ‘donor’ fluorophore to a nearby ‘acceptor’ fluorophore. FRET occurs through dipole-dipole transfer with simultaneous de-excitation of the donor and excitation of the acceptor. The rate at which FRET occurs from a donor to an acceptor is given by [1]

$$k_{\text{FRET}} = k_r \left(\frac{R_F}{r} \right)^6 , \tag{1.9}$$

where k_r is the radiative decay rate of the donor in the absence of acceptor, r is the distance between donor and acceptor, and R_F is the Förster critical radius (commonly referred to as R_0 in FRET literature). R_F is the donor-acceptor separation where the efficiency of FRET is 50%, and is determined by factors such as the spectral overlap of donor and acceptor and the relative orientations of their transition dipole moments [2]. The fluorescence lifetime of the donor in the presence of an acceptor is thus reduced according to

$$\tau_f = \frac{1}{k_r + k_{\text{FRET}}} = \frac{\tau_r}{1 + \left(\frac{R_F}{r}\right)^6}. \tag{1.10}$$

Typical values of R_F are $\sim 10^{-9}$m [1], meaning that significant FRET is only likely to occur in a highly concentrated solution or in cases where donor and acceptor fluorophores are immobilised close to each other. The latter case has applications in measuring molecular interactions in cell biology, discussed in Section 1.5.2.

1.1.7 The quantum yield of fluorescence

The quantum yield of fluorescence Φ_f represents the probability that, once excited, a fluorophore will emit a photon. It is given by the ratio of the radiative decay rate from S_1 to the total decay rate from S_1 as [1]

$$\Phi_f = \frac{k_r}{k_r + k_{nr}}. \tag{1.11}$$

The non-radiative decay rate represents the sum of the rates at which the non-radiative processes described above occur. The quantum yield is commonly used to assess efficiency of fluorophores, especially for biological fluorescence imaging where high fluorescence intensities are desirable.

1.2 Fluorescence anisotropy

As discussed above, the absorption and emission transition rates depend on the magnitude of the transition dipole moment for the $S_0 \to S_1$ and $S_1 \to S_0$ transitions. However, the orientations of a fluorophore's transition dipole moments can also impact upon transition probabilities and the polarisation of emitted fluorescence.

1.2.1 Orientational photoselection in single photon excitation

The absorption dipole moment is referred to here as $\boldsymbol{\mu}_{\text{abs}}$, which is equivalent to $\boldsymbol{\mu}_{\text{fi}}$ given in Eq. 1.4 for final state S_1 and initial state S_0, and is a measure of the electronic charge redistribution caused by absorption. For linearly polarised light with electric vector $\boldsymbol{E}$, the probability of excitation is proportional to $|\boldsymbol{E} \cdot \boldsymbol{\mu}_{\text{abs}}|^2$ and hence is proportional to $\cos^2\theta$, where θ is the angle in the laboratory frame between $\boldsymbol{E}$ and $\boldsymbol{\mu}_{\text{abs}}$ [1]. Therefore the probability of absorption is highest when $\boldsymbol{E}$ is parallel to $\boldsymbol{\mu}_{\text{abs}}$, and zero when it is perpendicular. Assuming that the excitation source is a short pulsed laser, such that there is no reorientation of dipole moments during excitation with the laser having well-defined linear polarisation, a $\cos^2\theta$ anisotropic laboratory frame distribution of excited state fluorophores is created. This is known as orientational photoselection and is shown in Fig. 1.5.

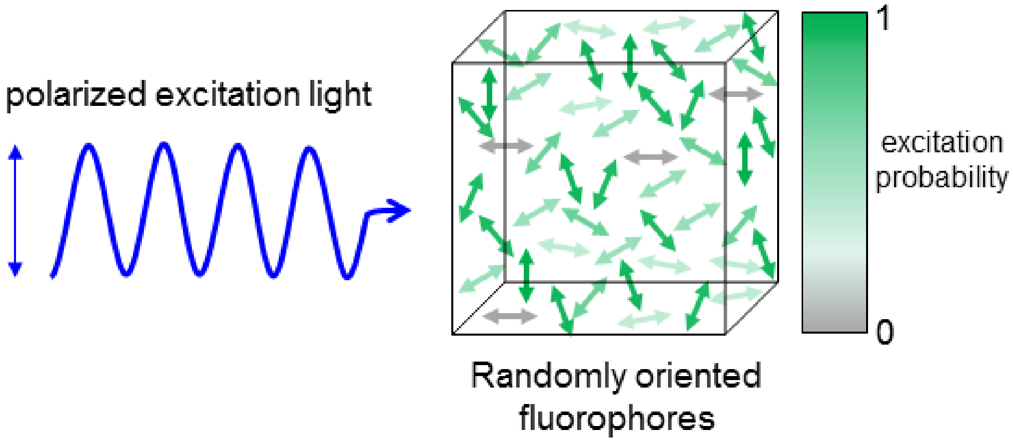

Figure 1.5: Photoselection in a randomly oriented solution of fluorophores (dipole moments along arrows) following excitation with plane polarised light.

In an isotropic solution the number of molecules with $\boldsymbol{\mu}_{\mathrm{abs}}$ oriented within the angles $\theta \to \theta + \mathrm{d}\theta$ and $\phi \to \phi + \mathrm{d}\phi$ is proportional to $\sin\theta \mathrm{d}\theta \mathrm{d}\phi$ (Fig. 1.6, where the polarisation of the excitation is parallel to the z axis). Therefore the number of molecules in which absorption has occurred according to the orientational conditions described above is proportional to [1]

$$p(\theta, \phi) \propto \cos^2\theta \sin\theta \mathrm{d}\theta \mathrm{d}\phi. \tag{1.12}$$

1.2.2 Polarised emission and anisotropy

Emission of fluorescence is also anisotropic and reflects the degree of order in the excited state population, as the photoselected excited state fluorophores emit fluorescence parallel to their emission dipole moments $\boldsymbol{\mu}_{\mathrm{em}}$ ($\boldsymbol{\mu}_{\mathrm{fi}}$ where the final state is S_0 and the initial state is S_1). To quantify fluorescence anisotropy, the intensities of fluorescence polarised parallel to ($I_{\|}$) and perpendicular to ($I_{\perp}$) the excitation polarisation $\boldsymbol{E}$ are measured; practical methods of achieving this are discussed further in Section 1.4.1.

The time-resolved anisotropy for linearly polarised excitation of an isotropic sample is given by

$$R(t) = \frac{I_{\|}(t) - I_{\perp}(t)}{I(t)} \tag{1.13}$$

where $I(t)$ is the total time-resolved fluorescence intensity given by

$$I(t) = I_{\|}(t) + 2I_{\perp}(t). \tag{1.14}$$

The z axis of the coordinate system used in the laboratory frame is the polarisation vector of the excitation field, and there is cylindrical symmetry about this axis such

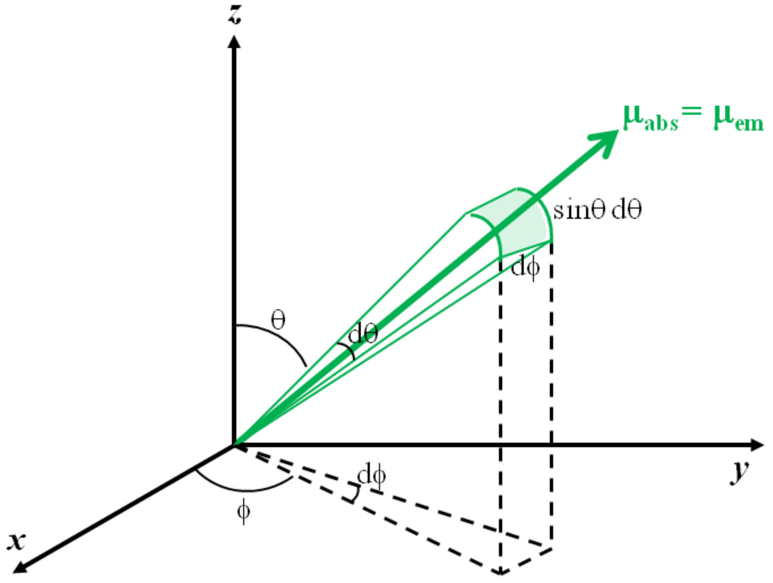

Figure 1.6: Coordinate system for the dipole moment of a fluorophore, with the assumption that the emission dipole moment and absorption dipole moment are parallel. The z axis is taken to be parallel to the polarisation vector of the excitation field. Adapted from Valeur (2001) [1]

that $I_{\|} = I_z$ and $I_\perp = I_x = I_y$. In this case anisotropy only depends on the angle θ made between the emission dipole moment and the z axis of the coordinate system described in Fig. 1.6. The angular distribution of the emission dipole moments (in the absence of any reorientation of the molecules) is given by [1]

$$R_0 = \frac{3\left\langle \cos^2\theta \right\rangle - 1}{2} \tag{1.15}$$

where $\left\langle \cos^2\theta \right\rangle$ is the population averaged value of $\cos^2\theta$, with θ denoting the angle between $\boldsymbol{\mu}_{\mathrm{em}}$ and the z axis (as opposed to Eq. 1.12 where θ refers to the angle between $\boldsymbol{\mu}_{\mathrm{abs}}$ and the z axis). However, for many common fluorophores $\boldsymbol{\mu}_{\mathrm{abs}}$ and $\boldsymbol{\mu}_{\mathrm{em}}$ are parallel to each other and the two definitions of θ are equivalent. In this case, the fraction of molecules in the excited state population is given by

$$W(\theta,\phi)\mathrm{d}\theta\mathrm{d}\phi = \frac{p(\theta,\phi)}{\int_0^{2\pi}\int_0^{\pi} p(\theta,\phi)}, \tag{1.16}$$

and when evaluated for $p(\theta,\phi)$ as defined for Eq. 1.12 with its associated assumptions is equal to $(3/4\pi)p(\theta,\phi)$. The average value of $\cos^2\theta$ across the excited state can then be calculated as

$$\left\langle \cos^2\theta \right\rangle = \int_0^{2\pi}\int_0^{\pi} \cos^2\theta W(\theta,\phi)\mathrm{d}\theta\mathrm{d}\phi = \frac{3}{4\pi}\int_0^{2\pi}\int_0^{\pi} \cos^2\theta p(\theta,\phi) \tag{1.17}$$

which evaluates to 3/5. Substituting $\left\langle \cos^2\theta \right\rangle = 3/5$ into Eq. 1.15 yields an anisotropy of $R_0 = 0.4$ [1].

1.2.3 Rotational diffusion

As emission of fluorescence following excitation is not instantaneous due to the finite excited state lifetime, processes can occur during this time which cause depolarisation of the emitted fluorescence. For photoselected fluorescent molecules in solution, the principle cause of fluorescence depolarisation is rotational diffusion of the molecules and hence their emission dipoles. The collisional timescale in a liquid is $10^{-14} - 10^{-13}$ seconds, which is short enough that many collisions between solvent molecules and fluorescent molecules can occur before either the fluorescent molecule can freely rotate (timescale $10^{-12} - 10^{-9}$s) or emit fluorescence (timescale $10^{-10} - 10^{-8}$s) [9]. Under such circumstances, molecular reorientation can be considered as due to a very large number of small random steps in (θ, ϕ) caused by solvent collisions. This diffusive angular motion is analogous to Brownian motion for translation. The standard treatment of rotational diffusion of fluorophores in solution is with the Stokes-Einstein-Debye relation [10]

$$\tau_{\text{rot}} = \frac{f \kappa V_h \eta}{k_B T} + \tau_0. \tag{1.18}$$

τ_{rot} is the rotational correlation time of the fluorescence molecule, V_h is the van der Waals volume of the molecule, η is the solvent viscosity, T is temperature and τ_0 is the free rotational correlation time of the fluorescent molecule. f is the 'form factor', a property describing the shape of a molecule, where $f = 1$ for a spherical molecule, $f < 1$ for a prolate molecule and $f > 1$ for an oblate molecule. κ describes the limits of motion between the fluorophore and the solvent which ranges from zero, where the fluorophore 'slips' and rotates independently of neighbouring solvent molecules, to one, where the fluorophore 'sticks' and neighbouring solvent molecules rotate with the fluorophore [11]. The rotational correlation times of fluorophores in solvents used in this thesis range from hundreds of picoseconds to several nanoseconds (Chapter 4).

The anisotropy of fluorescence emitted from a population of fluorophores in solution thus decays away from the initial anisotropy R_0 according to

$$R(t) = R_0 \exp\left(-\frac{t}{\tau_{\text{rot}}}\right) \tag{1.19}$$

with shorter rotational correlation times producing a more rapid depolarisation of fluorescence. The above expression assumes equal diffusivity in each direction (i.e. there is cylindrical symmetry) and that $\boldsymbol{\mu}_{\text{em}}$ is along the symmetry axis; if not, $R(t)$ is much more complex. More complex anisotropy decays are also obtained for fluorescent probes which are embedded in or attached to larger molecules, such as in labelling of biological structures (Section 1.6.1) [12]. However, a good approximation for common fluorophores is that they have single exponential anisotropies as described by Eq. 1.19. Validation of this approximation, as well as studies into systems where these assumptions cannot be made, can be found in references [11, 9, 13].

1.2.4 Spherical harmonics

The orientational distribution function $P(\theta, \phi)$ describes the probability of finding a molecule, or transition dipole moment, oriented between $\theta \rightarrow \theta + \mathrm{d}\theta$ and $\phi \rightarrow \phi + \mathrm{d}\phi$ in spherical polar coordinates in the laboratory frame of reference. This is formalised as [14]

$$P(\theta, \phi) = \sum_{KQ} \langle C_{KQ} \rangle \, Y_{KQ}(\theta, \phi) \tag{1.20}$$

where $\langle C_{KQ} \rangle$ are normalisation coefficients and $Y_{KQ}(\theta, \phi)$ are spherical harmonics of rank K and projection Q according to

$$Y_{KQ}(\theta, \phi) = \left(\frac{2K+1}{4\pi} \right)^{\frac{1}{2}} L_{KQ}(\theta, \phi), \tag{1.21}$$

where $L_{KQ}(\theta, \phi)$ are the Legendre polynomials. From a quantum mechanical perspective, spherical harmonics are the solutions of the Schrödinger equation for a particle on a sphere where rank K is analogous to the angular momentum quantum number l and projection Q is analogous to the magnetic quantum number m_l (where $m_l = -l ... 0 ... l$, similarly $Q = -K ... 0 ... K$) [3]. Spherical harmonics are a useful basis set of functions for describing molecular orientations as they are orthogonal, and as a result the orientational distribution function normalises such that the probability of finding a molecule in any orientation projected onto the unit sphere is unity as shown below

$$\sum_{KQ} \langle C_{KQ} \rangle \int_0^{2\pi} \int_0^{\pi} Y_{KQ}(\theta, \phi) \sin\theta \mathrm{d}\theta \mathrm{d}\phi = 1. \tag{1.22}$$

The total population of molecules is described as

$$P(\theta, \phi) = \langle C_{00} \rangle \, Y_{00}(\theta, \phi) \tag{1.23a}$$

$$= \langle C_{00} \rangle \left(\frac{1}{4\pi} \right)^{\frac{1}{2}} \tag{1.23b}$$

and to satisfy Eq. 1.22 it can be seen that $\langle C_{00} \rangle = \sqrt{1/4\pi}$. As this population is present in all orientational distributions of molecules, the orientational distribution function can be rewritten as

$$P(\theta, \phi) = \langle C_{00} \rangle \sum_{KQ} \langle \alpha_{KQ} \rangle \, Y_{KQ}(\theta, \phi), \tag{1.24}$$

where $\langle \alpha_{KQ} \rangle = \langle C_{KQ} \rangle / \langle C_{00} \rangle$. For cylindrically symmetrical excitation of an isotropic sample, transition probabilities can be decomposed into the $Y_{00}(\theta, \phi)$ and

$Y_{20}(\theta,\phi)$ components (Fig. 1.7), where

$$Y_{00}(\theta,\phi) = \left(\frac{1}{4\pi}\right)^{\frac{1}{2}} \tag{1.25a}$$

$$Y_{20}(\theta,\phi) = \left(\frac{5}{4\pi}\right)^{\frac{1}{2}} \frac{1}{2}\left(3\cos^2\theta - 1\right). \tag{1.25b}$$

For example, the $\cos^2\theta$ excitation probability can be expanded in spherical harmonics as

$$\cos^2\theta = \frac{\sqrt{4\pi}}{3}\left(Y_{00}(\theta,\phi) + \frac{2}{\sqrt{5}}Y_{20}(\theta,\phi)\right) \tag{1.26}$$

and so $P(\theta,\phi)$ (Eq. 1.24) can be written as

$$P(\theta,\phi) = \left(\frac{1}{4\pi}\right)^{\frac{1}{2}}\left(Y_{00}(\theta,\phi) + \frac{2}{\sqrt{5}}Y_{20}(\theta,\phi)\right). \tag{1.27}$$

This distribution is plotted in Fig. 1.7 (right). Thus $\langle\alpha_{20}\rangle = 2/\sqrt{5}$ and $\langle C_{20}\rangle = \langle C_{00}\rangle\langle\alpha_{20}\rangle$. Components such as $Y_{2\pm2}(\theta,\phi)$ are only non-zero in cases where there is not cylindrical symmetry [9].

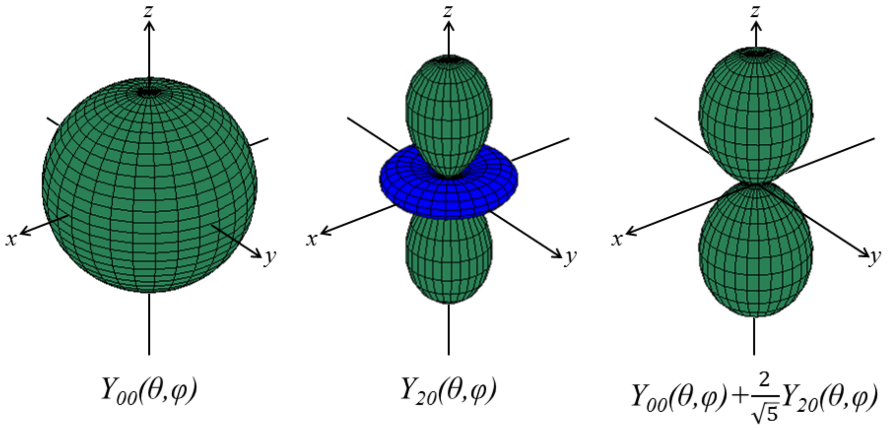

Figure 1.7: Spherical harmonics plotted in the Cartesian coordinate system.

Time-dependent orientational distribution functions $P(\theta,\phi,t)$ for parallel and perpendicular emitted fluorescence can be used to formulate the time-resolved fluorescence anisotropy as

$$R(t) = \frac{\langle\alpha_{20}(t)\rangle}{\sqrt{5}}, \tag{1.28}$$

which evaluates to $R_0 = 0.4$ at $t = 0$, where $\langle\alpha_{20}(0)\rangle = \langle\alpha_{20}\rangle$ as stated above. A full derivation of this relation can be found in Bailey (2013) [15].

1.3 Two photon absorption

Excitation of a molecule in S_0 to a higher excited state can be achieved by the simultaneous absorption of multiple photons, as opposed to one single photon, in a process known as multiphoton absorption. Here only the case of the simultaneous absorption of two photons (two photon absorption) will be discussed, as this is widely used in biological fluorescence microscopy (Section 1.6.2) as well as for manipulating the orientational distribution function of fluorophores in solution (Section 5.1).

Two photon absorption can be thought of as two consecutive single photon absorptions promoting the fluorophore from S_0 to S_n via a 'virtual' state. Virtual states do not necessarily correspond to a stationary state of the molecule and as a result are very short-lived, with lifetimes which can be calculated according to the uncertainty principle ($\Delta E \Delta t \geq \hbar/2$) as follows [16]

$$\Delta t \geq \frac{\lambda}{4\pi c}. \tag{1.29}$$

Evaluating Eq. 1.29 for an excitation wavelength of 800nm (as is typically used in two photon absorption of visible fluorophores) gives a virtual state lifetime of $\sim 2 \times 10^{-16}$s. For two photon absorption to occur, two photons must be absorbed by the fluorophore within the virtual state lifetime; as a consequence, two photon absorption generally requires the use of ultrashort laser pulses (typically femtosecond pulses such as those provided by Ti:Sapphire lasers). Two photon absorption is shown on a Jablonski diagram in Fig. 1.8a.

Although the two photons absorbed during two photon absorption can possess different energies, for the discussion below they are assumed to originate from the same pulsed laser source and thus possess equal energies. The probability that two photon absorption will occur within a single pulse is given by [17]

$$P_{\mathrm{2PA}} = \frac{g_p}{t_p}\left(\frac{E_p}{Ah\nu}\right)^2 \sigma_{2P}, \tag{1.30}$$

where g_p is a dimensionless quantity representing the temporal shape of the pulse, t_p is the pulse duration, E_p is the total energy delivered by a single pulse, A is the area covered by the laser beam, $h\nu$ is the energy of a single photon in the pulse and σ_{2P} is the two photon absorption cross-section of the molecule. The two photon cross-section is given in units of GM (1 GM $= 10^{-50}$cm^{4}s/photon, with typical values of $\sigma_{2P} = 10^1 - 10^2$ GM [18]).

Two photon absorption can be used to access excited states of fluorophores which cannot be accessed using single photon excitation as different selection rules apply [16]. Figure 1.8b and c show the two photon absorption spectra of two fluorophores plotted at half the two photon wavelength for comparison with their single photon absorption spectra. The two photon absorption spectrum of Lucifer yellow is a similar shape to that of its single photon absorption spectrum (Fig. 1.8b) with the

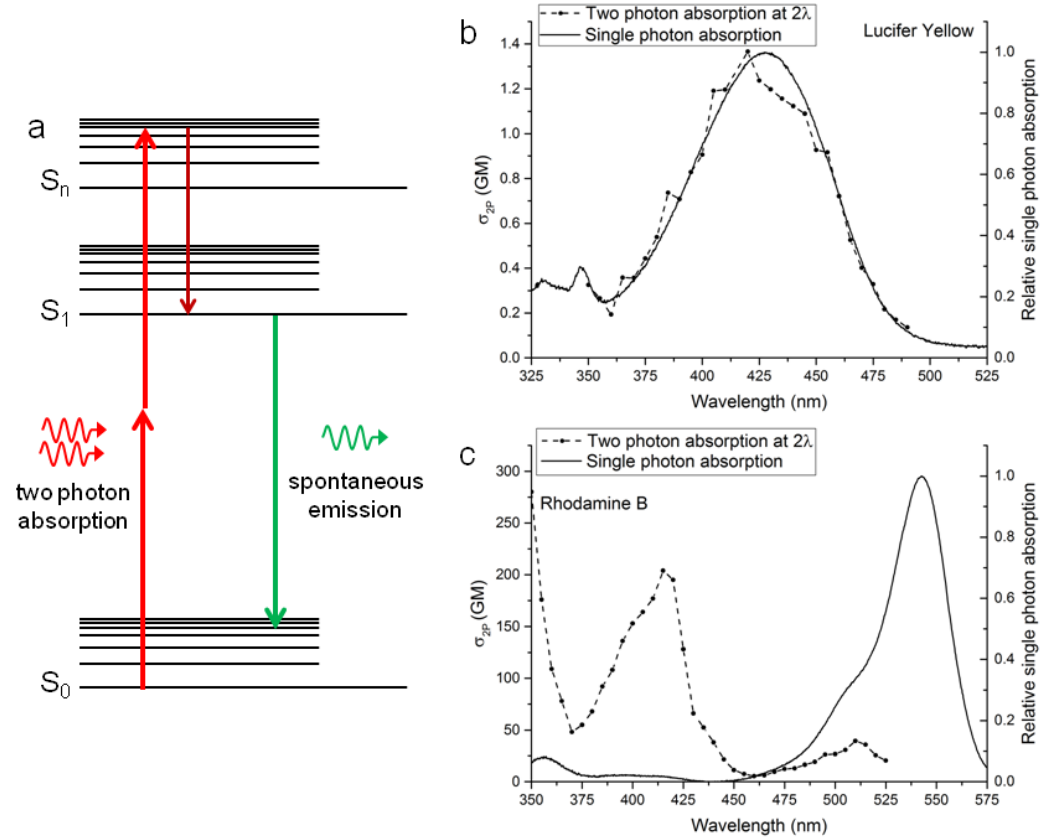

Figure 1.8: Two photon absorption Jablonski diagram and spectra. a) Jablonski diagram showing two photon absorption from S_0 to a higher singlet state S_n, vibrational relaxation (dark red) and spontaneous emission. Two photon and single photon absorption spectra of b) Lucifer yellow and c) Rhodamine B, two photon absorption spectra plotted at half the measured absorbed wavelength. Single photon absorption data from PhotoChemCAD resource [6], two photon absorption spectra from [19], data available at DRBIO online resource [20].

two photon peak appearing at approximately double the wavelength of the single photon peak, suggesting that both methods of excitation are accessing the same excited states. However, the two photon absorption spectrum of rhodamine B is significantly blue-shifted relative to double the single photon absorption spectrum (Fig. 1.8c). This suggests here that two photon absorption allows for access of higher energy excited states than with single photon absorption. The difference in accessible energy states for single and two photon absorption depends on features of the fluorophore such as structural symmetry and vibronic coupling [19]. The emission spectra of fluorophores are usually independent of absorption wavelength due to the rapid internal conversion and vibrational relaxation of any higher excited states back to lower vibrational levels of S_1 (Fig. 1.8a) [16].

1.3.1 Orientational photoselection with two photon absorption

Whereas single photon absorption depends on the projection of a single photon electric field onto a transition dipole moment, the amplitude of two photon absorption depends on the double projection of two electric field vectors onto a molecular tensor [21]. The general form of this tensor is given as a 3×3 matrix $\boldsymbol{S}$ and the transition rate can accordingly be written as [22]

$$\text{transition rate} \propto |E_1 \cdot \boldsymbol{S} \cdot E_2| = \left| \begin{pmatrix} e_{1x} \\ e_{1y} \\ e_{1z} \end{pmatrix} \begin{pmatrix} S_{xx} & S_{xy} & S_{xz} \\ S_{yx} & S_{yy} & S_{yz} \\ S_{zx} & S_{zy} & S_{zz} \end{pmatrix} \begin{pmatrix} e_{2x} & e_{2y} & e_{2z} \end{pmatrix} \right| \tag{1.31}$$

where E_1 and E_2 are the electric field vectors of the two incident photons. For absorption of two identical photons $E_1 = E_2$, and for the assumption that fluorophores are planar, $\boldsymbol{S}$ reduces to a 2×2 matrix with no z-components. Fluorophores such as fluorescein and rhodamine, which have strong transitions, typically have only one non-zero element (S_{xx}) and in such cases $\boldsymbol{S}$ can be approximated as a single element parallel to the single photon absorption dipole $\boldsymbol{\mu}_{\text{abs}}$ [23].

Using the approximation that the molecular tensor is a single element, and assuming that the excitation beam is linearly polarised and that the two absorbed photons are identical, each individual photon has a $\cos^2\theta$ probability of being absorbed and hence the number of excited molecules becomes

$$p_{\text{2PA}}(\theta, \phi) \propto \cos^4\theta \sin\theta \mathrm{d}\theta \mathrm{d}\phi. \tag{1.32}$$

This is the two photon equivalent of Eq. 1.12 and the maximum anisotropy following two photon absorption can be calculated as in Section 1.2.2 as $R_0 = 0.57$. Even though emission is still occurring from S_1 to S_0 following two photon absorption, the increased angular dependence of two photon absorption compared to single photon absorption generates a narrower angular range of excited dipoles and hence a higher emission anisotropy.

Two photon absorption introduces a $Y_{40}(\theta, \phi)$ spherical harmonic component

$$Y_{40}(\theta, \phi) = \left(\frac{1}{4\pi}\right)^{\frac{1}{2}} \frac{3}{8} \left(35\cos^4\theta - 30\cos^2\theta + 3\right), \tag{1.33}$$

and $\cos^4\theta$ can accordingly be expressed in spherical harmonics as

$$\cos^4\theta = \left(\frac{\sqrt{4\pi}}{5}\right) \left(Y_{00}(\theta, \phi) + \frac{20}{7\sqrt{5}} Y_{20}(\theta, \phi) + \frac{8}{21} Y_{40}(\theta, \phi)\right). \tag{1.34}$$

Using Eq. 1.24, $P(\theta, \phi)$ can be written as

$$P(\theta, \phi) = \left(\frac{1}{\sqrt{4\pi}}\right) \left(Y_{00}(\theta, \phi) + \frac{20}{7\sqrt{5}} Y_{20}(\theta, \phi) + \frac{8}{21} Y_{40}(\theta, \phi)\right). \tag{1.35}$$

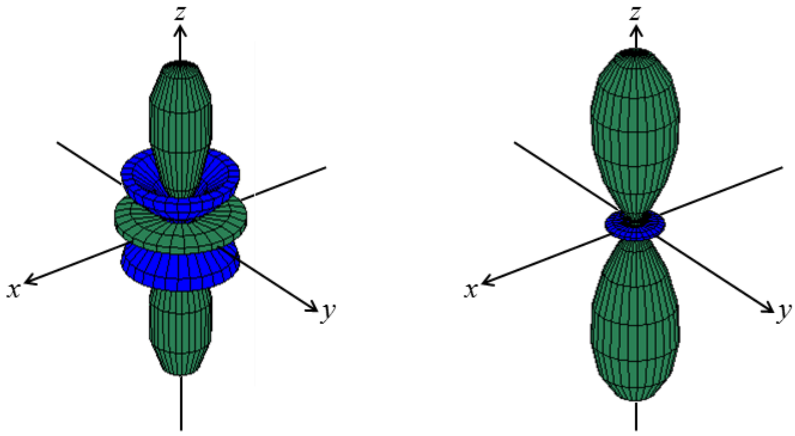

$Y_{40}(\theta,\varphi)$ $\qquad$ $Y_{00}(\theta,\varphi)+\frac{20}{7\sqrt{5}}Y_{20}(\theta,\varphi)+\frac{8}{21}Y_{40}(\theta,\varphi)$

Figure 1.9: Spherical harmonic plots showing components in two photon absorption.

1.4 Time correlated single photon counting

In order to obtain information about fluorescence behaviour over time, time-resolved detection is necessary. Throughout this thesis the method of time correlated single photon counting (TCSPC) will be used for observing fluorescence emission on a nanosecond timescale. TCSPC is essentially a highly accurate stopwatch which makes repeated measurements of the time between excitation (absorption) and emission and as such can build up a histogram of excitation-emission intervals representing the decay of the excited state.

1.4.1 TCSPC instrumentation

The basic requirements for TCSPC are a fast pulsed laser source, which provides a train of excitation pulses typically at kHz-MHz repetition rates, a detector sensitive to single photons, such as a photomultiplier tube or single photon avalanche diode, and electronics for sensitive measurement of times between excitation and emission events. The basic electronics for TCSPC are shown in Fig. 1.10. The two input signals for TCSPC are a synchronisation (sync) signal from the excitation laser and a photoelectron generated by the detector. There are two modes which can be used to generate timing information: forward start-stop mode, where the laser sync signal starts the ‘stopwatch’ and the detector signal stops it, and reverse stop-start mode where the detector signal starts the stopwatch and the next laser sync pulse stops it [24]. Most TCSPC systems operate in reverse stop-start mode as this allows for counting at a slower rate (i.e. one limited by the detection frequency, which is typically $< 1\%$ of the excitation frequency); this is usually necessary to avoid missing detections occurring during the time taken for the system electronics to reset (in the range 0.3 – 2µs [24]). However, the TCSPC system used throughout this thesis contains an inbuilt 'divider' which is capable of reducing the effective input rate in forward start-stop mode to a maximum of 10MHz without missing detections. Therefore in the description of TCSPC provided below, only the forward start-stop mode will be considered. Figure 1.10 shows a general overview of TCSPC instrumentation; the specific TCSPC apparatus used for experiments in this thesis is described in the Methods sections of later chapters.

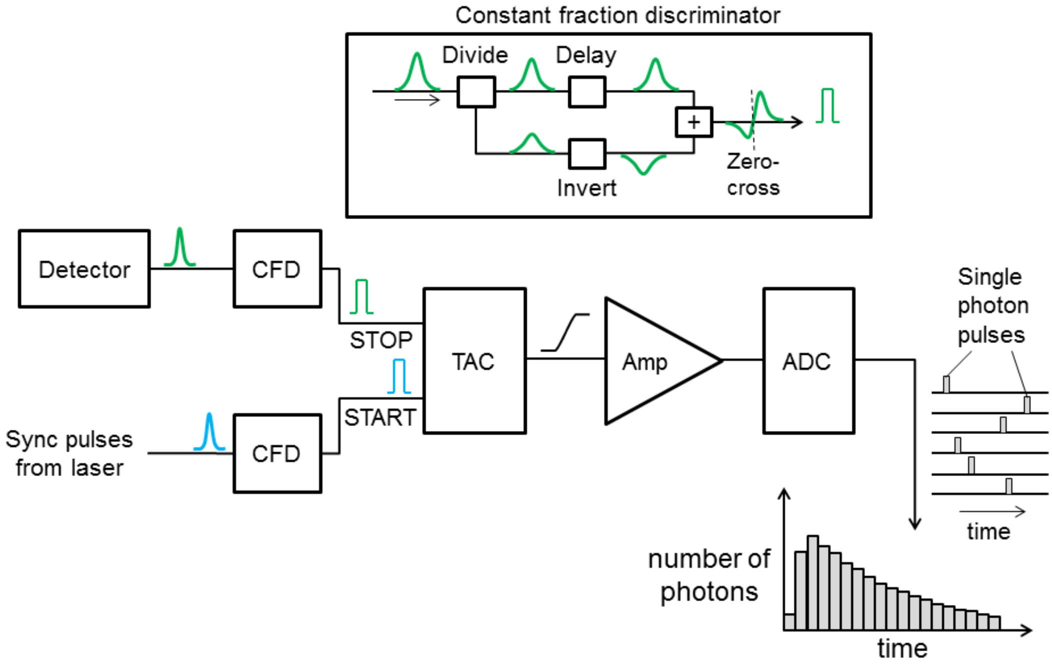

Figure 1.10: Schematic of TCSPC electronics. Inset: schematic of constant fraction discriminator operation. Abbreviations used: CFD - constant fraction discriminator, TAC - time to amplitude converter, Amp - amplifier, ADC - analog to digital converter. Adapted from [25].

The time between the 'start' sync signal and the 'stop' detector signal represents the time between absorption and spontaneous emission (plus a small amount of electronic delay). Only the first photon detected per excitation pulse is measured; TCSPC electronics are typically not fast enough to measure more than one photon from a single excitation pulse, and count rates in TCSPC are adjusted such that the majority of laser pulses do not result in an emission [2].

To combat timing discrepancies which could arise from determining signal times from threshold voltages (as there is non-preventable variation of the signal amplitude for each pulse), both signals pass through constant fraction discriminators (CFDs). A CFD manipulates the waveform of a signal pulse to produce a waveform whose zero crossing value is independent of its original amplitude (Fig. 1.10, inset). The sync and detector CFDs then send timing signals to a time to amplitude converter (TAC), which starts linearly increasing its voltage upon receiving the sync signal and stops increasing its voltage upon receiving the detector signal. The voltage from the TAC is then amplified and passed through an analog to digital converter (ADC) which converts the voltage into a numeric time value which is fed into computer memory. The individual times registered using TCSPC are binned and summed to form a fluorescence lifetime histogram, from which the fluorescence lifetime can be calculated through exponential fitting.

There are several practical considerations for collecting reliable data using TCSPC. The detector count rate should typically be $\sim 1\%$ of the laser repetition rate, as counting at a higher rate (i.e. > 1 photon per excitation pulse) could bias the lifetime histogram to shorter times: if multiple photons are produced per excitation pulse, the TCSPC system will detect the first photon but not the later ones [2]. As a result of this limitation measurement duration (rather than laser intensity) should be adjusted to ensure that enough photons are collected to satisfy exponential fitting statistics for lifetime calculations [26]. Appropriate choice of detector is also important, as the detector needs a fast response time and sufficient gain.

It is important to note that the measured fluorescence lifetime histogram is a convolution of the true excited state decay of the fluorophore with the instrument response function (IRF) of the TCSPC system. The IRF limits the timing precision of TCSPC and arises from a combination of factors such as the uncertainty in the detector timing, the finite width of the excitation pulses and timing jitter in the electronics [27]. Therefore fluorescence lifetime histograms are frequently deconvolved with the measured IRF of the TCSPC system before fitting to gain a more accurate measurement of the excited state decay. In TCSPC systems where the detector is unlikely to be damaged if exposed to low-intensity laser light, the IRF can be measured by examining the histogram obtained from back-reflecting the excitation laser off a glass coverslip. Otherwise, to avoid damage to more sensitive detectors, the IRF can be measured from the histogram obtained from illuminating a non-fluorescent sample such as a scatterer (e.g. dilute milk [15]) or a sample displaying second harmonic generation (e.g. KDP crystals [10]) with the excitation laser.

1.4.2 Polarisation-resolved fluorescence measurements

The measurement of total (anisotropy-free) fluorescence intensity decays and time-resolved anisotropy decays requires polarisation-resolved measurements of fluorescence such that the intensity components parallel to and perpendicular to the excitation polarisation ($I_{\|}$ and $I_{\perp}$, Section 1.2.2) can be separated.

When a single detector is used, a polariser placed at the 'magic angle' of 54.7° allows for detection of a signal proportional to the total fluorescence intensity $I = I_{\|} + 2I_{\perp}$ [1]. However, if an anisotropy decay is to be obtained then $I_{\|}$ and $I_{\perp}$ must be measured separately. This can be achieved using either one or two detectors; with one detector, a linear polariser in the detection path can be alternately rotated between parallel and perpendicular polarisations with sequential collection of $I_{\|}$

and $I_\perp$ (e.g. [28, 15]). With two detectors, the fluorescence can be split into its $I_{||}$ and $I_\perp$ components using a cube polariser, with each component directed to a different detector. The polarisation-resolved measurements presented in this thesis exclusively use the latter two detector approach.

To account for any detector polarisation sensitivity, or different detector efficiencies, in polarisation-resolved measurements a correction known as the G-factor must be made. This can be achieved by comparing measurements taken with vertically and horizontally polarised excitation beams, by 'tail-matching' the intensities of the two detected polarisations in later parts of the decay, or by 'head-matching' the anisotropy decay such that R_0 equals its predicted value [25].

1.5 Use of fluorescence in biological imaging

Microscopy has been a valuable tool throughout the history of biological research for studying the structure and function of cells. Simple compound microscopes developed in the 15th and 16th centuries by scientists such as Robert Hooke and Antonie van Leeuwenhoek were capable of magnifying specimens but not of generating contrast. The need for greater contrast formation for identification of different biological features was satisfied with the advent of sample staining techniques in the 19th century. Examples of stains used in this period include carmine, which stains the nucleus but not the cytoplasm, and silver nitrate, which selectively stains nerve cells [29].

The first uses of fluorescence in biological microscopy were in observing autofluorescence, which arises from endogenous fluorescent molecules within cells, such as NADH and tryptophan, which fluoresce when excited by UV wavelengths. Fluorescent dyes were first used in the early 20th century when fluorophores such as fluorescein were injected into organs to generate contrast [29]. However, it was not until the 1960s and the development of dichroic mirrors that fluorescence microscopy became a major tool in cell biology. Dichroic mirrors have different transmission and reflection properties depending on the wavelength of incident light; for example, short wavelength light can be reflected by a dichroic mirror to excite a fluorescently labelled sample, and the longer wavelength Stokes-shifted fluorescence can be transmitted to an ocular or detector. Sample labelling methods also became more advanced and fluorescent dyes could be conjugated to antibodies for highly specific labelling of biological molecules to generate high contrast. From this point onwards fluorescence microscopy became an incredibly important tool, leading to instrument development and advances in fluorescence labelling techniques.

1.5.1 Confocal microscopy

One of the most important advances in modern fluorescence microscopy has been the development of the confocal microscope. In epifluorescence (widefield) microscopy a source of excitation light, such as a xenon or mercury arc lamp, is focused through an objective onto a large area of a labelled sample and fluorescence emitted from the sample is collected back through the objective and used to create an image. However the images produced by this method suffer from contamination from out-of-focus fluorescence - that is, fluorescence arising from fluorophores in the light path outside the focal plane. A solution to this problem was first suggested by Marvin Minsky [30] and is known as the confocal principle.

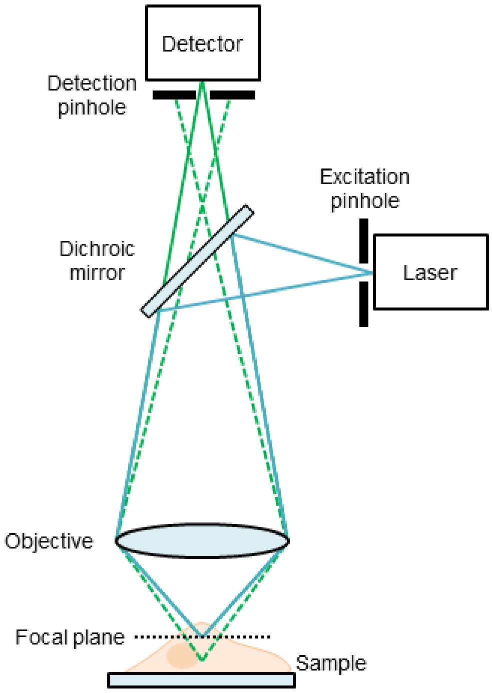

Figure 1.11: Illustration of the confocal principle. Excitation light (blue) passes through an excitation pinhole, is reflected off a dichroic mirror and is focused into the sample through an objective lens. Fluorescence from the focal plane (solid green line) is collected through the objective, passes through the dichroic mirror and through the detection pinhole into the detector. Fluorescence arising from outside the focal plane (dashed green line) is rejected by the detection pinhole.

In confocal microscopy, instead of illuminating a large area of the sample with a widefield source, a point source of illumination is used. This can be achieved either by placing a pinhole after a widefield source of illumination, or by illuminating the sample with a laser. The fluorescence is then collected in the same way as for epifluorescence microscopy, except that a second pinhole is placed before the detector. The pinhole is positioned such that only light emitted from the focal plane will correctly focus down and pass through the pinhole, whereas out of focus fluorescence will be rejected by the pinhole (Fig. 1.11). An image can then be generated by sequentially (raster) scanning the point source of illumination over the sample and collecting fluorescence emitted from each point.

Whilst confocal microscopy on its own can produce detailed images of subcellular structure, this information is more qualitative than quantitative. Many techniques have grown from confocal microscopy which can provide more quantitative information, such as fluorescence lifetime imaging and FRET among many others.

1.5.2 Fluorescence lifetime imaging

Fluorescence lifetime imaging (FLIM) is a method by which fluorescence lifetimes of fluorophores are measured in a biological sample and represented in an image. Fluorescence lifetime measurements can provide important information about the immediate environment of a fluorophore, such as local protein binding.

There are various implementations of FLIM including widefield FLIM and frequency domain FLIM, however the focus here will be on laser-scanning time domain FLIM. Time domain measurements are taken using TCSPC, with fluorescence lifetime histograms generated for each pixel within the image. To collect sufficient photons for reliable fitting of these histograms for determination of fluorescence lifetimes, image acquisition times in FLIM are often substantially longer than in confocal microscopy as is subsequent image analysis, where exponential fitting is performed at each pixel in the image.

One use of FLIM is to assess the lifetime properties of autofluorescence for imaging cell metabolism. The coenzymes NAD and NADP are involved in cell metabolism, and are required for ATP production and biosynthesis respectively. The reduced forms of these two coenzymes, NADH and NADPH, display autofluorescence upon excitation with UV light (or two photon excitation), and fluorescence lifetime measurements can reveal whether these molecules are bound to proteins or not. From these measurements the metabolic state of a cell can be determined and so the metabolic requirements of different cell lines and diseased cell states can be investigated without exogenous fluorophores or biochemical intervention [17].

The other main way in which FLIM is commonly used is in FRET microscopy, which assesses close-range (nanometre scale) interactions between biomolecules. The biomolecules of interest are labelled with donor and acceptor fluorophores and the characteristics of the donor and/or acceptor fluorescence are monitored (see Section 1.1.6). By using time-resolved fluorescence measurements, quantitative information can be gained on the nature of the donor-acceptor interaction (e.g. intermolecular distances, orientations). FRET microscopy is often used to study protein oligomerisation, for example in determining the conformation in which the protein PDK1 undergoes homodimerisation [31]. A more complete review of the applications of FLIM microscopy for FRET of biological molecules is provided by Wallrabe and Periasamy (2005) [32].

1.6 Biological requirements for imaging

Fluorescence imaging of biological tissue presents three basic requirements: 1) development and selection of appropriate fluorophores for biological imaging and strategies for introducing them into samples; 2) the use of appropriate illumination sources for obtaining sufficient signal with minimisation of sample degradation; 3) specific considerations for the imaging of living samples.

1.6.1 Fluorophore requirements and labelling techniques

While endogenous fluorescence and non-specific fluorescent stains were used in the early years of fluorescence microscopy, the majority of modern microscopy techniques are performed on samples which have been specifically labelled. Fluorophores used in biological imaging can be broadly classed into two categories: those which can be genetically encoded into the sample and those which cannot. Both classes of fluorophore must be specifically targeted to label the biological molecule of interest, and must have means by which to access these molecules. They also need to have high enough quantum yields to generate sufficient contrast in images and appropriate spectra for excitation with commonly available laser lines. Figure 1.12 shows the structures and sizes of components used in fluorescence labelling.

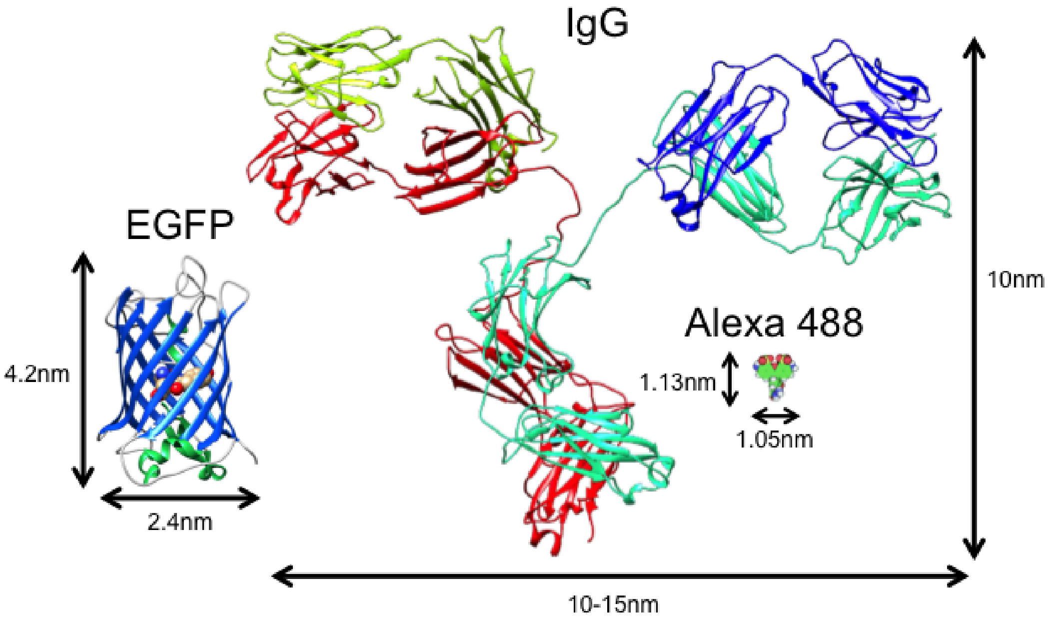

Figure 1.12: Structures and sizes of molecules used in fluorescent labelling of biological structures. EGFP dimensions obtained from Hink et al (2000) [33], structure rendered from PDB entry 2Y0G, chromophore represented in spacefill. IgG dimensions obtained from Reth (2013) [34], structure rendered from PDB entry 1IGT. Alexa 488 spacefill structure and dimensions obtained from Weber et al (2004) [35]. All three structures drawn to scale.

Non-genetically encodable fluorophores

An important breakthrough in sample labelling came with the development of immunofluorescence. Immunofluorescence is a technique by which antibodies against a specific molecule are raised and chemically labelled with a fluorophore, a technique first developed in 1942 [36]. The general structure of an antibody (IgG) is shown in Fig. 1.12 for comparison with the size of fluorophores. There are now antibodies against many different proteins, which can be conjugated to fluorophores spanning the visible spectrum. Common fluorophores used in immunofluorescence include the Alexa dyes [37] (e.g. Fig. 1.12, Alexa 488), and the Cy dyes [38].

Immunofluorescence can be used to directly label molecules, i.e. where a single, fluorescently labelled antibody species is applied to the sample, however indirect immunofluorescence is more commonly used (Fig. 1.13). Indirect immunofluorescence is a two-step process whereby unlabelled primary antibodies raised against the protein of interest are applied to the sample first, and then fluorescently-labelled secondary antibodies are applied which bind to the primary antibodies. In indirect labelling methods, many secondary antibodies bind to a single primary antibody which leads to amplification of the fluorescence signal [39].

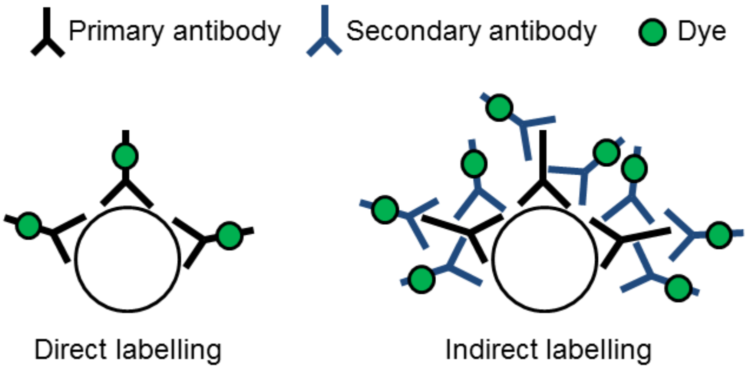

Figure 1.13: Demonstration of two different labelling strategies for immunofluorescence.

Cells are not permeable to macromolecules such as antibodies and fluorophores, and so the sample needs to be prepared, or ‘fixed’, such that the antibodies can access intracellular proteins. However fixation kills the sample and so immunofluorescence cannot be used for live-cell imaging (except for cases where the molecules of interest are found on the external surface of cells and can be readily accessed by antibodies without the need for fixation). Examples of non genetically encodable fluorophores used in cellular imaging which do not require antibody labelling techniques include fluorophores which sense ions such as Ca^{2+} (e.g. the OGB family of dyes, Fura-2 [40]) and fluorophores which preferentially stain DNA (e.g. DAPI).

Genetically encodable fluorophores

A major drawback of immunofluorescence is the requirement for the fixation of samples for studying intracellular components. An alternative class of fluorophores, known as fluorescent proteins (FPs), can be expressed in living cells with specificity for the protein of interest. FPs occur naturally in animals such as jellyfish and corals, but have been exploited by biologists for labelling purposes. This was first demonstrated with green fluorescent protein (GFP), which was purified from the jellyfish *Aequorea victoria* and the gene encoding the protein sequenced. This genetic code has since been introduced into other organisms, where GFP forms a photostable fluorescent protein without the need for any other *A. victoria* gene products, and does not cause toxicity [41].

The chromophore of wild type GFP is formed from three amino acids - serine, tyrosine and glycine - attached to an α-helix running through the centre of an 11-stranded β-barrel (Fig. 1.12, EGFP) [42]. This tertiary protein structure essentially shields the chromophore from the local environment, which helps prevent collisional de-excitation and photobleaching. Genetic mutations have been made to GFP to enhance its photostability [43], with variants such as EGFP, and also to modify the GFP chromophore such that both emission and excitation spectra are shifted (the absorption maximum of EGFP is $\sim$ 488nm and maximum emission is at $\sim$ 509nm), leading to a variety of different coloured FPs such as cyan fluorescent protein (CFP) and yellow fluorescent protein (YFP) [44]. All of the GFP-derived fluorescent proteins have tertiary structures similar to that shown in Fig. 1.12, with the differences between variants arising from amino acid substitutions in the chromophore itself or in the local environment of the chromophore [43].

FP genes are introduced into the genomes of cell lines and model organisms to create fusion proteins, whereby the protein of interest is expressed with the FP intrinsically attached to it. Indeed, GFP has been successfully targeted to virtually all known subcellular compartments and organelles [42]. As all cells expressing a FP fusion protein do not require further labelling, they can be studied without further fixation, enabling live cell imaging both *in vitro* and *in vivo*.

1.6.2 Interaction of light with biological tissue

Light travelling through labelled biological specimens can interact not just with the fluorophores, but also with the biological structures themselves. This can lead to degradation of image contrast and in extreme cases damage to the sample.

Scattering

Scattering is an inevitable phenomenon for light travelling through an inhomogeneous medium, especially in an environment such as a cell where there are structures on scales smaller than, comparable to and larger than the wavelength of the illuminating light. There are three regimes by which light can be scattered in a biological sample: Rayleigh, where objects $\sim$ 10% of the wavelength λ cause wavelength-dependent scattering proportional to λ^{-4} [45], Mie, caused by objects of all sizes, and Raman, where energy is transferred between photons and vibrational modes of molecules [46].

Scattering can be problematic as it impedes both excitation light travelling to the focal plane of the sample, but also fluorescence emitted from fluorophores within the sample. As a result, scattering leads to poor signal from samples and decreases the contrast of images. This also impacts upon the penetration depth of excitation light into a sample, with Rayleigh scattering occurring more frequently at shorter wavelengths and limiting the use of visible wavelengths to shallow ($< 100\mu$m) imaging [45].

To negotiate the problem of penetration depth, two photon excitation (TPE) is used for deep tissue imaging. TPE microscopy works similarly to confocal microscopy, with a laser beam raster scanning across a region of interest in the sample, but with an illumination source suitable for inducing two photon absorption (i.e. a pulsed laser capable of generating wavelengths at approximately double the single photon absorption peak, Section 1.3). Wavelengths used in TPE microscopy are typically in the near-infrared region of the spectrum, and these longer wavelengths are scattered less by the sample than those used in (single photon excitation) confocal microscopy. A further benefit of TPE microscopy is that fluorescence is typically confined to the focus of the excitation beam, as this is the only region where there is sufficient spatio-temporal photon density for excitation of fluorophores to occur, and as such there is inherent confocality in TPE microscopy. However, exponentially increasing laser powers are required for deeper penetration [45], and this combined with the quadratic dependence on pulse intensity for TPE means that laser power in TPE microscopy is substantially higher than in single photon excitation microscopy (Eq. 1.30).

Sample heating

Sample heating in laser scanning microscopy occurs predominantly through absorption of photons by water molecules, which is a wavelength-dependent process. Water is effectively transparent to UV and visible wavelengths, and so little heating occurs during single photon excitation. However the absorption coefficient of water becomes non-negligible as wavelength increases into the infrared, leading to the occurrence of sample heating in TPE microscopy. The temperature increase depends on the laser power and size of the beam waist, and as such sample heating is mainly confined to the focal volume in TPE microscopy rather than the whole beam path [47].

Phototoxicity

Whilst many fluorophores used in fluorescence microscopy are not directly toxic to cells, they can undergo photochemical reactions which can produce toxic entities. The most common example of this is the production of singlet oxygen, also referred to as reactive oxygen species (ROS), which can be formed through the reaction of fluorophores which have crossed into the triplet manifold with molecular oxygen. Although cells produce ROS as a by-product of normal metabolism, an imbalance of ROS can lead to oxidative stress and subsequent triggering of apoptotic (cell death) pathways [48].

A limited number of studies have made attempts to quantify phototoxicity in living cells. Dixit and Cyr (2003) [49] used mitotic (dividing) cells expressing FPs as an assay for cellular function. As single photon excitation intensity was increased, cells arrested mitosis in progressively earlier phases, with cells imaged at the highest laser intensities tested completely unable to undergo mitosis. Furthermore, shorter wavelengths (<500nm) exacerbated photodamage compared to longer wavelengths. The high powers required for TPE microscopy are also capable of triggering ROS production, despite the longer wavelengths, but can also cause non-ROS phototoxicity through direct breakage of DNA strands and optical breakdown of other cellular structures [50].

1.6.3 Specific requirements for live cell imaging

Fluorescence microscopy of living samples requires an additional set of considerations; not only must the intensity of the detected fluorescence signal be high enough to generate sufficient contrast within the image, but measures must be also be taken to prevent death of the sample, as a result of phototoxic processes (Section 1.6.2) or otherwise. Living samples must be surrounded by medium of physiological pH and metabolite and ion concentrations to maintain cell homeostasis, and this medium should be free from fluorescent compounds to minimise background fluorescence [51]. Furthermore, the sample itself must be labelled using a minimally invasive technique such as with fluorescent proteins (Section 1.6.1). Living samples may also require temperature-controlled microscope stages, chambers where the level of CO_2 can be regulated and regular perfusion of fresh medium, all of which complicate experimental set-ups.

Live cell imaging is frequently preformed to observe dynamic processes in cells which can occur over several minutes (such as membrane recycling [52]) to fractions of seconds (such as calcium signalling [53]). Therefore it is clear that microscope hardware must be capable of acquiring images at an appropriate rate to characterise such processes. For confocal laser scanning microscopy, the highest rates of image acquisition are obtained using resonant scanning mirrors, which can scan regions of interest at rates up to ~ 30 frames per second [54] or acousto-optic deflectors which can rapidly move the laser focus between regions of interest in the sample [53].

Chapter 2

Development of a novel super resolution microscopy technique. Part I: Theory and Methods

Elements of this chapter have been published in: R.J. Marsh, S. Culley and A. J. Bain, "Low power super resolution fluorescence microscopy by lifetime modification and image reconstruction," Optics Express vol. 22, pg. 12327-38, 2014. This manuscript is provided in Appendix C.

Chapters 2 and 3 document the theory, development and application of a novel super resolution microscopy technique: lifetime image reconstruction super resolution (LIR-SR). Aside from the fundamental photophysical processes discussed in Chapter 1, LIR-SR uses stimulated emission as a tool to generate fluorescence lifetime variations in confocal microscopy images, which in turn can be reconstructed to produce super resolution images. This chapter introduces the physics of stimulated emission and the concept of the resolution limit in fluorescence microscopy, along with a brief description of commonly used super resolution microscopy techniques. The theory behind LIR-SR is then developed along with simulated data, and the experimental and computational procedures used to implement the technique are described.

2.1 Stimulated emission depletion

Stimulated emission is the process whereby a quantum system in an excited state can be de-excited to a lower energy level via resonant interaction with a photon. The lost energy is released as a photon with the same frequency, phase and propagation direction as the stimulating photon [55]. Stimulated emission was introduced phenomenologically by Einstein [8] and is the basis for optical amplification and laser action. The technique of stimulated emission depletion (STED) was initially

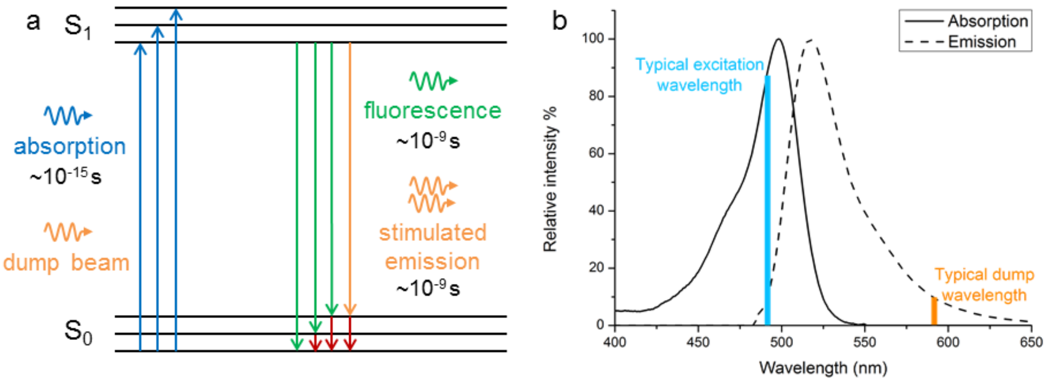

Figure 2.1: Stimulated emission schematic. a) Jablonski diagram showing stimulated emission transition. b) Absorption and emission spectra of fluorescein showing typical excitation and dump wavelengths.

developed in spectroscopy to study high vibrational energy levels in the electronic ground states [56], using a laser pulse resonant with $S_1 \rightarrow S_0$ transitions (the 'dump' beam) to remove population from the excited state. The amount of STED can then be quantified as a reduction in fluorescence from S_1 to S_0. Stimulated emission is shown on a Jablonski diagram in Fig. 2.1a.

STED is governed by the same electric dipole selection rules as spontaneous emission and absorption. The changes to the excited state population and its alignment depend on the energy and polarisation of the dump field, in addition to the dynamics of population flow between S_1 and other states in the molecule [28]. Qualitatively the STED probability is maximised for molecules whose emission transition dipole moments are oriented parallel to the dump polarisation and minimised for molecules whose emission transition dipole moments are oriented perpendicular to the dump polarisation, with the angular dependence again following a $\cos^2\theta$ dependence (where θ is the angle between the emission dipole moment of the molecule and the dump electric field vector) [28]. As a result, as well as altering the population of the excited state by providing an additional route back to the ground state, STED also alters the orientational distribution of the excited state.

The efficiency of STED depends on several other factors such as the temporal profiles of the excitation (here referred to as the pump) and dump beams, the shape of the dump pulse, the wavelength of the dump beam and the intensity of the dump beam. The lifetime of the higher vibrational levels of S_0 is on the order of 200-800fs [9, 57, 15], and a consequence of this finite lifetime is that the dump beam can cause repumping from these energy levels to S_1. This can be minimised by using a pulsed dump beam with a pulse length of $>$ 1ps, or a continuous wave (CW) dump beam. The effect of dump pulse length on STED efficiency is discussed in more detail in Chapter 4; in this chapter only CW dump beams are considered. Conversely, shorter pump pulses provide higher STED efficiencies as these minimise subsequent absorption in molecules which have been rapidly returned to S_0 through stimulated emission. The shape of the dump pulse can also impact upon the efficiency of STED. For example, for short, high energy dump pulses, rectangular pulses are less efficient than Gaussian pulses of equivalent pulse energy. This is due to rectangular pulses causing an abrupt transition into a saturating regime where the rate of STED exceeds that of ground state vibrational relaxation, leading to re-excitation from S_0 to S_1; for Gaussian pulses this regime is only reached at the peak of the pulse and thus the majority of a Gaussian dump pulse is non-saturating [15]. As dump pulses become longer, with the pulse energy spread over a longer time, neither Gaussian or rectangular pulses are expected to reach this saturating regime and thus for longer pulses the efficiency of the two different pulse shapes is expected to be comparable. The dependence of STED on dump wavelength follows the spontaneous emission spectrum of the fluorophore: stimulated emission is more efficient when the dump is tuned to regions of the spectrum where non-negligible emission is observed from the fluorophore (e.g. [9, 57]). However, the dump wavelength must also remain at a value where the fluorophore displays negligible absorption to avoid further population of the excited state (Fig. 2.1b). Finally, the rate at which STED occurs is linearly dependent on the dump beam intensity, and so when the intensity of the dump beam is sufficiently high the excited state will be increasingly likely to de-excite through stimulated emission as opposed to fluorescence.

The temporal and spatial evolution of fluorescence in a sample imaged with a pulsed pump beam and CW dump beam is the basis of LIR-SR, and is discussed further in Sections 2.4 and 2.5.

2.2 The resolution limit in microscopy

Whilst the fluorescence microscopy techniques described in Chapter 1 are commonplace tools used in cell biology, they also have limitations. One major limitation of conventional fluorescence microscopy is resolving power, which is limited to 200-300nm for single photon excitation, and imaging biological specimens at higher resolutions than this has historically required the use of electron microscopy. Although electron microscopy can yield single nanometre scale resolution, samples must undergo intensive preparation (e.g. fixation, dehydration, embedding in resin and sectioning) prior to imaging, precluding the possibility of live cell imaging [58]. In the last decade the necessity for optical techniques capable of imaging at higher resolutions than conventional fluorescence microscopy can provide has led to the development of several so-called super resolution microscopy techniques.

Resolution in fluorescence microscopy is limited by diffraction, and as such the highest resolution achievable in conventional fluorescence microscopy is often termed the ‘diffraction limit’. Point sources of light diffracting through a circular aperture produce a broadened diffraction pattern known as an Airy disk, and overlapping

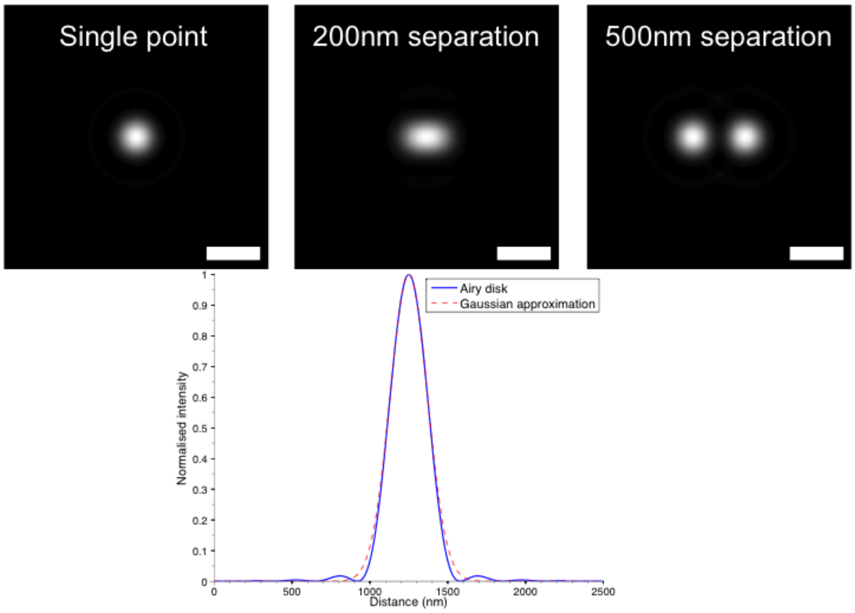

Figure 2.2: Airy disk created by diffraction of a single point source of fluorescence, and two point sources of fluorescence separated by distances smaller than and greater than the resolution limit of the simulated system (resolution limit of simulated system ∼ 205nm, NA = 1.2 and λ = 490nm). Line plot shows 1D profile across the centre of a single point with Gaussian approximation plotted as a red dashed line. Scale bars = 500nm.

of these Airy disks fundamentally limits the resolution of a microscope (Fig. 2.2) [59]. The smallest resolvable separation between two light sources, or fluorescent objects, was first described by Ernst Abbe in 1873, and depends on the illumination wavelength and focusing power (numerical aperture) of the objective lens. This resolution limit is mathematically formalised as [59]

$$\Delta d = \frac{0.5\lambda}{n \sin\alpha}, \tag{2.1}$$

where Δd is the resolvable distance between two objects in the xy plane, n is the refractive index and α is the half-angle of the cone of focused light. The quantity $n \sin\alpha$ equals the numerical aperture, NA, of the objective. There are other methods of determining the resolution limit, such as the Rayleigh criterion which is identical to the Abbe limit except that it contains a coefficient of 0.61 as opposed to 0.5 [60], and defines diffraction-limited resolution as the distance where the central maximum of one diffraction pattern overlaps with the first minimum of a neighbouring diffraction pattern. However, regardless of the exact definition of resolution, the common factors limiting the resolution of an optical microscope are the wavelength of the illuminating light and the numerical aperture of the objective.

The three-dimensional volume occupied by the laser light focused in a microscope is referred to as the point spread function (PSF), and an image can be described as the convolution of the fluorescently-labelled structure with the PSF as

$$I(x, y, z) = S(x, y, z) \otimes P(x, y, z) \tag{2.2}$$

where I, S and P are the image, structure and PSF respectively. The intensity profile of the PSF in the xy plane is typically approximated to a Gaussian distribution of full width at half maximum (FWHM) approximately equal to Δd (Eq. 2.1, Fig. 2.2). The mathematical form of the PSF in the z direction has been calculated to be a $\text{sinc}^2(z)$ function for a microscope with an ideal point source of illumination and an ideal point detector [61]. However in many practical applications such as fluorescence correlation spectroscopy, the form of the axial PSF is frequently approximated to a Gaussian or Lorentzian distribution, although for an overfilled, high-NA objective (such as that used for imaging in this thesis) the true analytical form has not been determined [62]. Inspection of the axial intensity distributions measured with the confocal microscope used in this thesis (Section 3.3) showed none of the side-lobes expected from a $\text{sinc}^2(z)$ function or seen by Hess and Webb (2002) [62]; these were likely blurred out due to the low signal-to-noise ratio above and below the focal plane. As these distributions were adequately fitted by Lorentzian distributions, here the axial component of the PSF is approximated to a Lorentzian function.

2.3 Established super resolution techniques

Several super resolution techniques have been developed and are now available commercially. The most popular super resolution techniques currently used are PALM, STORM, SIM and STED, which are capable of providing sub-diffraction limited resolution. The relative merits of these techniques and their limitations are described below.

2.3.1 PALM and STORM

PALM (photoactivated light microscopy) [63] and STORM (stochastic optical reconstruction microscopy) [64] are similar techniques which are often referred to as pointillistic, localisation or stochastic microscopies, and are both widefield techniques. The basic mechanisms underlying PALM and STORM are the same; samples are labelled with photoswitchable or photoactivatable fluorophores and these are turned on and off, with the precise locations of each individual fluorophore eventually determined and used to reconstruct a super resolution image (Fig. 2.3).

Photoswitchable fluorophores have a dark ('off') state and an excitable ('on') state, and methods must be available to facilitate switching between these two states. During a PALM or STORM imaging cycle, all fluorophores in the sample are first forced into their non-fluorescent off state, typically via bleaching with an intense flash of laser light. A small subset of fluorophores are then activated into their on

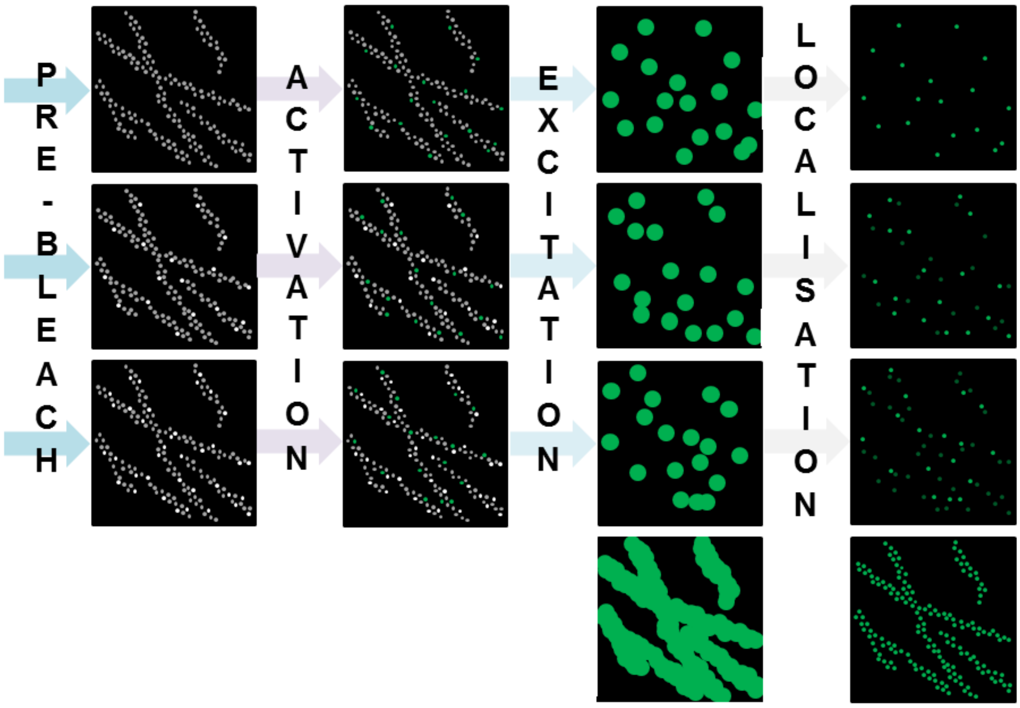

Figure 2.3: Imaging cycles for PALM and STORM microscopy. Top row: a labelled sample undergoes pre-bleaching to force all fluorophores into the dark state (grey circles). A small subset of these fluorophores are then activated (small green circles) and then excited and imaged to produce a diffraction-limited image of the activated fluorophores (large green circles). The centres of these points are then localised using appropriate software. Second and third rows: the cycle is repeated, except that the previously imaged fluorophores can no longer be excited due to bleaching (white circles). Bottom row: summing the images acquired will build a diffraction limited image (left), whereas summing the localised centres of each fluorophore will produce a super resolution image (right).

state capable of fluorescence, often via irradiation with a UV laser, and this activated subset of fluorophores is then imaged using a (longer wavelength) excitation laser until these fluorophores have undergone photobleaching. A different subset of fluorophores is then activated and imaged until bleaching, and this process is repeated until the majority of fluorophores in the sample have undergone this process [63]. Control of the density of activated fluorophores (i.e. the number of 'on' fluorophores per micron in each camera frame) is determined largely by modulating the intensities of the activation and excitation lasers, as these determine on-switching and bleaching rates respectively. Specialist imaging buffers are also frequently used in PALM and STORM to modulate switching rates and improve photostability of fluorophores [65].

For each set of images taken between activation pulses the location of each fluorescent point is accurately determined, for example by fitting with the known PSF of the microscope. The error in this fitted location is

$$\sigma_{x,y} \approx \frac{s}{\sqrt{N}} \tag{2.3}$$

where s is the standard deviation of the Gaussian PSF being fitted and N is the number of photons collected [63]. Performing this localisation process for each set of collected images and overlaying all localised points yields a super resolution image, with resolutions obtained using PALM and STORM typically on the order of tens of nanometres.

There are a number of factors which limit the performance of PALM and STORM. The photophysical properties of the fluorophores are crucial, as the level of background intensity in images is dictated by the ratio of fluorescence obtained from activated molecules to fluorescence obtained from dark fluorophores, which are still weakly fluorescent [63, 66]. The activated state must also have a sufficiently high quantum yield and be robust enough against photobleaching to generate a high enough number of photons to satisfy Eq. 2.3. In order to get a high enough number of photons to yield high resolution, as well as cumulatively activating a large enough number of fluorophores to obtain sufficient information about the labelled structures, image acquisition times in PALM and STORM are are often several minutes. As such there must be very little motion of fluorophores within the sample and of the sample itself, plus any microscope drift must be corrected to avoid blurring [67]. Longer acquisition times also make the sample susceptible to photodamage, especially as UV wavelengths are often necessary for activation, and so the majority of PALM and STORM imaging is performed on fixed samples.

Despite the challenges, there is considerable interest in developing live cell PALM and STORM. The strategies for implementing this include non-antibody methods of labelling cells with synthetic fluorophores, finding non-toxic buffers to sufficiently maintain the photoswitching behaviour of fluorophores, use of lower laser intensities and development of localisation algorithms to enable concurrent reconstruction during image acquisition [66].

2.3.2 SIM

SIM (structured illumination microscopy) is also a widefield super resolution technique, but does not rely on the photophysical properties of fluorophores, and was first described by Gustafsson (2000) [68]. Here the sample is illuminated with an excitation field with spatially varying intensity, typically a sinusoidal pattern of intense and dim stripes. When two patterns are superimposed upon each other a ‘beat’ frequency or moiré fringes are observed, which depend on the structures of the two patterns (Fig. 2.4a). In the case of SIM there is one known pattern, the excitation field, and one unknown pattern, the fluorophore distribution within the sample, and these lead to the generation of observable moiré fringes. By repeating

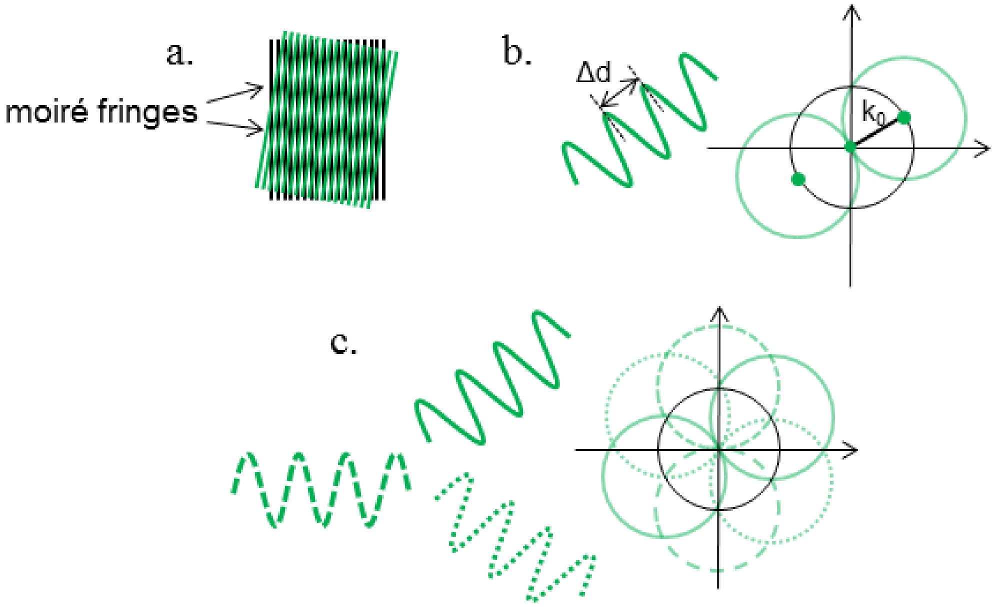

Figure 2.4: Concept of SIM. a) Generation of moiré fringes by overlapping two patterns. b) Left: patterned illumination represented as a sinusoidal waveform of high and low intensities with diffraction-limited spacing. Right: transformation of this pattern in the Fourier domain gives three non-zero components (represented by green dots). The illumination pattern will produce moiré fringes in the areas represented by the green circles, and these are the areas where information has 'moved'. The observable region (radius k_0) now contains information originating from the outer regions. c) Different orientations of illumination pattern allow for information to be gathered from a large region outside of the observable region. Adapted from Gustafsson (2000) [68] and Gustafsson (2005) [69].

the imaging process with different orientations and phases of the excitation pattern, the distribution of fluorophores can be subsequently extracted at higher resolution than when imaging with conventional diffraction-limited widefield methods.

In Fourier space, the number of different spatial frequencies observable in conventional microscopy lie within a circle of radius $k_0 = 1/\Delta d$ (Δd as described by Eq. 2.1), where structural components with higher spatial frequencies (i.e. smaller structures) lie further towards the edge of the circle. This same circle also governs the pattern spacing that can be used in SIM - patterns cannot be used where the spacing is smaller than the diffraction limit. If the illumination pattern in SIM contains a spatial frequency k_1 and the fluorophore distribution in the sample has a frequency k, then moiré fringes will be created at the difference frequency $k - k_1$, which will be observable if $|k - k_1| < k_0$ [69]. Therefore the image created in Fourier space is offset by an amount depending on k_1, and as a result information normally lying outside the circle of radius k_0 becomes accessible as this now lies within the circle (Fig. 2.4b). To isolate the contribution of the fluorophore distribution from the contribution of the structured illumination pattern, imaging is repeated with the pattern shifted to different orientations and phases (Fig. 2.4c). This series of images can then be used to reconstruct the super resolution image [68].

As the highest observable spatial frequency is increased from k_0 to $k_0 + k_1$ using SIM, and the maximum frequency of k_1 equals k_0, the maximum obtainable resolution is a two-fold increase ($2k_0$). For a high numerical aperture objective, this translates to a maximum image resolution of $\sim$ 100nm, which is a relatively minor improvement compared to PALM and STORM where <50nm resolution is readily obtainable. However, SIM is compatible with standard fluorophores used in conventional fluorescence microscopy, laser intensities used are compatible with live cell imaging [70], and image acquisition times are also substantially shorter than in PALM and STORM.

One method which has been developed for increasing the resolution of SIM uses non-linear illumination effects, where saturating emission leads to the generation of harmonics with higher spatial frequencies. The achievable resolution in this case is limited by the number of harmonics that can be distinguished against the background noise, and resolutions down to 50nm have been observed with this method [69]. However the light intensities required for producing a non-linear emission rate increase both photobleaching of the fluorophores and phototoxicity in the sample.

2.3.3 STED microscopy

STED (stimulated emission depletion, as above) microscopy is a laser scanning technique, in contrast to the widefield techniques described above, and was first proposed by Hell and Wichmann (1994) [71]. The sample is scanned with two overlapping laser beams, one of which is an excitation beam as used in laser scanning microscopy with the other being a annular ('donut') shaped beam referred to as the STED beam. The STED beam causes stimulated emission, which strongly suppresses fluorescence from regions where this beam is intense, with fluorescence only emitted from the small hole within the centre of the beam pair (Fig. 2.5).

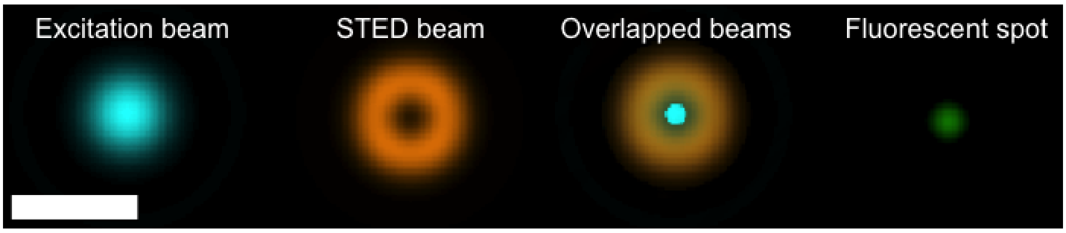

Figure 2.5: Intensity distributions of beams used in STED microscopy and the comparative size of the effective point spread function (fluorescent spot). Scale bar = 500nm.

The excitation wavelength typically coincides with a region of the absorption spectrum where the absorption cross-section is high, as is required for conventional laser scanning microscopy, whereas the STED wavelength is tuned to coincide with the emission spectrum but not the longer wavelengths of the absorption spectrum, as described in Section 2.1. A high degree of STED removes fluorescence from areas around the 'hole' in the annular intensity distribution leaving an fluorescent region significantly smaller than the diffraction-limited focus of the excitation beam (Fig. 2.5); in order to attain close to 100% depletion at the peak of the annular STED beam, on-sample laser intensities on the order of $\sim 10^2\mathrm{MW/cm}^2$ are required [72]. The size of the dark hole in the centre of the STED beam also affects the performance of a STED microscope with smaller, darker holes yielding higher resolutions. For example, most STED microscopes use a vortex phase plate to shape the STED beam, with the quality of the resultant donut sensitive to input polarisation [73, 74] and the spectral width of the laser source [75].

The effect of STED beam intensity on resolution scaling in STED microscopy is given by [76]

$$\Delta d \approx 0.45 \frac{\lambda}{n \sin\alpha \sqrt{1 + \frac{I_{\mathrm{max}}}{I_{\mathrm{sat}}}}}, \tag{2.4}$$

where $n \sin\alpha$ is the numerical aperture as described previously, $\lambda = \lambda_{\mathrm{exc}} \approx \lambda_{\mathrm{STED}}$ where λ_{exc} and λ_{STED} are the wavelengths of the excitation and STED beams respectively. I_{max} is the maximum intensity of the STED beam and I_{sat} is the intensity required to suppress fluorescence intensity to $1/e$ (or $1/2$ as stated in some papers e.g. [77]) of its undepleted value. Equation 2.4 also implies that there is no theoretical limit on the resolution gain in STED microscopy, provided that $I_{\mathrm{max}}/I_{\mathrm{sat}}$ can be sufficiently maximised. There are evidently two main strategies for maximising $I_{\mathrm{max}}/I_{\mathrm{sat}}$: increasing I_{max} and decreasing I_{sat}. Increasing I_{max} simply involves increasing the intensity of the STED beam to yield greater fluorescence suppression and higher resolution; however, this cannot be increased infinitely due to the finite powers of the lasers used and also as fluorophores experience photobleaching at high STED intensities [78]. I_{sat} is a fundamental property of the fluorophore, and as such fluorophores with high quantum yields, high photostability, long fluorescence lifetimes and small cross-sections for multiphoton absorption have lower I_{sat} values [78]. Indeed, fluorophores with such characteristics have been specifically developed for used in STED microscopy [79, 80].

Initial implementations of STED microscopy used pulsed lasers for both excitation and STED beams [72, 81], as the required intensities for the STED beam are more readily obtained in this mode compared to continuous wave (CW) laser sources. However, this pulsed-pulsed regime is complex to achieve experimentally, as the two laser sources must be synchronised to operate at the same repetition rate, the STED beam must be temporally stretched to avoid unwanted two photon excitation [82] and the beams must be precisely overlapped not just spatially but also temporally. The high power pulsed laser sources required are also expensive and as such successful pulsed STED microscopy has been mainly limited to spectroscopy laboratories already possessing appropriate lasers. A commercial pulsed-pulsed STED microscope was produced by Leica in 2007, but cost in the region of \$1,000,000 [83] and was subsequently discontinued.[1]

STED microscopy has been attempted with CW laser sources for both excitation and STED beams, as such set-ups avoid the temporal alignment aspects of pulsed-pulsed STED microscopy. However the downside of this approach is that the STED beam is constantly working against re-excitation, which is not an issue when excitation is pulsed due to the time delay between pulses. Additionally the prolonged exposure of the sample to two continuous beams increases the probability of photobleaching [85].

Currently the most popular implementation of STED microscopy is 'gated STED', also referred to as gSTED [86]. gSTED uses a pulsed excitation beam and a CW STED beam, with the key feature of this method being that only fluorescence detected after a certain time gate is used to create the super resolution image. Fluorescence detected at very early times after excitation (within ∼2-3ns, depending on the fluorophore) may have arisen from the central minimum of the donut-shaped STED beam; however it is also possible that it originated from the area beneath the intense region of the STED beam, as the probability of stimulated emission occurring in CW STED increases over time and so unwanted peripheral fluorescence is more likely to occur soon after excitation. Therefore by using only fluorescence detected from later times after excitation ($> 2-3$ns) in the image, there is a higher probability that stimulated emission has depleted fluorophores beneath the intense region of the STED beam and hence there is less contaminating fluorescence from this region [86]. This implementation avoids the problems of STED pulse stretching and temporal alignment, and cheaper solid state lasers can be used to provide the excitation and STED beams.

Aside from the complex experimental set-up required for STED microscopy (which is still non-trivial even for CW STED applications as it involves precise spatial alignment of the beams), the major disadvantage is the on-sample laser powers required to achieve 100% depletion. Even in gSTED the STED beam intensity is similar to that required in pulsed STED, which is on the same order of magnitude where sample damage has been documented in two photon microscopy [50]. However, STED microscopy does benefit from rapid sample acquisition as a consequence of laser scanning, it can be used with conventional fluorophores and the image is obtained instantly without need for subsequent computational processing. The highest resolutions reported for STED microscopy of biological samples are on the order of ~ 30nm for fixed specimens [72] and ~ 50nm for living specimens [87].

---

[1] Although the Leica TCS SP5 STED microscope had been discontinued for at least a year, during the course of writing this thesis an improved pulsed-pulsed microscope, the Leica TCS SP8 STED, was announced [84]. The website for the discontinued microscope has been replaced with that of the new microscope.

2.4 Basic principles of LIR-SR

LIR-SR is a laser-scanning super resolution technique drawing principles from fluorescence lifetime imaging and stimulated emission. In LIR-SR two spatially overlapped beams scan the sample, one of which is a pulsed excitation (pump) and the other is a CW depletion (dump) beam. The theoretical basis of LIR-SR was initially formulated by Bain and Marsh (2012) [88] and preliminary results have been published in Marsh et al. (2014) [89], with the work presented here and in Chapter 3 showing further simulated data, computational methods and a wider range of results.

Of the super resolution techniques discussed thus far LIR-SR is most closely comparable with gSTED as both techniques combine pulsed excitation, continuous wave stimulated emission depletion and time-resolved detection of fluorescence, although there are several key differences. The dump beam used in LIR-SR is simply the fundamental Gaussian output of the CW laser, as opposed to the annular STED beam used in gSTED. The intensity of the dump beam is also much lower than that of the STED beam used in gSTED, as the purpose here is not to completely suppress fluorescence from excited fluorophores, but rather to modify their fluorescence lifetimes using weak CW stimulated emission. As the rate of stimulated emission is linearly dependent on dump intensity, the fluorescence lifetimes of the excited fluorophores will vary depending on whether they are beneath a more intense part of the Gaussian dump beam (i.e. towards the centre) or a less intense part of the dump beam (i.e. towards the edges). As a consequence of these lifetime variations, the PSF in LIR-SR has different intensity distributions at different points in time (over several nanoseconds) and the time-evolving image obtained can be split up in time post-acquisition to extract this additional spatial information. Again, this is in contrast to gSTED where only one temporal portion of the time-resolved image is utilised, with the rest of the information (i.e. fluorescence detected immediately after excitation) discarded. The resolution gain in LIR-SR subsequently arises from recombining spatially distinct images obtained from different points in time in the correct proportions.

The invention of LIR-SR initially arose from modelling of CW STED to optimise the performance of a proposed conventional STED microscope to be built in the group [88], and motivating factors in the development of LIR-SR have been the need for a super resolution technique that is simple to implement and is compatible with live cell imaging. The microscope set-up used here is a simple modification to a commercial fluorescence lifetime imaging microscope, and in theory LIR-SR should not require specialised fluorophores to succeed. Furthermore, the low on-sample laser powers (compared to STED microscopy) and relatively short image acquisition times (compared to PALM and STORM) should mean that LIR-SR can be used on live biological samples.

2.5 Theory of LIR-SR

As LIR-SR is based on the dynamics of stimulated emission, rate equations are first presented which describe the two state model used here to analyse stimulated emission. The translation of these dynamics into three-dimensional imaging space is then presented, along with simulated images demonstrating the principles of LIR-SR operation.

2.5.1 Rate equation analysis

The basic theory of LIR-SR requires the analysis of a two state system consisting of the lower vibrational levels of S_1 and the upper vibrational levels of S_0. Throughout the following formulations these will be described as having fractional populations N_{ex} (excited state) and N_{gs} (ground state) respectively, with a schematic of the simplified system used for this analysis shown in Fig. 2.6. The effect of orientation is not considered in the analytical description of CW STED required for LIR-SR provided here, but is explored in detail in Chapters 4 and 5.

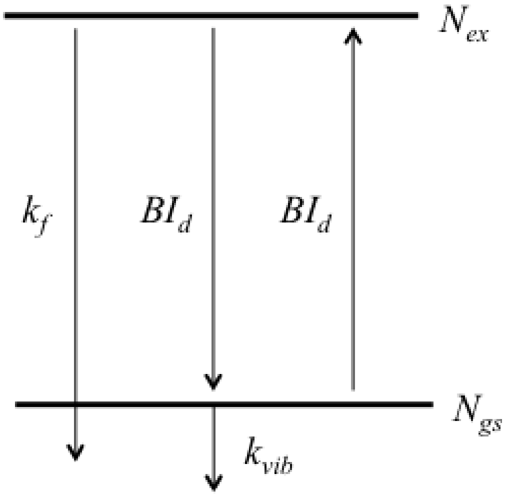

Figure 2.6: Two level system used for analysis of emission dynamics.

In the presence of a CW dump beam, the rate of stimulated emission is linearly dependent on the intensity of this beam I_d as follows:

$$k_d = BI_d, \tag{2.5}$$

where B is a constant dependent on factors such as the stimulated emission cross section (σ_{STED}) of the fluorophore. Thus, immediately following an excitation pulse and in the presence of a CW dump field, the populations N_{ex} and N_{gs} can be described as

$$\frac{\mathrm{d}N_{\mathrm{ex}}}{\mathrm{d}t} = -BI_d\left(N_{\mathrm{ex}} - N_{\mathrm{gs}}\right) - k_f N_{\mathrm{ex}} \tag{2.6a}$$

$$\frac{\mathrm{d}N_{\mathrm{gs}}}{\mathrm{d}t} = BI_d\left(N_{\mathrm{ex}} - N_{\mathrm{gs}}\right) - k_{\mathrm{vib}} N_{\mathrm{gs}} \tag{2.6b}$$

where k_f is the sum of radiative and non-radiative decay rates, equal to $1/\tau_f$ (Section 1.1.6), and k_{vib} is the rate of vibrational relaxation from upper vibrational levels of S_0. As $k_{\mathrm{vib}} \gg k_f$, there is negligible population build-up in N_{gs} and it can be assumed that $N_{\mathrm{gs}} \approx 0$. Therefore Eq. 2.6a becomes

$$\frac{\mathrm{d}N_{\mathrm{ex}}}{\mathrm{d}t} = -\left(BI_d + k_f\right) N_{\mathrm{ex}} \tag{2.7}$$

which has the solution

$$N_{\mathrm{ex}}(t) = N_{\mathrm{ex}}(t=0)\exp\left(-(BI_d + k_f)t\right). \tag{2.8}$$

The total excited state population can then be obtained by integrating over time and, using the identity $\int_0^\infty \exp(-at)\mathrm{d}t = 1/a$, evaluates to

$$N_{\mathrm{ex}} = \frac{N_{\mathrm{ex}}(t=0)}{BI_d + k_f}. \tag{2.9}$$

The fraction of the excited state population in the presence of CW STED relative to the excited state population in the absence of CW STED (i.e. $I_d = 0$) is termed the fractional depletion F_d, and is given by

$$F_d = \frac{N_{\mathrm{ex}}\left(I_d = 0\right) - N_{\mathrm{ex}}(I_d)}{N_{\mathrm{ex}}\left(I_d = 0\right)} \tag{2.10a}$$

$$= \frac{\dfrac{N_{\mathrm{ex}}(t=0)}{k_f} - \dfrac{N_{\mathrm{ex}}(t=0)}{BI_d + k_f}}{\dfrac{N_{\mathrm{ex}}(t=0)}{k_f}} \tag{2.10b}$$

$$= \frac{BI_d}{BI_d + k_f}. \tag{2.10c}$$

2.5.2 Spatial effects of CW STED

As the pump and dump beams used in LIR-SR are both the fundamental Gaussian modes of the respective lasers used, both beams have Gaussian intensity profiles when focused through the objective [90]. For algebraic simplicity it is assumed that the intensity profiles of both beams have the same FWHM in the plane of the sample.

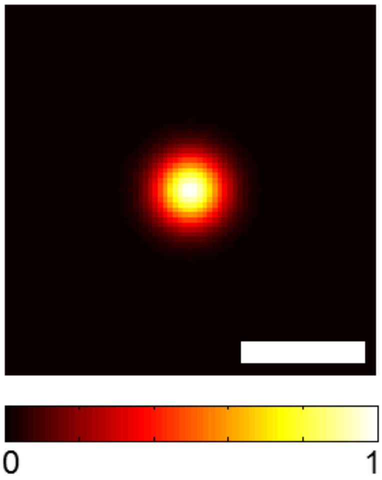

Figure 2.7: I_d plotted in the xy plane. Calculated using λ = 550nm and NA=1.2. Scale bar = 500nm.

The spatially varying intensity of the dump beam is thus described by

$$I_d(x,y) = I_{d_0} \exp\left(-\left(\frac{(x-x_0)^2}{2\omega_x^2} + \frac{(y-y_0)^2}{2\omega_y^2}\right)\right), \tag{2.11}$$

where I_{d_0} is the intensity at the beam centre (x_0, y_0) and ω_x and ω_y represent the standard deviations of the beam in x and y. Figure 2.7 shows a simulation of I_d for a dump beam where $\omega_x = \omega_y = \omega$, and the FWHM of the intensity distribution is assumed to approximate to Abbe's diffraction limit such that FWHM $= 2\omega\sqrt{2\ln 2} = \lambda/2$NA. The pump beam is assumed to have an identical intensity distribution to I_d. The effective decay rate of the excited state in the presence of the dump beam is given by the combined rates of stimulated emission and fluorescence. Thus the effective fluorescence lifetime in the presence of the dump beam at position (x, y) is given by

$$t_d(x,y) = \frac{1}{BI_{d_0} I'_d(x,y) + k_f}, \tag{2.12}$$

where BI_{d_0} is the rate at which stimulated emission occurs at the beam centre and $I'_d(x,y) = I_{d_0}/I_d(x,y)$. Rearranging Eq. 2.10c with $I_d = I_{d_0}$ gives

$$BI_{d_0} = \frac{k_f F_{d_0}}{1 - F_{d_0}}, \tag{2.13}$$

where F_{d_0} refers to the fractional depletion at the beam centre. Substitution into Eq. 2.12 and rearranging gives

$$t_d(x,y) = \frac{(1 - F_{d_0})t_f}{1 + F_{d_0}(I'_d(x,y) - 1)}. \tag{2.14}$$

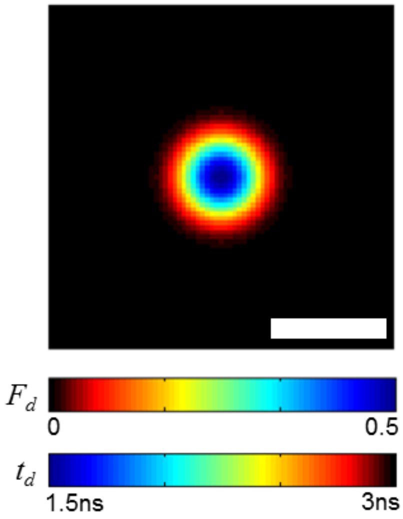

Figure 2.8: Lifetime variations in the xy plane. Calculated using λ = 550nm, NA=1.2, F_{d_0}=0.5, t_f=3.0. Scale bar = 500nm.

Equation 2.14 thus describes the shortened fluorescence lifetime of a fluorophore located at position (x, y) when subject to pulsed pump and CW dump. This implies that fluorophores located beneath high intensity regions of the dump beam (i.e. towards the centre) have the shortest fluorescence lifetimes, and experience fractional depletions close to F_{d_0}, whereas fluorophores located beneath low intensity regions of the dump beam (i.e. towards the periphery) have lifetimes closer to the undepleted lifetime t_f and experience fractional depletions much lower than F_{d_0} (Fig. 2.8).

When imaging samples in the microscope the beam pair is scanned across a two dimensional region of the sample in a pixel-wise fashion, where the pixel sizes are typically much smaller than the FWHM of the beam pair. As a result, fluorescence will not only originate from fluorophores within the pixel beneath the centre of the beam pair, but also from fluorophores within adjacent pixels. The contribution of fluorescence from the pixels follows the distribution of the PSF, here approximated to I_d (Fig. 2.7), meaning that fluorophores in pixels directly neighbouring the pixel being imaged will have a greater contribution to the total fluorescence intensity detected than fluorophores in pixels further away. The total number of fluorescence events in pixel (n_x, n_y) at time t can be calculated according to:

$$\begin{aligned} &I_f^{\text{total}}(n_x, n_y, t) = \\ &\sum_{y=y_{\min}}^{y=y_{\max}} \sum_{x=x_{\min}}^{x=x_{\max}} N_{(x,y)} \exp\left(-\frac{(x-n_x)^2+(y-n_y)^2}{2\omega^2}\right) \exp\left(-\frac{t}{t_d(x,y)}\right). \end{aligned} \tag{2.15}$$

This considers a scanning region extending from $(x_{\min}, y_{\min})$ to $(x_{\max}, y_{\max})$ where $N_{(x,y)}$ is the number of fluorescence sources in pixel (x, y).

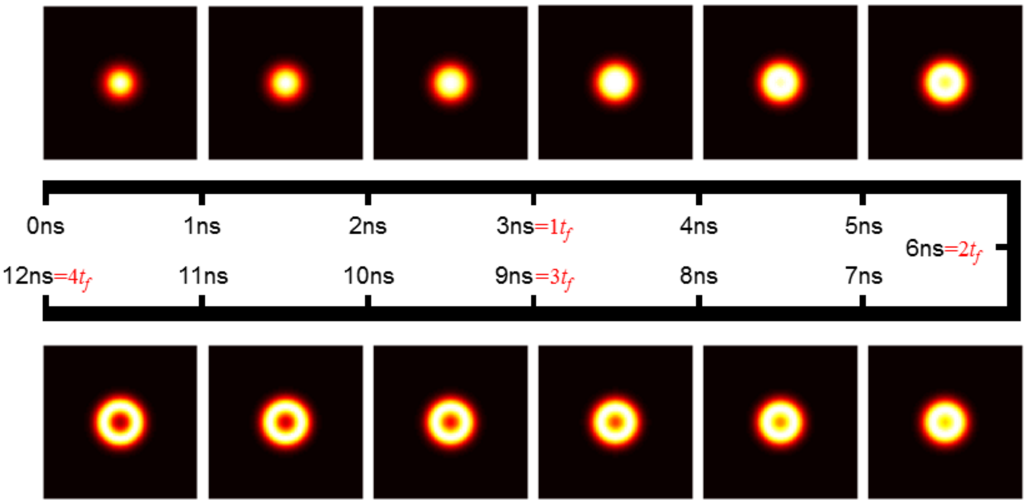

Figure 2.9: Evolution of the fluorescence distribution in the xy plane over several fluorescence lifetimes following excitation at 0ns. At later times, fluorescence will increasingly arise from the periphery of the PSF relative to the centre, resulting in an annular fluorescence distribution. Parameters used to generate plots are as in Figs. 2.7 and 2.8. The intensity in each image is normalised to 1. Fluorescence evolution was simulated using `FluoEvolution` program, code provided in the Appendix B.1.

2.5.3 Image division and reconstruction

Image acquisition using TCSPC assigns an arrival time to every detected photon and so an acquired image can be split up into ‘time windows’ according to photon detection times. The arrival times assigned to photons in TCSPC are binned into discrete channels t_{ch} and so a time window can be defined as the period of time from a ‘start’ channel to an ‘end’ channel, $t_{\mathrm{ch}_{\mathrm{start}}} \rightarrow t_{\mathrm{ch}_{\mathrm{end}}}$. Hence the number of fluorescence events in pixel (n_x, n_y) in one such time window is given by

$$I_f^{\mathrm{TW}}(n_x, n_y) = \sum_{t_{\mathrm{ch}}=t_{\mathrm{ch}_{\mathrm{start}}}}^{t_{\mathrm{ch}}=t_{\mathrm{ch}_{\mathrm{end}}}} I_f^{\mathrm{total}}(n_x, n_y, t_{\mathrm{ch}}), \tag{2.16}$$

and these temporally-summed pixels then comprise a time window image $\mathrm{Im}_f^{\mathrm{TW}}$. Several of these time window images can be created spanning the course of the fluorescence decay, and from these it can be seen that the spatial distribution of fluorescence varies on a nanosecond timescale (Fig. 2.9).

The key stage in attaining sub-diffraction limit resolution in LIR-SR is the reconstruction of the final image from a linear superposition of the time window images. The reconstructed image $\mathrm{Im}_f^{\mathrm{rec}}$ is created from n time window images combined as follows:

$$\mathrm{Im}_f^{\mathrm{rec}} = \sum_{i=1}^{n} c_i \mathrm{Im}_f^{\mathrm{TW}}(i). \tag{2.17}$$

Each time window image $\mathrm{Im}_f^{\mathrm{TW}}(i)$ is created from a unique set of time channels $t_{\mathrm{ch}_{\mathrm{start}}} \rightarrow t_{\mathrm{ch}_{\mathrm{end}}}$, and c_i are coefficients, one for each time window, which can take any real positive or negative value. The time window images are henceforth referred to in the simulations and experimental results as TW1, TW2..., which correspond to $\mathrm{Im}_f^{\mathrm{TW}}(1)$, $\mathrm{Im}_f^{\mathrm{TW}}(2)$... .

There is no theoretical limit on the resolution attainable using this method. Higher resolutions can be achieved by using numerous single time channel images (i.e. $t_{\mathrm{ch}_{\mathrm{start}}} = t_{\mathrm{ch}_{\mathrm{end}}}$), as opposed to the summed time window images which contain contributions from many different spatial distributions. As such the narrower the time window is, the fewer different spatial distributions of fluorescence exist within it. However, this would not be an appropriate approach for experimental data as the number of photons detected per individual time channel will be low, and so summation over broader time windows is necessary to maintain a sufficiently high signal to noise ratio, especially at later times when fluorescence intensity is inherently lower. Therefore to demonstrate the resolution enhancement of this technique, only five time windows have been used covering increasingly long periods of time to mimic the realistic application.

An example of five time windows used in model image reconstruction and the resultant reconstructed image are shown in Fig. 2.10. The reconstructed image was produced with coefficients: $c_1 = 1.0000, c_2 = -2.2903, c_3 = 4.0935, c_4 = -6.1337, c_5 = 6.7128$. Strategies for calculating appropriate reconstruction coefficients are discussed in Section 2.6.5; the coefficients generated for the simulated data discussed here were obtained using the ‘simultaneous equations’ approach. As a common method for quantifying the resolution of a fluorescence microscopy image is through measurement of the FWHM of the PSF [59], here the FWHM is determined from fitting Gaussian functions to intensity distributions within the image. The graph in Fig. 2.10 shows intensity profiles across the centre of the TW1 image, which is a good approximation for a confocal image, and the centre of the reconstructed image along with fitted Gaussian functions. The confocal profile has a FWHM of 238.1 ± 0.3nm, whereas the reconstructed profile has a FWHM of 75.6 ± 0.8nm, corresponding to a 3.1-fold increase in resolution.

If two different images are obtained where the same fluorophores and degree of fractional depletion F_d are present in both images, the reconstruction coefficients will be the same in both images if identical time windows are selected. This is shown in Fig. 2.11, which shows the temporal evolution of two dimensional structures and the reconstructed image which is produced using the same time windows and coefficients as calculated for the reconstruction in Fig. 2.10. Substantial detail is recovered from reconstruction, which was originally blurred by the diffraction limited PSF in TW1, although faint ring-like artefacts are visible surrounding structures which are likely to arise from the finite widths of the time windows used. Pixel size does not affect the reconstruction coefficients, as the pixels in Fig. 2.11 are 40×40nm compared to

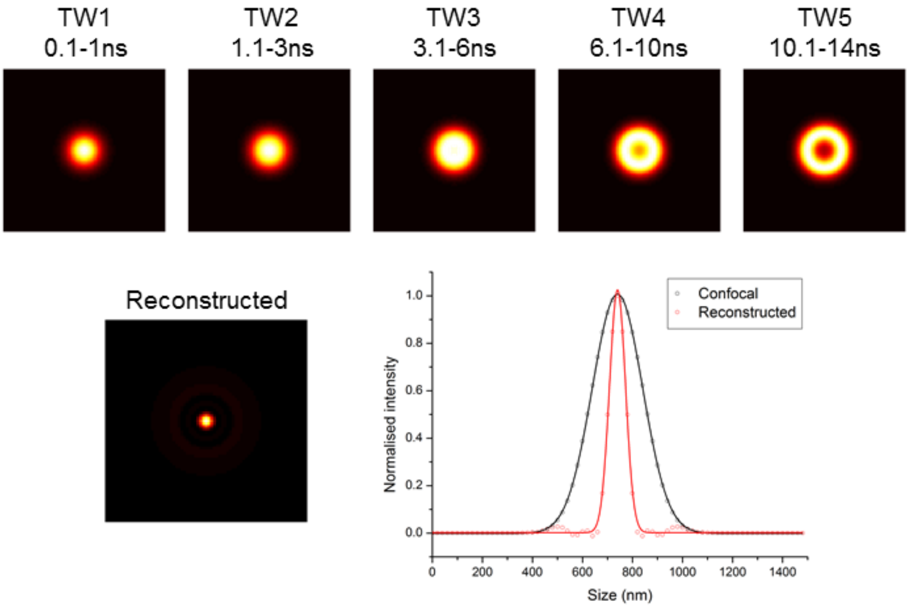

Figure 2.10: Reconstruction of a single point in the xy plane. Top row: Time window images used in the reconstruction with their associated time periods (excitation at 0ns). Bottom row: Reconstructed image from combining the time window images in the proportions as described in the text, and profiles taken across the centre of the reconstructed and TW1 images to illustrate increase in resolution. Intensities in the graph are normalised, with solid lines indicating Gaussian fits to data. Model parameters were as for Figs. 2.7 and 2.8. Reconstruction was performed using `SimEqRecon` MATLAB program (Appendix B.2).

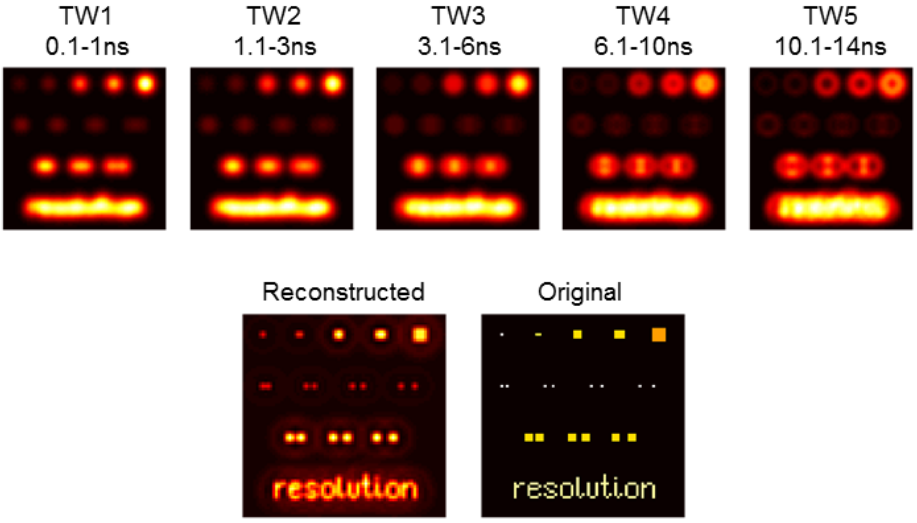

Figure 2.11: Time windows and reconstruction for a two dimensional structure (‘Original’). Model parameters were as for Figs. 2.7 and 2.8, except for pixel size, which here is 40nm as opposed to 20nm previously, `FluoEvolution` program used to produce images.

20×20nm in Fig. 2.10.

2.5.4 Axial resolution

As features in biological samples are usually three-dimensional structures, obtaining information in the z (axial) direction is often desirable. In confocal microscopy this is commonly achieved by obtaining a stack of xy scanned images at different z-planes within the sample such that fluorescence distributions in all three dimensions can be examined. The resolution in the axial direction (i.e. along the direction of beam propagation) of the focused laser spot is given by [91]

$$z_{\text{min}} = \frac{2\lambda n}{\text{NA}^2} \tag{2.18}$$

where n is the refractive index and NA is the numerical aperture of the objective. As a result, the axial resolution of a microscope is poorer than its lateral resolution by a factor of $4n/\text{NA}$.

Whilst PALM and STORM are capable of obtaining high resolutions (50-60nm) in the axial direction through the integration of optics such as cylindrical lenses [92], conventional STED microscopy techniques are typically limited to $\sim 500 - 700$nm maximum axial resolution [93]. The poorer axial performance of STED microscopy results from the confinement of the annular STED beam to the focal plane, and whilst a z-stack of images could be obtained in STED microscopy as for confocal microscopy, the increased exposure to the intense STED beam causes photobleaching [94]. Methods for increasing the z-resolution in STED microscopy have thus far been limited to STED-4Pi microscopy, a complex experimental set-up where opposing objective lenses are required for increasing the axial resolution to < 50nm [95], physical sectioning of a fixed sample with subsequent imaging of each section [94], and use of an additional ‘z STED’ beam, which requires custom-made optics to increase the axial resolution to < 200nm [77, 96]. Due to the apparent lack of an experimentally simple technique for obtaining super resolution of living samples, the axial performance of LIR-SR was modelled.

As the shape of the laser spot in the axial direction can be approximated by a Lorentzian function [90] with FWHM Γ approximately equal to z_{min}, the three dimensional form of the focused depletion beam can be formulated as

$$I_d(x, y, z) = I_{d_0} \exp\left(-\left(\frac{(x - x_0)^2}{2\omega_x^2} + \frac{(y - y_0)^2}{2\omega_y^2}\right)\right) \frac{1}{4} \frac{\Gamma^2}{(z - z_0)^2 + (\frac{1}{2}\Gamma)^2} \tag{2.19}$$

where I_{d_0} is the intensity at $I_d(x_0, y_0, z_0)$. The axial intensity and F_d distributions are plotted in Fig. 2.12.

The spatial distribution of fluorescence in the axial direction evolves over time as governed by Eq. 2.14, and super resolution can be achieved in the axial direction using the same principles of splitting the image into time windows and recombining

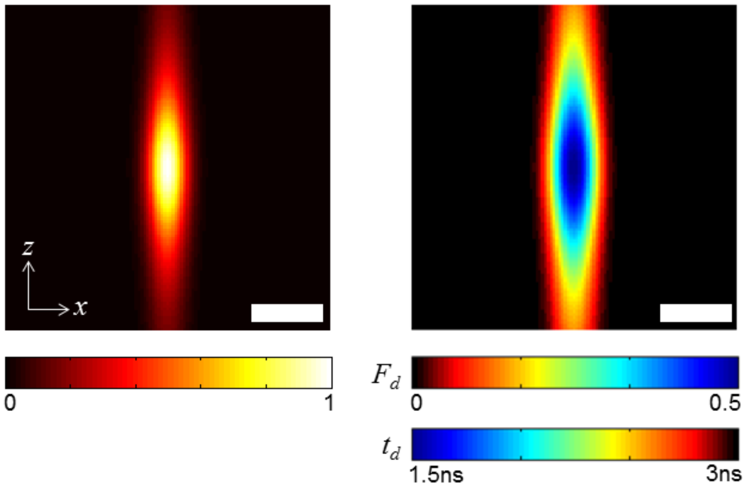

Figure 2.12: Intensity and lifetime distributions in the xz plane. Model parameters are as for Figs. 2.7 and 2.8. Scale bar = 500nm.

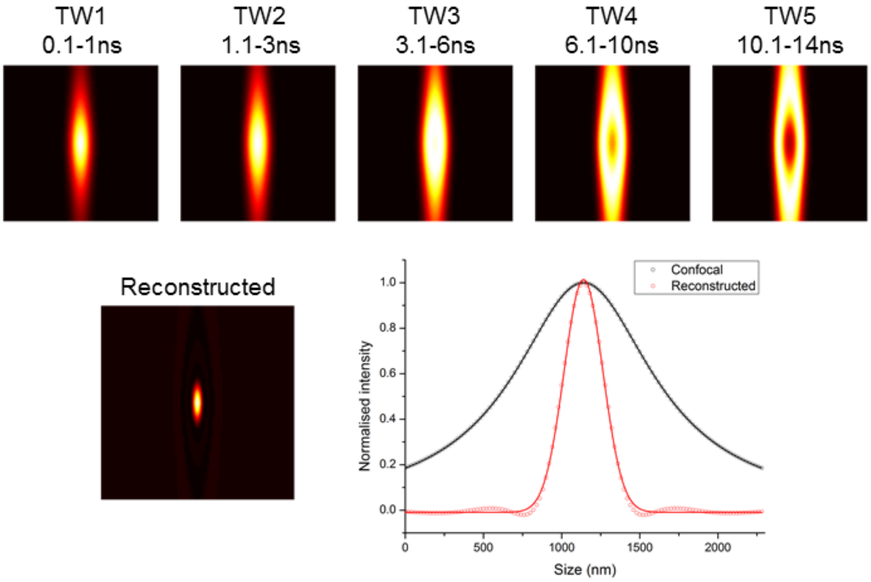

Figure 2.13: Reconstruction of a single point in the xz plane. Top row: Time window images used in the reconstruction. Bottom row: Reconstructed image from combining the time window images (proportions as described in the text) and profiles taken down the centre of the reconstructed and TW1 images to illustrate increase in axial resolution. Intensities in the graph are normalised, with solid lines indicating Lorentzian (confocal) and Gaussian (reconstructed) fits to data. Model parameters were as for Figs. 2.7 and 2.8. Time windows produced using `AxialEvolution` (Appendix B.3).

them as for the lateral direction as described in Eqs. 2.16 and 2.17. This is shown in Fig. 2.13, which again uses the same lifetime, F_{d_0}, time window positions and coefficients as for the lateral reconstructions. The resolution improvement in the axial direction is slightly greater than in the lateral direction; the confocal resolution in z is 1089.6 ± 0.1nm and the reconstructed resolution is 293 ± 2nm, indicating a 3.7-fold increase.

2.6 Methods

For the practical realisation of LIR-SR, a basic modification was made to a commercial fluorescence lifetime imaging microscope to perform the imaging itself, and computer programs were written for the temporal division and subsequent reconstruction of images.

2.6.1 Microscope set-up

All imaging was performed on an inverted microscope (IX71, Olympus) with fluorescence lifetime imaging system (MicroTime 200, PicoQuant GmbH). A schematic of the system is shown in Fig. 2.14.

The pump beam was provided by a 490nm pulsed diode laser (PicoTA 490, Toptica) with variable repetition rate (imaging performed at 20MHz and 5MHz). The PicoTA output, after passing through a neutral density wheel for controlling intensity, was then reflected off a beam combiner (560 DCXR, Chroma) into a 3 metre single mode polarisation maintaining fibre. The dump beam was provided by a 100mW CW 594nm diode pumped solid state (DPSS) laser (Mambo, Cobolt) which was transmitted through the beam combiner into the same optical fibre as the pump. The combined beams were reflected off the major dichroic (BS5100, Chroma) through an adjustable prism (for fine adjustment of beam angle) into the objective (UPLSAPO 60×/1.2 NA WI, Olympus). The serial port of the dump laser was connected via USB interface to a computer whereby power could be controlled via custom-written software (written by Dr Richard Marsh). All powers quoted in the text are the powers set through this software as it was not practical to repeatedly measure the on-sample power between acquisitions; however there were considerable power losses arising from fibre coupling ($\sim 40\%$ transmission) and between the major dichroic and sample ($\sim 34\%$ transmission). For example, a ‘set’ power of 50mW (as is used most commonly in Chapter 3) corresponded to $\sim$ 17mW after the back apertures and $\sim$ 6mW on-sample.

Fluorescence collected by the objective was transmitted through the major dichroic and passed through two filters (HQ510LP, Chroma and NF03-594W-25, Semrock) to remove residual pump and dump respectively, and was then focused by the tube lens into a 50µm pinhole for confocal detection. There was further filtering to ensure minimal dump beam remained (FES0550, Thorlabs) and the fluorescence

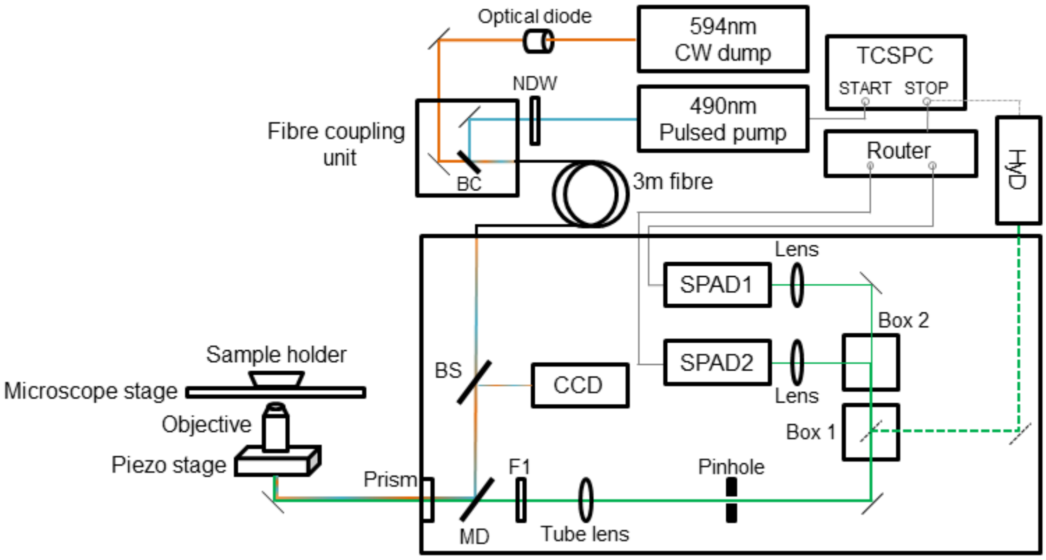

Figure 2.14: Microscope set-up for LIR-SR. Pump path shown as a blue line, dump path shown as an orange line, combined beams shown by blue/orange striped line. Fluorescence path shown by green line. Dashed lines indicate path taken when hybrid detector is used. Abbreviations used: NDW - neutral density wheel, BC - beam combiner, BS - beam splitter, MD - major dichroic, F1 - filter, SPAD - single photon avalanche diode, HyD - hybrid detector. Box 1 and Box 2 contain exchangeable optics; when the SPAD detectors are used, Box 1 contains a filter and Box 2 contains a cube polariser. When the HyD is used, Box 1 contains a mirror and filter. Not shown: piezo controller, delay line, laser drivers.

was then split into its parallel- ($I_{\|}$) and perpendicular- ($I_{\perp}$) polarised components using a cube polariser. The parallel- and perpendicular- polarised components were focused into separate single photon avalanche diode (SPAD) detectors (PDM series, Micro Photon Devices). The intensity in all images presented here was the sum of these two detector signals ($I_{\|}+I_{\perp}$). The system was also equipped with a CCD camera (ZC-F10C2, Ganz) for beam diagnostics. A small fraction of pump and dump light reflected back off the major dichroic were reflected into the CCD camera by an achromatic beamsplitter (no further details provided in microscope documentation).

Signals from the detectors were sent to a router (PHR 403E, PicoQuant GmbH) which then passed 'stop' signals to the TCSPC system (PicoHarp 300, PicoQuant GmbH). Sync signals from the pump laser passed through a delay box (425A, Ortec) and provided the 'start' signals to the TCSPC. The TCSPC channel width was 16ps. The objective was mounted on a z piezo scanner (PIFOC P-721.CLQ, Physik Instrumente GmbH) and an x, y piezo stage (P-733.2CL, Physik Instrumente GmbH) such that it could scan the sample in three dimensions. These two devices were controlled by a digital piezo controller (E-710, Physik Instrumente GmbH) which also provided an input to the router.

Some experiments were performed using a hybrid detector[2] (HPM-100-40, Becker & Hickl GmbH) which detected un-separated parallel- and perpendicular- polarised fluorescence. Fluorescence was filtered as for the SPAD detectors up until 'Box 1' (Fig. 2.14) and was then filtered further to remove dump beam (FES0550, Thorlabs) and reflected into the detector. The output of this detector was sent directly to the TCSPC system to act as the 'stop' signal.

Images ware acquired using commercial software (SymPhoTime 5.3.2.2, PicoQuant GmbH) and subsequent analysis was performed in MATLAB (R2011a, MathWorks), ImageJ (1.43u, National Institutes of Health) and Origin (Origin Pro 8.6, OriginLab). Statistical tests were performed using GraphPad Prism (Version 6, GraphPad Software).

2.6.2 Samples

Beads on coverslips

Fluorescent beads of various diameters (20nm, 40nm, 100nm and 200nm FluoSpheres, Invitrogen) were evaporated using the following protocol [97]. Stock solutions of the beads were sonicated, diluted 1:1000 in dH_2O and then diluted 1:1000 in 100% ethanol. 6µl of this solution was then pipetted onto a thickness No. 1 glass coverslip and allowed to evaporate.

---

[2] Hybrid detector on loan courtesy of Dr Simon Ameer-Beg, King's College London

Beads within HEK-293 cells

Uptake of 20nm fluorescent beads into living HEK cells was achieved using a method adapted from Zauner et al. [98]. HEK-293 cells were cultured in advanced DMEM (Invitrogen) supplemented with FBS (10%), penicillin (100 units/ml), streptomycin (100µg/ml) and l-glutamine (2mM), and plated onto glass coverslips at a density of 100,000 cells per coverslip. The following day cells were incubated with a 1:1000 dilution of 2% bead solution in DMEM for 4 hours at 37° C before re-immersion in phenol red-free HEPES-buffered DMEM (Sigma), in which the cells remained immersed during imaging.[3] A trypan blue exclusion test was used to assess cell viability after imaging following the protocol described by Strober [99].

2.6.3 Time window selection

Time windows were selected from the fluorescence decay of the image using a custom-written MATLAB program (Fig. 2.15, `TWSelect` code provided in Appendix B.4). Time windows were selected by the user on a visual basis where images were judged to have sufficient spatial variation from other time window images whilst maintaining acceptable signal to noise ratios; thus far no suitable automated or quantitative method for selecting time windows has been developed. For all images five time windows were used and were contiguous between the time at which excitation occurred and the time at which the signal to noise ratio was visually assessed to be unacceptable (typically 12-15ns after excitation). Once a successful set of time windows had been found, only minor modifications to the window widths were necessary between different samples, as the lifetimes of the fluorescent beads imaged were broadly similar (Fig. 3.11b).

2.6.4 Imaging parameters

In all experiments presented the pixel dwell time was set to 0.6ms, which corresponded to a maximum image acquisition time of 2.5 minutes for the largest (512×512 pixels) images. The pixel size in each image was chosen such that the Nyquist sampling criterion would be satisfied following pixel binning [100].

2.6.5 Image reconstruction strategy

Model data: simultaneous equations

In the simulations in Section 2.5 image reconstruction was performed by setting up a system of simultaneous equations (`SimEqRecon` code). This approach involved finding a suitable combination of the time window images which resulted in the intensities of the pixels away from the central maxima in the image becoming zero in the reconstructed image. A practical way to do this was to measure the intensity

---

[3] Cell culture and handling performed by Dr Thomas Blacker

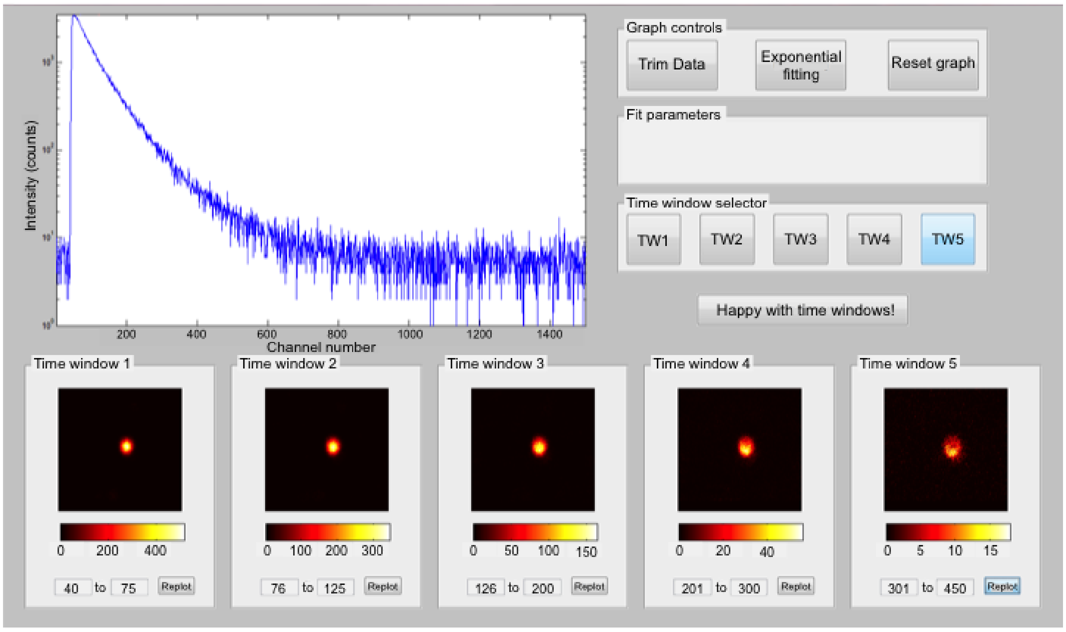

40 to 75

76 to 125

126 to 200

201 to 300

301 to 450

Figure 2.15: Screenshot of `TWSelect` program used for time window selection. The line plot indicates the total measured fluorescence intensity decay over TCSPC channels for the entire image, and the five time window images are plotted for the channel range indicated below each image. TCSPC channel widths in this screenshot are 32ps.

profile across a diffraction-limited region of fluorescence (i.e. an object whose size appeared equal to the confocal PSF) for the five time windows and use pixel values in these profiles to build the simultaneous equations. Figure 2.16 shows an example of pixel selection using the method. A system of simultaneous equations can be created for n time windows (5, in Fig. 2.16) using pixels $p \rightarrow q$ (29 to 33 in Fig. 2.16) as shown below:

$$\begin{pmatrix} N_{1,p} & N_{2,p} & \dots & N_{n,p} \\ N_{1,p+1} & N_{2,p+1} & \dots & N_{n,p+1} \\ \vdots & \vdots & \ddots & \vdots \\ N_{1,q} & N_{2,q} & \dots & N_{n,q} \end{pmatrix} \begin{pmatrix} c_1 \\ c_2 \\ \vdots \\ c_n \end{pmatrix} = 0 \qquad (2.20)$$

where $N_{i,j}$ is the intensity of pixel j in time window i.

Whilst this approach was successful for reconstructing simulated data with no noise (3.1 fold increase in resolution as demonstrated in Section 2.5.3), it did not perform as well for simulated data where Poisson-distributed noise was present (noise was added to each pixel as a random number from a normal distribution of mean $= 0$ and standard deviation $= \sqrt{N}$, where N was the intensity of the pixel). This is shown in Fig. 2.17, generated using `NoisyEvolution` code (Appendix B.5). The coefficients generated for the reconstruction of the noisy data were $c_1 = 1.000, c_2 = -0.3213, c_3 = -2.4987, c_4 = 2.5841, c_5 = 7.4317$ and the reso-

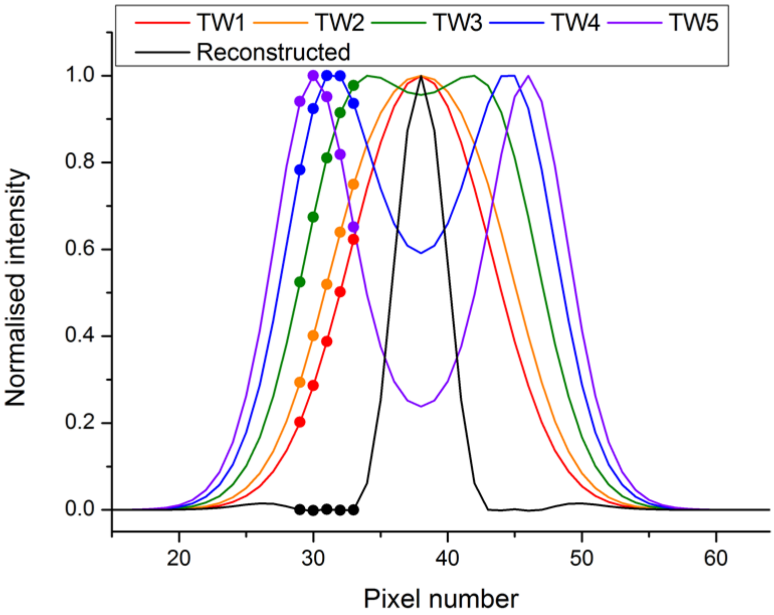

Figure 2.16: Line profiles across the centre of five simulated time windows (coloured) and a reconstructed profile produced from these (black). Pixels used in setting up the system of simultaneous equations are marked by solid coloured circles, with the values of the corresponding 'solution' reconstructed pixels shown as black solid circles.

lution enhancement compared to the TW1 image was now just 2.1 fold (112 ± 5nm reconstructed compared to 237.3 ± 0.7nm confocal).

There are other issues with this approach to reconstructing images. For example, the background in an acquired image may have local, non-zero variations which would mean that solving Eq. 2.20 would not be valid. Also, a fundamental principle in super resolution imaging is that the size of an object in an image is essentially unknown if it appears to be the same size as the PSF. Without prior knowledge of the size of the object it is conceivable that artefacts could arise from attempting to make regions which actually contain fluorescent structures equal zero. Ideally there should also be the same number of pixels used to set to zero as there are time window images to prevent multiple solutions to the simultaneous equations. For a better reconstruction with higher resolution and fewer artefacts (e.g. sidebands, as in reconstructed image in Fig. 2.17) a larger number of pixels should be set to zero, implying that a larger number of time windows should be used which, as discussed previously in Section 2.5.3, may not be practical.

Genetic algorithm reconstruction strategy

There are several factors which are important to consider when attempting to create a practical reconstruction strategy. Firstly, the underlying structure of the image is unknown, and may contain different sized objects below the diffraction limit.

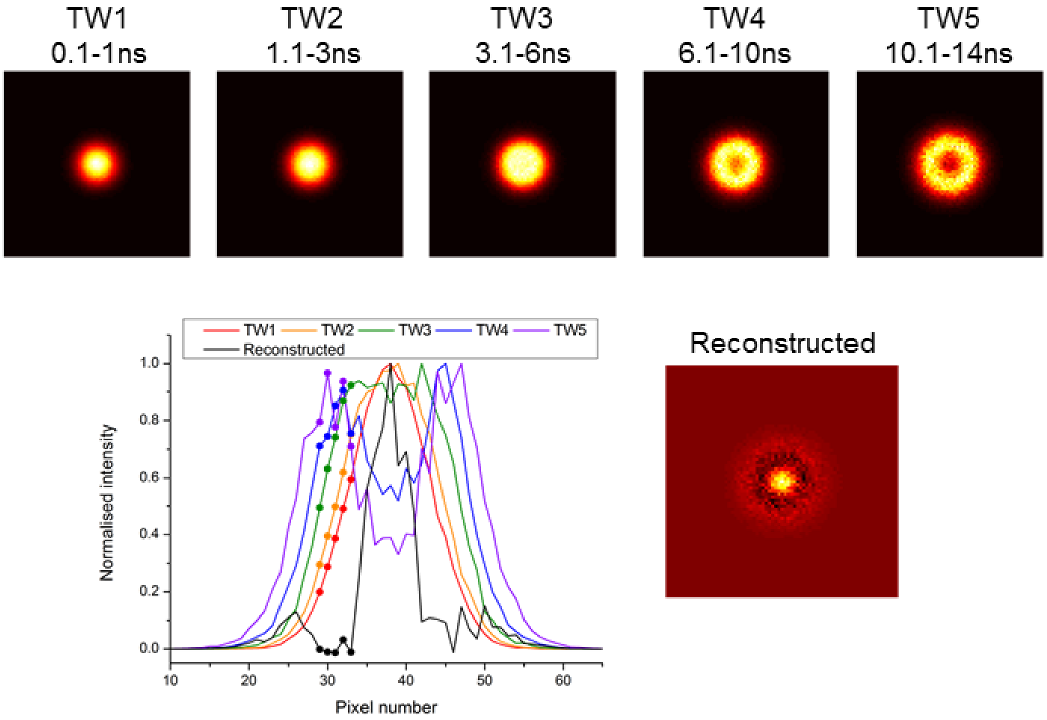

Figure 2.17: Reconstructing images using noisy data. Top row: Five time window images simulated using $t_f = 3$ns and $F_{d_0} = 0.5$ with Poisson noise added. Bottom row: Graphs showing profiles across centres of above time windows with pixels used in setting up simultaneous equations marked (as in Fig. 2.16). Black line indicates profile across centre of reconstructed image (right). Pixel size in all images is 20nm.

Secondly, each coefficient to be calculated can theoretically take any positive or negative value leading to a large parameter space. Thirdly, there is no prior information on the values that the coefficients can take, as even the addition of Poisson noise to model data dramatically changes the reconstruction coefficients compared with coefficients obtained with no noise. Finally, the reconstruction process should produce super resolution images quickly such that appropriate alterations to imaging parameters or perturbations to samples can be applied in real time.

The reconstruction strategy described here and used for reconstruction of all images in Chapter 3 was based on the genetic algorithm optimisation technique [101]. This was chosen as genetic algorithms are capable of operating successfully from a starting point of a set of randomly generated coefficients, rather than a pre-informed initial point. The mechanism by which genetic algorithms work is based on natural selection. Initially, a ‘founder’ population is generated consisting of several different potential solutions (here several sets of randomly generated coefficient values). The success of each of these founders is assessed using a fitness function, which determines how well they perform at finding a good solution to the problem, and the fittest founders proceed unmodified to the next ‘generation’ (iteration) of the algorithm.

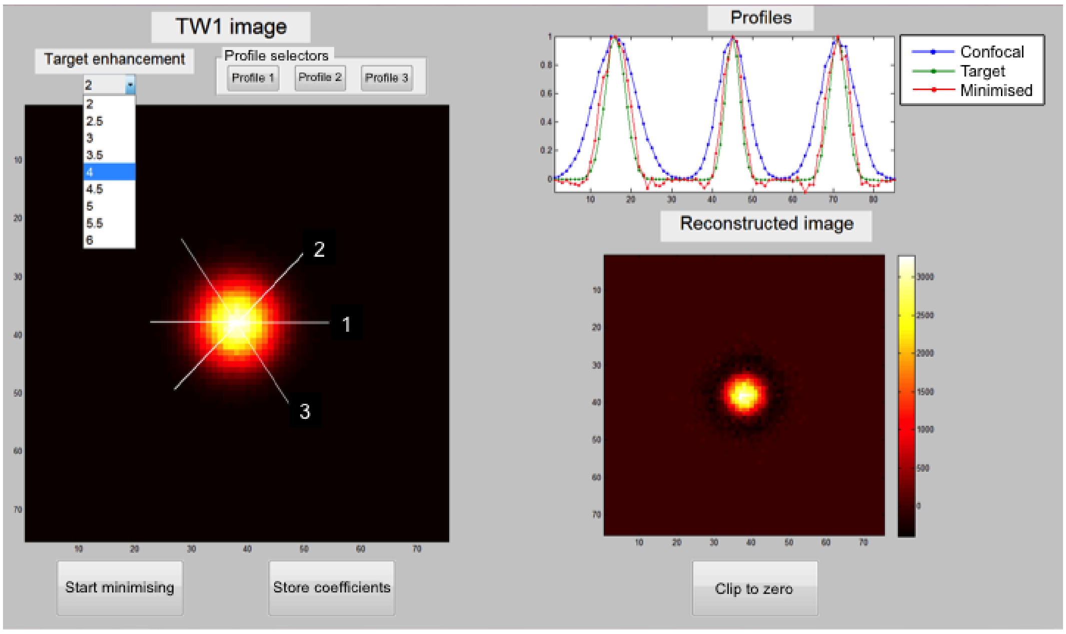

Figure 2.18: Screenshot of the `GARecon` program used for image reconstruction via the genetic algorithm approach.

The next generation is also populated by 'children' generated from the 'reproduction' of two 'parent' founders. This reproduction process is subject to crossover, as in biological reproduction, and so the child has some features (here, coefficients) from one parent and some from the other. By passing the fittest founders and children of sufficiently fit parents to the next generation, the algorithm is led to search in areas of parameter space more likely to produce good results. Children can also be produced from the random mutation of parents, which forces the algorithm to maintain a degree of searching in other areas of parameter space to prevent becoming stuck in a small area which may represent a local minimum. This process is repeated for many generations until a solution is found which has an acceptably high fitness. Alternatively the algorithm stops once the highest fitness in a population does not change for a large number of generations [101]. A screenshot of the program created to perform this image reconstruction is shown in Fig. 2.18, and accompanying code `GARecon` is provided in Appendix B.6. The specific features of the genetic algorithm reconstruction technique are detailed below.

Central algorithm

The image reconstruction algorithm used the MATLAB function `ga`, part of the Global Optimisation Toolbox.

Setting up the problem

The central minimisation problem which the genetic algorithm tackled was finding the proportions in which to combine five time window images to yield a super resolution image. The proportions are represented by c_{1-5} as before; for simplicity c_1 was set to 1 in all cases and coefficients c_{2-5} were found by the

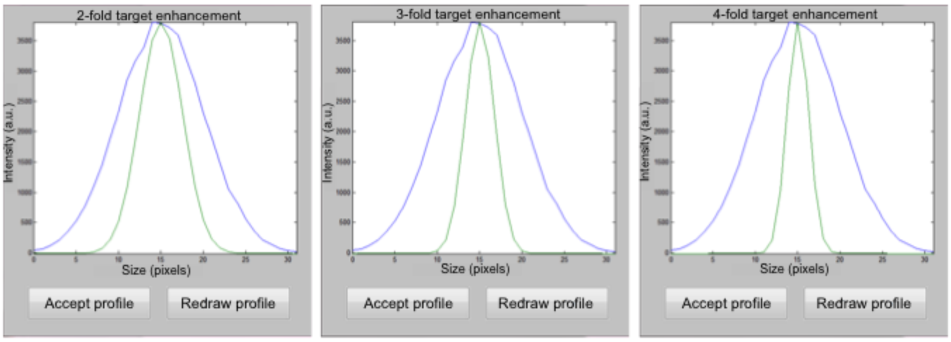

Figure 2.19: Target function generation for two-, three- and four-fold target resolution enhancements respectively. Blue lines indicate intensity along profile ‘1’ in Fig. 2.18, green lines indicate target intensity profiles for respective resolution enhancements.

algorithm along with an additional normalisation coefficient c_{norm} to maintain similar intensity levels in the reconstructed image.

To represent the confocal image, three line profiles were selected across features in the first time window image (TW1) and fluorescence intensity distributions along these lines stored. A target enhancement in resolution was then selected (e.g. 3, for a target 3-fold increase in resolution) and target profiles were generated for each intensity distribution by fitting these TW1 profiles with Gaussian functions, reducing the FWHM of these Gaussian functions by the target resolution enhancement and then recalculating target intensity values at each pixel (Fig. 2.19). These three target profiles were then concatenated to generate a ‘target function’ (Fig. 2.18, ‘Profiles’ panel). The purpose of using multiple profiles was to prevent over-optimisation to one specific feature in the image and also to reduce bias if the structures beneath the profiles were markedly different in size.

Fitness function

To assess the performance of generated coefficient sets a fitness function must be defined. Here the fitness function was the sum of squares difference between the concatenated target profile and the equivalent profile from an image produced using the generated coefficients. The smaller the value generated by the fitness function, the fitter the set of coefficients.

Parameters

Parameters used in genetic algorithm are shown in Table 2.1.

Examples of model reconstructions obtained using the genetic algorithm strategy compared to the simultaneous equations approach are shown in Fig. 2.20. For the simulated data without noise (Fig. 2.20a), the simultaneous equations approach significantly outperformed the genetic algorithm approach (75.6 ± 0.8nm reconstructed

Parameter	Value
Initial coefficients	Array of 5 randomly generated numbers from standard normal distribution (MATLAB `randn` function), $[c_2, c_3, c_4, c_5, c_{\mathrm{norm}}]$ for each founder.
Population size in each generation	20
Maximum number of generations	1000
Number of individuals passed to next generation without alteration	2
Proportion of next generation populated by reproduction (crossover)	0.8
Target fitness	0
Tolerance	1e-6
Number of generations without a change in fitness value greater than 'Tolerance' after which algorithm stops	50

Table 2.1: Selected parameters used in the genetic algorithm.

resolution with simultaneous equations compared to 108 ± 4nm with the genetic algorithm). However, both methods performed similarly when reconstructing the simulated data with noise (Fig. 2.20b, 112 ± 5nm compared to 114 ± 4nm). To evaluate the consistency of the two reconstruction approaches, 10 noisy data sets of a single point source of fluorescence were simulated and reconstructed with both simultaneous equations and the genetic algorithm. Whilst sometimes capable of generating images representative of the known structure (e.g. Fig. 2.20b, Sim. Eqs.), the simultaneous equations approach also produced garbled, structureless images. This is shown in Fig. 2.20c where the profiles across the repeated noisy reconstructions are shown: the red and blue plots are striking examples of reconstructions bearing little resemblance to the known structure. The genetic algorithm approach however produced images which were consistently representative of the known structure (reconstructed profiles shown in Fig. 2.20d). Gaussian fits were performed on the plotted profiles in Fig. 2.20c and d to further quantify the reliability of the two reconstruction approaches: the average R^2 goodness-of-fit statistic for the simultaneous equations reconstructions was 0.8 ± 0.2 compared with 0.95 ± 0.02 for the genetic algorithm reconstructions, further indicating better representation from the latter approach.

Therefore, as the genetic algorithm matched the reconstructed resolution obtained with simultaneous equations for noisy simulated data, with the added advantage of producing consistently similar results for the same known structure, this was deemed a suitable reconstruction strategy for use with experimental data.

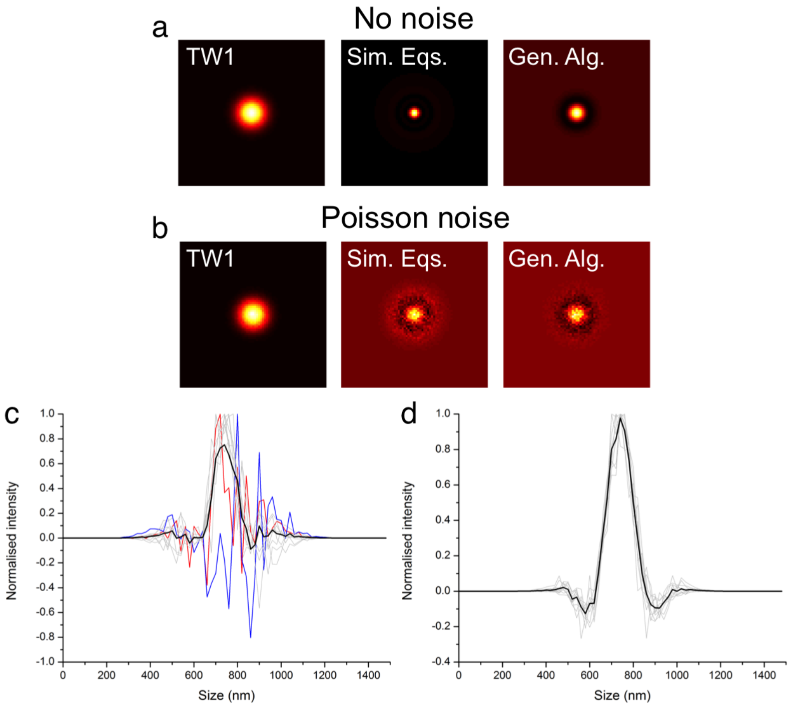

Figure 2.20: Comparison of reconstruction strategies for simulated data with and without noise. 'Sim. Eqs.' denotes reconstruction using simultaneous equations and 'Gen. Alg.' using the genetic algorithm. TW1 and reconstructed images are shown for a) noise-free simulated data and b) simulated data containing Poisson noise. Profiles across the centre of 10 reconstructions performed on noisy simulated data are shown for c) simultaneous equations and d) genetic algorithm. Bold black line indicates average of all 10 reconstructions for each strategy. Coloured lines in c) are particularly poor reconstructions. Parameters used for creating simulated data are as in Fig. 2.17, except without Poisson noise for the top row of images.

2.6.6 Image processing

To reduce noise, time window images were 2×2 binned using the `imresize` function in MATLAB, whereby the noise was averaged out over the four binned pixels [102]. The cost of doing this was that the pixel size became larger and the maximum obtainable resolution decreased. Images were also smoothed after reconstruction (`imfilter` in MATLAB) using a Gaussian kernel of width equal to the maximum measured resolution in the reconstructed image.

One common artefact in the reconstructed images was the presence of negative valued pixels, and the reasons for their presence will be discussed in more detail in Chapter 3. To maintain suitable contrast in images, a modified version of the MATLAB 'hot' colourmap was applied to the images presented in Chapter 3. The level of the colourmap closest to zero was set to be black, with positive valued pixels following the black-red-yellow-white hot map as is standard. The most negative level of the colourmap was set to be dark blue, with more negative values becoming increasingly bluer. An overview of the stages in the image processing are shown in Fig. 2.21.

To quantify resolution, ImageJ was used to plot intensity profiles across regions of interest in images which were then fitted with Gaussian functions using Origin. All fitting was performed on data from binned but unsmoothed images. Where the sizes of structures have been compared between TW1 (confocal) images and reconstructed images, the profiles were selected from the TW1 image and the same coordinates then applied to the reconstructed image for fair and accurate comparison. Errors quoted on average FWHM values are a combination of errors [103] generated during the fitting process and the standard deviation of average FWHM values, calculated as:

$$\Delta Z = \sqrt{s^2 + \frac{1}{n^2}\sum_i^n (\Delta w_i)^2}. \tag{2.21}$$

The mean FWHM is given by $Z = \frac{1}{n}\sum_i^n w_i$ for n measured FWHMs of widths w_i. The standard deviation of the n measured FWHMs is given by s, and the individual fitting error associated with each FWHM (as generated by Origin) is given by Δw_i.

2.6.7 Statistical testing

For each experimental data set presented in Chapter 3, statistical testing was performed to establish whether changes in resolution following image reconstruction in LIR-SR were statistically significant. The results of these statistical tests are presented alongside the results to which they refer in Chapter 3.

All data sets were tested for normality using the D'Agostino-Pearson test, and all were found to require non-parametric statistical tests. This was not unexpected, as the distribution of bead sizes within an image should have an absolute minimum value, corresponding to either the diffraction limit in confocal images or maximum resolution afforded by time window selection and reconstruction coefficients, and a larger range of maximum values potentially corresponding to variability in bead size and out of focus beads. This would result in a positive skew in the distribution of measured FWHMs in an image, rather than a normal distribution.

For assessment of the increase in resolution, the FWHM of each imaged bead was measured in the confocal (TW1) image and again in the reconstructed image, with the Wilcoxon matched-pairs test used to test whether there was a significant difference between confocal and reconstructed resolutions of individual beads of the same size imaged under the same conditions. For comparisons of average FWHM values obtained under two different imaging conditions (for example, with different detectors), the Mann-Whitney U test was used to test for statistical significance.

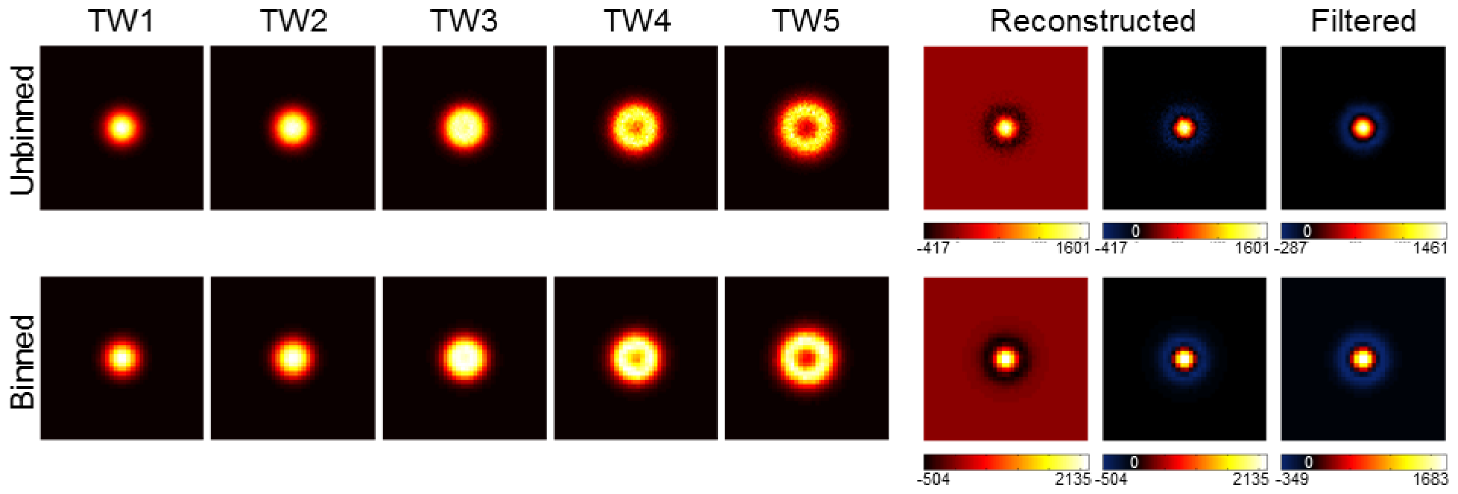

Figure 2.21: Overview of image processing strategies. Top row: Unbinned, noisy time window images, unprocessed reconstructed image, reconstructed image with modified colourmap and reconstructed image following Gaussian filtering. Pixel size = 20nm. Bottom row: 2 × 2 binned noisy time window images, unprocessed reconstructed image created using the binned time windows, reconstructed image with modified colourmap and reconstructed image following Gaussian filtering. Pixel size = 40nm. Simulation parameters were $t_f = 3$ns and F_{d_0}=0.5.

2.7 Summary

Although there are several different super resolution techniques in common use, these all have associated shortcomings and there is currently no technique which is experimentally simple and can more than double the resolution in living cells. The modelling provided in this chapter has shown that a theoretical > 2 fold increase in resolution is achievable in LIR-SR using parameters similar to those expected in experimental realisation of the technique, such as the fluorescence lifetime, maximum fractional depletion and time window widths. The effect of Poisson noise on image evolution and reconstruction has also been demonstrated for the first time. Furthermore, a novel image reconstruction strategy has been presented which consistently yields an increase in resolution for noisy simulated image data. Experimental validation of the discussed theoretical aspects of LIR-SR will be presented in Chapter 3.

Chapter 3

Development of a novel super resolution microscopy technique. Part II: Results and Discussion

Elements of this chapter have been published in: R.J. Marsh, S. Culley and A. J. Bain, "Low power super resolution fluorescence microscopy by lifetime modification and image reconstruction," Optics Express vol. 22, pg. 12327-38, 2014. This manuscript is provided in Appendix C.

This chapter contains LIR-SR images obtained using the theory and experimental and computational methods detailed in Chapter 2. Various sub-diffraction limit sized beads have been imaged and subsequently reconstructed in both the lateral and axial planes, and beads have also been imaged within living cells *in vitro*, with the microscope set-up and computational techniques as presented in Chapter 2. The effect of CW STED on the photophysics of the beads has also been investigated and detector performance for LIR-SR has been assessed. These results are then discussed with future improvements and investigations suggested.

3.1 Spatial lifetime variations in fluorescent beads

Individual 100nm fluorescent beads were imaged with a range of dump powers to ascertain a suitable power to use for imaging. Figure 3.1 shows the average fluorescence lifetime of beads imaged at four different dump powers, where increasing powers produced shorter fluorescence lifetimes. The pump power was measured prior to injection into the optical fibre as $< 1\mu W$ (subsequently undergoing similar losses to those observed for the dump beam, Section 2.6.1) and was not altered between different dump powers, with all other imaging parameters (pixel size, number of pixels per image, pixel dwell time) also kept constant. When beads were imaged with the pump beam alone, the fluorescence lifetime was largely homogeneous across

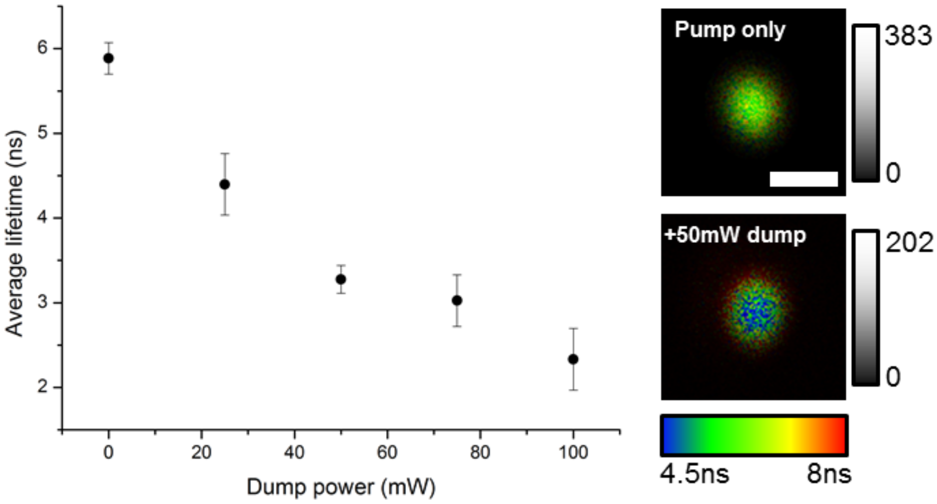

Figure 3.1: Relationship between dump power and measured fluorescence lifetime of 100nm fluorescent beads. Left: Average fluorescence lifetimes calculated for 100nm beads imaged with different dump powers. N=3 single bead images were analysed for each point, and error bars indicate combined fitting errors and standard deviations of data. Laser powers are the uncorrected values set via the computer interface (on-sample powers are typically $10 - 15\%$ of these values). Right: fluorescence lifetime images showing spatial distributions of lifetimes for 100nm beads imaged without (top) and with (bottom) 50mW dump. Grey bars indicate fluorescence intensity in each image, coloured bar indicates fluorescence lifetime (same scale for both beads). Scale bar = 500nm.

each bead (Fig. 3.1, top right), whereas imaging with both beams together produced spatial variations in lifetime across each bead (Fig. 3.1, bottom right) as predicted by the modelling in Chapter 2. Imaging with higher dump powers also reduced the measured intensity of each bead, as can be seen in the images in Fig. 3.1.

To successfully perform LIR-SR, the lifetime shortening (fractional depletion) must be large enough that the spatial variations appear early enough in the fluorescence decay to be distinguishable, but dump power must not be so high as to suppress so much intensity that there is insufficient signal in late time window images. The dump power yielding the most appropriate balance between fluorescence intensity and lifetime shortening was judged to be 50mW (set power at laser output, on-sample power is $\sim$ 6mW), producing an average fractional depletion of $F_d = 0.44 \pm 0.03$. Figure 3.2 shows time windows for a population of 100nm beads imaged with 50mW dump. It can be seen that despite the increasingly broad time windows, peak image intensities decreased dramatically in later time windows. Also shown are line profiles taken horizontally across individual beads demonstrating the broadening of the fluorescence distributions over time. The fourth and fifth time windows did not display the neat ‘donut’ shape that was predicted by the modelling and fluorescence depletion appeared to occur asymmetrically, with the left side of each bead depleting more than the right.

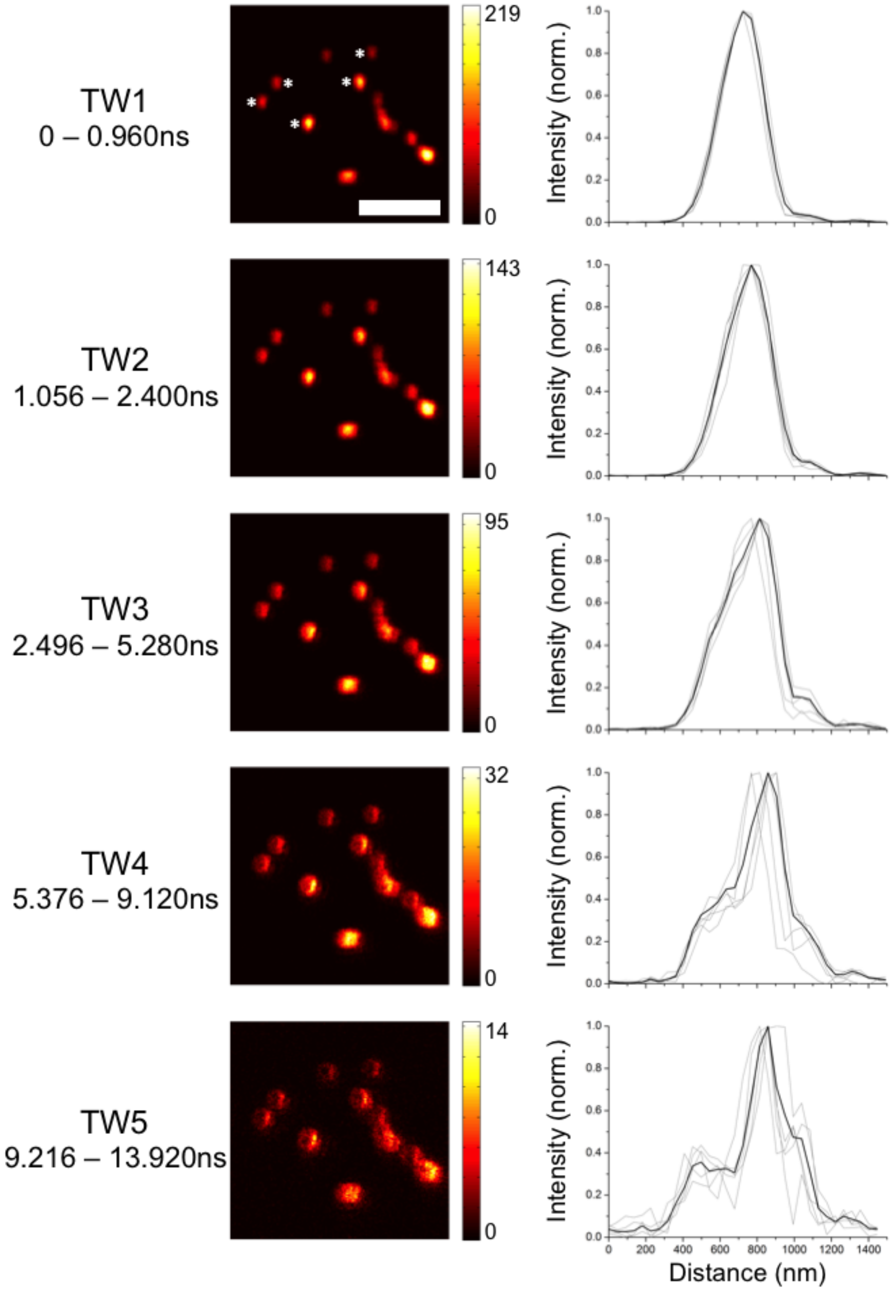

Figure 3.2: Time window images obtained using 50mW dump to image 100nm beads. Time windows are located along the fluorescence decay as indicated by the time ranges next to images (where excitation occurs at 0ns). Scale bar = 1µm. Images are 2 × 2 binned but not smoothed. Line plots show normalised intensity distributions taken horizontally across five beads in the time window images (grey lines) and the average of these profiles (black line). The beads used for profiles are marked by asterisks in the TW1 image.

The asymmetry seen in the later time windows is thought to be due to a slight misalignment of the pump and dump beams as they are reflected off the major dichroic; an investigation of this is presented in Section 3.7. However, the asymmetry in the time window images did not prevent image reconstruction due to the optimisation (genetic algorithm) approach used throughout this chapter. If coefficients were being calculated using simultaneous equations then this could have been problematic as it would prevent simplification of the system of equations which is possible with a symmetrically evolving point spread function (e.g. Fig. 2.16).

3.2 Reconstructions on various sized fluorescent beads

To rigorously test the performance of LIR-SR, beads measuring 20nm, 40nm, 100nm and 200nm were evaporated onto coverslips and imaged. For all bead sizes the first time window (TW1) was taken as the 'confocal' image for comparison. The validity of this approach was verified by comparing bead sizes measured in pump only images with those measured in the TW1 image after subsequent imaging of the same area with both pump and dump beams. For the 20nm, 40nm and 100nm beads the measured sizes from the pump only and TW1 images agreed within the calculated error values. Some measured bead sizes for 200nm beads taken from the TW1 images were slightly smaller than for the pump only images but still corresponded to a reasonable confocal approximation. Using the TW1 image as a confocal approximation is advantageous for comparing resolution as it is inherently aligned with the final reconstructed image (and as such there is no need for drift correction between the two images) and minimises laser exposure to the sample by removing the need to acquire a reference pump only image.

All reconstructed images contained negative-valued pixels, and negative values were also observed when reconstructing noisy simulated data. There are two predominant reasons why negative pixels appear: the finite widths of each time window and noise contributions. Having time windows of finite width means that each time window does not contain a unique spatial distribution associated with an infinitesimal time point but a continuum of spatial distributions, which in an ideal situation would all be present in different proportions but are here forced to contribute equally. Different time windows will also possess different noise profiles, with later time windows containing higher background intensity (relative to the fluorescence intensity) from scattering and dump-induced fluorescence, for example. It has been seen by manually optimising coefficient values that images can be forced to have higher resolutions at the expense of increasingly negative valued pixels; however the target function in the genetic algorithm reconstruction strategy used through this chapter attempts to maintain a background intensity comparable to that in the confocal image. This provides a compromise between obtaining a high image resolution and limiting the quantity and magnitude of negative pixels. The impact of negative valued pixels on image quality are discussed further in Section 3.9.

3.2.1 200nm beads

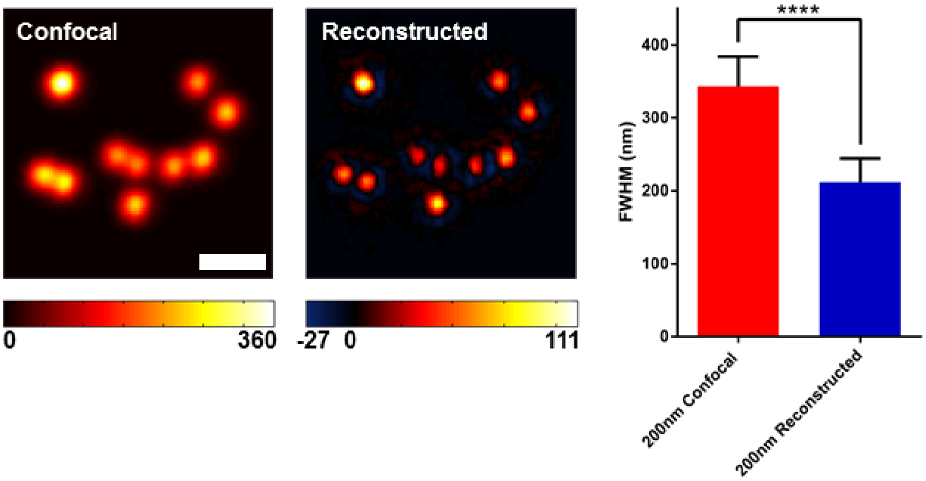

Figure 3.3: Examples of confocal and reconstructed images of 200nm fluorescent beads. Scale bar = 1µm. Right: Bar chart showing average measured bead sizes across all confocal and reconstructed images of 200nm beads. **** indicates statistical significance of P<0.0001, error bars correspond to standard deviation.

The 200nm beads were imaged and reconstructed as a control to see whether the reconstruction algorithm created images with resolutions higher than the known object size (Fig. 3.3). Reconstruction significantly increased the resolution of individual beads (P<0.0001, N=63 beads in 12 images, Wilcoxon matched pairs test) with average measured values shown in Table 3.1, and measured bead sizes in the reconstructed images agreed well with the actual size of the beads. A small number of beads (N=6) reconstructed to sizes <190nm, which was likely due to noise and fitting errors.

Bead size (nm)	Confocal (nm)	Reconstructed (nm)	Relative increase
207 ± 13.8	350 ± 40	210 ± 30	1.6 ± 0.2
100 ± 7.2	270 ± 20	170 ± 20	1.6 ± 0.3
48 ± 6	250 ± 20	170 ± 30	1.5 ± 0.4
24 ± 3	270 ± 30	180 ± 40	1.5 ± 0.4

Table 3.1: Comparison of lateral resolutions for measured bead sizes. Actual bead size and errors are from manufacturer's specification for bead batches used. Relative increase is an average of the increases in resolution for individual beads. Errors are generated from the fitting process combined with the standard deviations of the averaged data as formulated in Section 2.6.6.

3.2.2 20nm, 40nm and 100nm beads

Significant increases in resolution were also seen for the other three bead sizes (Table 3.1, Fig. 3.4). For all three sizes the difference between average confocal and reconstructed bead sizes was statistically significant with $P<0.0001$ (Wilcoxon matched pairs test). The bead populations analysed were as follows: N=99 100nm beads in 13 images, N=114 40nm beads in 13 images and N=69 20nm beads in 13 images. Figure 3.5 illustrates the spreads of confocal and reconstructed bead sizes obtained, as well as the range of resolution increases observed. For these smaller beads, there were no cases where the reconstructed size was smaller than the actual bead size. It can be seen in Fig. 3.5 that some of the beads underwent relatively large 2-3 fold increases in resolution, but also that there were instances for the 20nm beads where the bead size was larger in the reconstructed image than in the confocal image. This was observed for two beads, and closer examination of the fits revealed that Gaussian function fitting to the reconstructed profiles was poor with large errors associated with the calculated FWHM values.

The three different sub-diffraction limit bead sizes all reconstructed, on average, to similar sizes of 170-180nm (Table 3.1). The reasons for this similarity could be attributed to the similar experimental conditions and time windows chosen for the different bead sizes: the lifetimes of the beads were comparable across the different bead sizes (particularly the 20nm and 40nm beads, discussed further in Section 3.6), the dump intensity was not altered between different samples and similar time windows appeared to perform well for the different bead sizes. More rigorous selection of the time windows for individual acquired images may help in uncovering more accurate resolutions for these smaller beads; strategies for this are addressed in Section 3.8.

Some coverslips were prepared with a mixture of the different bead sizes evaporated onto the surface and imaged; however, due to the similar reconstructed sizes of the smaller beads, the different sized beads could not be distinguished in this polydisperse sample. If time window selection could be optimised for the individual bead sizes, this could then present an interesting problem for a sample containing beads with very slightly different fluorescence lifetimes and depletion efficiencies. That is, one set of time windows would perform optimally for one bead size, but not necessarily for the other bead sizes in the image. One solution to this problem could be to partition the image pixels according to fluorescence lifetime or fractional depletion and optimise reconstruction for each part of the image independently with its own set of time windows and reconstruction coefficients. This would be an approach applicable to biological imaging applications where different microenvironments within a cell could result in different fluorescent lifetimes for the same fluorophore dependent on its subcellular localisation.

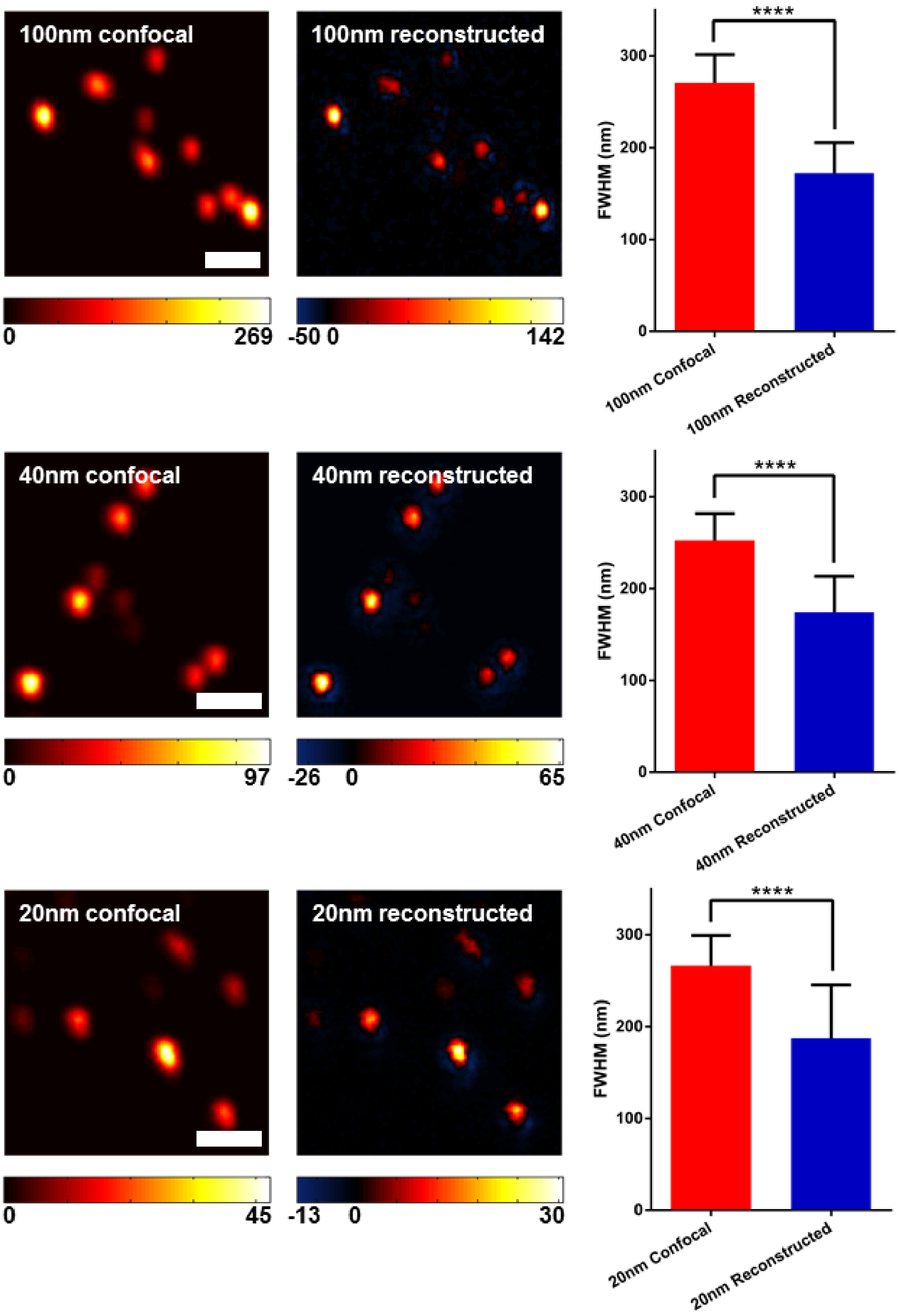

Figure 3.4: Examples of confocal and reconstructed images of 100nm, 40nm and 20nm beads. Scale bars = 1µm. Right: bar charts showing average measured bead sizes across all confocal and reconstructed images for each set of bead sizes. **** indicates statistical significance of P<0.0001, error bars correspond to standard deviations.

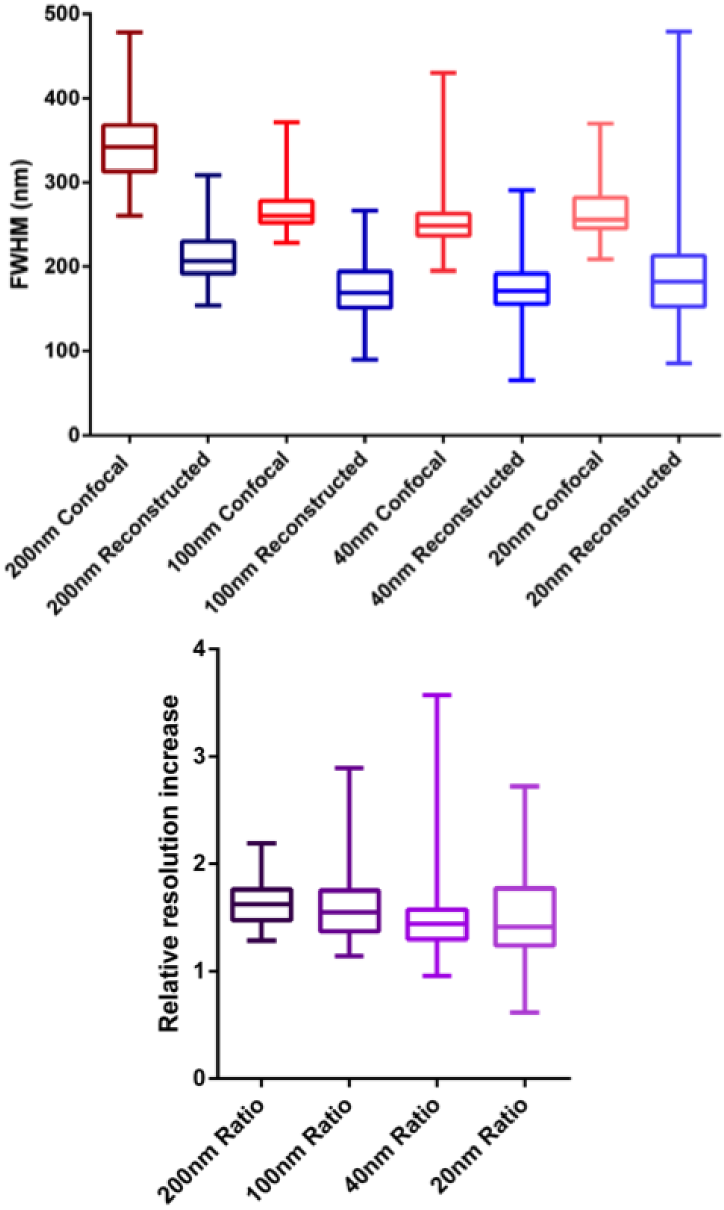

Figure 3.5: Box and whisker summary of lateral resolution for all analysed beads. Top: Measured bead sizes for all beads tested, both confocal and reconstructed. Bottom: Relative increases in resolution (confocal bead size ÷ reconstructed bead size) for all beads tested. In both plots boxes represent the mean and upper/lower quartiles of data, and whiskers extend to the minimum and maximum values.

3.2.3 Control images taken with pump only

Control experiments were also performed where images acquired with the pump beam only were split into time windows with reconstruction attempted as for the images taken with both pump and dump. A summary of the average bead sizes obtained when measured from the confocal (TW1) images, images reconstructed following imaging with pump only, and images reconstructed from subsequent imaging of the same region with pump and dump (pump + dump) is shown in Fig. 3.6. The 40nm and 20nm bead sizes measured from the pump only reconstructions were not significantly different from their confocal counterparts (P=0.69, N=26 40nm beads in 3 images and P=0.05, N=22 20nm beads in 5 images, Wilcoxon matched pairs test), but were both significantly larger than the sizes measured in the reconstructed pump + dump images. The larger bead sizes showed some significant resolution increase from the pump only reconstruction. In the case of the 100nm beads, modest resolution improvement was obtained from the pump only reconstructed images, but this improvement was still less than in the reconstructed images obtained using both beams. For the 200nm beads there was a large increase in resolution obtained from the pump only images, which was not significantly different to the increase obtained through reconstructing the pump + dump images (P=0.60, N=26 beads in 4 images, Wilcoxon matched pairs test).

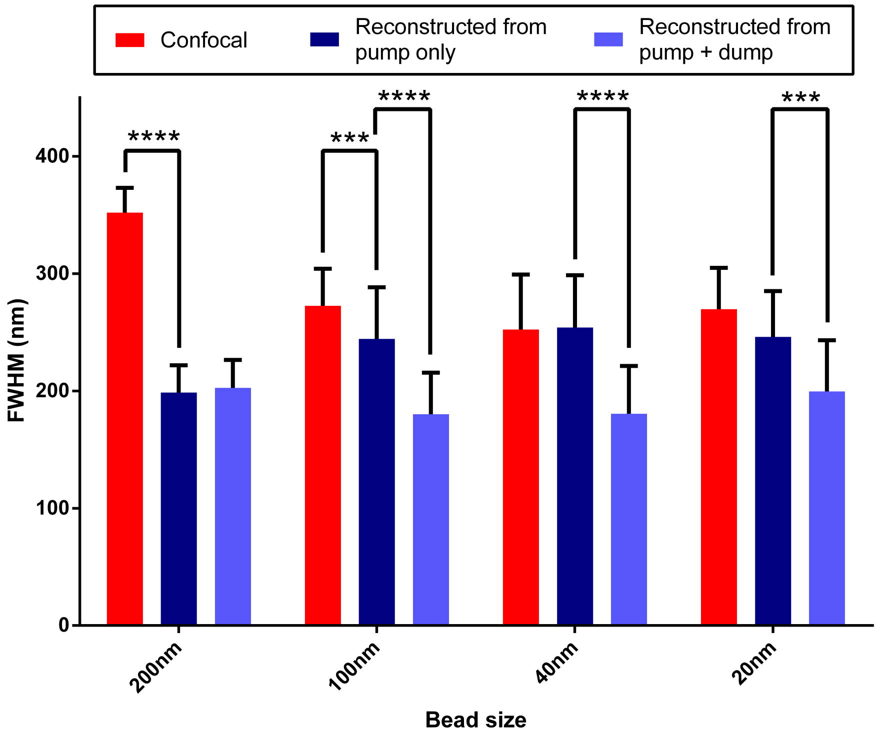

Figure 3.6: Comparison of measured bead sizes with and without the dump beam. Error bars indicate standard deviations of data sets. *** = P<0.001, **** = P<0.0001.

These results can be explained by the fluorescence lifetime images of the beads obtained using pump only (Fig. 3.7). Rather than displaying spatially homogeneous lifetimes, the 200nm beads had shorter lifetimes at the centre and longer lifetimes towards their edges, the same effect as was expected when imaging with both beams together (e.g. Fig. 3.1, bottom right). Fluorescence intensity from the 200nm beads also began to saturate in the centre of the beads even when the excitation intensity was reduced as much as possible without altering any other imaging conditions (e.g. laser repetition rate, pixel dwell time). This effect could be seen to a lesser extent for the 100nm beads, where some beads displayed the expected homogeneous lifetimes but others did have some degree of spatial lifetime variation; the 40nm beads displayed the expected homogeneity of lifetimes. The 20nm beads displayed lifetime variation in the pump only images, but this variation appeared to occur as a gradient along the y-axis of each bead as opposed to radially from the centre of the bead. This may suggest some bleaching effect by the pump beam, as each row of pixels is scanned by the pump beam from left to right, starting from the top of the image and working downwards. Therefore any potential bleaching or local heating effects could be caused by the pump beam scanning the top of the bead and result in different lifetimes when the lower parts of the bead are imaged. However, this effect disappeared when the 20nm beads were imaged with both pump and dump beams, with the lifetimes varying spatially as for the other bead sizes and predictions of modelling.

The lifetime distribution observed in the 200nm beads could be a result of concentration-dependent quenching, whereby more concentrated solutions display shorter fluorescence lifetimes as a result of dipole-dipole interactions between neighbouring fluorophores [104]. Here, fluorophores within the centres of the spherical 200nm beads have more neighbours (i.e. are more highly concentrated) than fluorophores located at the edge of the sphere, which could explain the spatial lifetime differences. However, it is not known why this effect is not as pronounced (or indeed is absent) in the smaller sized beads.

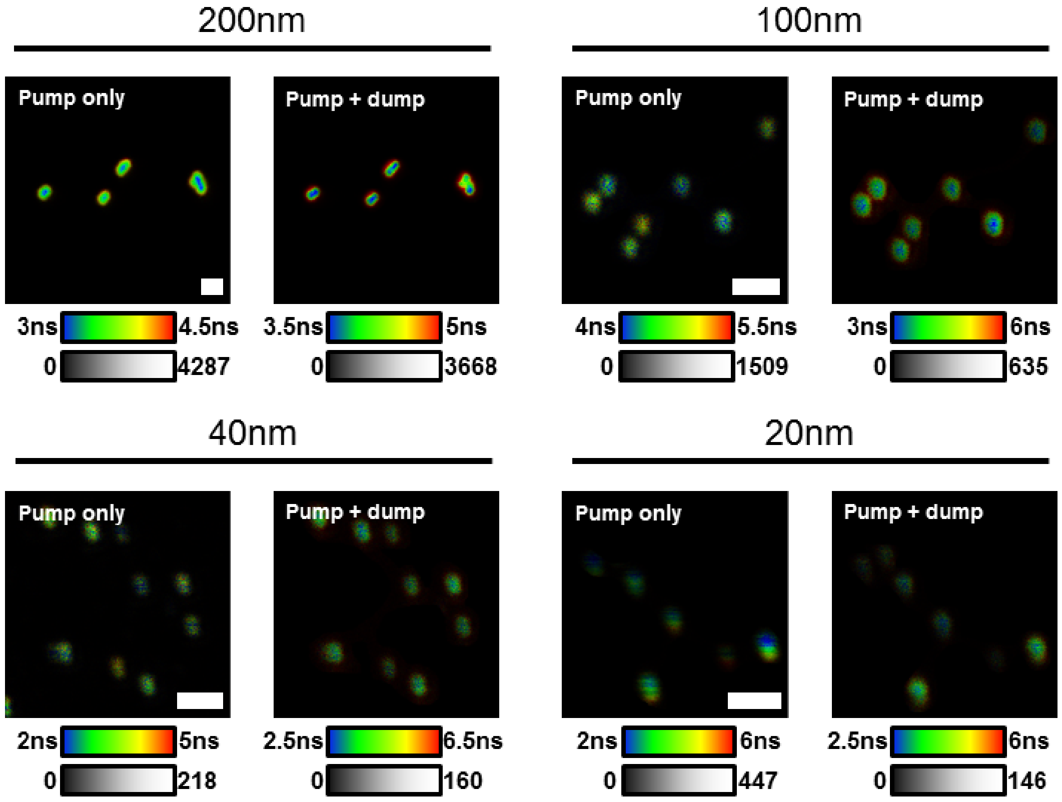

Figure 3.7: Fluorescence lifetime images of beads measured with pump only followed by pump + dump to compare lifetime distributions in the two imaging conditions. Coloured bars indicate lifetime range in each image, grey bars indicate fluorescence intensity in each image. Scale bars = 1µm.

3.3 Axial resolution

The modelling in Section 2.5.4 indicates a theoretical improvement in the axial resolution in LIR-SR, and so to test this, the different sized beads were imaged in the xz-plane as opposed to the xy-plane. For all bead sizes improvements in resolution were observed in the z-direction, as shown in Table 3.2 and Fig. 3.8. The reconstructed 200nm, 100nm and 40nm beads displayed higher axial resolutions compared to their confocal counterparts with significance of $P \leq 0.0005$ (Wilcoxon matched pairs test: N=13 200nm beads in 5 images, N=12 100nm beads in 6 images, N=24 40nm beads in 8 images), however the axial resolutions of the reconstructed 20nm beads were not significantly different to the confocal resolutions (P=0.13, Wilcoxon matched pairs test, N=4 20nm beads in 4 images). Reasons for this relatively poor axial resolution compared to results seen in modelling is discussed in Section 3.7.2.

One prediction from the modelling was that axial resolution improvement should be greater than lateral resolution improvement and so the x and z resolution increases were compared for the beads imaged in the xz-plane. The increase in axial resolution was significantly higher than the increase in lateral resolution for the 200nm beads

Bead size (nm)	Confocal (nm)	Reconstructed (nm)	Relative increase
207 ± 13.8	1400 ± 400	700 ± 200	1.8 ± 0.5
100 ± 7.2	1000 ± 200	700 ± 100	1.6 ± 0.3
48 ± 6	900 ± 200	600 ± 200	1.5 ± 0.3
24 ± 3	1000 ± 100	800 ± 100	1.21 ± 0.05

Table 3.2: Comparison of reconstructed and confocal axial resolutions. Relative increase is an average of the increases in axial resolution for individual beads.

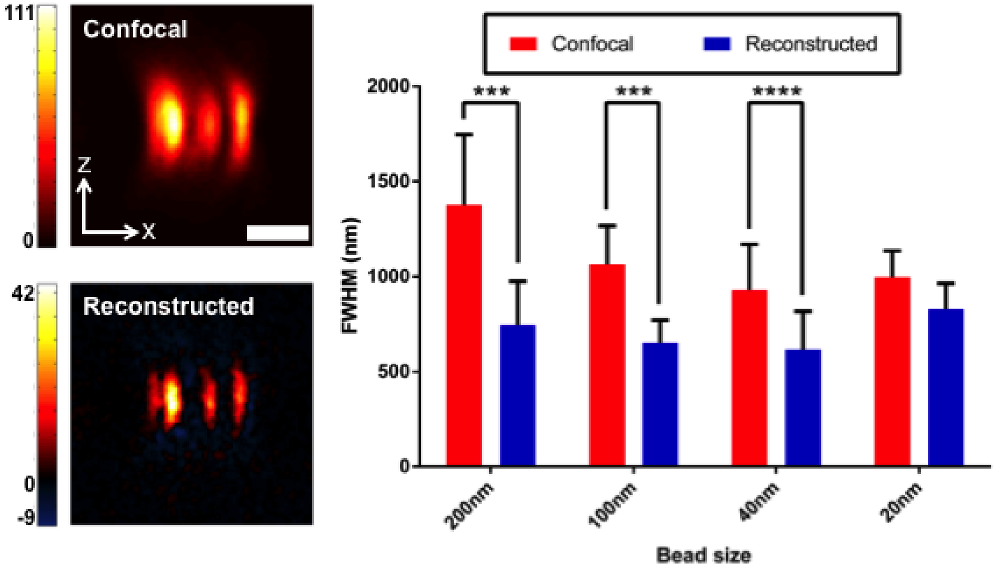

Figure 3.8: Increase in axial resolution of fluorescent beads. Left: Confocal and reconstructed images of 100nm beads in the xz-plane. Scale bar = 1µm. Right: Bar chart summarising measured axial resolutions for various bead sizes in confocal and reconstructed images. Error bars indicate standard deviations of data sets. *** = $P < 0.001$, **** = $P < 0.0001$

(1.8 ± 0.5 vs 1.48 ± 0.08, $P<0.01$, Wilcoxon matched pairs test, N=12 beads in 5 images) but there was no significant difference for any of the other bead sizes tested.

3.4 Beads imaged within living cells

To test the compatibility of LIR-SR with live cell imaging, 20nm fluorescent beads within living HEK-293 cells were imaged. Care was taken to minimise laser exposure to the sample by reducing scan times as much as possible whilst maintaining a sufficiently high photon count to attempt to prevent photodamage. This was achieved by using the same pixel dwell time as for imaging beads on coverslips, but with larger pixel sizes and fewer pixels per image. Figure 3.9 shows an example of a cluster of beads within a living HEK-293 cell which displayed a significant increase in resolution upon image reconstruction. Resolution was consistently higher in the reconstructed images than in the confocal images (Fig. 3.9, right); average confocal bead size was measured to be 290 ± 40nm and average reconstructed bead size was measured to be 160 ± 50nm ($P<0.0001$, Wilcoxon matched pairs test, N=23 20nm beads in 9 images of 6 cells). The average increase in bead resolution was calculated as 1.9 ± 0.6, significantly higher than the resolution increase per bead seen in the images of 20nm beads on coverslips (1.54 ± 0.05, $P<0.05$, Mann-Whitney U test). Causes of this improved resolution in the live cells compared to the bead on coverslips are discussed in Section 3.7.2.

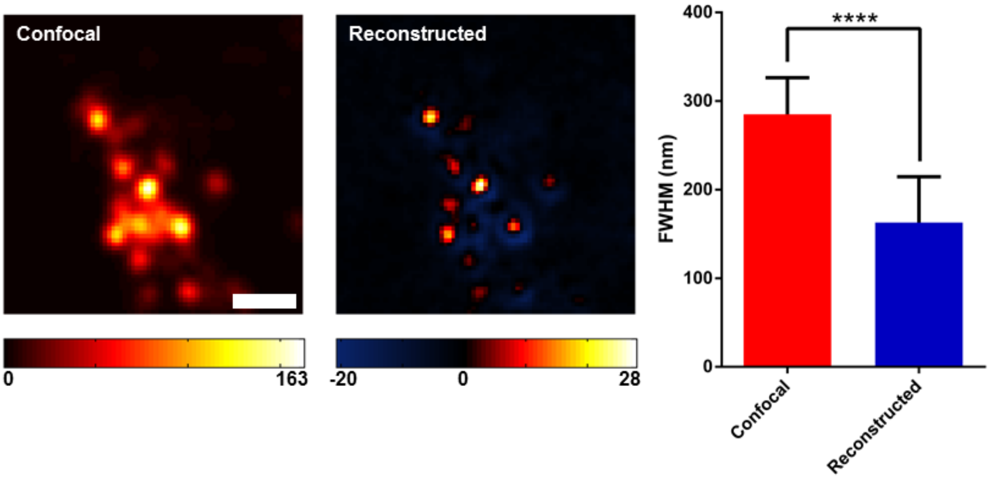

Figure 3.9: Imaging fluorescent beads within a biological sample. Confocal (left) and reconstructed (centre) images of a cluster of 20nm fluorescent beads within a living HEK-293 cell. Scale bar = 1µm. Right: Bar chart showing average measured bead sizes before and after reconstruction across all acquired images. Error bars indicate standard deviations of data sets.

The trypan blue exclusion test was used as an assay for cell viability following imaging. The intact plasma membranes of healthy cells act as a barrier to molecules such as trypan blue, whereas dead cells tend to have compromised membrane integrity and as such become permeable to larger molecules, including trypan blue. As a result, dead cells appear bright blue during this test. Imaging was performed as for all other imaging experiments, including multiple pump only scans to locate suitable regions for imaging, followed by imaging with both beams together. Trypan blue was then applied to the sample medium and the imaged cells were observed with transmitted white light through the microscope eyepiece. Figure 3.10 shows photographs of a cell prior to imaging and then for approximately 9 minutes after application of trypan blue (which was applied as soon as was practical following imaging). This example shows that the cell remained impermeable to trypan blue for a substantial time period following imaging with no major morphological changes compared to the morphology prior to imaging. These initial results suggest that LIR-SR is compatible with live-cell super resolution imaging.

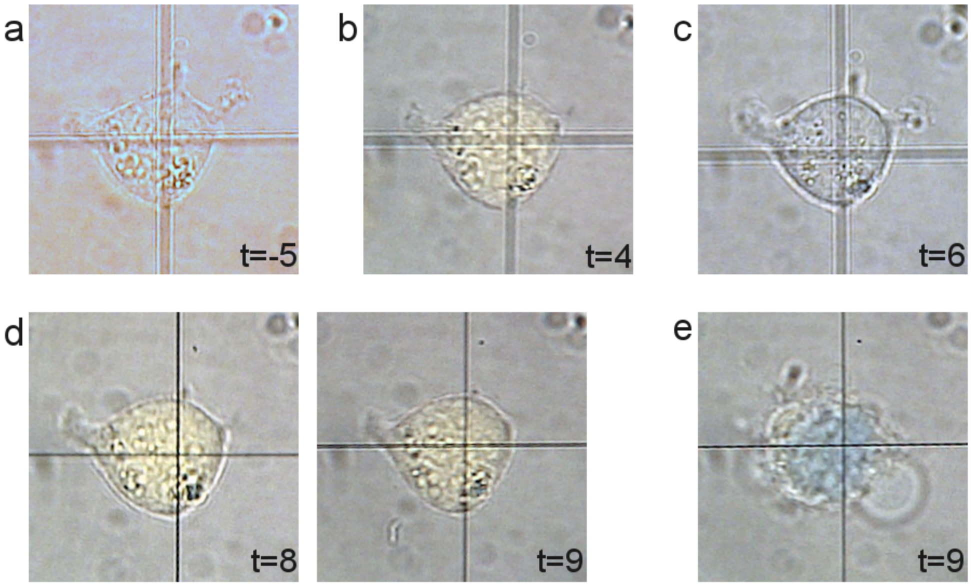

Figure 3.10: Trypan blue test for cell viability following imaging. t indicates time in minutes, where imaging was performed at t=0 mins. a) Cell prior to any laser-scanning imaging, no trypan blue in bath. b) Same cell following imaging, no trypan blue. c) Following bath addition of trypan blue at t=5 mins. d) Following second bath application of trypan blue (at t=7 mins) to ensure sufficient trypan blue concentration. e) Example of a dead cell on the same coverslip that had not been imaged demonstrating uptake of trypan blue and membrane blebbing associated with cell death. The background colour was normalised between images.

3.5 Detector effects

A known issue with the SPAD detectors used here (Section 2.6.1) is that they experience afterpulsing [105]. SPAD detectors operate using a p-n junction biased above the breakdown voltage such that a single photon is capable of imparting sufficient charge to the depletion layer of the junction to trigger an avalanche of charge carriers. This avalanche creates an increase in current, the leading edge of which is used to provide timing information on photon arrival at the detector. This current is then quenched by the electronics within the detector and the voltage bias subsequently restored [106]. However, during the avalanche charge carriers can become trapped within deep layers of the depletion layer which can then be emitted and thus trigger a new avalanche in the absence of a photon, with this ‘false’ signal known as an afterpulse. There is no way of distinguishing afterpulse signal from real fluorescence signal as afterpulse avalanches are temporally correlated with photon-generated avalanches [107]. In images this manifests as noise, and is particularly evident in late time windows as true signal is lower in this region of the decay. Therefore it was a concern that afterpulsing in the SPAD detectors may have been contaminating the spatial information contained in late time windows and impairing reconstructed resolution.

To address the issue of afterpulsing, imaging was repeated at a high pump repetition rate (20MHz) and a lower repetition rate (5MHz). Characterisation of the brand of SPAD detectors used here has shown that there is an order of magnitude decrease in the afterpulsing probability density from 50ns following an initial avalanche pulse (i.e. 20MHz repetition rate) to 200ns following the initial pulse (i.e. 5MHz repetition rate) [105]. Therefore a carrier trapped during detection from an excitation pulse is more likely to contaminate the fluorescence decay detected from one of the next few pulses at the 20MHz repetition rate than it is at the 5MHz repetition rate. In the latter case, afterpulse signals are likely to arrive in the longer interval between the tail of one fluorescence decay and the peak of the next fluorescence decay; the time channels in this interval are not used in image formation anyway, due to their low fluorescence intensity.

As the relative lateral resolution increase for each bead did not significantly vary with bead size (e.g. Table 3.1), all bead sizes tested were grouped together for analysis. The average resolution increase per bead for imaging at 20MHz (1.5 ± 0.4, N=135 beads) was not significantly different to the average resolution increase for imaging at 5MHz (1.5 ± 0.3, N=134 beads, P=0.97, Mann-Whitney U test), and there were no significant differences between the ratios of increase within each set of bead sizes. This implies that either afterpulsing was not impacting upon image quality to the extent that the reconstructed resolution was reduced, or that the the 5MHz repetition rate was still sufficient to induce non-negligible afterpulsing. Reducing the repetition rate further below 5MHz would need to be compensated for by increasing the pixel dwell time to gain sufficient photon counts and would hence increase the overall imaging time, a solution which is not desirable for a system with the goal of live-cell imaging.

To further verify whether the SPAD detectors were creating any artefacts that could diminish image resolution a hybrid PMT detector (HyD) was also used for imaging (Section 2.6.1). Hybrid PMTs are detectors which combine the electron acceleration component of PMTs with the avalanche generation in photodiodes. Photons incident on the photocathode of the HyD produce photoelectrons, which are accelerated in an electric field before reaching an avalanche diode. These vastly accelerated electrons are capable of producing a large number of electron-hole pairs within the diode and thus an avalanche is generated, amplifying the signal. This controlled avalanche formation, as opposed to the avalanche breakdown which occurs in SPAD detectors, is devoid of afterpulsing without compromising timing resolution or single-photon detection [108, 109].

The 100nm, 40nm and 20nm beads were all imaged with the HyD, and the confocal and reconstructed resolutions of beads compared to those obtained with the SPADs (20MHz repetition rate for both detectors); these are shown in Table 3.3. Whilst the confocal and reconstructed resolutions of the 100nm beads were insensitive to the detector type - the 100nm beads displayed no significant difference between SPAD imaging or HyD imaging for measured confocal bead sizes, reconstructed bead sizes or relative resolution increase - there were differences between the two detectors for the 40nm and 20nm beads. The confocal sizes of the 40nm beads were measured to be significantly smaller in the SPADs than in the HyD ($P<0.005$, Mann-Whitney U test, N=37 beads with SPADs vs N=33 beads with HyD), whereas there was no significant difference between the reconstructed 40nm bead sizes. Conversely, the confocal sizes of the 20nm beads were measured to be significantly smaller in the HyD than in the SPADs ($P<0.005$, Mann-Whitney U test, N=31 beads with SPADs vs N=24 beads with HyD), and the reconstructed bead sizes were also smaller in the HyD compared to the SPADs ($P<0.0005$, Mann-Whitney U test).

Bead size (nm)	Detector	Confocal (nm)	Reconstructed (nm)	Relative increase
100 ± 7.2	SPADs	270 ± 30	170 ± 30	1.6 ± 0.4
	HyD	270 ± 40	180 ± 30	1.5 ± 0.2
48 ± 6	SPADs	280 ± 20	170 ± 30	1.5 ± 0.2
	HyD	260 ± 30	150 ± 30	1.8 ± 0.4
24 ± 3	SPADs	250 ± 20	210 ± 40	1.4 ± 0.2
	HyD	270 ± 30	150 ± 40	1.7 ± 0.4

Table 3.3: Comparison of reconstructed and confocal lateral resolutions for the two detectors tested at 20MHz repetition rate. Relative increase is an average of the increases in lateral resolution for individual beads.

For both the 40nm and 20nm beads, the average relative resolution increase per bead was significantly larger for the HyD than for the SPADs ($P<0.01$ for 40nm beads, $P<0.05$ for 20nm beads, Mann-Whitney U test). These results indicate that hybrid PMT detectors are a more suitable choice of detector for LIR-SR imaging, although whether the improved performance with the HyD was related to afterpulsing characteristics or other properties of the detector cannot be deduced. The apparent discrepancies between the confocal bead sizes measured between the two detectors may have arisen from differences in imaging planes between different experiments.

3.6 Lifetime recovery

As one predicted benefit of LIR-SR is that the lower on-sample laser powers used (compared with PALM/STORM and STED) should result in less photobleaching of fluorophores within samples, the photophysical properties of the beads were measured before and after imaging. Images were taken with the pump beam only (‘pump 1’), then with both pump and dump (‘pump + dump’) as usual for LIR-SR, and finally with the pump beam only again (‘pump 2’). Biexponential decays (discussed in more detail in Section 4.6.3) were fitted to the fluorescence intensity decays (in these experiments signals from the two SPAD detectors were combined as $I = I_{\parallel} + 2I_{\perp}$,

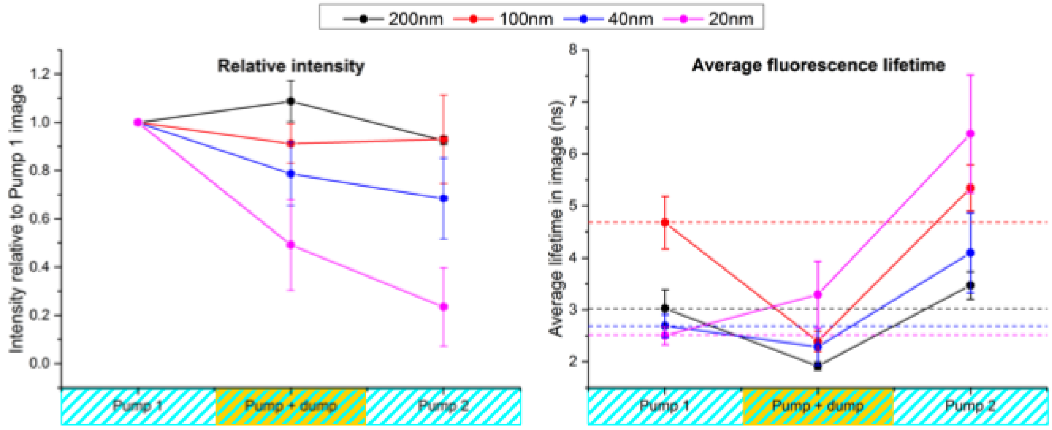

Figure 3.11: Quantification of intensity and lifetime changes of various sized fluorescence beads following LIR-SR. Left: relative intensities of images containing 200nm, 100nm, 40nm or 20nm beads before and following LIR-SR imaging. The total bead intensity within in each image is normalised by division by the intensity of the corresponding Pump 1 image. Right: average fluorescence lifetime of images containing 200nm, 100nm, 40nm or 20nm beads. Dashed lines indicate the Pump 1 average lifetime for each bead size. Error bars combine standard deviations of several images with the exponential fitting errors used to obtain intensities and lifetimes. Data obtained from: N=3 200nm images, N=5 100nm images, N=6 40nm images, N=5 20nm images.

Section 1.4.2) obtained from imaging different bead sizes with this beam sequence and the parameters of these fits were used to calculate the intensities and average fluorescence lifetimes of each imaged region (Fig. 3.11).

It was expected that all bead sizes would follow the same qualitative pattern across the three images; the pump + dump images were expected to display lower intensities and shorter fluorescence lifetimes compared to the pump 1 images as a result of CW STED, whilst the pump 2 images were expected to display similar intensities and lifetimes to the pump 1 images. The 200nm and 100nm beads generally obeyed these relations, although the average intensity of the 200nm pump + dump images was slightly higher than in the pump 1 images (potentially due to dump-induced fluorescence). The 40nm and 20nm beads, however, deviated from the expected behaviour. The intensities of both bead sizes steadily decreased across the imaging sequence, with a $\sim$ 30% decrease in intensity between the pump 1 and pump 2 images for the 40nm beads, and a $\sim$ 75% decrease in intensity for the 20nm beads. Furthermore, the lifetimes of the 40nm and 20nm beads also behaved anomalously, as the average lifetimes of both bead sizes were longer in the pump 2 image than in the pump 1 image ($\sim$ 50% longer for the 40nm beads and $\sim$ 150% longer for the 20nm beads).

Providing a definitive explanation for these results is challenging as many properties of the beads used here, such as their expected fluorescence lifetimes, fluorophore identity and diffusivity of the fluorophores within the beads, could not be obtained from the manufacturers. The lifetimes and intensities of individual beads of the same size also displayed considerable heterogeneity. The most obvious explanation for the consecutive losses in intensity for the 40nm and 20nm beads is that fluorophores within the beads are being photobleached; further experiments would be required to ascertain whether this is due to the pump beam or the dump beam, and hence whether LIR-SR is exacerbating any photobleaching which would be present in pump only confocal imaging. Photobleaching could also explain the lengthening of fluorescence lifetimes, a phenomenon which has also been seen in gSTED microscopy where repeated imaging of microtubules labelled with the fluorophore ATTO647N resulted in an increase in its fluorescence lifetime from 1.9ns to 3.3ns [110]. The explanation offered in this study was that repeated imaging was causing cumulative photobleaching of fluorophores, which reduced the amount of concentration-dependent fluorescence quenching by neighbouring molecules (Section 1.1.6). This is a plausible explanation for the lifetime lengthening observed here, and indicates that this is not necessarily an abnormal feature of imaging with a CW dump beam.

3.7 Comparison of results with theory

The results presented here show that the presence of a CW dump beam is effective in inducing spatially varying fluorescence lifetimes. These were seen across all bead sizes imaged, with significant spatial evolution through the five time windows used to create super resolution images. Resolution improvements were seen for all bead sizes following imaging and reconstruction in both lateral and axial dimensions, and this was also demonstrated in a living sample which survived the imaging process.

Theoretically generated data showed that each point source of fluorescence should broaden symmetrically as time progresses before exhibiting 'donut' intensity distributions at late times following excitation, even when noise was added into the model (e.g. Fig. 2.17). The imaged fluorescent beads were also seen to broaden throughout their fluorescence decays with a donut distribution of fluorescence appearing approximately 2-3 fluorescence lifetimes after excitation (Fig. 3.2), albeit asymmetrically, which is a similar timescale as predicted by the model.

3.7.1 Asymmetric depletion and beam alignment

In contrast to the images produced from simulated data, the fluorescence broadening and donut fluorescence distribution in the experimentally obtained images appeared asymmetric, a phenomenon which was observed for all bead sizes tested and with both detectors. During imaging it had been assumed that the pump and dump beams were well aligned as they were both collimated into an optical fibre (Fig. 2.14), which should act as a pinhole for the beams with the beams exiting the fibre coaxially. Furthermore, the objective used here is super-apochromatic and is designed to 'completely eliminate' (manufacturer's wording) chromatic aberration from 400-900nm. To confirm the extent to which the beams were aligned, a 200nm bead was repeatedly imaged with pump only then dump only (as the 200nm beads were the only size beads yielding a measurable fluorescence signal when imaged with the dump only) and the central coordinates of the bead calculated for each image in ImageJ using the centre-of-mass calculation following background subtraction.

Figure 3.12a shows successive pump only (blue) and dump only (orange) images of the bead overlaid following drift correction between the two images. The repeated imaging allowed for an estimation of the drift in the xy plane, which can be seen in Fig. 3.12b. If there were no drift, the centre of the bead should be at the same (x,y) coordinate in each image, and so the gradients of the fitted lines in Fig. 3.12b should be zero. However, there appeared to be significant drift in both x and y as can be seen from the gradients of the lines fitted to the data in Fig. 3.12b, with an x drift of 17.5 ± 0.2nm/image towards the left side of the image and a y drift of 25.5 ± 0.4nm/image towards the bottom of the image taken with pump only (image acquisition time = 29s, errors generated from straight line fitting). If the beams were perfectly aligned, then the blue and orange lines for both x and y would lie on top of each other. However, this was not the case, and the difference in the intercepts of the fitted lines suggested that the misalignment between the two beams in x was 42 ± 6nm and in y was 60 ± 10nm. The misalignment was not so great that the any of the area of the pump beam lay outside of the boundaries of the dump beam though, so all excited molecules beneath the beam pair should have experienced some degree of CW STED.

Prior to collecting the sequence of images used to assess beam misalignment and drift, the focus was adjusted such that the imaging plane was in the centre of the xz point spread function imaged using pump only. The FWHMs of the 200nm bead repeatedly imaged with each beam (same data set as in Fig. 3.12) were calculated to estimate whether there was any measurable drift in the z direction. There were no significant increases or decreases in the measured FWHMs for either beam with repeated imaging, suggesting that there was little axial drift over the 20 images taken. The ratio of the two average FWHM values was 1.26 ± 0.05 (average dump only FWHM÷average pump only FWHM), which is in agreement with the ratio of the two wavelengths, 1.216 ± 0.003 ($\lambda_{\mathrm{dump}} \div \lambda_{\mathrm{pump}}$), indicating that the beams seem well-aligned in z.

The lateral beam misalignment may be due to wavelength-dependent refraction through optics between the fibre output and the microscope objective, such as the beamsplitter to the CCD camera, the prism and unknown optics in the body of the inverted microscope which cannot be accessed. In earlier work to implement conventional pulsed-pulsed STED microscopy using the same microscope [111], where the dump and (two photon) pump beams were combined in free space rather than through the optical fibre, the dump beam was 'walked' onto the pump beam until

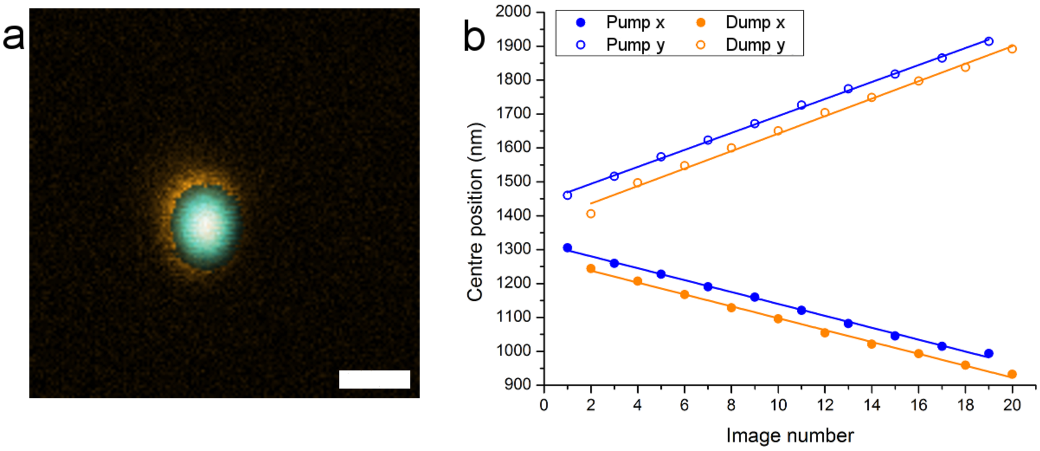

Figure 3.12: Beam alignment and lateral drift. a) Images of the same 200nm bead imaged with dump only (orange) and pump only (blue) overlaid after applying a small correction for drift. Scale bar = 500nm. b) x and y positions of the centre of the 200nm bead calculated for 20 alternating pump only and dump only images. Straight lines are fitted to the determined values. The image was 2760 × 2760nm in total, with all positions relative to the top left corner of the image. Total acquisition time per image was 29s, including switchover of beams.

maximum STED was observed (as measured by fluorescence intensity suppression from a small volume of fluorophores in solution). Following this optimisation it was often observed that the back-reflections of the two beams in the CCD camera appeared slightly misaligned, despite this alignment yielding maximum depletion. Another possible explanation could be bending or warping of the major dichroic caused by clamping it into its holder. Therefore the beam misalignment seen both here and previously may be the result of a fundamental misalignment within the microscope beam path.

Misalignment of the pump and dump beams is likely to be the cause of the asymmetric depletion of the fluorescent beads seen in Fig. 3.2. It is likely that this misalignment varies on a day-to-day basis as a result of adjustments to optical components between the fibre output and the objective. Such adjustments include removing and replacing the major dichroic for various other experiments performed using the microscope and altering the correction collar on the objective. This could explain why the asymmetrical depletion in Fig. 3.2 is more prominent in the x direction than the y direction despite the misalignment measured in Fig. 3.12 being similar in both x and y directions.

3.7.2 Comparison of obtained resolution with theory

Another divergence from theoretical predictions was that the increase in resolution was not as high as predicted. The model data consistently produced a 3-fold increase in lateral resolution without noise, and a 2-fold increase with noise and using the same image reconstruction algorithm as the experimental data. In contrast, whilst some of the experimental images showed these large increases in lateral resolution, many only showed a modest improvement, with an average 1.5-fold increase in resolution. This increase in lateral resolution was consistent across all bead sizes tested, although the 20nm beads appeared to perform better inside the HEK cells (Fig. 3.9). Possible explanations for this could be that the environment of the cell acted as a heat sink for the beads, which was not provided when they were adsorbed onto coverslips, and a smaller refractive index mismatch between the sample and the objective immersion medium (here water), although the correction collar on the objective was adjusted in an attempt to minimise this. The image acquisition times were shorter when imaging the cells than the beads on the coverslips; this could have caused less photobleaching than in the images obtained with longer scan times, where both the intensity and lifetime recovery of the beads were affected.

Further investigations into imaging parameters such as pixel dwell time and pixel size are required to verify whether these impact upon fluorophore photophysics. For example, in conventional STED and gSTED microscopy, when samples such as nitrogen vacancies which are known to experience very little photobleaching (discussed further in Section 5.8.3) are imaged, pixel dwell times are similar to those used for the imaging experiments here (600µs) [86, 112]. However, when both fixed and living biological samples are imaged, pixel dwell times are dramatically reduced to $< 1\mu s$ [86, 113]. The use of such short pixel dwell times on fixed samples implies that there is additional benefit to this rapid scanning other than preservation of live specimens, perhaps regarding bleaching of fluorophores, and as such future development of LIR-SR should include optimisation of image acquisition times.

The model data predicted that a larger increase in resolution should be obtained in the axial direction, and whilst this was seen for the 200nm beads, the increase in axial resolution for the other bead sizes was comparable to or poorer than the increase in lateral resolution (Table 3.2). The improvement in axial resolution was greater for larger bead sizes, with the smallest bead size tested (20nm) showing no significant improvement in resolution. One possible explanation for the poor axial resolution could again be due to the refractive index mismatch; it has been shown that when the refractive index of the objective immersion medium (here water, n=1.33) is greater than that of the sample immersion medium (here air, n=1.00) creates distortion in objects such that they become elongated along the optical axis [114]. It was also observed when using the microscope that axial drift could often be severe: a more rigorous testing of this axial drift could reveal whether this was also contributing to the poor axial resolution.

3.8 Assessment of computational methods

Part of the development of LIR-SR described here has been computational work on dividing the acquired image into time windows and calculating coefficients for reconstruction. The program written for time window selection requires the subjective selection and assessment of time windows by the user. Whilst this process has been sufficient to generate time window images for super resolution reconstruction, sub-optimal choice of time windows may be a contributing factor in the lower than expected resolutions, including the lower resolutions seen in the noisy simulated data in Chapter 2.

One method for automating the time window selection process could involve the design of an objective metric for assessing whether the generated time windows were sufficiently structurally distinct from one another, along with measures to ensure that the signal to noise ratio in each time window image was large enough. Whilst assessment of the signal to noise ratio is computationally straightforward, assessment of evolution in the fluorescence distribution between different images may be more complex due to noise fluctuations on the same scale as the expected variation in the fluorescence distribution. Another approach could be to combine time window selection with the reconstruction process using an area of machine learning known as reinforcement learning [115]. Reinforcement learning is the computational equivalent of 'trial-and-error'; for this application time windows would be generated and run through the reconstruction algorithm, and the obtained resolution used as a measure of time window quality. By assessing the final product (i.e. reconstructed image resolution), the time window selection algorithm would 'learn' good and bad properties of time windows and use this gained experience to generate better time windows.

The major benefit of the genetic algorithm image reconstruction process used in LIR-SR is its speed, as following the selection of profiles in the image by the user, the algorithm takes < 2 seconds to run. However, this algorithm is based on the estimation of resolution through Gaussian curve fitting, which may not accurately describe the shape of the object in the sample. Again, this method also has an element of subjectivity as the user must manually choose the profiles for fitting. Whilst resolution in super resolution literature is usually quantified by the FWHM of either a Gaussian or Lorentzian fitted function (e.g. [80]), here it may be beneficial to use a parameter such as edge steepness of objects within the image, as this should not be affected by the unknown internal structure of each fluorescent object. A potential method to do this would be to detect feature edges within an image [116] and then attempt to maximise the gradients of these edges.

3.9 Image quality

One by-product present in both noisy model and experimental reconstructed images is negative-valued pixels. These do not correspond to any real physical quantities, and arise from the noise in images and the finite widths of the time windows. A more rigorous process for time window selection, as discussed above, may help alleviate this problem.

Minimal processing of images was performed following reconstruction. This is in contrast to STED microscopy where deconvolution is frequently performed on images following acquisition. Deconvolution is a procedure which attempts to remove the blurring effect of the point spread function from acquired images, but is computationally intensive and requires accurate knowledge of the structure of the PSF. However, deconvolution of noisy images typically produced using STED microscopy can produce artefacts such as negative-valued pixels, yet when presented in the literature these negative values are frequently 'clipped' (i.e. set to zero) [72].

STED microscopy also generates negative values through methods other than deconvolution. For example, Vicidomini et al. (2012) [117] used STED wavelengths closer to the emission maximum in a gated STED apparatus, and then performed a subtraction of a late time gate to remove fluorescence induced by the STED beam. However, in the figures in this paper these negative values are not displayed. Reanalysis of the data in this paper shows that the negative values generated in this process are distributed at the edges of bright objects (Fig. 3.13), which is similar to the locations of negative values observed in LIR-SR.

3.10 Future directions

Preliminary results on imaging culture cells indicate that LIR-SR is a suitable technique for live cell imaging. The on-sample intensity was calculated to be $< 10\text{MW/cm}^2$ (for 50mW output from the dump laser), which is at least an order of magnitude lower than that used in STED microscopy, and the image acquisition times are far shorter than required in PALM and STORM. However, as enough photons need to be collected per pixel to generate sufficient intensity in the late time windows (a requirement similar to that of conventional fluorescence lifetime imaging) the image acquisition speed in LIR-SR is currently too slow to image dynamic processes occurring in cells, such as the transport of cargo, which moves at tens of microns per second [118], and calcium transients which last hundreds of milliseconds [119]. One solution for speeding up image acqusition could be to scan multiple beamlet pairs through the sample simultaneously with fluorescence collected by an array of detectors [120]. The results shown here also indicate that use of a hybrid PMT detector could enhance the performance of LIR-SR. Faster image acquisition could also alleviate any potential photobleaching as discussed in Section 3.7.

The next step in testing LIR-SR will be to image a biological sample with bi-

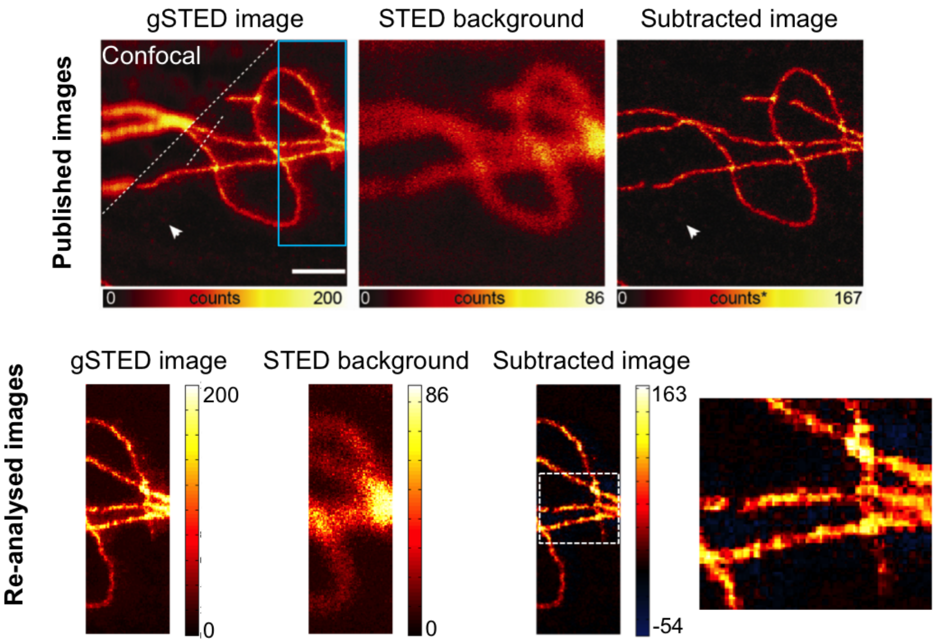

Figure 3.13: Re-analysis of published STED data showing negative values. The top row of images are taken from a figure in Vicidomini et al. (2012) [117] and show images of fluorescently labelled microtubules. In this paper, the second image was subtracted from the first image to yield the final image, where the asterisk in the colourbar indicates that negative values have been clipped to zero. The bottom row shows extracted regions (blue rectangle in top row) from the first two images in the paper, which were appropriately scaled according to the colourbars presented in the paper using Matlab, and the result of performing the same subtraction process but displaying the image using the colourmap defined in Chapter 2 for LIR-SR images. The white dashed region in the re-analysed subtracted image is enlarged.

ological structures labelled, as opposed to containing fluorescent beads. This will test how LIR-SR performs in more challenging imaging environments where fluorophores are distributed more sparsely, autofluorescent molecules may be present and fluorophores may experience more photobleaching. In addition to the computational improvements suggested above, integration of a drift correction system (e.g. [121]) into the microscope would also be beneficial in ensuring sample stability, as small sample displacements during imaging could be eroding the nanoscale changes in spatial fluorescence that are core to LIR-SR.

Whilst the results presented in this chapter do not provide resolutions comparable to that of PALM, STORM or STED microscopy, great care has been taken to rigorously test LIR-SR on a range of different-sized test samples and to present an honest representation of the resolutions obtained in these images. The quoted resolutions are averages of the measured resolutions of every bead imaged, as opposed to selecting only the beads which displayed large increases in resolution. Furthermore, the resolution quantification method (FWHM of fitted Gaussian function) has been consistent across all imaged beads, rather than selecting different quantification methods (e.g. Lorentzian fitting [80] or direct measurement across the bead profile [113]) to yield the highest resolutions from individual beads.

Chapter 4

Quantitative investigations of continuous wave STED dynamics

Chapters 4 and 5 describe investigations into factors affecting the efficiency of CW STED of fluorophores in solution. This chapter firstly summarises previous work by the group on the dynamics of pulsed STED, as well as STED dynamics as described in super resolution microscopy. A description of the time- and polarisation- resolved fluorescence measurements is provided for the CW STED experiments performed here, and mathematical modelling of CW STED behaviour is presented. In this chapter, the effects of rotational diffusion on CW STED dynamics are explored for the fluorophores coumarin 6 and 2',7'-dichlorofluorescein when dissolved in solvents of varying viscosities. The implications of these results are then discussed in relation to modelling and observations from pulsed STED experiments.

4.1 Understanding photophysics in LIR-SR

As CW STED is the fundamental physical process underpinning LIR-SR microscopy, it is important to have a quantitative understanding of its dynamics. The images obtained using LIR-SR were of lower resolution than predicted from theory, and although possible explanations for this have been presented, these are primarily concerned with the image acquisition process and computational methods as opposed to the photophysics of CW STED. Indeed, quantitative descriptions of the underlying photophysics of CW STED are largely absent from published literature. Hence a thorough investigation of CW STED dynamics could provide useful insight for the future development of LIR-SR.

Here, CW STED dynamics were investigated for fluorophores in solution as opposed to the fluorophores contained within polystyrene beads which were imaged in Chapter 3. Such an approach was chosen to ascertain the photophysics of CW

STED as it allowed for experimental control of parameters such as fluorophore concentration and environment, whereas the fluorescent beads used previously were limited in these respects and may have presented confounding factors such as local concentration gradients within the beads and local heating effects. This allows for a fundamental analysis of CW STED photophysics which can be used as a basis for understanding CW STED of more complex confined fluorophore systems such as those which would be present in samples imaged with LIR-SR. Furthermore, by studying CW STED on fluorophores in solution comparisons can be drawn between the work presented here and pulsed STED photophysics in solution presented previously in the literature.

4.2 Deviations from model behaviour in pulsed STED experiments

The group has a strong history of characterising STED dynamics following two photon excitation [28], notably in specially-designed two photon chromophores [122], chromophores with non-planar geometries [123] and biologically relevant fluorophores such as enhanced green fluorescent protein (EGFP) [57]. These experiments have been performed predominantly using pulsed two photon pump and pulsed dump with time-resolved detection, with subsequent modelling and quantification of the behaviour of the fluorophore population and anisotropy. Although different permutations of pump and dump polarisations have been used in these studies, only the results obtained using parallel polarised pump and dump will be discussed in detail here, as these are the beam polarisations used throughout this thesis.

Parameters such as dump wavelength, pump-dump delay (the time difference between the arrival of the pump and dump pulses at the sample) and dump pulse width (duration of each dump pulse) have been extensively investigated. It has been shown that the stimulated emission cross-section σ_{STED} as a function of wavelength mirrors the emission spectrum for two photon chromophores, conventional organic fluorophores [9], and EGFP [57]. Investigations of the pump-dump delay have provided insight into the orientational dependence of STED, as this delay dictates the amount of time available for rotational diffusion away from the highly ordered excited state population created by two photon excitation (Section 1.3.1) before the dump pulse can take effect.

Investigations of STED dynamics as a function of dump pulse width have produced results deviating from those predicted by modelling based on a simple two state system (similar to that described in Section 2.5.1). For pulsed STED, again only the fractional populations of the lower vibrational levels of S_1 (N_{ex}) and the upper vibrational levels of S_0 (N_{gs}) are considered, with the population of the excited state described by

$$\frac{\mathrm{d}N_{\mathrm{ex}}(\theta,\phi,t)}{\mathrm{d}t} = -\frac{S}{\tau_p}W_d(\theta,\phi)N_{\mathrm{ex}}(\theta,\phi,t), \tag{4.1}$$

where $W_d(\theta,\phi)$ is the angle-dependent STED transition probability and τ_p is the dump pulse width (typically $10^{-13} - 10^{-11}$s). S is a dimensionless quantity termed the saturation parameter, given by

$$S = \frac{\sigma_{\mathrm{STED}}E_d}{h\nu A} \tag{4.2}$$

where σ_{STED} is the STED cross section, E_d is the dump pulse energy and A is the dump pulse area [28]. As for the CW case described in Section 2.5.1, rapid vibrational relaxation decouples N_{ex} from N_{gs}; however in pulsed STED, $S/\tau_p \gg k_f$ and so there is no dependence of N_{ex} on the decay rate k_f in contrast to the CW case. Equation 4.1 can thus be solve to yield

$$N_{\mathrm{ex}}(\theta,\phi,t) = N_{\mathrm{ex}}(\theta,\phi,0)\exp\left(-\frac{S}{\tau_p}W_d(\theta,\phi)t\right) \tag{4.3}$$

which can be evaluated over the duration of the pulse ($t = 0 \rightarrow \tau_p$). STED efficiency in pulsed STED is again quantified as fractional depletion F_d, as in CW STED, but for the pulsed case is measured in terms of fluorescence intensity suppression in the presence of the dump beam as opposed to lifetime shortening (as was used for the CW case in Section 2.5.1).

In the model system, increasing dump pulse width τ_p should increase STED efficiency as the probability of re-excitation from high vibrational levels of S_0 decreases with increasing τ_p, as does the probability of dump-induced two photon excitation. However, experimental results for increasing τ_p have not increased STED efficiency as expected [9, 57, 15]. Modelling of the two state system has been performed with the orientational distribution of the excited state accounted for with various pulse widths and rotational correlation times τ_{rot} (Section 1.2.3). Whilst the model described the relationships between dump power and fractional depletion F_d and change in anisotropy ΔR well for short pulses ($\tau_p < \sim$ 10ps), fractional depletion, and hence STED efficiency, was seen to decrease as τ_p was increased [9, 15]. For pulse widths where $\tau_p > 10^{-3}\tau_{\mathrm{rot}}$, the model also suggested that the ground state relaxation time τ_R - which should be independent of STED - was increasing with τ_p [9, 57]. Thus, previous work on quantifying STED by the group has been successful for short dump pulses, but unexpected results and disparities with model predictions have been seen for longer dump pulses.

One proposed explanation for this unexpected behaviour was that the process used to temporally stretch the dump pulse introduced positive chirp such that the early part of the dump pulse contained longer wavelengths than the later part. If so, the later part of the pulse could be re-pumping molecules dumped by the early part of the pulse, manifesting as a reduction in the observed F_d which would be interpreted as an increased τ_R in the fitting of the model [28, 9]. However, more recent experiments on EGFP and other chromophores using a grating-based pulse stretching system where the stretched pulse was negatively chirped (shorter wavelengths arrive before longer wavelengths) produced the same result of lower than expected STED efficiency (F_d) for longer pulses. These experiments produced maximum F_d values for short pulses of $0.95 - 0.99$, but only $0.92 - 0.95$ for long pulses; the expected F_d for the long pulses at the dump energies used (∼50nJ) was $0.99 - 1.0$.

Having ruled out pulse chirping, the proposed explanations for these effects were excited state absorption of the dump beam and the effects of modelling the dump pulse with a square temporal profile rather than a Gaussian [57], though it was later argued that a Gaussian pulse profile should be more efficient than a square one, as in a Gaussian pulse there are regions that are not saturating [15]. However, since the study on EGFP an excited state absorption spectrum for EGFP has been published which shows that there would have been negligible excited state absorption at the dump wavelengths used [124].

Recent experiments investigating dump pulse width have been performed using fluorescein - a simple, well-characterised fluorophore in contrast to some of the more complex fluorophores studied previously - however the same result of poor STED efficiency and deviation from model behaviour was still observed. Furthermore, an apparent relationship between the dump pulse width where the model failed and the solvent viscosity (and hence τ_{rot}) was observed [15].

The experiments producing the non-model behaviour described above were performed using either a streak camera or TCSPC system with low numerical aperture focusing into the sample, with the repetition rates of both beams at 250kHz and the dump pulses provided by an optical parametric amplifier (OPA) pumped by a regenerative amplifier. However, two photon pulsed STED has also been used in the group to attempt to perform conventional STED microscopy in the microscope used for LIR-SR; here the beams were focused into the sample using a high numerical aperture objective at repetition rates of 76MHz, with the dump pulses instead provided by an optical parametric oscillator (OPO). Dump pulses stretched to > 20ps were again incapable of ‘turning off’ all of the excited state population, with maximum values of F_d measured as 0.87 for fluorescein and 0.79 for EGFP in solution [111]. No modelling was performed for this data, but the results indicated that poor STED efficiency was not unique to the apparatus used.

4.3 Deviations from model behaviour in CW STED experiments

CW STED essentially refers to pulsed STED in the limit of an infinitely long dump pulse and so has been studied in the group as a natural progression from pulsed STED experiments with long dump pulses [15]. In particular the commonly used fluorescent proteins EGFP and mCherry have been studied, with single photon excitation as opposed to two photon excitation previously used in pulsed STED experiments.

In the absence of CW dump, both EGFP and mCherry displayed biexponential fluorescence decays and hence two lifetime components, and so the behaviour of these two lifetime components were analysed for each fluorescent protein when measured in the presence of a CW dump beam. For example, the individual STED rates (k_{STED}) of the two components were measured. As in Chapters 2 and 3 the STED efficiency was quantified as the fractional depletion, which was obtained from measuring the shortening of the fluorescence lifetime. In both fluorescent proteins, one fluorescence lifetime component showed significantly more lifetime shortening than the other component, indicating that one fluorescence lifetime component was being depleted more strongly than the other within the same fluorescent protein. The relative contributions (amplitudes) of the two lifetime components to the overall fluorescence lifetime were also seen to vary with dump power for EGFP, with the lifetime component exhibiting stronger depletion increasing in amplitude at higher dump powers. This behaviour was not observed in mCherry. These results suggest complex behaviour for CW STED of fluorescent proteins.

Both proteins have long rotational correlation times compared to their fluorescence lifetimes (EGFP: $\tau_{\mathrm{rot}} = 18$ns, average $\tau_f = 2.7 - 2.8$ns; mCherry: $\tau_{\mathrm{rot}} = 30$ns, average $\tau_f = 1.6 - 1.7$ns) and so as a first approximation, rotational diffusion of both proteins was assumed to be negligible during their fluorescence lifetimes. As a starting point the orientational distribution of fluorophores in both cases was initially assumed to be $\cos^2\theta$ (Section 1.2.1) with the STED rate assumed to be independent of the molecular orientation (again, both pump and dump beam were V-polarised). The total detected intensity over time, $I(t) = I_{||}(t) + 2I_{\perp}(t)$, was modelled as

$$I(t) = \frac{2}{3} C N_{\mathrm{ex}}(0) \exp(-k_f t) \exp\left(-\frac{3BI_{\mathrm{dump}}}{7} t\right) \tag{4.4}$$

where B and C are constants of proportionality, $N_{\mathrm{ex}}(0)$ is the excited state population immediately following excitation, k_f is the undumped rate of fluorescence and I_{dump} is the intensity of the dump beam. A detailed derivation of this relationship can be found in [15]. For simplicity the angular average of the dump field intensity was applied to all orientations; however this model did not describe the experimental observations well.

To rectify this, Eq. 4.4 was reformulated for a fluorophore with two excited state populations as

$$I(t) = \sum_{i=1}^{2} N_i(0)\exp(-k_{fi}t)\frac{3}{4\pi}\int_0^{\pi}\cos^2\theta \exp\left(-(S_i'\cos^2\theta)t\right)\sin\theta \mathrm{d}\theta \tag{4.5}$$

where the two lifetime components are $i = 1$ and $i = 2$, where S_i' is the depletion rate of state i and is the CW equivalent of S in Section 4.2, given by

$$S_i' = \frac{\sigma_{\mathrm{STED}} P_d}{h\nu A} \tag{4.6}$$

where P_d is dump beam power. The orientational dependence of STED is now described by the $\cos^2\theta$ term in the exponent within the integral (the other $\cos^2\theta$ term describing the orientational dependence of the initial excited state population). This equation was numerically solved for different ratios of S_i' (i.e. relative STED rates of the two lifetime components) for both EGFP and mCherry and theoretical intensity decays $I(t)$ were produced and fitted to obtain theoretical values of parameters such as fluorescence lifetimes, STED rates and relative component contributions which were then compared with the experimental data.

For mCherry, the parameter values derived from the experimental data agreed well with theoretical values. However, for EGFP if theoretical parameters were generated which agreed well with experimental values obtained for the shorter lifetime component, these theoretical values did not agree with the longer lifetime component and vice versa. Thus, for EGFP the model was unable to fit both lifetime components simultaneously. These results suggest that while the group's current model of CW STED may sufficiently describe some fluorophores, it cannot accurately account for the behaviour of EGFP in the presence of CW dump.

4.4 Quantification of STED efficiency in super resolution literature

Whilst many technical refinements have been made to conventional STED microscopy since its inception, there has been little quantitative analysis of the underlying photophysics of STED microscopy. Correspondingly there is little discussion of STED efficiency in super resolution literature, and quantification of the necessary STED power to successfully perform super resolution imaging appears to be decided by spatial resolution measurements as opposed to measurements of lifetime shortening or intensity suppression [125].

A commonly used parameter for quasi-quantification of STED microscopy is the 'saturation factor' ζ, which is given by I_{STED}/I_S, where I_{STED} is the on-sample STED beam intensity and I_S is the STED beam intensity required to reduce the probability of spontaneous emission by $1/e$ [126]. However, ζ itself does not account for any orientational ‘holeburning’ (the process by which the dump beam preferentially removes excited state molecules with $\boldsymbol{\mu}_{\mathrm{em}}$ oriented parallel to its polarisation), time-dependent orientational effects or re-pumping effects. Simulations have been performed which describe the effect of polarisation and molecular orientation in pulsed STED microscopy, and these indicate that there is a range of molecular orientations which will experience no increase in resolution even when using circularly polarised pump and dump beams (polarisations most commonly used in STED microscopy) [127]. However, such polarisation effects are often neglected in analytical treatments of STED microscopy.

Leutenegger et al. [128] made an effort to model the effect of dump pulse length (which is inversely proportional to ζ) on STED efficiency in STED microscopy, parametrised as the probability of spontaneous decay (fluorescence) occurring. This modelling showed that for very long dump pulses (small ζ) STED was inefficient as the rate of spontaneous emission was faster than the rate of STED; STED was also predicted to be inefficient for very short pulses (large ζ) as there was insufficient time for vibrational relaxation of S_0 to occur and hence there was a high level of re-pumping back into S_1. The optimal dump pulse length was calculated to be 20-30ps, as this caused a steep decrease in the probability of spontaneous emission with increasing ζ. However, it was also stated that in practical applications of STED microscopy, dump pulses of 100-150ps were found to be most efficient, a significant departure from the theoretical estimation. Reasons provided for this discrepancy were that longer pulses allowed for reorientation of the excited state, caused less photobleaching than shorter pulses and minimised multiphoton excitation. This was not further investigated experimentally and no corrections were made to the model to account for this, so as yet the contributions of these effects have not been quantified. It can also be inferred that, if longer pulses are required than predicted by this simple model, ζ is also smaller than expected as it does not account for these effects.

As the resolution obtained in conventional STED microscopy is given by [76]

$$d_{\mathrm{STED}} = 0.45\frac{\lambda_{\mathrm{STED}}}{\mathrm{NA}\sqrt{1+\zeta}}, \tag{4.7}$$

the effect of ζ being smaller than expected will be an increase in d_{STED} and hence a poorer obtained resolution. Therefore I_{STED} must be increased to raise the value of ζ and subsequently counteract the effects of orientation, photobleaching and multiphoton excitation. This may explain why the dump powers used in conventional STED microscopy seem much higher than predictions from the pulsed STED model for shorter pulses used in previous work by this group. Although the modelled increase in STED efficiency with pulse length by Leutenegger et al. is in agreement with the modelling performed by this group, the experimental need for longer pulses for STED microscopy to perform more efficiently is clearly at odds with the pulse length experiments described in Section 4.2, where longer pulses resulted in lower STED efficiency. Quantification of thus far neglected photophysical properties of STED may therefore benefit understanding of the behaviour of conventional STED microscopy.

Whilst it is acknowledged that CW STED microscopy is less efficient than pulsed STED microscopy due to the lower instantaneous intensity of the dump beam [110], again there is little description of the underlying photophysics. For example, whilst Vicidomini et al. [110] have presented a theoretical framework for g-STED, the population of the excited state is described using the same simple two state model as is used in LIR-SR theory (Eq. 2.7) again neglecting orientational effects, with the majority of the theory concerning the spatial distribution of fluorescence.

4.5 Overview of experiments

To investigate the photophysics of CW STED, time- and polarisation-resolved fluorescence measurements were made for the fluorophores coumarin 6 and 2',7'-dichlorofluorescein in solution for a range of CW dump powers. These measurements were made using the microscope TCSPC system as used for LIR-SR imaging and previous CW STED work in the group.

Coumarin 6 and 2',7'-dichlorofluorescein were chosen for investigation of CW STED in solution as they have monoexponential undumped fluorescence lifetime decays, in contrast to the biexponential decays displayed by mCherry and EGFP in previous work. As simulations of CW STED on molecules with monoexponential decays experiencing little rotation produced theoretical decays which were better described by biexponential functions (described in detail in Section 4.7.1), fluorophores which are known to possess monoexponential decays should be easier to interpret using this model than the fluorescent proteins.

Furthermore, the use of these small organic fluorophores allowed for the investigation of the effects of rotation on STED efficiency, which was not possible for the fluorescent proteins due to their innately slow rotational correlation times. Here, the rotational correlation time τ_{rot} was varied by dissolving the fluorophores in three different solvents of varying viscosities, as τ_{rot} is proportional to viscosity η (Section 1.2.3).

4.6 Methods

4.6.1 Samples

Coumarin 6 (Exciton Inc.) and 2',7'-dichlorofluorescein (Sigma-Aldrich, referred to throughout as fluorescein) were used for all experiments. The structures and spectra of these two fluorophores are provided in Appendix A. A summary of the combinations of fluorophores and solvents is shown in Table 4.1. Coumarin 6 was measured when dissolved in glycerol (2.5×10^{-3}M) and ethylene glycol (1×10^{-5}M), and fluorescein was measured when dissolved in water (1×10^{-5}M) and ethylene glycol (1×10^{-5}M). Coumarin 6 was insoluble in water and fluorescein exhibited a biexponential undumped fluorescence decay when dissolved in glycerol, and as such these experiments were not performed on these combinations. In all experiments 50µl of solution was pipetted onto a thickness 1 coverslip. For fluorescein in water this volume was topped up midway through the experiment to compensate for any sample evaporation.

	Water	Ethylene glycol	Glycerol
Coumarin 6	Insoluble: no decay obtainable	Soluble: monoexponential	Soluble: monoexponential
2'7'-dichlorofluorescein	Soluble: monoexponential	Soluble: monoexponential	Soluble: biexponential

Table 4.1: Solubility and pump-only decay characteristics of coumarin 6 and 2',7'-dichlorofluorescein in water, ethylene glycol and glycerol. Only fluorophore/solvent combinations yielding a monoexponential pump-only fluorescence decay were examined with CW STED: greyed-out combinations were not used.

4.6.2 Experimental set-up

The experimental set-up was the same as used in LIR-SR (Fig. 2.14), including 490nm pulsed diode pump laser and 594nm CW DPSS dump laser, filters and 50µm pinhole. The hybrid detector was not used in any of the experiments here. For all measurements the two SPAD detectors were used in conjunction with the cube polariser such that the V- (parallel) and H- (perpendicular) polarised fluorescence signals were separately detected. The polarisations of both pump and dump beams were both V-polarised when focused through the objective. The repetition rate of the 490nm pump beam was $\leq$ 20MHz in all experiments and the power was adjusted such that detection rate satisfied the 1% sampling rate criterion (over both detectors, Section 1.4.1); this typically corresponded to a pump power of $\sim$ 1µW ($\sim$ 2µW per unit bandwidth for 0.5nm spectral bandwidth of pump laser) before entry into the optical fibre. Measurements of the pump power after the major dichroic were seen to be indistinguishable from background light measurements taken with the same powermeter elsewhere within the box containing the intermediate optics of the microscope ($\sim$ 300nW).

Each experiment commenced with a measurement of the undumped (i.e. pump beam only) lifetime of the sample, and then dumped (i.e. pump beam and dump beam together) measurements were taken starting with the highest dump power and incrementally decreasing it. Undumped measurements were repeated every four dump powers tested to monitor whether the undumped lifetime of the sample was altered over time by the dump beam. A second measurement at the highest dump power tested was repeated at the end of each experiment. Each measurement comprised the detected fluorescence from a fixed point for 30 seconds (i.e. the objective was not scanned through the sample, in contrast to the imaging experiments described previously).

For the measurements of coumarin 6 in ethylene glycol a vertical-external-cavity surface-emitting laser (VECSEL) was used as the dump source.[1] Here the VECSEL was pumped by a 200W 808nm diode source and tuned to operate in continuous wave mode at 595nm [129]. The 595nm VECSEL output followed the same light path as the 594nm DPSS dump laser and was hence coupled into the same fibre as the 490nm pump laser. VECSELs have the advantages of being both tunable and high-power; here the latter property was exploited, with maximum power after the major dichroic measured as 82mW.

4.6.3 Polarised fluorescence detection and fitting

As V- and H-polarised fluorescence components were detected in two separate detectors, a G-factor correction was made to account for differences in detector efficiency, and the V-polarised measurements were normalised by division by the G-factor (Section 1.4.2). For fluorescein in water, the G-factor was adjusted such that calculated anisotropy decayed to zero for the first undumped measurement taken. For the samples in ethylene glycol, the G-factor was calculated from a measurement of fluorescein in water as described above and then applied to the measurements in ethylene glycol (no adjustments to any optics or the pinhole were made between the measurement in water and the measurements in ethylene glycol). For coumarin 6 in glycerol, the G-factor was adjusted such that the calculated anisotropy had an initial value of 0.4 (as expected from Section 1.2.2) at t=0 (set as halfway up the fluorescence rise). Values of the G-factor measured for the various experiments were consistently in the range $G = 1.1 - 1.2$.

The intensity decays displayed and fitted here are not deconvolved and hence contain a contribution from the instrument response function (IRF). However, the FWHM of the IRF of the microscope was measured to be $\sim$ 140ps, which is substantially faster than the fluorescence lifetimes of the fluorophores used here and so should not have a significant impact on lifetime measurements. IRF deconvolution is also a time-consuming process and can introduce additional errors and noise [130]. Total intensity decays were thus calculated as

$$I(t) = \frac{1}{G} I_V(t) + 2I_H(t) \tag{4.8}$$

---

[1] VECSEL construction and operation performed by Ms. Emmi Kantola, Optoelectronics Research Group, Tampere University of Technology

and anisotropy decays were calculated as

$$R(t) = \frac{\frac{1}{G}I_V(t) - I_H(t)}{\frac{1}{G}I_V(t) + 2I_H(t)} \tag{4.9}$$

where $I_V(t)$ and $I_H(t)$ are the vertically and horizontally polarised fluorescence intensities respectively, and G is the G-factor.

The total undumped intensity decays were fitted to a monoexponential function, and the total dumped intensity decays were fitted to either a monoexponential function or a biexponential function. The form of the monoexponential function fitted for both undumped decays and, when appropriate, dumped decays was

$$I(t) = N \exp\left(-\frac{t}{\tau}\right) + I_0 \tag{4.10}$$

where N = absolute amplitude, τ = lifetime ($= \tau_f$ in undumped decays) and I_0 = background signal, and the form of the biexponential function fitted (dumped decays only) was

$$I(t) = N_1 \exp\left(-\frac{t}{\tau_1}\right) + N_2 \exp\left(-\frac{t}{\tau_2}\right) + I_0 \tag{4.11}$$

where N_1 and N_2 are the absolute amplitudes of lifetime components τ_1 and τ_2 respectively. The background signal I_0 arises from residual dump beam reaching the detectors, detector afterpulsing and any stray light detected.

The zero time point t_0 was fixed to be the time at which the rise of the fluorescence intensity reached approximately half its maximum intensity. The fitting range was from after the early period following excitation known to be contaminated by the IRF of the microscope to after the end of the fluorescence decay. Statistical weighting was used during the fitting process with weights

$$w_i = \frac{1}{I_i} \tag{4.12}$$

where w_i is the weight for data point i having intensity I_i. All fitting was performed using a non-linear least squares fitting algorithm (Levenberg-Marquadt) built into the Origin software (as used in Chapters 2 and 3).

In all cases the undumped intensity decays were monoexponential. Dumped intensity decays were usually fitted to the biexponential function, with the exception of some low dump power decays which fitted adequately to the monoexponential function. Fit quality was assessed using the χ^2 fitting statistic and visual inspection of the residual plot (residual = actual value - fitted value for each data point), with good fits expected to have low χ^2 values and a residual plot symmetric about zero [131].

4.6.4 Definitions of measured and derived parameters

For biexponential fits, τ_1 was defined as the faster lifetime component and τ_2 as the slower lifetime component. Where dumped decays fitted adequately to a monoexponential function the lifetime was designated as τ_1 and τ_2 was assumed to be zero. For consistency the same parameters were extracted as for the previous work on CW STED of fluorescent proteins in the group [15]. As such testing of the model on the fluorophores possessing monoexponential lifetimes used here could be used to ascertain whether orientational effects and different radiative rates were a sufficient explanation for the results seen for the biexponentially decaying fluorescent protein mCherry [15].

Fractional amplitudes were defined as

$$A_1 = \frac{N_1}{N_1 + N_2};\ A_2 = \frac{N_2}{N_1 + N_2} \tag{4.13}$$

indicating the relative contributions of each lifetime component to the total intensity decay.

The STED rates were defined as the difference between the dumped decay rates and undumped decay rates as

$$k_{\text{STED1}} = \frac{1}{\tau_1} - \frac{1}{\tau_f};\ k_{\text{STED2}} = \frac{1}{\tau_2} - \frac{1}{\tau_f} \tag{4.14}$$

where τ_f was the mean undumped fluorescence lifetime calculated from the undumped measurements made throughout the course of each experiment. It should be noted that k_{STED1} and k_{STED2} have a slightly different meaning to the k_{STED} parameters defined for the fluorescent proteins EGFP and mCherry [15]. For these fluorescent proteins, k_{STED1} and k_{STED2} corresponded to the two lifetimes present in the undumped decays, which were then further modified by CW STED. Here the two lifetimes are solely a product of the different rates of STED experienced by differently-oriented fluorophores which display monoexponential undumped decays.

The fraction of the excited state population removed by STED is termed the fractional depletion (as in Section 2.5.1) and was defined as

$$F_d = \frac{\tau_f - \tau_d}{\tau_f} \tag{4.15}$$

where τ_d is the average dumped fluorescence lifetime as given by

$$\tau_d = A_1\tau_1 + A_2\tau_2, \tag{4.16}$$

where for monoexponential dumped decays $\tau_d = \tau_1$.

Errors in the values of τ_1, τ_2, N_1 and N_2 were taken as the errors produced by the fitting algorithm. Errors in the derived parameters $A, k_{\text{STED}}, \tau_d$ and F_d were propagated using the formula [103]

$$(\Delta Z)^2 = \sum_i^n \left(\frac{\partial Z}{\partial x_i}\right)^2 (\Delta x_i)^2 \tag{4.17}$$

where $Z = f(x_1, x_2 ... x_n)$, for example $k_{\text{STED1}} = f(\tau_1, \tau_f)$ and Δx_i is the error associated with variable x_i (e.g. τ_1, τ_f for the case of k_{STED1}).

No individual parameters are extracted from the anisotropy decays. A useful presentation of the qualitative degree of the dump induced depolarisation of the excited state was instead obtained by measuring the change in anisotropy as

$$\Delta R(t) = R(t)_{\text{undumped}} - R(t)_{\text{dumped}}. \tag{4.18}$$

4.6.5 Calibration of on-sample powers

Prior to the acquisition of each decay, the dump power was measured after reflection off of the major dichroic, and all powers stated in the results refer to this measurement. All power measurements were made using a digital powermeter (PM100D with S130C sensor, Thorlabs, USA) set to the appropriate wavelength. Powers were taken as the average of a 10 second measurement (sampling rate = 3.5Hz), with the error taken to be the standard deviation of this measurement as calculated by the powermeter.

Figure 4.1 shows how these powers relate to the approximate on-sample power. On-sample power was estimated by affixing the sensor of the powermeter to the microscope stage and raising the objective to its maximum height to mimic the small distance between objective and sample in experiments. The on-sample power was approximately linear with power measured after the major dichroic, with 35.1±0.3% transmission at 594nm through the objective as calculated by a linear fit to the data.

4.6.6 Mathematical modelling

Modelling of the behaviour of a fluorophore assumed to undergo no rotation (i.e. coumarin 6 in glycerol) was performed using a program written by Dr Richard Marsh in Mathematica 4.1 (Wolfram Research Inc.). The model also assumes that the pump and dump are both V-polarised and that the fluorophores are isotropically distributed, and is described below for single photon pump and a fluorophore with a monoexponential undumped intensity decay.

The model was based on temporal dynamics of CW STED as discussed in Section 2.5.1, with the equation describing the population of the excited state N_{ex} in the presence of the CW dump the same as Eq. 2.7 except here with orientational dependence included:

$$\frac{\mathrm{d}N_{\text{ex}}}{\mathrm{d}t} = -k_f N_{\text{ex}} - S' \cos^2\theta N_{\text{ex}} \tag{4.19}$$

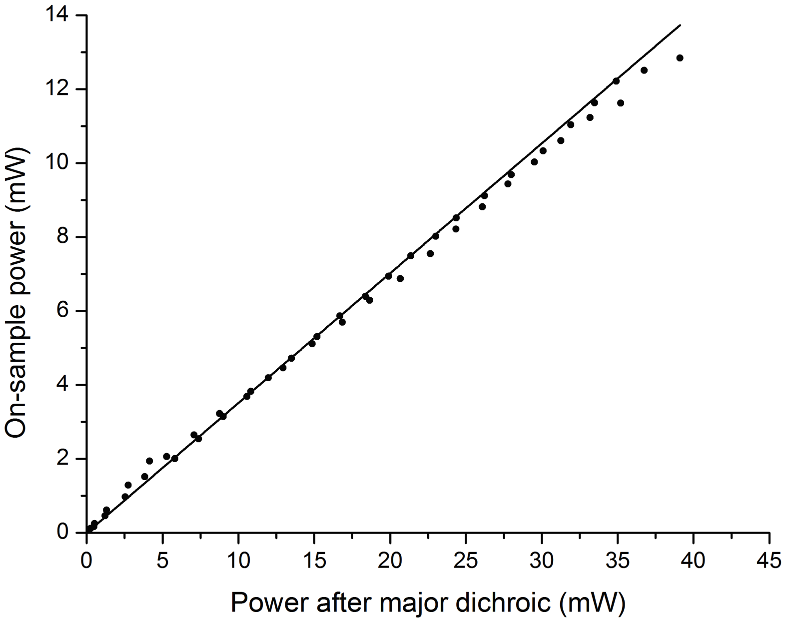

Figure 4.1: Calibration curve for on-sample dump powers. Power measured after the major dichroic is plotted against corresponding power measured after the objective. Error bars on individual measurements are too small to plot; instead measurements were repeated on two different days and combined into one dataset to account for variations in measurement precision and optical system alignment. Black line is fit through data of $y = (0.351 \pm 0.003)x$, $R^2 = 0.995$. Laser source is 594nm DPSS laser with same major dichroic as used throughout.

where $k_f = 1/\tau_f$. Here, θ is the angle between the emission transition dipole moment (assumed to be parallel to the absorption transition dipole moment) and the electric field vector of the dump field (parallel to that of the pump field for these experiments), and so $\cos^2\theta$ describes the angular dependence of depletion. S' is the CW depletion rate as given by

$$S' = \frac{\sigma_{\mathrm{STED}} P_d}{h\nu A} \tag{4.20}$$

where σ_{STED} is the STED cross-section, P_d is the dump power, and A is the area of the focal spot. Following single photon excitation the orientational distribution of the undumped excited state population is assumed to be

$$P_u(\theta,\phi) = \frac{1}{4\pi}\left(1 + \frac{2}{\sqrt{5}}\frac{Y_{20}(\theta,\phi)}{Y_{00}(\theta,\phi)}\right) \tag{4.21}$$

as in Section 1.2.4. The dumped excited state population is therefore described as the product of the undumped excited state distribution (Eq. 4.21) and the angle-dependent solution to the temporal evolution of the excited state population due to dumping (solution of Eq. 4.19),

$$P_d(\theta,\phi,t) = P_u(\theta,\phi)\exp\left(-\left(k_f + S'\cos^2\theta\right)t\right). \tag{4.22}$$

The value of k_f is the reciprocal of the experimentally obtained value of the undumped fluorescence lifetime τ_f, and $S'\cos^2\theta$ is the rate of STED weighted by its angular dependence. The intensity decay is then given by

$$I(t) \propto \int_0^{\pi}\int_0^{2\pi} P_d(\theta,\phi,t)\sin\theta \mathrm{d}\theta\mathrm{d}\phi \tag{4.23}$$

and the anisotropy decay is given by [28]

$$R(t) = \frac{\int_0^{\pi}\int_0^{2\pi} P_d(\theta,\phi,t)\left(\frac{4\pi}{5}\right)^{\frac{1}{2}} Y_{20}(\theta,\phi)\sin\theta \mathrm{d}\theta\mathrm{d}\phi}{\int_0^{\pi}\int_0^{2\pi} P_d(\theta,\phi,t)\sin\theta \mathrm{d}\theta\mathrm{d}\phi}. \tag{4.24}$$

Simulated intensity and anisotropy decays were produced by numerical integration of Eqs. 4.23 and 4.24 over a time range of 0-20ns for various values of S' (i.e. different dump powers) for accurate comparison with experimentally obtained data. Simulated data was then fitted using Origin as described in Section 4.6.3 and expected values for the parameters in Section 4.6.4 were obtained from these fits.

4.7 Results

Results were obtained for fluorescence detected from the fluorophores in three different rotational regimes. The first regime is for fluorophores in glycerol, where there is minimal rotational diffusion. Here, orientational holeburning should be observed, where the dump beam removes molecules oriented at $\theta \sim 0°$ to the dump field (molecules whose dipole moments are parallel to the polarisation of the dump field) from the excited state more efficiently than it removes molecules oriented at $\theta \sim 90°$ (molecules whose dipole moments are perpendicular to the polarisation of the dump field). Secondly, in water, where rotational diffusion should be fast enough to constantly refill the orientational hole burnt in by the dump beam. Thirdly, an intermediate regime is shown for fluorophores in ethylene glycol which should behave as a transition between the first two extreme cases.

4.7.1 Limit of no rotation

Following on from previous work in the group measuring and modelling CW STED in fluorescent proteins [15], whose rotational correlation times τ_{rot} are substantially longer than their fluorescence lifetimes, a similar situation where τ_{rot} is slower than τ_f was investigated here using coumarin 6 dissolved in the viscous solvent glycerol ($\eta = 1.29\text{Ns/m}^2$ at 21°C, compared to 0.001Ns/m^2 for water [132]). Very few solvents are more viscous than glycerol, and so this system is as immobile as coumarin 6 can be without entering the solid phase. In contrast to EGFP and mCherry, which exhibited biexponential undumped decays, coumarin 6 was selected as it displayed a monoexponential undumped lifetime in glycerol ($\tau_f = 2.483 \pm 0.002\text{ns}$, average of N=5 decays taken throughout the course of a single experiment on the same batch of sample). The rotational correlation time for coumarin 6 in glycerol was estimated from monoexponential fitting to undumped anisotropy decays to be $\tau_{\text{rot}} = 100 \pm 10\text{ns}$ (N=5 decays), where the initial anisotropy R_0 was fixed as 0.4 and the steady state anisotropy R_∞ was fixed as 0. As τ_{rot} is approximately 40 times slower than τ_f, coumarin 6 experiences minimal rotation during the lifetime of the excited state.

To test agreement between experimental behaviour and the model described in Section 4.6.6, experimental parameters measured at a variety of dump powers (examples of measured intensity decays shown in Fig. 4.2) were plotted on the same axes as simulated theoretical parameters generated at different values of S' (examples of simulated intensity decays shown in Fig. 4.3) . S' is proportional to dump power, and so scaling of S' was performed such that the model-generated curves agreed as closely as possible with as many experimental data points as possible simultaneously for the seven plotted parameters ($\tau_{1,2}$, $k_{\text{STED}1,2}$, $A_{1,2}$ and F_d). A range of scaling factors was tested and no factors were found which could force the theoretical and experimental datasets agree at experimental dump powers $> 10\text{mW}$; any agreement was consistently confined to the low dump power regime.

The 'dump powers' at which simulated data are plotted are the values of S' used in the model scaled by a factor of 13 (i.e. theoretical dump power after major dichroic $= 13 \times S'$). Plots showing the values of the intensity decay parameters from both measured and simulated data are shown in Fig. 4.4.

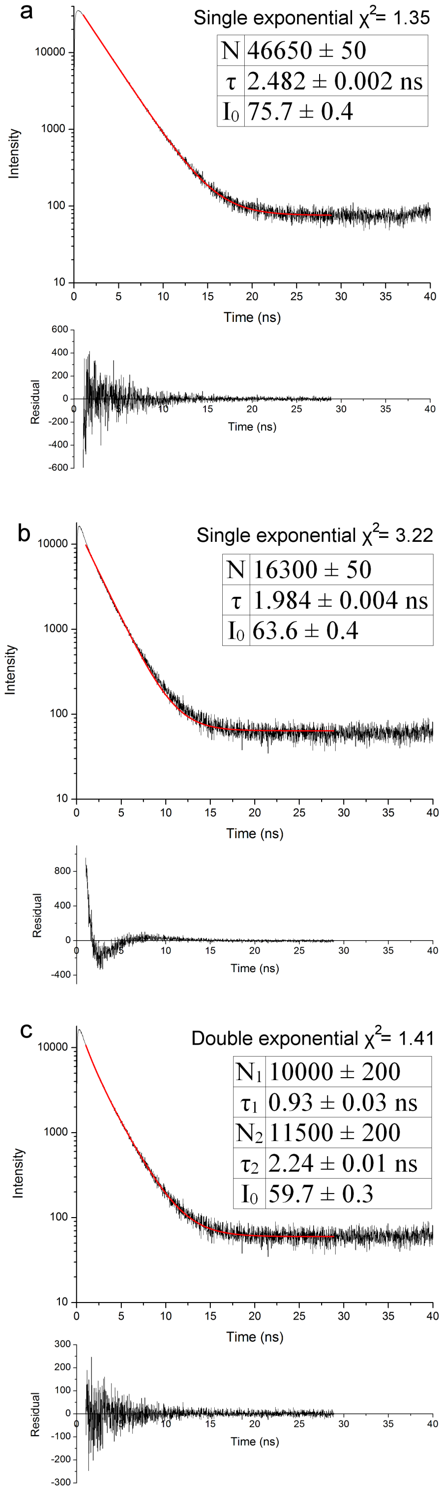

Figure 4.2: Examples of measured fluorescence intensity decays for coumarin 6 in glycerol. Intensity data (photon counts) are plotted in the top panels and residuals are plotted in the bottom panels, red lines are fits to data. a) Undumped decay with monoexponential fit. b) Decay with 26mW dump (measured after major dichroic) and monoexponential fit: asymmetric residual plot indicates poor fit. c) Decay with 26mW dump and biexponential fit, which has lower χ^2 and a more symmetric residual plot than the monoexponential fit.

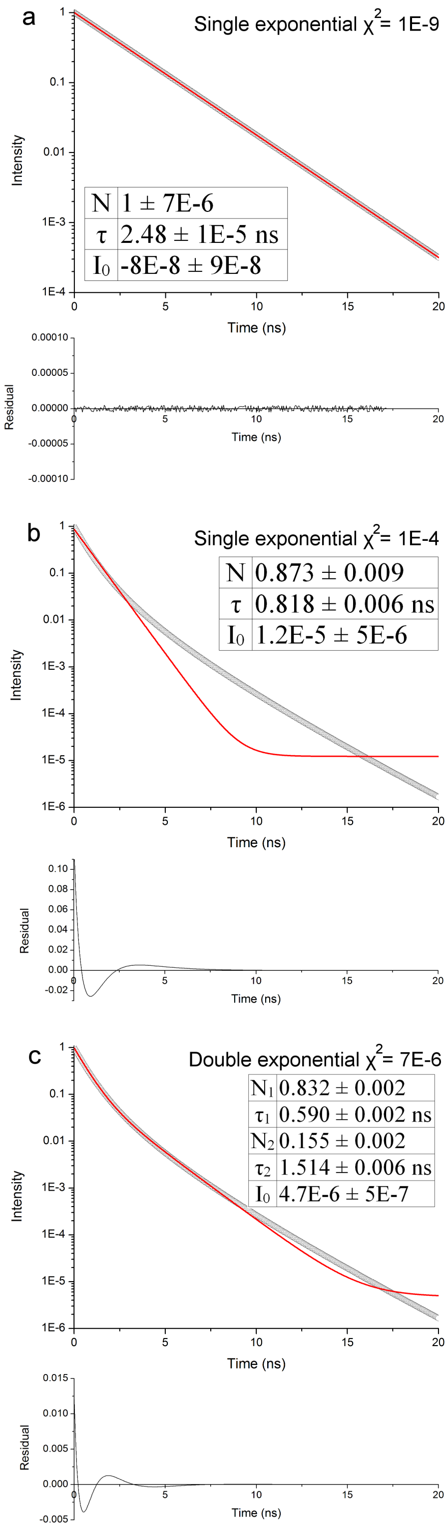

N	1 ± 7E-6
τ	2.48 ± 1E-5 ns
I_0	-8E-8 ± 9E-8

N	0.873 ± 0.009
τ	0.818 ± 0.006 ns
I_0	1.2E-5 ± 5E-6

N_1	0.832 ± 0.002
τ_1	0.590 ± 0.002 ns
N_2	0.155 ± 0.002
τ_2	1.514 ± 0.006 ns
I_0	4.7E-6 ± 5E-7

Figure 4.3: Examples of normalised simulated fluorescence intensity decays for coumarin 6 in glycerol. Data are plotted as open circles, red lines are fits to data. a) Undumped decay with monoexponential fit. b) Decay corresponding to 26mW dump with monoexponential fit: fit to data is visibly poor. c) Decay corresponding to 26mW dump with biexponential fit. The fit is visibly improved, with residual values much smaller than for the monoexponential fit in b) (although still asymmetric) and smaller χ^2.

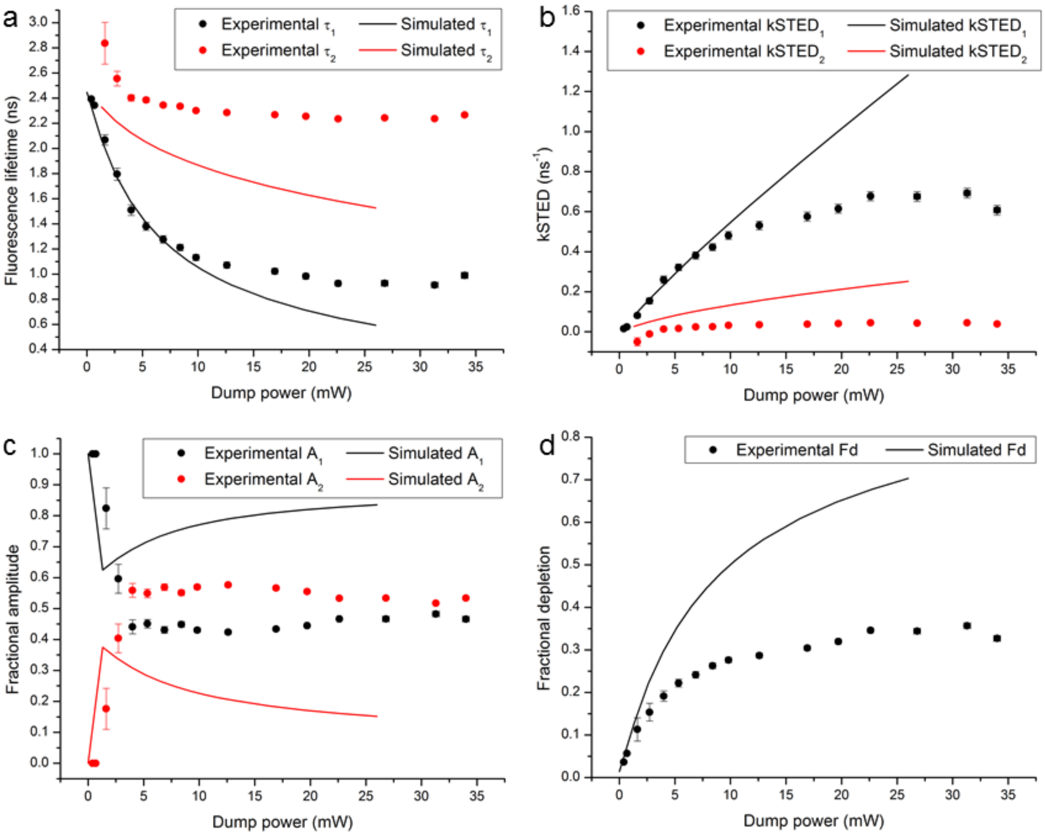

Figure 4.4: Parameters derived from intensity decays of coumarin 6 in glycerol. Scatter points are experimentally obtained values, lines are model predictions scaled to experimental data. a) Fluorescence lifetime components of the biexponential decay. b) Corresponding STED rates for each lifetime component. c) Fractional amplitudes for each lifetime component. d) Fractional depletion. Fit errors in model data generation were so small that error bars were not plotted. Measured intensity decays at 0.394mW and 0.686mW dump fitted sufficiently well to monoexponential decays and so lack values for τ_2, $k_{\mathrm{STED}2}$ and A_2.

Intensity decay parameters

The values of the dumped fluorescence lifetime components for coumarin 6 in glycerol at various dump powers are shown in Fig. 4.4a. In the presence of CW dump, both the measured and simulated data approximated well to having two fluorescence lifetime components compared to the single fluorescence lifetime seen in the undumped decays. In reality this 'biexponential' decay is a complicated function containing a broad range of lifetime components; indeed, it can be seen in Fig. 4.3c that this simulated dumped decay does not follow a true biexponential decay. However, the residual values associated with this decay are small ($< 1\%$) compared to the data values, and as such a biexponential decay was taken to be a sufficient approximation to the theoretical data. Furthermore, while it may have been possible to fit the simulated intensity decays to an exponential function with more than two terms, generated parameters would not have been comparable with those generated from experimental intensity decays as these were too noisy to fit to a function containing more than two exponential terms.

Exceptions to the biexponential fitting were the two lowest experimental dump powers (first two black points in Fig. 4.4a): whilst the intensity decay was still likely to be biexponential, at low dump powers the difference between τ_1 and τ_2 was smaller than could be differentiated through the curve fitting method used here. Therefore for these points monoexponential decays were instead fitted.

Whilst the behaviour of the experimental and simulated lifetimes appeared to agree qualitatively - there was one 'short' lifetime and one 'long' lifetime, both of which became shorter with increasing dump power - they did not agree well quantitatively. Whilst the simulated τ_1 values matched the experimental τ_1 values for dump powers $\leq$ 10mW, at higher powers the two data sets deviated substantially, with the simulated τ_1 values continuing to shorten to a greater extent than the measured τ_1 values. The simulated values of τ_2 did not agree with the experimental values at any of the measured dump powers, nor could any scaling factor for S' force the values to agree. The experimental τ_2 values also did not shorten to the degree predicted by the model; from 4mW to 20mW the simulated τ_2 values shortened by 0.49ns (23%) whereas over the same dump power range the experimental τ_2 values only shortened by 0.14 ± 0.03ns (6%).

The STED rates of the two lifetime components for the experimental and simulated data are shown in Fig. 4.4b. The simulated STED rates both increased almost linearly with increasing dump power; this was again seen in the experimental values for the STED rate of τ_1 (k_{STED1}) at low dump powers ($\leq$ 10mW), but at higher dump powers this rate appeared to plateau. The experimental k_{STED2} values were very low at all dump powers (maximum rate $k_{\mathrm{STED2}} = 0.045 \pm 0.002\mathrm{ns}^{-1}$) compared to the simulated data (maximum rate $k_{\mathrm{STED2}} = 0.25\mathrm{ns}^{-1}$ at 26mW).

Whilst there was at least qualitative agreement between experimental and simulated data for lifetimes and STED rates, this was not the case for the fractional amplitudes (Fig. 4.4c). In the experimental data the fractional amplitudes underwent large changes for dump powers up to $\sim$ 5mW and then remained at a constant 0.45:0.55 (A_1:A_2) ratio for all other dump powers. Notably the longer lifetime component τ_2, with fractional amplitude A_2, became more dominant than the shorter lifetime component τ_1, with fractional amplitude A_1. In contrast, although the relationship between the two fractional amplitudes for both experimental and simulated data was similar at low dump powers, in the simulated data the shorter lifetime component was always dominant over the longer lifetime component ($A_1 > A_2$) with a larger difference between the contributions of the two components.

The discrepancies between the experimental and simulated data further manifest in the fractional depletion, shown in Fig. 4.4d. The fractional depletion indicates that the excited state was depleted much less efficiently in the experiment compared to the simulated data. Both data sets showed an initial rapid increase of F_d with dump power (<4mW), but then the experimentally measured values of F_d plateaued (as seen for the lifetime components and STED rates) whilst the simulated values continued to rise with dump power, although at a progressively slower rate. The maximum value of F_d reached in the experimental data set was 0.357 ± 0.005, compared to 0.703 in the simulated data set.

Anisotropy decays

The anisotropy decays of coumarin 6 in glycerol were measured and simulated to examine the orientational distribution of the excited state in the presence of CW dump. Figure 4.5a shows the experimentally measured undumped anisotropy decay and anisotropy decays at various dump powers over the first 10ns following excitation. The undumped decay (black line) decayed monoexponentially with time constant $= \tau_{\mathrm{rot}}$; over the course of the plotted decay ($\sim 4\tau_f$) the anisotropy only decreased from $R_0 \approx 0.4$ to $R = 0.37 \pm 0.02$ (average anisotropy from 8-10ns) due to minimal rotation away from the initial excited state distribution. In the presence of CW dump there was greater decay away from R_0, which increased for higher dump powers; this was indicative of more efficient removal of molecules oriented at $\theta \sim 0°$ by the dump beam leading to a greater contribution of fluorescence from molecules oriented at $\theta \sim 90°$. This qualitatively agreed with the simulated data (Fig. 4.5b), but quantitatively did not agree, with much lower anisotropies generated in the simulated decays than the measured decays. As with the intensity-derived parameters, the quantitative discrepancy between the experimental and simulated anisotropy decays became greater at higher dump powers.

One key difference between the simulated and experimental anisotropy decays was that the simulated decays show high dump powers driving the anisotropy to negative values (i.e. greater contribution of $\theta \sim 90°$ molecules than $\theta \sim 0°$ molecules). This was not seen in the experimental decays and was a similar result as was previously observed in pulsed STED experiments by the group, where large changes in

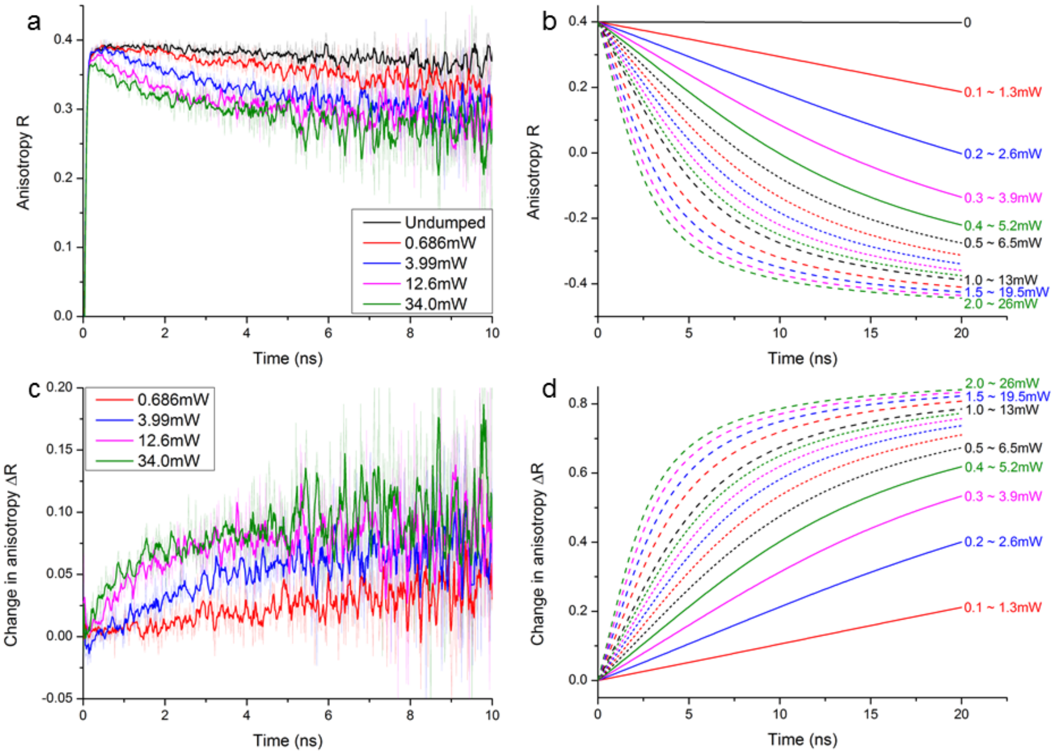

Figure 4.5: Measured and simulated anisotropy data for coumarin 6 in glycerol. a) Experimentally measured undumped and dumped anisotropy decays. b) Simulated undumped and dumped anisotropy decays. c) Measured change in anisotropy for the four dump powers as plotted in a). d) Simulated changes in anisotropy for dumped decays as shown in b). Experimental data are truncated at 10ns as decays became noisy beyond this point with contamination from the polarised background. Faint lines in experimental plots are raw data, bold lines are smoothed data (5 point adjacent averaging). Simulated data are shown for the various values of S' in the model with corresponding powers after scaling.

anisotropy were generated by the model but not replicated in the experimental data.

Figure 4.5c shows the change in anisotropy ΔR for the dump powers shown in Fig. 4.5a, and Fig. 4.5d shows this anisotropy change for the model data in Fig. 4.5b. Again, there was no quantitative agreement between the experimental and simulated changes in anisotropy, with the simulated ΔR plots reaching ~ 8 times higher increases than the measured data.

Addition of noise to simulated decays

One concern was that the simulated data was not accurately comparable with experimental data, as simulated intensity decays were generated with relative intensities (i.e. maximum intensities of 1) and no noise contributions (Fig. 4.3); this was in contrast to the measured decays which had peak intensities on the order of 10^4 photons and contained both noise arising from the stochastic nature of spontaneous emission and detector noise such as afterpulsing and dark count (Fig. 4.2). However, both data sets were analysed using the same fitting process. A consequence of this could have been differences in exponential fitting statistics, which would have affected the fitted lifetimes and amplitudes, and hence the other derived parameters.

Therefore, to verify whether the discrepancies between simulated and experimental data described above were due to these differences in the decays, noise was added to simulated intensity decays and exponential fitting was repeated on these decays (Fig. 4.6). The noisy decays were generated by multiplying the simulated decays in Fig. 4.3 by 25,000 (typical peak intensity seen in measured experimental decays) and adding noise to each generated point in the decay as a random number from a normal distribution of mean = 0 and standard deviation = $\sqrt{N}$ where N is the intensity at each time point. This is a good approximation for Poisson noise at high N [133] and serves as a suitable initial approximation for the effect of noise on fitting.

The monoexponential fits to the simulated 'noisy' decays (Fig. 4.6a,b) produced lifetimes which agreed with the lifetimes from monoexponential fits of the simulated decays without noise (Fig. 4.3a,b) to within fitting error. The individual lifetime components obtained from the biexponential fitting (Figs. 4.3c, 4.6c) did not agree for the two simulated data sets; however their average fluorescence lifetimes did agree to within fitting error (noisy decay $\tau_d = 0.734 \pm 0.005$ns, no noise $\tau_d = 0.735 \pm 0.003$ns).

Parameters calculated from fits of simulated noisy decays are shown in Fig. 4.7, plotted alongside the same experimental data as in Fig. 4.4. The fluorescence lifetime, k_{STED} and F_d plots all behaved identically to the noise-free simulation with similar deviations from the experimental data. For the noisy simulations, the fractional amplitude data were more erratic at lower dump powers than in the initial simulations and as such may be a more accurate reflection of the experimental data. At higher dump powers however the deviation of the simulated noisy fractional amplitudes from experimental data was similar to that seen in the noise-free simulations. As a whole, the parameters generated from fitting simulated noisy decays appeared to behave substantively in a similar way to the noise-free simulations to rule out the possibility that differences between the experimental and model data arose from fitting statistics.

Reasons for the repeated deviation of CW STED dynamics in the limit of no rotation from expected model behaviour are explored further in Chapter 5, and proposed alterations to this model are subsequently suggested in Section 5.8.

4.7.2 Limit of fast rotation

Whereas the initial excited state orientational distribution $P_u(\theta, \phi)$ for coumarin 6 molecules in glycerol greatly affects STED dynamics due to the lack of rotation, fluorescein molecules in water should rotate away from $P_u(\theta, \phi)$ sufficiently quickly that CW STED dynamics are independent of $P_u(\theta, \phi)$. The rotational correlation

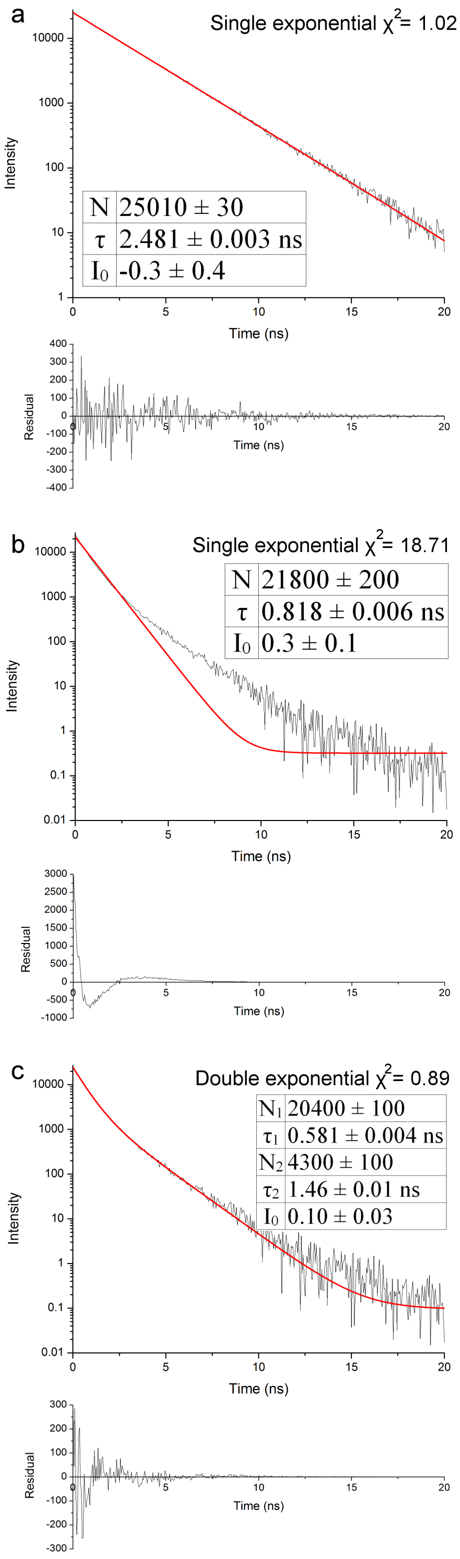

Figure 4.6: Examples of simulated fluorescence intensity decays with noise for coumarin 6 in glycerol. Data are plotted in top panels, residuals are plotted in bottom panels, red lines are fits to data. a) Undumped decay with monoexponential fit. b) Decay with approximately 28mW dump and monoexponential fit; asymmetric residual plot indicates poor fit to data. c) Decay with approximately 28mW dump and biexponential fit.

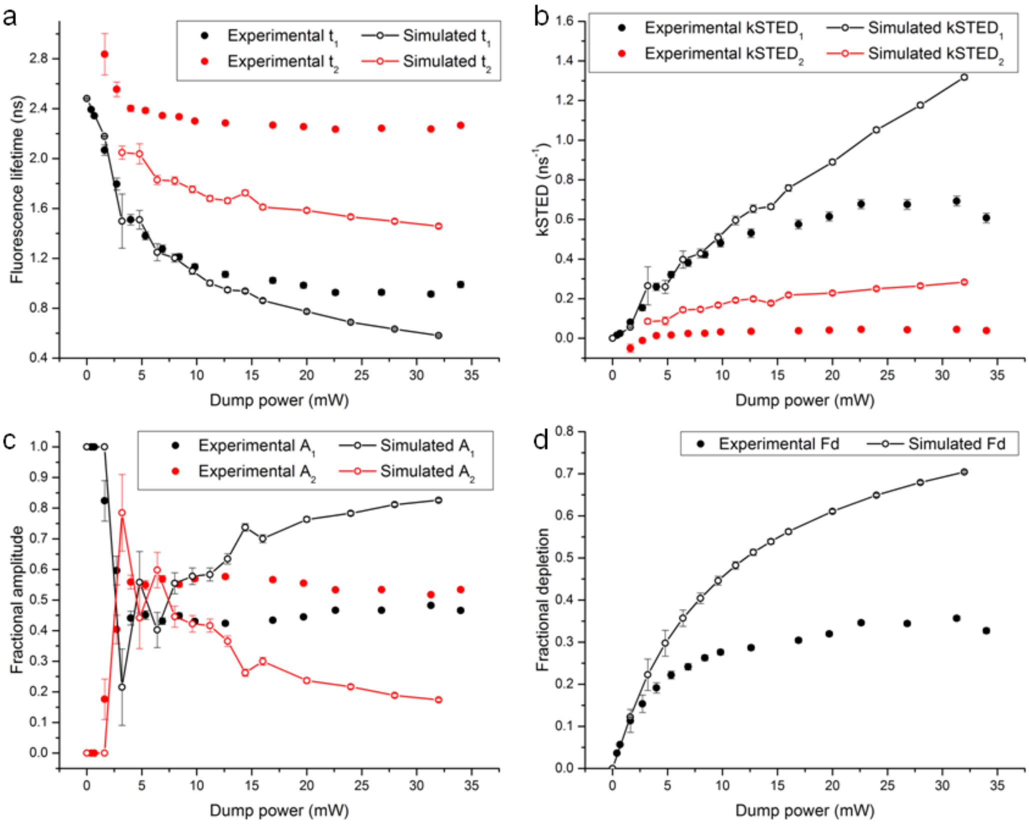

Figure 4.7: Comparison of parameters derived from noisy simulated data with experimental data for coumarin 6 in glycerol. Experimental data are as for Fig. 4.4, empty points joined by lines are predictions for model with noise added scaled to experimental data. a) Fluorescence lifetime components of the biexponential decay. b) Corresponding STED rates for each lifetime component. c) Fractional amplitudes for each lifetime component. d) Fractional depletion.

time for fluorescein in water was measured as $\tau_{\mathrm{rot}} = 0.25 \pm 0.02$ns (N=4 decays) which is an order of magnitude shorter than its (monoexponential) undumped fluorescence lifetime (3.568 ± 0.004ns, N=5 decays). As a result the orientational effects seen for coumarin 6 in glycerol - i.e. the orientational holeburning - should not be present for fluorescein in water, where all molecules should have the same STED rate and same effective lifetime at a given dump power. As a consequence, the dumped lifetimes of fluorescein are expected to remain monoexponential and simply become shorter as dump power increases. However, whilst the undumped decays (Fig. 4.8a) and decays at very low dump powers (< 2mW) were well fitted by monoexponential functions, the decays measured at higher dump powers were again better described by biexponential functions (Fig. 4.8b,c).

Intensity decay parameters

Similar analysis was performed for intensity decay parameters for fluorescein in water as for coumarin 6 in glycerol, as shown in Fig. 4.9. Figure 4.9a shows the appearance of a second lifetime component as dump power was increased. As seen for coumarin 6 in glycerol the shorter lifetime component τ_1 experienced greater shortening than the longer lifetime component τ_2, with τ_1 becoming 2.50 ± 0.05ns (70%) shorter than the undumped lifetime τ_f at the highest dump power tested (35mW) and τ_2 only becoming 0.57 ± 0.03ns (16%) shorter.

This is reflected in the calculated values of k_{STED} (Fig. 4.9b). For fast rotation there should be a linear dependence on k_{STED} with dump power, as all molecules should be dumped equivalently independent of their initial orientation and thus should depend only on dump power. Experimental results were shown to deviate from this prediction firstly by the appearance of the second lifetime discussed above, but also by the deviation of k_{STED1} from a linear relationship. Linear fits of the form $k_{\mathrm{STED1}} = mP_{\mathrm{dump}}$ (m = constant, intercept = 0 as $P_{\mathrm{dump}} = 0$ should yield no depletion i.e. $k_{\mathrm{STED}} = 0$) were performed on the data; the best fit (judged by the highest value of the R^2 fitting statistic) was obtained when fitting through the first six dump powers only (black line in Fig. 4.9b, $R^2 = 0.96$). At higher dump powers k_{STED1} then fell below this straight line, indicating that the rate of the depletion for this lifetime component was lower than expected at higher dump powers. Again, as for coumarin 6 in glycerol k_{STED2} was comparatively small across all dump powers (maximum value = $0.053 \pm 0.003\mathrm{ns}^{-1}$).

The fractional contributions of the two lifetime components are shown in Fig. 4.9c. The first two decays (dump powers, < 2mW) fitted well to monoexponential decays and so it was assumed here that $A_1 = 1$ and $A_2 = 0$. The intensity decays for the next two dump powers (2.8mW, 4.3mW) were clearly not monoexponential as indicated by their χ^2 values and residual plots, but there were substantial fitting errors to a biexponential decay, leading to the large errors associated with these points. These fitting errors were greater for the amplitudes than for the correspond-

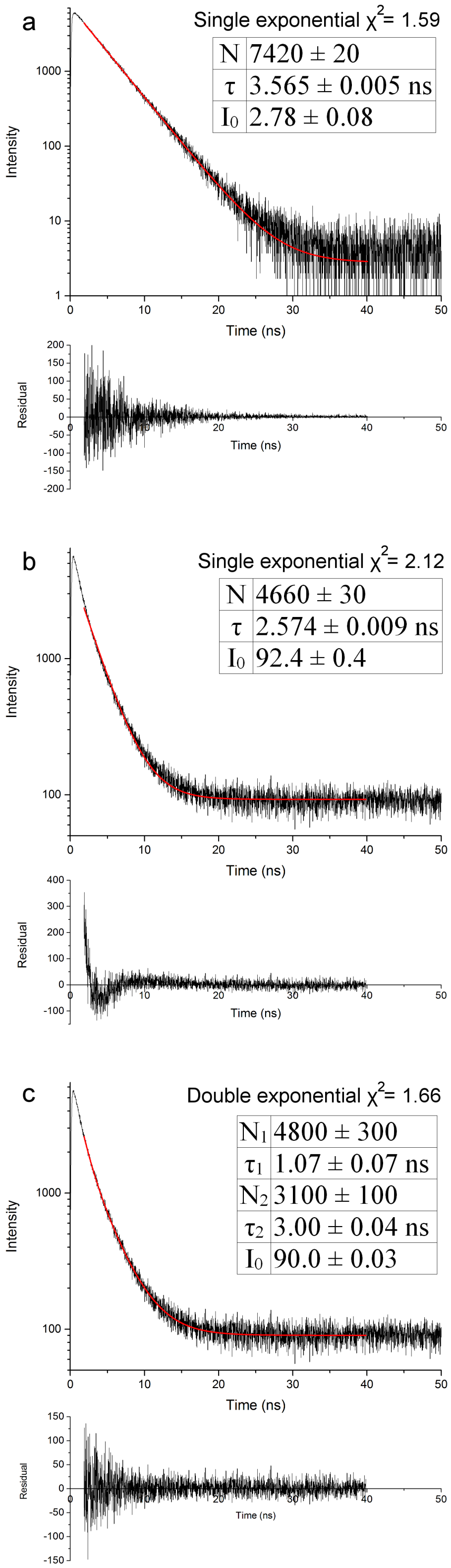

Figure 4.8: Examples of measured fluorescence intensity decays for fluorescein in water. Data are plotted in the top panels and residuals are plotted in the bottom panels. Red lines are fits to data. a) Undumped decay with monoexponential fit. b) Decay with 35mW dump (measured after major dichroic) and monoexponential fit. Asymmetric residual plot indicates poor fit. c) Decay with 35mW dump and biexponential fit.

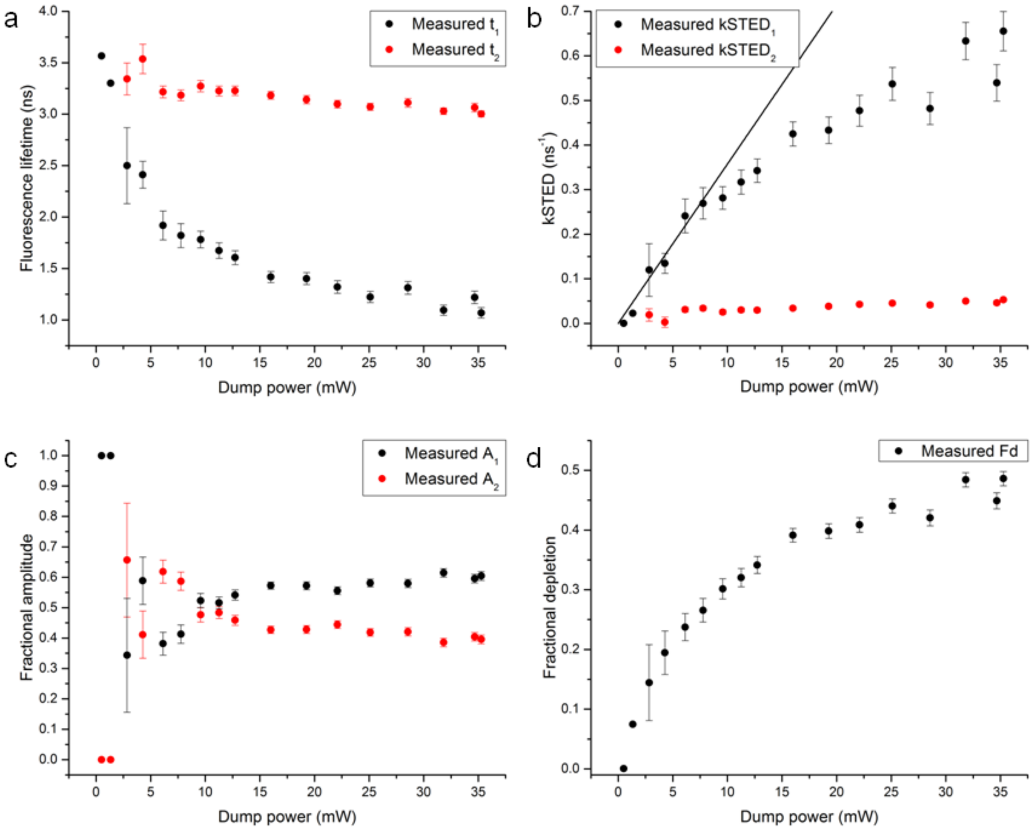

Figure 4.9: Parameters derived from experimentally measured intensity decays of fluorescein in water. a) Fluorescence lifetime components of the biexponential decay. b) Corresponding STED rates for each lifetime component. Black line is a straight line fit ($y = mx$) through first six data points. c) Fractional amplitudes for each lifetime component. d) Fractional depletion. The intensity decays at 0.499mW and 1.338mW fitted sufficiently to monoexponential functions.

ing lifetimes. At dump powers < 11mW the dominance of A_1 and A_2 alternated somewhat, before A_1 became stably dominant at higher dump powers with an approximate ratio of $60 : 40$ ($A_1 : A_2$). This was in contrast to the results obtained for coumarin 6 in glycerol where the longer lifetime component (amplitude A_2) was dominant at high dump powers.

The fractional depletion of fluorescein in water is shown in Fig. 4.9d. F_d increased rapidly with lower dump powers but more slowly with higher dump powers. However, F_d did not display the dramatic plateau as seen for coumarin 6 in glycerol and reached a maximum $F_d = 0.486 \pm 0.001$, indicating that the faster rotation does overall increase STED efficiency.

Anisotropy decays

The undumped and dumped anisotropy decays for fluorescein in water are shown in Fig. 4.10a. In contrast to coumarin 6 in glycerol, the undumped R_0 was not the predicted value of 0.4. This was presumably due to rotation within the instrument response function that consequently could not be measured. None of the dump powers altered either R_0 or the decay constant τ_{rot}, confirming that molecules rotate quickly enough to negate the orientational dependence of depletion. The dumped ΔR plots are shown in Fig. 4.10b, where $\Delta R = 0$ for all dump powers (average from 2-10ns, within experimental error at all powers), and were consistent with the notion that fast rotation was averaging out the orientational dependence of the depletion rate.

4.7.3 Intermediate rotation regime

Coumarin 6 and fluorescein were also examined in the solvent ethylene glycol, which is more viscous than water but less viscous than glycerol (dynamic viscosity of ethylene glycol = 0.020Ns/m^2 at 21°C [134]). Both the rotational correlation times and fluorescence lifetimes were on the same order of magnitude for the two fluorophores in ethylene glycol; for fluorescein, $\tau_{\mathrm{rot}} = 1.77 \pm 0.07$ns (N = 4 decays) and $\tau_f = 3.916 \pm 0.002$ns (N = 5 decays), and for coumarin 6 $\tau_{\mathrm{rot}} = 1.78 \pm 0.09$ns (N = 4 decays) and $\tau_f = 2.28 \pm 0.01$ns (N = 5 decays). The undumped lifetime of fluorescein was slightly longer than it was in water, whereas for coumarin 6 the undumped lifetime was slightly shorter than it was in glycerol. In both cases these differences were attributed to solvation effects. As the rotational correlation times and fluorescence lifetimes are similar, STED and rotation will be competing to respectively remove and refill $\theta \sim 0°$ fluorophores on a similar timescale.

Whilst the DPSS laser used in the previous experiments was again used for CW STED of fluorescein in ethylene glycol (maximum on-sample power $\sim$ 12mW), a higher power tunable VECSEL laser was used to dump coumarin 6 in ethylene glycol (maximum on-sample power $\sim$ 28mW). This had the advantage of providing higher dump powers but also a slightly different spectral profile (DPSS wavelength =

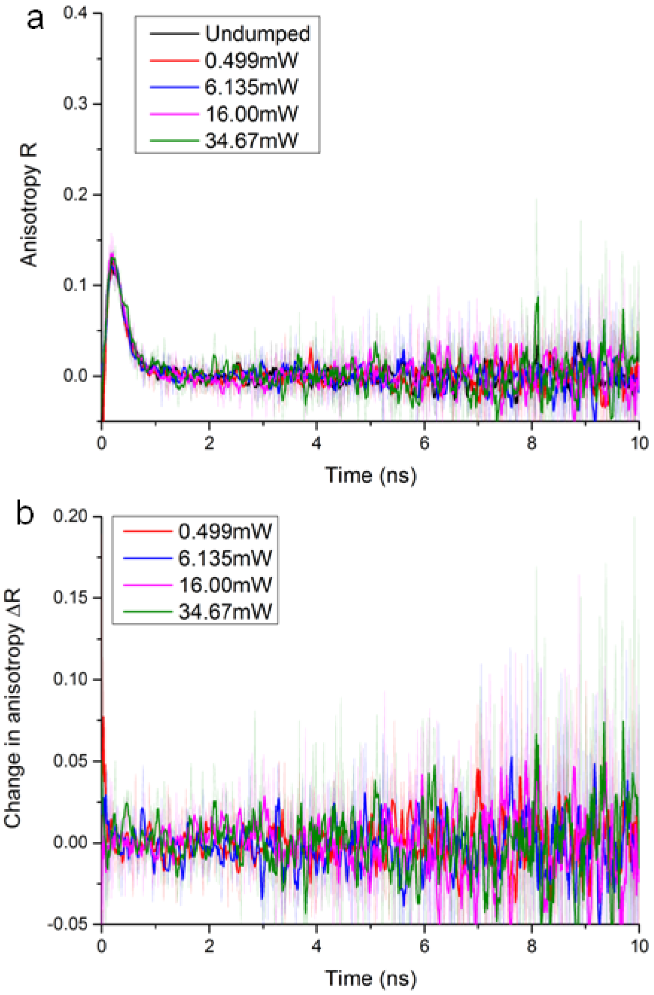

Figure 4.10: Measured anisotropy data for fluorescein in water. a) Undumped and dumped anisotropy decays. b) Change in anisotropy for four dump powers as plotted in a). Data are truncated at 10ns as decays become noisy beyond this point with contamination from the polarised background. Faint lines are raw data, bold lines are smoothed data (5 point adjacent averaging).

593.6 ± 0.3nm with linewidth $< 1 \times 10^{-6}$nm (manufacturer's specification), VECSEL wavelength $= 595 \pm 1$nm with linewidth ~ 0.2nm [129]), with the spectral bandwidth more similar to that of the OPA dump source previously used in pulsed STED experiments.

Intensity decay parameters

As observed for coumarin 6 in glycerol and fluorescein in water, the dump beam produced a biexponential intensity decay from undumped monoexponential intensity decays for both fluorophores in ethylene glycol (Fig. 4.11a). Again, the decays of both fluorophores contained a fast lifetime component τ_1 which showed substantial variation with dump power and a slow lifetime component τ_2 which showed little variation with dump power. The corresponding k_{STED} values (Fig. 4.11b) behaved similarly to the results seen in the other two solvents; k_{STED1} for both fluorophores increased and then began to plateau at higher dump powers whilst k_{STED2} was small and virtually unchanging. Coumarin 6 in ethylene glycol had higher STED rates for both components compared to fluorescein.

The fractional contributions of the two lifetimes within coumarin 6 and fluorescein followed a similar pattern to that seen for fluorescein in water (Fig. 4.11c). There was rapid variation of the fractional contributions with dump powers < 7mW for fluorescein and < 11mW for coumarin 6, with A_1 becoming consistently dominant over A_2 at higher dump powers; for both fluorophores the components remained at a $65 : 35$ ($A_1 : A_2$) ratio for high dump powers.

The fractional depletion curves for coumarin 6 and fluorescein in ethylene glycol are shown in Fig. 4.11d. Both curves showed a similar relationship between dump power and F_d to that seen for fluorescein in water; a rapid increase in F_d at low dump powers which became a slower increase at high dump powers. Whilst it can be seen from the higher powers tested for coumarin 6 that the F_d curve again reached a plateau, this occurred at a higher power than the plateau seen for coumarin 6 in glycerol. The highest F_d for fluorescein was measured as 0.454 ± 0.005 at 33mW and for coumarin 6 was measured as 0.507 ± 0.003 at 82mW.

Anisotropy decays

Figures 4.12a and b show the anisotropy decays for coumarin 6 and fluorescein respectively in ethylene glycol. The initial anisotropy R_0 was again lower than the predicted value of 0.4; this is likely due to a combination of rotation during the instrument response function (as seen in water) but could also be due to additional polarisation effects arising as a result of high numerical aperture focusing. For example, it has been shown that the polarisation component parallel to the beam propagation direction becomes enhanced when linear polarised light is focused with a high numerical aperture [135]. For both fluorophores the undumped anisotropy

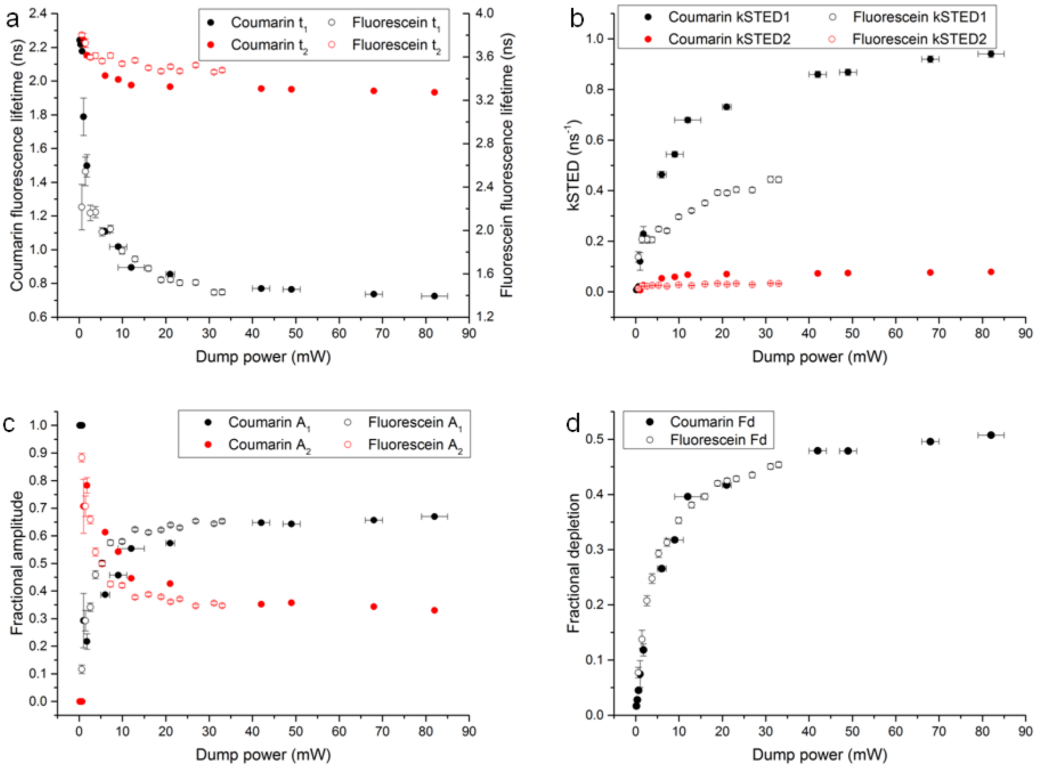

Figure 4.11: Parameters derived from experimentally measured intensity decays of coumarin 6 (solid circles) and fluorescein (empty circles) in ethylene glycol. a) Fluorescence lifetime components of the biexponential decays. b) Corresponding STED rates for each lifetime component. c) Fractional amplitudes for each lifetime component. d) Fractional depletion. For coumarin 6, decays at 0.18mW, 0.36mW and 0.68mW fitted sufficiently to monoexponential decays. All fluorescein decays fitted well to biexponential decays.

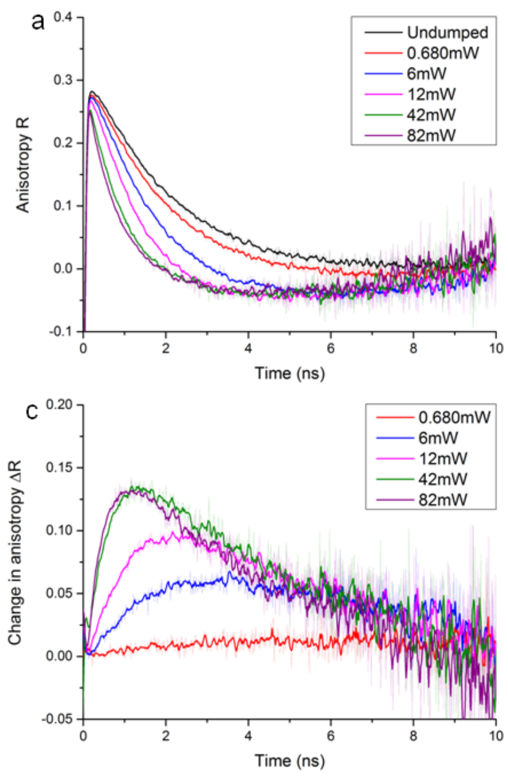

Figure 4.12: Measured anisotropy data for coumarin 6 and fluorescein in ethylene glycol. a) Undumped and dumped anisotropy decays for coumarin 6. b) Undumped and dumped anisotropy decays for fluorescein. c) Changes in anisotropy (undumped data - dumped data) for coumarin 6 for five dump powers as plotted in a). d) Changes in anisotropy (undumped data - dumped data) for fluorescein for four dump powers as plotted in b). Data are truncated at 10ns as decays become noisy beyond this point. Faint lines are raw data, bold lines are smoothed data (5 point adjacent averaging).

decayed to zero over approximately 10ns. These decays became more rapid with increasing dump power, with the highest dump powers producing negative anisotropy values for both fluorophores. Negative anisotropy indicates that $I_H(t) > I_V(t)$, with the number of molecules oriented at $\theta \sim 0°$ having decreased to below the number of molecules oriented at $\theta \sim 90°$. For the three highest dump powers tested for coumarin 6 (Fig. 4.12a), the anisotropy began to increase again from $\sim$ 6ns onwards: this was as a result of the polarised background signal becoming dominant over the fluorescence signal.

The corresponding ΔR plots are shown in Figs. 4.12c and d. At dump powers of 5-6mW upwards, the change in anisotropy ceased to increase and then began to 'turn over', with the highest dump powers then producing a small decrease in ΔR. Again, only the data from 0-6ns has sufficient fluorescence signal compared to the polarised background and as such the further decreases in ΔR beyond this time can not be reliably attributed to any orientational behaviour of the sample.

4.8 Discussion

The experiments presented above demonstrate the effect of solvent viscosity on the CW STED dynamics of fluorophores, although not necessarily in the manner predicted by modelling of orientational dependence. The results of these experiments and the performance of the model are discussed in detail here, with a comparative pulsed STED experiment included for comparison with previous work of the group.

4.8.1 CW STED dynamics of fluorophores in different rotation regimes

Fluorescein and coumarin 6 have monoexponential undumped lifetime decays; this was in contrast to the previous work modelling CW STED of fluorescent proteins, which displayed biexponential undumped fluorescence decays and possess more than one emitting state, which meant that there could be multiple contributing factors to CW STED dynamics other than orientational dependence [15].

Coumarin 6 in glycerol was used as a model sample for a case where molecular rotation is slow in comparison with the rate of fluorescence/STED and can therefore be ignored; fluorescein in water was used as a model sample for a case where molecular rotation is rapid enough compared with the rate of fluorescence/STED for rotational diffusion to homogenise the excited state distribution, thus negating the initial excited state orientational distribution $P_u(\theta, \phi)$. The anisotropy decays measured in these two systems indicated that they were both adequate approximations of these regimes. For coumarin 6 in glycerol, orientational ‘holeburning’ was seen, where the dump beam removed a significant proportion of $\theta \sim 0°$ excited state molecules which rotational diffusion was too slow to replenish. This was in contrast to the case of coumarin 6 (or fluorescein) in ethylene glycol where rotational diffusion was sufficiently fast to limit the hole created by depletion, which was seen as a ‘turning over’ of the ΔR curves (Fig. 4.12c,d). The anisotropy decays of fluorescein in water were identical from the undumped case through to maximum dump power, indicating that STED was having no net effect on the orientational distribution of excited molecules. This is due to rotation recreating an isotropic excited state distribution on a shorter timescale than the rate of STED, and any orientational hole created by STED was immediately being refilled. However, although the anisotropy decays indicated that our qualitative understanding of the effect of orientation on CW STED is correct, the orientational model used here did not agree quantitatively with the experimental data. For example, ΔR was measured to be substantially lower than was predicted for coumarin 6 in glycerol (Fig. 4.5).

The general shape of the ΔR curves in glycerol can be explained using the dumped fluorescence intensity decay (Fig. 4.13). The early part of the intensity decay is dominated by emission from $\theta \sim 0°$ molecules which, at high dump powers, are removed efficiently with this population decaying rapidly compared to the

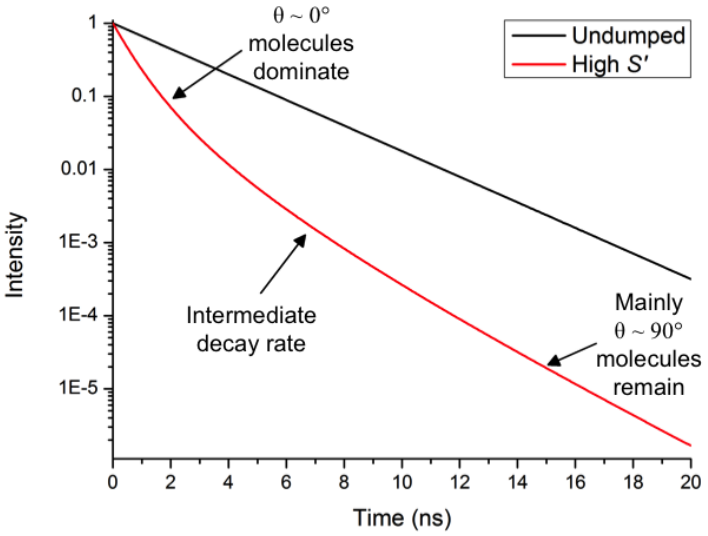

Figure 4.13: Simulated undumped and high dump power decays for coumarin 6 in glycerol with annotations showing different orientational regimes. High S' curve is simulated with $S' = 2$, which is scaled to an approximate dump power of 26mW.

undumped case. Thus, here ΔR is also varying rapidly as can be seen in the steep gradients for high dump powers within the first 2ns in Fig. 4.5c,d. However, later in the fluorescence decay, emission from $\theta \sim 90°$ molecules dominates as few $\theta \sim 0°$ molecules remain in the excited state. As STED is least efficient for these molecules oriented perpendicular to the dump beam polarisation, they display decay rates similar to a population of fluorophores not undergoing any STED, making the undumped and dumped intensity decays near-parallel in this region ($\sim$ 14ns onwards in Fig. 4.13). This manifests in the ΔR curves as a plateau in ΔR at late times for high powers. The region of the decay curve between these two extreme cases is a transitional phase where the proportion of $\theta \sim 0°$ emitters is decreasing whilst the proportion of $\theta \sim 90°$ emitters is increasing. The anisotropy decay thus mirrors this changing contribution of $\theta \sim 0°$ and $\theta \sim 90°$ emitters to the intensity decay.

The lower ΔR seen in the experimental data therefore reflects a larger than expected contribution to total fluorescence from $\theta \sim 0°$ molecules, implying a lower than expected rate of depletion for these molecules (or a diffusional refilling of the orientational hole burnt in by STED, which is negligible given the value of τ_{rot} in glycerol). This could also be seen in the plots of k_{STED}, which showed substantial deviation from the near-linear behaviour observed in the model. The gradients of the k_{STED} plots are proportional to the STED cross section σ_{STED}, and so the increasingly smaller gradients at higher dump powers imply that coumarin 6 in glycerol is experiencing an apparent reduction in σ_{STED} as the dump power increases, which is much greater than that expected from the modelling.

For coumarin 6 in glycerol the dump beam creates a range of different lifetimes which vary with the orientation of the fluorophores relative to the dump polarisation, and so in reality there is a distribution of lifetime components contributing to the total decay. However, a biexponential decay was used to approximate the intensity decays (also used in [15]), as it is difficult to reliably distinguish more than two exponential components through curve fitting. Indeed, even biexponential decay fitting was not possible at some very low dump powers (e.g. the two lowest experimental dump powers used for coumarin 6 in glycerol), as here the difference between a monoexponential decay and a biexponential decay containing two similar lifetimes was small in comparison to the contribution from noise. This was also seen in the noisy model where the first two values of S' created decays which were sufficiently fitted by monoexponential decays. In future work, a more sophisticated approach to fitting the model and experimental data may be required. For example, the biexponential fitting function could be replaced by a stretched exponential function [136], or Bayesian fitting procedures [137, 138] could be used as an alternative to the Levenberg-Marquardt fitting algorithm used here. However, additional care would need to be taken in the interpretation of the larger number of fitted parameters generated through these alternative methods.

As fluorescein rotates quickly in water, there should not be a varying distribution of lifetimes as each molecule samples all possible orientations within the timescale of depletion and therefore all molecules should experience the same average rate of depletion for a given dump power. However, the dumped decays for fluorescein in water fitted better to biexponential decays again, which here should not be a consequence of orientational effects. Indeed, the fractional contribution of the τ_2 lifetime component was comparable to the contribution of τ_1, which should have been the only lifetime present. One possible explanation for this observation is that there was a population of fluorophores which were largely insensitive to STED. If this population were completely 'unSTEDable' then the value of τ_2 would have remained at the undumped lifetime τ_f and k_{STED2} would not have altered with dump power. This was not the case, and k_{STED2} increased with dump power albeit to a much lesser extent than seen for k_{STED1}; these two rates are replotted in Fig. 4.14, where each component has been normalised by division with its maximum value. Furthermore the fractional contribution of an unSTEDable component would not change with dump power, which is again contrary to the result seen in Fig. 4.9c.

Therefore for fluorescein in water, the intensity decay suggests that there is lifetime variation within the population, but the anisotropy strongly indicates that there is no angular variation of the fluorophore lifetime. This is qualitatively inconsistent with the orientational model. This discrepancy between the observed STED behaviour and the model predictions does not appear to be an anomalous characteristic of fluorescein, as fluorescein and coumarin 6 behave very similarly in

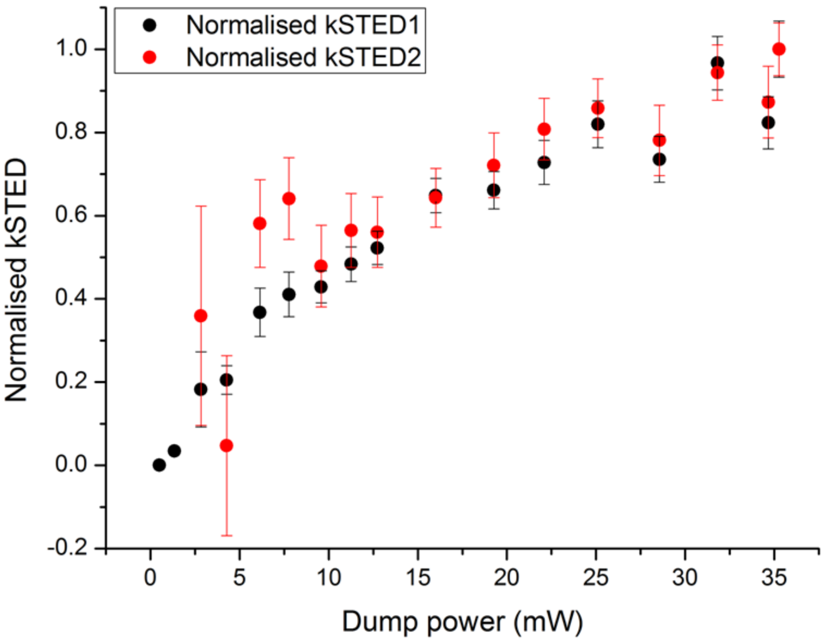

Figure 4.14: STED rates for fluorescein in water normalised by division by maximum k_{STED1} and k_{STED2} accordingly. Same data as plotted in Fig. 4.9b.

ethylene glycol, and so the same underlying mechanism may also be the reason for the departure from the model for coumarin 6 in glycerol.

4.8.2 Phenomenological comparison with pulsed STED experiments

The results presented here broadly represented an extrapolation of the previous results of the group investigating the effect of dump pulse length on STED efficiency [9, 57, 15]. In these cases, there was less gain in F_d for longer pulses than modelling suggested, and furthermore values of ΔR were lower than expected and deviated increasingly from the predicted model values with longer pulses. Despite the fundamental differences in the STED rates of the two processes - in pulsed STED the rate of fluorescence is negligible compared to that of STED, even with long pulses, whereas in CW STED the two rates are comparable - there may be other photophysical mechanisms common to both regimes contributing to STED inefficiency.

Therefore, there is value in undertaking a quantitative comparison between the experiments and modelling of pulsed STED and that of CW STED. However, there are several differences between the experimental set-ups used in the previous pulsed STED experiments and the microscope set-up of CW STED. These include excitation wavelength (two photon excitation in the streak camera versus single photon excitation in the microscope) and numerical aperture (NA ≈ 0.1 in the streak camera compared to NA=1.2 in the microscope). Hence a brief study was undertaken into pulsed STED in the microscope to verify whether pulsed STED behaved similarly between the experimental set-up here and that used previously. Ideally CW STED experiments also would be performed using the low numerical aperture streak camera system, however this would have required several watts of CW dump power which was not available at an appropriate wavelength.

The pump source was again the 490nm pulsed diode laser coupled into the microscope through an optical fibre, this time at a repetition rate of 3.8MHz. The dump source was a synchronously pumped optical parametric oscillator (Mira-OPO, Coherent) tuned to 598nm with a repetition rate of 76MHz, with the $\sim$ 400fs pulses produced by the OPO coupled into the same 3 metre fibre as the pump beam, stretching the pulses to $\sim$ 7ps (exact measurement of pulse width was not possible due to the geometry of the microscope and so was estimated from previous measurements showing that OPO pulse length was 21ps when stretched through a 10 metre fibre [111]). Again, this set-up contains further important differences from previous pulsed STED experiments: namely in the laser source used for providing dump pulses (previous work used a regenerative amplifier and OPA) and method for pulse stretching (previous work stretched pulses through water cells or diffraction gratings). An electronic delay line was used for temporal alignment of the pump and dump pulses, and the pump-dump delay (time between the pump pulse and the next dump pulse arriving) was set to 1.02 ± 0.01ns. The sample used was 1×10^{-5}M fluorescein in water as described in Section 4.6.1 and filtering was unchanged from CW STED experiments, except here a 30µm pinhole was used rather than the 50µm pinhole. This was in an effort to closer replicate the performance of the streak camera, where out-of-focus fluorescence can be identified and excluded due to its ability to image in the z-direction (discussed further in Section 5.2).

At each dump power tested, three intensity decays were measured: pump-only, pump + dump, and dump-only (Fig. 4.15, top row). For each measurement, total intensity was calculated from the detected I_V and I_H components as in Eq. 4.8. Here F_d was calculated from fluorescence intensities, rather than lifetimes, as follows:

$$F_d = \frac{I_P - I_{PD'}}{I_P} \tag{4.25}$$

where I_P is the pump-only fluorescence intensity decay and $I_{PD'}$ is the dump-subtracted pump + dump fluorescence intensity decay, given by $I_{PD'} = I_{PD} - I_D$ where I_{PD} is the pump + dump fluorescence decay and I_D is the dump-only fluorescence decay. Figure 4.15, second row, shows F_d plotted for the first 12ns of measurements at three dump powers. F_d for each dump power was calculated as an average of the F_d values between the dashed lines shown on the plots (2.27-8.51ns after excitation) with the error given by the standard deviation of these values. Using the subscripts V and H to denote the V- and H-polarised components of the fluorescence intensities, change in anisotropy was calculated as

$$\Delta R = \frac{I_{P(V)} - I_{P(H)}}{I_{P(V)} + 2I_{P(H)}} - \frac{I_{PD'(V)} - I_{PD'(H)}}{I_{PD'(V)} + 2I_{PD'(H)}}. \tag{4.26}$$

Examples of anisotropy decays are plotted in Fig. 4.15, third row, and the corresponding ΔR plots are shown beneath. ΔR for each dump power was calculated as the average value of points between the dashed lines in Fig. 4.15, bottom row (1.14-1.22ns after excitation) with the standard deviation providing the error.

The same model was used as for previous work [28, 9, 57, 15] as described in Section 4.3 to model the behaviour of fluorescein in water subject to pulsed STED for various values of τ_P/τ_R (pulse length/ground state vibrational relaxation time). Briefly, the populations of the excited and ground states were modelled as

$$\frac{\mathrm{d}N_{\mathrm{ex}}}{\mathrm{d}t} = \frac{S\cos^2\theta}{\tau_P}\left(N_{\mathrm{gr}} - N_{\mathrm{ex}}\right) \tag{4.27a}$$

$$\frac{\mathrm{d}N_{\mathrm{gr}}}{\mathrm{d}t} = \frac{S\cos^2\theta}{\tau_P}\left(N_{\mathrm{ex}} - N_{\mathrm{gr}}\right) - \frac{N_{\mathrm{gr}}}{\tau_R} \tag{4.27b}$$

where S is the pulsed saturation parameter as given by

$$S = \frac{\sigma_{\mathrm{STED}}E_D}{h\nu A} \tag{4.28}$$

with E_D the energy of the dump pulse (all other parameters are the same as for the CW saturation parameter, Eq. 4.20). Following single photon excitation the undumped excited state population is given by

$$P_u(\theta,\phi,t) = \frac{1}{4\pi}\left(1 + \frac{2}{\sqrt{5}}\exp(-t)\frac{Y_{20}(\theta,\phi)}{Y_{00}(\theta,\phi)}\right) \tag{4.29}$$

following excitation at $t = 0$. The dumped population is thus described as the product of the undumped excited state population and the probability of depletion occurring, equivalent to the excited state population N_{ex} (Eqs. 4.27a,b):

$$P_d(\theta,\phi,t) = P_u(\theta,\phi,t)N_{\mathrm{ex}}(t). \tag{4.30}$$

Fractional depletion can then be calculated as

$$F_d(t) = 1 - \int_0^{\pi}\int_0^{2\pi} P_d(\theta,\phi,t)\sin\theta\mathrm{d}\theta\mathrm{d}\phi, \tag{4.31}$$

and change in anisotropy is calculated as

$$\Delta R(t) = \frac{2}{5}\exp(-t_{\Delta pd}) - \frac{\int_0^{\pi}\int_0^{2\pi} P_d(\theta,\phi,t)Y_{20}(\theta,\phi)\sqrt{\frac{4\pi}{5}}\sin\theta\mathrm{d}\theta\mathrm{d}\phi}{\int_0^{\pi}\int_0^{2\pi} P_d(\theta,\phi,t)\sin\theta\mathrm{d}\theta\mathrm{d}\phi} \tag{4.32}$$

where $t_{\Delta pd}$ is the delay between the pump and dump pulses with the first term de-

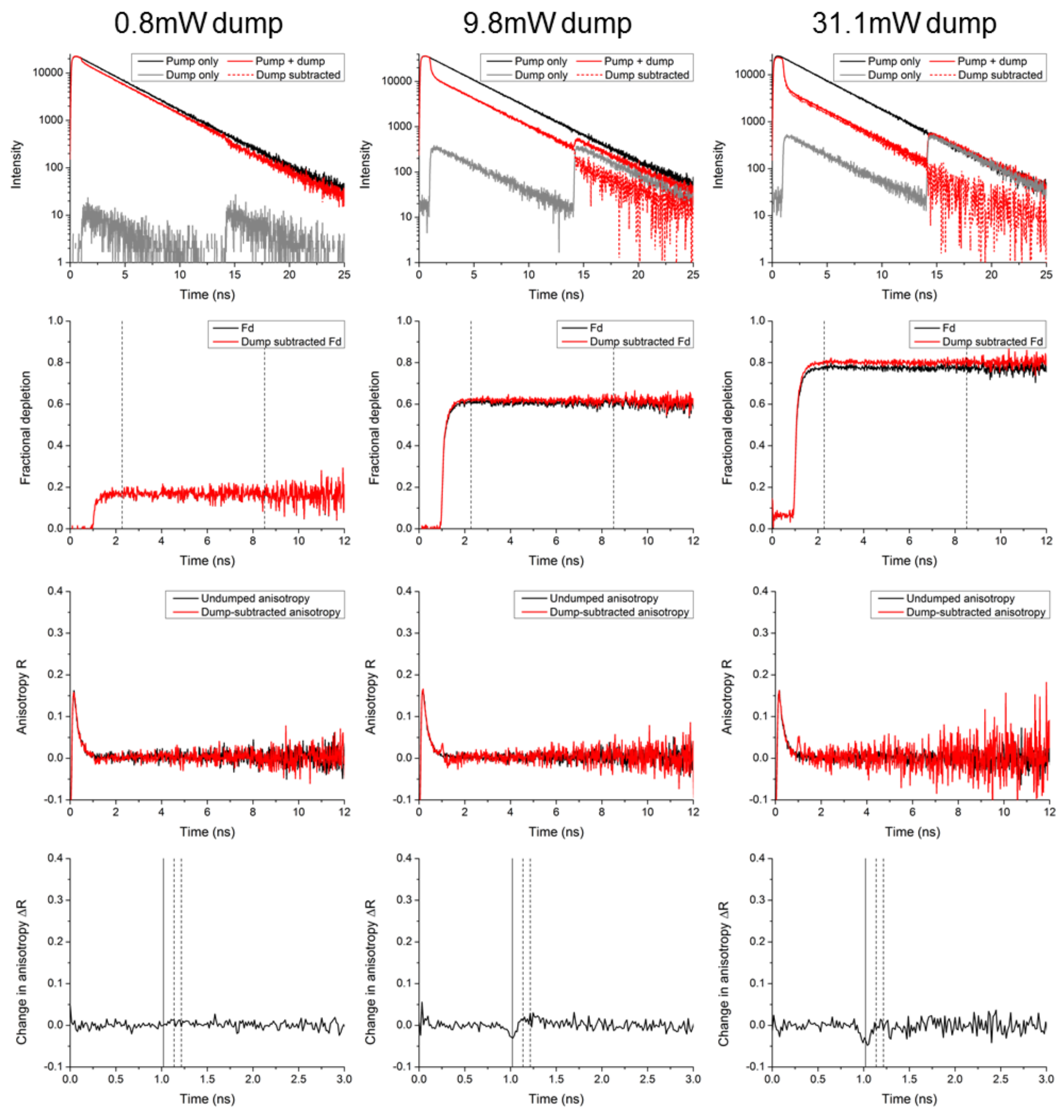

Figure 4.15: Examples of pulsed STED measurements at three different dump powers (0.8mW, 9.8mW and 31.1mW as measured after the major dichroic). Top row: Fluorescence intensity decays measured with pump only, dump only or both beams together, as per the legends. Red dashed lines show the 'corrected' pump + dump decays where the dump-only signal has been subtracted. Second row: Fractional depletion plots for the first 12ns of the above decays. Black lines show F_d calculated without subtraction of dump-only signal, red lines show F_d where this correction has been made. Dashed lines indicate time period used for calculation of average F_d. Third row: Anisotropy decays (first 12ns) for pump-only measurements and corrected pump + dump measurements. Bottom row: ΔR plots for the first 3ns of the (dump-subtracted) anisotropy decays above. Vertical solid line indicates arrival time of dump pulse, dashed lines indicate time period for calculation of average ΔR.

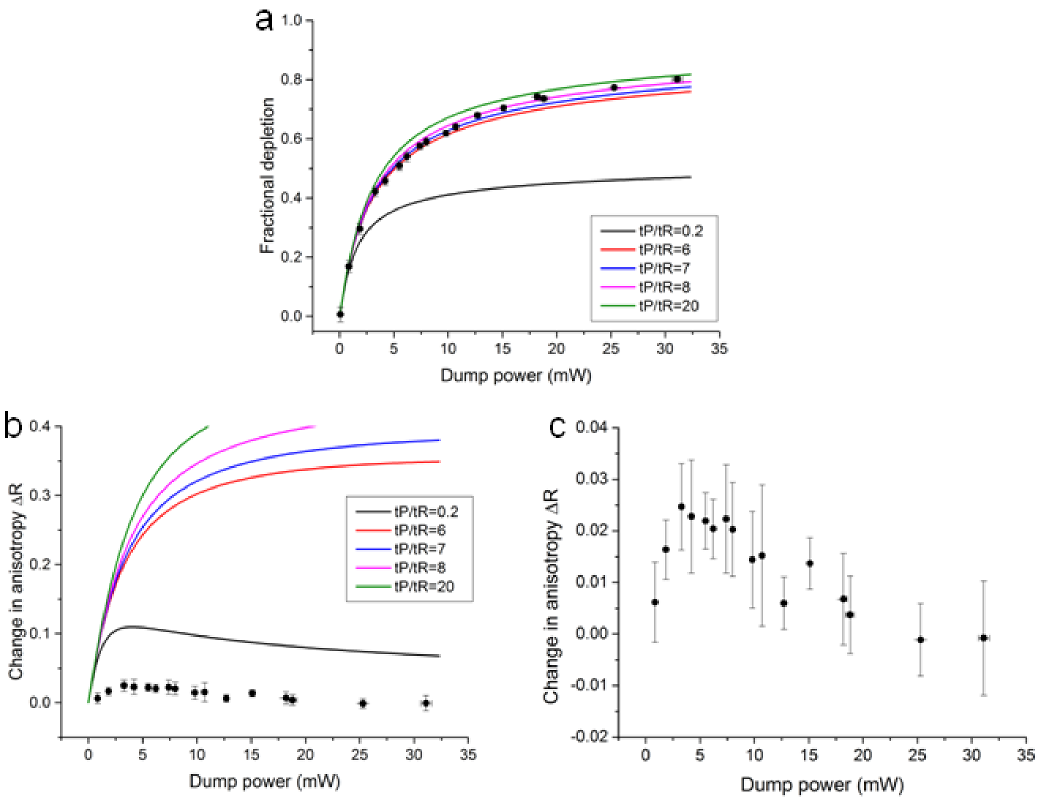

Figure 4.16: Comparison of model and experimental F_d and ΔR for pulsed STED. a) Experimental values of F_d (black circles) with simulated data for different ratios of τ_P/τ_R overlaid. b) Experimental values of ΔR (black circles) with simulated data for different ratios of τ_P/τ_R overlaid. c) Expanded plot of experimental ΔR data.

scribing rotational diffusion away from the expected R_0 during this time. Equations 4.31 and 4.32 can then be evaluated at $t = \tau_P$ (i.e. the end of the dump pulse) as a function of S for different values of τ_P/τ_R.

The results of this modelling are shown in Fig. 4.16. Figure 4.16a shows the F_d curves generated by the model for different values of τ_P/τ_R scaled onto the experimentally obtained values of F_d. At low dump powers the experimental F_d data closest matched the $\tau_P/\tau_R = 6$ and $\tau_P/\tau_R = 7$ curves, and at higher dump powers better matched the $\tau_P/\tau_R = 8$ curve. It should be noted from previous work that experimental data rarely fits to $\tau_P/\tau_R > 8$ [15]. However, the experimentally obtained values of ΔR were all much smaller than any of the simulated ΔR curves (Fig. 4.16b), although the data did appear to follow a similar shape to the $\tau_P/\tau_R = 0.2$ curve (experimental data expanded in Fig. 4.16c). For the data to fully agree with the model, the F_d and ΔR data must both match onto curves generated with the same simulated value of τ_P/τ_R, but it is clear that in the data presented here there is no value of τ_P/τ_R which will satisfy this.

These deviations from model behaviour, notably for ΔR, fit in well with the group's previous pulsed STED experiments, where the pulse length at which the model breaks down appears to be dependent on the ratio of the pulse length to rotational time. For ratios of the order $\tau_{\text{rot}}/\tau_P \sim 100$ (as used here) the measured F_d curves were observed to adequately fit to the model, but to an unrealistically long vibrational relaxation time τ_R, whereas the observed ΔR values were much smaller than predicted by modelling, even for the low values of τ_P/τ_R implied by the F_d fits [15]. In the short pulse length STED experiments where both F_d and ΔR fitted well to the same values of τ_P/τ_R, the relaxation times τ_R obtained were 592fs (fluorescein in ethylene glycol) [9], 204fs (EGFP) [57] and 380fs (fluorescein in glycerol) [15]. If the value of τ_P/τ_R is taken from the F_d curve in Fig. 4.16a to be approximately 8, then this gives a relaxation time of $\sim$ 875fs, which is at the least on the correct order of magnitude. This longer value also agrees with the previously observed relationship where τ_R appears to lengthen with longer pulses. It is clear here that the ΔR curve will not yield any physically accurate measurement of τ_R.

It can be argued that the method of quantifying depletion in CW STED, i.e. the relative reduction in fluorescence lifetime, is a more reliable measure of the actual depletion than the changes in fluorescence intensity measured in pulsed STED. In pulsed STED intensity can be lost through a variety of non-STED, non-fluorescent processes such as bleaching and excited state absorption, which cannot be distinguished from depletion using intensity measurements. It is also necessary to subtract the sometimes significant fluorescence background caused by direct excitation by the dump beam (Fig. 4.15, top row), and small variations in this background level between taking the pump + dump measurement and dump only measurement could lead to significant errors when the fractional depletion is close to 1. The pulsed STED experiment performed in the microscope has an advantage over the pulsed STED experiments performed using other equipment as the fibre coupling used in the microscope produces high-quality stable beams for focusing into the objective, although the beam alignment is not perfect (Section 3.7). Stable beams are more difficult to achieve in the other experimental set-ups which are based on free-space beam alignment, and the degree of alignment of the two beams may change from day to day or indeed as measurements are being taken. However, measurements using the streak camera do have the advantage that the focal plane can be clearly isolated and depletion examined in this region only, removing any effects of out-of-focus fluorescence that may be present in the microscope set-up. This is why it has been important to repeat a pulsed STED experiment in a very different experimental set-up to the previous pulsed STED experiments and see a similar effect, as this reduces the probability that either set of results are due to the measurement method.

4.9 Summary

In this chapter, CW STED experiments on fluorophores in solution have shown significant departures from expected depletion dynamics. This departure has been quantified by comparisons with mathematical modelling of CW STED dynamics in the absence of molecular rotational diffusion. Strikingly, the marked deviation from linearity and the appearance of a second lifetime component for the fast-rotating case of fluorescein in water suggests the presence of a fluorophore population largely unaffected by CW STED. A pulsed STED experiment was also performed which replicated deviations from model behaviour for long dump pulses that have been previously observed by the group. The similarities between the results of this experiment and those of previous experiments performed with different equipment indicate that there is no apparent anomalous microscope-specific STED behaviour. The pulsed STED experiment, when taken along with previous pulsed STED studies, further implies that there are additional factors or processes occurring for fluorophores in solution when subject to increasing dump exposure times which are currently unaccounted for in mathematical modelling; it is plausible that these are related to the STED-insensitive population seen in CW STED experiments.

The results of this chapter also have interesting implications for LIR-SR. For all of the imaging performed in Chapter 3, the dump power was approximately 17mW after the major dichroic; the results presented in this chapter suggest that using dump powers higher than this will not necessarily be beneficial as there is limited shortening of fluorescence lifetime components above $\sim$ 10mW. Therefore the dump power used for LIR-SR imaging in Chapter 3 appears to be an appropriate choice, and the use of higher dump powers would come at the cost of increased photodamage to the sample without any significant further lifetime shortening. Further work investigating the CW STED dynamics of immobilised fluorophores, such as those present in fluorescently-labelled biological samples, would be useful to fully confirm this.

Chapter 5

Experimental and theoretical exploration of CW STED anomalies

To investigate the CW STED inefficiencies seen in the previous chapter and their potential origin, a number of experiments were performed controlling alternative experimental parameters. These include pump beam parameters such as wavelength, power and repetition rate, the wavelength of the dump beam, the volume from which fluorescence is detected, triplet production and an alternative method for quantifying CW STED efficiency. These investigations are presented separately, with their individual methods and results grouped together; all results are then discussed collectively in the context of potential model modifications to better describe the photophysics of CW STED.

5.1 CW STED following two photon excitation

Firstly, CW STED experiments in water and glycerol were repeated with two photon excitation as opposed to single photon excitation. Previous pulsed STED experiments by the group have been performed using two photon excitation; in these cases use of two photon excitation was necessary as no appropriate single photon source was available. Here, two photon excitation will result in a more highly ordered excited state, as the orientational distribution function for two photon excitation has a $\cos^4\theta$ dependence compared to the $\cos^2\theta$ dependence seen for single photon excitation (Section 1.3), thus better approximating a delta function of $\theta \sim 0°$ molecules only. Furthermore, the spatiotemporal dependence of two photon excitation confines the excitation volume to a small region at the focus of the pump with little excitation above and below the focal plane, in contrast to single photon excitation where there is considerable excitation along the whole beam path. As a result, there will be less fluorescence arising from regions of the sample where there is low dump intensity (i.e. away from the dump focal plane).

The combined effect of increased excited state ordering and axially limited excitation should thus increase the efficiency of CW STED, and so experiments with single photon and two photon pump were compared for fluorophores in water and glycerol.

5.1.1 Methods

The two photon pump beam was provided by a Ti:Sapphire laser (Mira 900, Coherent) pumped by a Verdi laser (V-10, Coherent), with the optical path and simplified triggering electronics shown in Fig. 5.1, and the dump source was the 594nm DPSS CW laser. The (V-polarised) pump was tuned to 797nm for all two photon experiments, and was emitted from the laser at a repetition rate of 76MHz. This output then passed through a pulse picker (Pulse Select, APE) which uses acousto-optic modulation to diffract individual pulses from the beam at a desired frequency, here 1 in 20 pulses to obtain an effective repetition rate of 3.8MHz at the sample. Sync signals from the pulse picker were sent to the external triggering port of the 490nm PicoTA laser driver to slave the PicoTA to a 3.8MHz repetition rate and thus generate appropriate sync signals for the TCSPC (PicoTA laser and driver omitted from Fig. 5.1 for simplicity). The output of the 490nm laser was blocked for the duration of the two photon experiments.

The 3.8MHz two photon pump beam exited the pulse picker and was passed through a filter wheel containing various neutral density filters for power control. The beam was then resized using a two-lens telescope; beam size was finely adjusted until a peak in fluorescence intensity was detected from a solution of test sample. The pump beam was directed into the free-space port of the microscope optical unit and then combined with the dump beam exiting the optical fibre using a beam combiner (PCXR725, Chroma); the combined beams were reflected into the objective using the same major dichroic as for previous single photon experiments. Fluorescence transmitted through the major dichroic was filtered to remove residual pump (e700sp, Chroma) and then passed through the tube lens, a 50µm pinhole and another filter (FES550 within Box 1 as before) to remove residual dump beam before being split into the two SPAD detectors using a cube polariser (Box 2).

The samples used were 1×10^{-5}M 2'7'-dichlorofluorescein in water and 2.5×10^{-3}M coumarin 6 in glycerol, with the single photon pump results taken from Chapter 4 for comparison. The pump power measured after the major dichroic was 836 ± 4µW for fluorescein in water and 758 ± 2µW for coumarin 6 in glycerol.

5.1.2 Results

CW dump series with two photon excitation were measured for both fluorescein in water and coumarin 6 in glycerol. The undumped lifetimes with two photon pump were measured as 3.55 ± 0.01ns (fluorescein in water, average of $N = 5$ decays) and

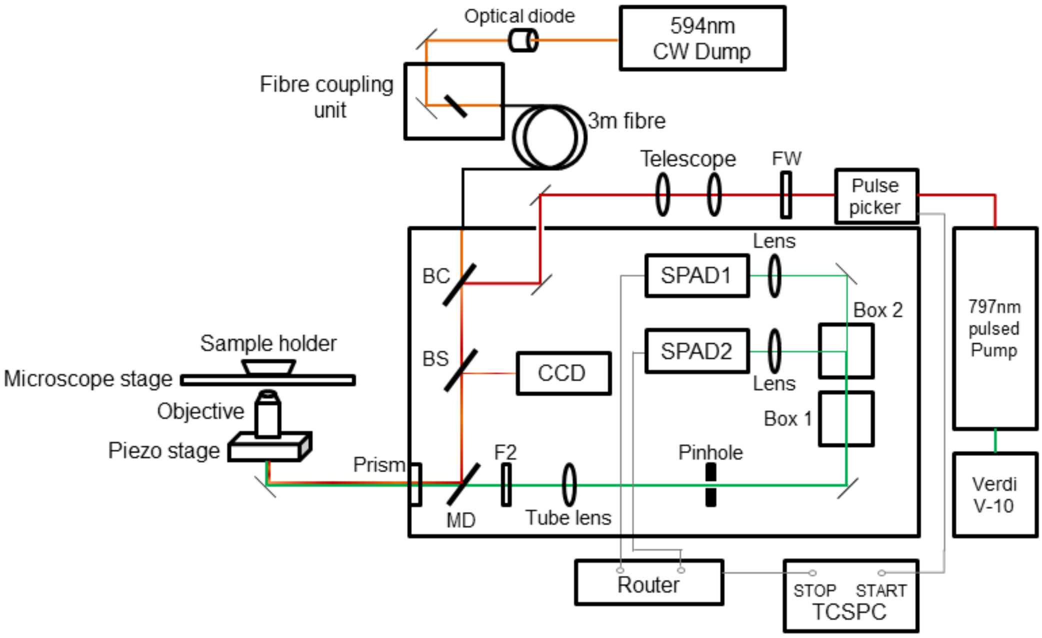

Figure 5.1: Microscope set-up with two photon pump. Two photon pump (free space) path shown as a red line, dump path shown as an orange line, combined beams shown by a red/orange striped line. Fluorescence path shown by green line. Abbreviations used: FW - neutral density filter wheel, BC - beam combiner, BS - beamsplitter, MD - major dichroic, F2 - filter. Not shown: piezo controllers, delay line, laser drivers.

2.48 ± 0.01ns (coumarin 6 in glycerol, average of $N = 5$ decays), which were in agreement with the undumped lifetimes measured with single photon pump. Figure 5.2 shows the intensity parameters for fluorescein in water as defined in Section 4.6.4 plotted for both two photon and single photon excitation. As with single photon excitation, fluorescein in water displayed a monoexponential undumped decay with two photon excitation, which again became biexponential in the presence of CW dump; the exception to this was at the two lowest dump powers, which were better fitted by a monoexponential function. Figure 5.2a shows the variation of these two lifetime components with dump power, and it can be seen that both the short (τ_1) and long (τ_2) lifetime components were shorter for two photon excitation than for their single photon counterparts. This was also reflected in the higher STED rates measured with two photon excitation as plotted in Fig. 5.2b. However, the two photon STED rates also displayed similar deviations from the expected linear relationship with dump power as was seen with single photon excitation.

The fractional contributions of the two lifetime components are shown in Fig. 5.2c, where the fractional amplitude A_1 (short lifetime component) dominated the lifetime decay at powers > 12mW for both pump wavelengths. However, the domination of the short lifetime component τ_1 over the long lifetime component τ_2 was much greater for two photon excitation ($75 : 25$ ratio of $A_1 : A_2$) than for single photon excitation ($60 : 40$). A comparison of the STED efficiencies with single and two photon excitation can be seen in the fractional depletion plots (Fig. 5.2d). With the exception of the points at ~ 2.8mW, where poor biexponential fitting resulted in large uncertainty for both data sets, there was no agreement between the F_d values obtained using single photon and two photon excitation. At all dump powers, two photon excitation yielded higher F_d values, with greater divergence between the two excitation regimes at higher dump powers. The maximum F_d obtained with two photon excitation was 0.634 ± 0.005 compared to 0.49 ± 0.01 for single photon excitation, although F_d again plateaued at the highest dump powers tested as observed with the single photon pump. There was no change in anisotropy introduced by any of the dump powers with two photon excitation (Fig. 5.3), indicating that rotation in water is fast enough even to negate the two photon excited state orientational distribution.

Figure 5.4 shows the intensity parameters for coumarin 6 in glycerol when measured with two photon and single photon excitation. The data set obtained with the two photon pump was much noisier than with the single photon pump, namely because the peak fluorescence intensity measured with two photon excitation was ten times lower than measured with single photon excitation. As a result exponential fitting was poorer, as is evident in the erratic distribution of two photon data points in Fig. 5.4a,b,c compared to the single photon data points which display smooth trends. Therefore a quantitative comparison will not be drawn for the lifetime components, STED rates or fractional amplitudes between single and two photon excitation of

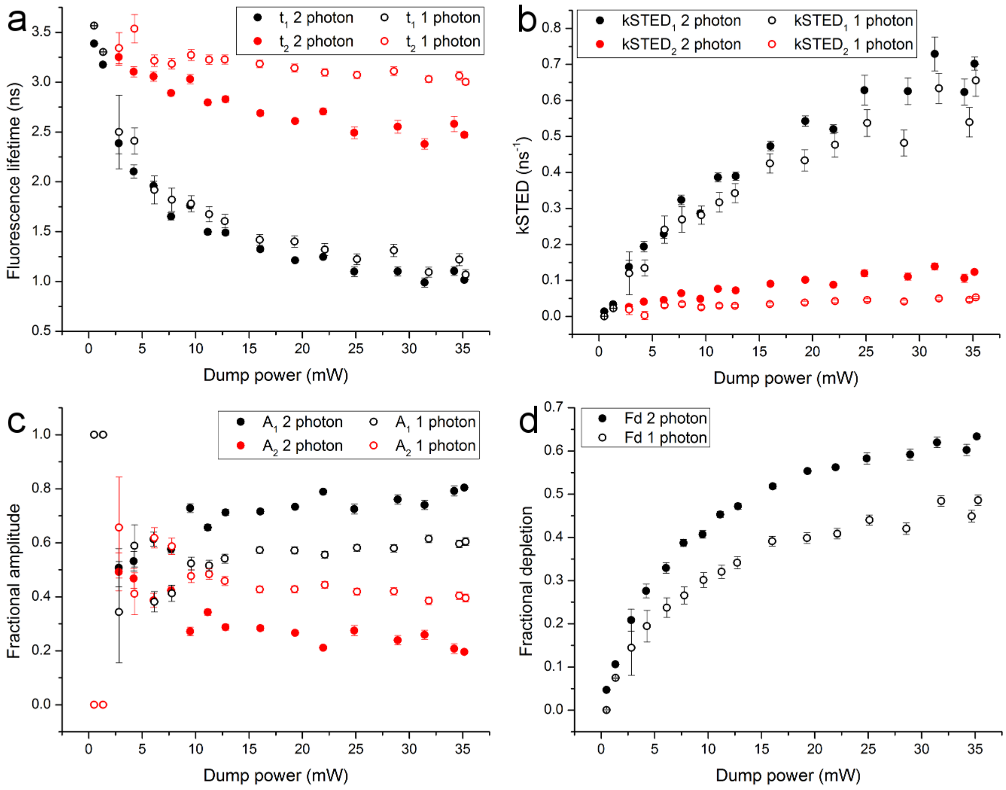

Figure 5.2: Parameters derived from intensity decays of fluorescein in water with two photon pump. Solid circles are data obtained using two photon pump, empty circles are data obtained using single photon pump. a) Fluorescence lifetime components of the biexponential decay. b) Corresponding STED rates for each lifetime component. c) Fractional amplitudes for each lifetime component. d) Fractional depletion.

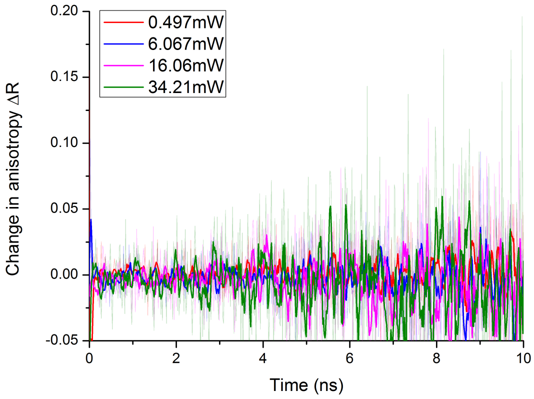

Figure 5.3: Change in anisotropy measured for fluorescein in water with two photon pump at four different dump powers. Data are truncated at 10ns as decays become noisy beyond this point. Faint lines are raw data, bold lines are smoothed data (5 point adjacent averaging).

.

coumarin 6 in glycerol. However, the recurring theme that CW dump produces two lifetime components, one short and one long, from a monoexponentially decaying fluorophore was again observed.

The fractional depletion of coumarin 6 in glycerol with two photon excitation increased with dump power (Fig. 5.4d). The F_d values obtained with two photon excitation largely agreed with the values obtained using single photon excitation up to 10mW, with a further increase in F_d seen for two photon excitation at higher dump powers compared to the single photon series. The maximum F_d obtained with two photon pump was 0.48 ± 0.02 compared with 0.357 ± 0.005 when measured with single photon pump. Simulated F_d curves are also shown for two photon and single photon excitation; the single photon curve is the same as in Section 4.7.2, and the two photon curve was calculated as in Section 4.6.4 except with

$$P_u(\theta,\phi) = \frac{1}{4\pi}\left(1 + \frac{4\sqrt{5}}{7}\frac{Y_{20}(\theta,\phi)}{Y_{00}(\theta,\phi)} + \frac{8}{21}\frac{Y_{40}(\theta,\phi)}{Y_{00}(\theta,\phi)}\right) \tag{5.1}$$

to describe the two photon excited state orientational distribution function. The simulated F_d curves also indicated that higher STED efficiencies should be obtained with two photon excitation as opposed to single photon excitation; however, as for single photon excitation discussed previously, the STED efficiency with two photon excitation obtained experimentally was again significantly lower than predicted by the model.

Changes in anisotropy for two photon excitation were also calculated and plotted in Fig. 5.5a-d. Again, the two photon data were noisier than the single photon data, but it can be seen that larger values of ΔR were obtained with higher dump powers indicating orientational holeburning as seen previously which cannot be counteracted due to lack of rotation. Modelled ΔR plots for CW STED with single photon and two photon excitation are shown in Fig. 5.5e, calculated as in Section 4.6.4 with the undumped orientational distribution function as in Eq. 5.1. At the lowest displayed dump power ($<$ 1mW, Fig. 5.5a) a greater change in anisotropy was observed for single photon excitation than two photon excitation, which matched the prediction of the model at the lowest dump power simulated (black lines, Fig. 5.5e). The model predicted that ΔR should also be greater for single photon excitation than two photon excitation for $\sim$ 3.9mW dump; however, this behaviour cannot be verified using the experimental data in Fig. 5.5b as there is a considerable discrepancy between the dump powers chosen for display of the single and two photon cases (there was not a ΔR plot of sufficiently high quality obtained for a more comparable dump power with two photon excitation).

At higher dump powers (Fig. 5.5c,d) the ΔR obtained with single photon excitation initially increased more rapidly than for two photon excitation, but ΔR continued to increase in a near linear fashion for two photon excitation whereas ΔR increased little after 5ns for single photon excitation. Consequently, at times $>$ 5ns, two photon ΔR became larger than ΔR measured with single photon excitation. Thus, the shape of the ΔR plots for two photon excitation agreed with the model predictions, although the values of ΔR observed in the two photon excitation data were significantly lower than those predicted by the model, as was the case previously discussed for single photon excitation.

5.1.3 Discussion

For both fluorescein in water and coumarin 6 in glycerol, two photon excitation increased the efficiency of CW STED as quantified by the fractional depletion. The anisotropy data for water again confirmed that the rotation of fluorescein in water is sufficiently fast to negate the initial orientation of the excited state population, even in the highly ordered case following two photon excitation. Therefore the increased ordering of the excited state is unlikely to have contributed greatly to the substantially increased F_d values for two photon excitation of fluorescein in water, as rotational diffusion was again homogenising the excited state distribution as for single photon excitation. The predominant cause of increased CW STED efficiency following two photon excitation must thus be a non-angle dependent factor; this could be the increased axial confinement of excitation. A consequence of this is that STED is also confined to a smaller volume than for single photon excitation, where there is out-of-focus excitation along the beam path which is not depleted as efficiently as that at the focus which could be contaminating the detected signal.

The anisotropy data for coumarin 6 in glycerol also suggest that our understanding of the effect of orientation in CW STED is correct: the ΔR plots obtained with two photon excitation qualitatively agreed with model predictions, as did the differences between ΔR for single and two photon excitation. The differences in the anisotropy change between the two excitation regimes are a result of the increased excited state alignment following two photon excitation; the more highly aligned the excited state, the smaller the variation in STED rates will be and thus the longer the exposure to CW dump will need to be before an orientational hole is burnt in. The extreme limit of this would be the case where all molecules were aligned at exactly $\theta = 0^\circ$ where, with no rotational diffusion, the excited state population following depletion would still only consist of $\theta = 0^\circ$ molecules and so there would be no depolarisation of fluorescence and accordingly no change in anisotropy.

5.2 The effect of out-of-focus fluorescence

In previous pulsed STED experiments, a streak camera has been used for measuring fluorescence intensity decays; one advantage of this system is that fluorescence intensity is recorded both in time and in one spatial dimension along the emitted fluorescence path [15], as shown in Fig. 5.6a. As a result out-of-focus fluorescence can be identified and excluded from analysis, and only the fluorescence arising from

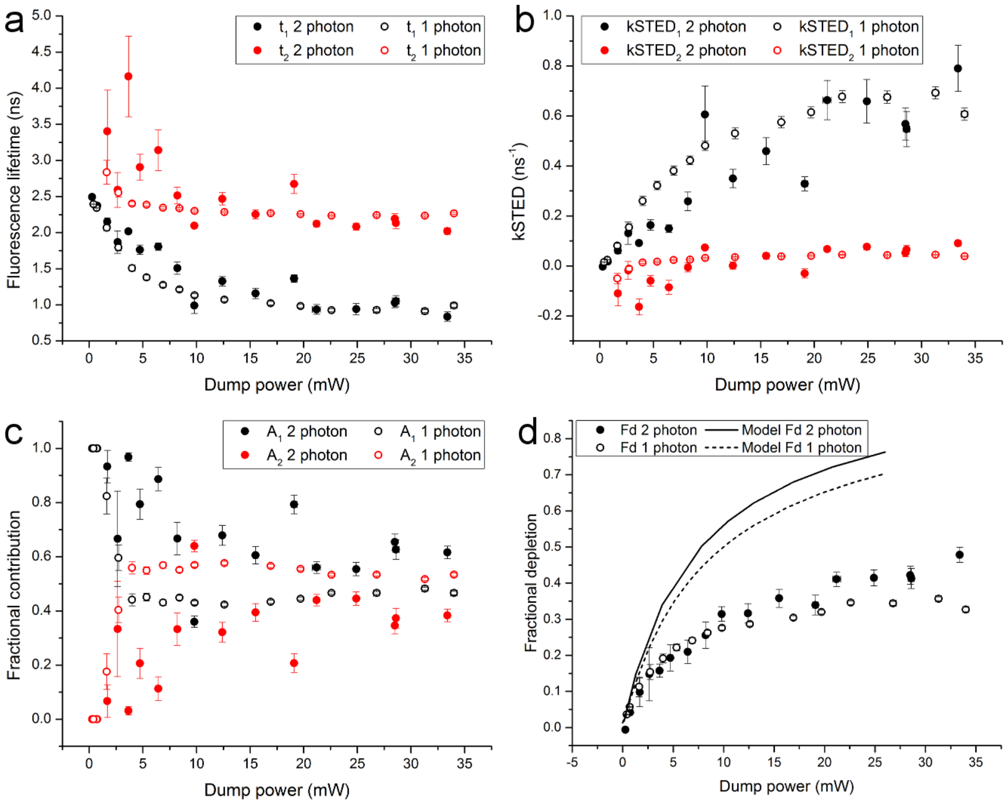

Figure 5.4: Parameters derived from intensity decays of coumarin 6 in glycerol with two photon pump. Solid circles are data obtained using two photon pump, empty circles are data obtained using single photon pump. a) Fluorescence lifetime components of the biexponential decay. b) Corresponding STED rates for each lifetime component. c) Fractional amplitudes for each lifetime component. d) Fractional depletion with simulated curves for two photon (solid line) and single photon (dashed line) excitation.

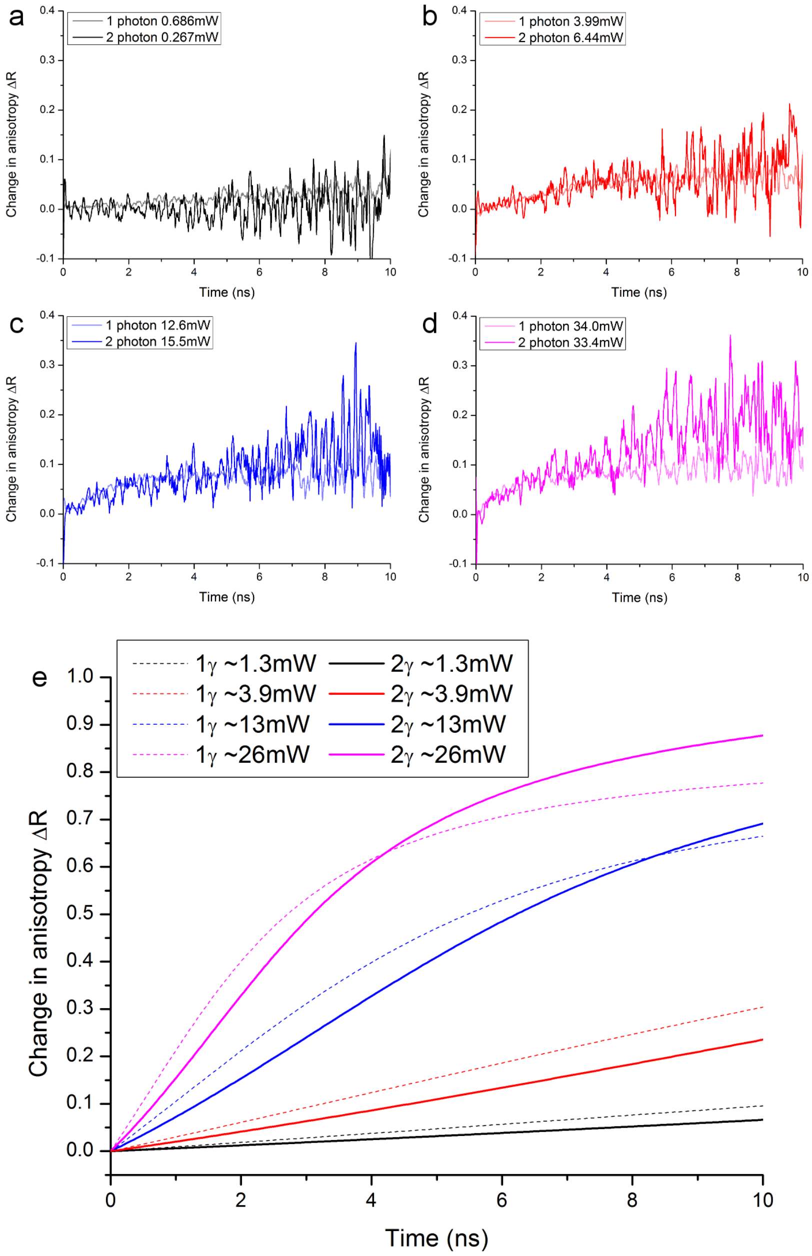

Figure 5.5: Change in anisotropy measured for coumarin 6 in glycerol with two photon pump compared with single photon pump at four different dump powers. a) - d) Smoothed (5 point adjacent averaging) one photon (faint) and two photon (bold) data for the dump powers indicated in graph legends. e) Modelled plots of ΔR for single photon (dashed) and two photon (solid) pump for approximate dump powers to match experimental data as indicated in the legend.

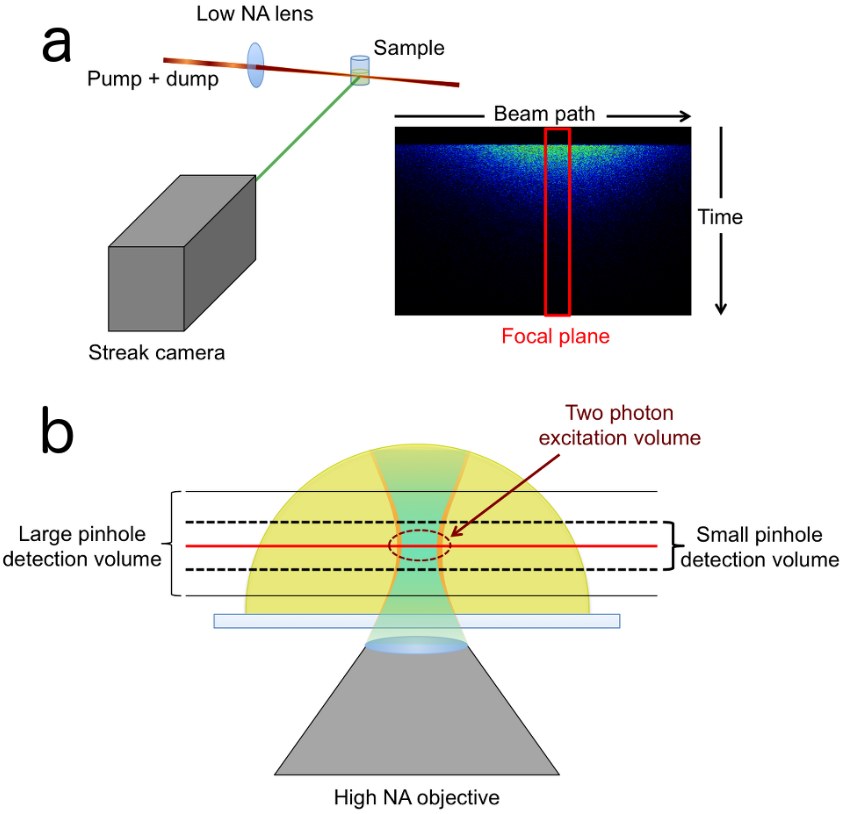

Figure 5.6: Comparison of detection regimes for streak camera and confocal microscope. a) Schematic showing fluorescence (green) detection from a cuvette of fluorophore using a streak camera and an example of data obtained using the streak camera (courtesy of Dr Daven Armoogum). b) Focusing of single photon pump (blue) and dump (orange) beams into a volume of sample on a coverslip using a microscope objective. The focal plane is marked in red, and the depths over which fluorescence is detected are marked with black lines. Dashed dark red line shows two photon excitation volume. Diagrams are not to scale.

the focus of the beam pair (i.e. the most efficiently depleted volume) used for quantification. Furthermore the OPA dump source used in previously described streak camera experiments was not tightly focused and as such the focal volume of the dump beam was much larger than that of the two photon pump, meaning that all excited molecules experienced a similarly intense dump field. However, in the microscope the only method for rejecting out-of-focus fluorescence is by using a pinhole for confocal detection of fluorescence (Fig. 5.6b), and the use of the optical fibre to inject the combined pump and dump beams into the microscope optics prevents resizing of the dump beam.

One explanation for the low fractional depletion seen in the microscope could be contamination with out-of-focus fluorescence, as discussed briefly for two photon excitation in Section 5.1.3. With single photon pump, molecules are excited along the whole beam path and, whilst the probability of excitation occurring is lower above and below the focal plane due to the lower pump intensity, the undumped fluorescence lifetime does not alter (with the low pump intensities used here). However, when the CW dump beam is also present, depletion also occurs all the way along the beam path, again not just at the focal plane. Out-of-focus excited molecules will experience lower dump intensity than molecules within the focal plane, and so will experience less lifetime shortening (and hence have lower F_d) than the in-focus molecules. As a result, detection of out-of-focus fluorescence in CW dump experiments will contain a significant proportion of molecules with lower F_d values than expected.

To investigate the effect of out-of-focus fluorescence on measured STED efficiency, fluorescence lifetime decays were measured at different dump powers for a range of different fixed pinhole sizes. Larger pinholes allow more fluorescence from above and below the focal plane to reach the detectors, whereas smaller pinholes allow only fluorescence originating from a narrower depth around the focal plane to reach the detectors.

5.2.1 Methods

Single photon (490nm) pulsed pump and 594nm CW dump were used for all experiments, with the beam paths and filtering as in Fig. 2.14. Fixed diameter pinholes provided with the microscope (150µm, 100µm, 75µm, 50µm and 30µm) were exchanged into the detection pathway, and measurements were also taken with no pinhole in place. Pinhole position was finely adjusted to centre the pinhole on the beam axis, judged to be the position yielding the highest undumped fluorescence intensity. Following pinhole installation the lenses in front of the detectors were also adjusted to ensure that the fluorescent spot remained centred on the active area of each detector.

The samples used were 1×10^{-5}M 2’7’-dichlorofluorescein in water and 2.5×10^{-3}M coumarin 6 in glycerol, with the two photon pump results measured with 50µm pinhole taken from Section 5.1. Pump powers were again $< 1\mu$W prior to fibre coupling.

5.2.2 Results

Fluorescence intensity decays were measured over a range of dump powers with the various pinhole sizes for both samples. The fractional depletion curves obtained from these decays are shown in Fig. 5.7.

For both samples, when excited with single photon pump, decreasing the pinhole size increased the maximum obtained F_d up to a pinhole size of 50µm, with the 30µm pinhole producing no further improvement in F_d. For coumarin 6 in glycerol, the average F_d at the three highest powers measured was 0.38 ± 0.02 for the 50µm pinhole and 0.38 ± 0.03 for the 30µm pinhole; for fluorescein in water average highest F_d was 0.47 ± 0.02 for the 50µm pinhole and 0.43 ± 0.07 for the 30µm pinhole. Decreasing

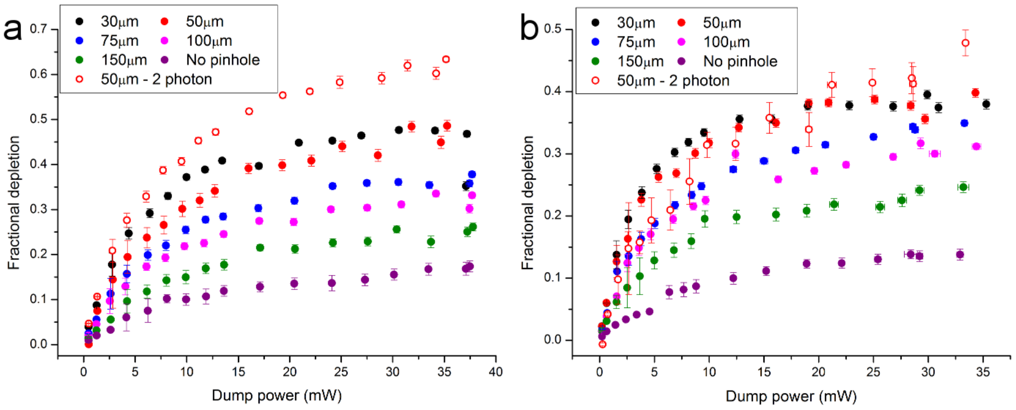

Figure 5.7: Fractional depletion curves measured with different sized pinholes for a) fluorescein in water and b) coumarin 6 in glycerol. All solid circles are measured with single photon pump whereas empty circles are measured with two photon pump.

pinhole size also increased the gradient of the F_d curves in the low dump power regime (generally $<$ 10mW) where the relationship between dump power and F_d is approximately linear. The undumped fluorescence lifetimes agreed for all pinhole sizes for each sample to within 9ps for fluorescein in water and 30ps for coumarin 6 in glycerol, and there was no correlation between pinhole size and undumped fluorescence lifetime (P=0.50 for fluorescein in water and P=0.33 for coumarin 6 in glycerol, two-tailed Pearson's correlation test).

The two photon measurements are also superimposed upon the plots in Fig. 5.7 for comparison. It can be seen that for fluorescein in water, fractional depletion measured with two photon pump (Fig. 5.7a, empty red circles) was higher at the majority of dump powers than for single photon pump, even with the smallest pinholes. The noisier two photon F_d values obtained for coumarin 6 in glycerol were only larger than the single photon measurements for the highest dump powers tested.

5.2.3 Discussion

The results presented above indicate that our understanding of the effect of out-of-focus fluorescence on measured STED efficiency is correct, as larger pinholes yielded lower values of F_d. The results also confirmed that selection of the 50μm pinhole for CW STED experiments was appropriate, as decreasing the pinhole size to 30μm did not appear to increase F_d further. This could be because the diameters of the smaller pinholes become comparable to the diameter of the fluorescence spot travelling back out of the objective, and so further decreases in pinhole size will begin to reject signal in the lateral direction rather than just the axial direction. The diameter of one Airy unit reaching the pinhole is given by [139]

$$1\text{A.U.} = \text{mag}_{\text{obj}} \times \frac{1.22\lambda_{\text{ex}}}{\text{NA}}, \tag{5.2}$$

where mag_{obj} is the magnification of the objective. For the system here, if it is perfectly aligned, this corresponds to 1A.U. = 29.89µm reaching the pinhole.

The data obtained using two photon excitation were also shown alongside the pinhole data to compare the two methods of detecting fluorescence from a smaller focal volume: the focal volume using two photon excitation is calculated to be 0.053fl [140], compared to the measured focal volume of this microscope of 0.6 ± 0.2fl for single photon excitation (Section 5.6). It should be noted that it is not possible to separate the relative contributions of improved optical sectioning and increased photoselection (Section 5.1) underlying the improved F_d obtained with two photon excitation. One way to examine this could be to calculate the detection volume for different pinhole sizes and plot the single photon excitation F_d as a function of detection volume: the F_d obtained at the two photon detection volume could then be compared with this relationship. Qualitatively, a large deviation from this relationship would imply that the effect of photoselection on CW STED efficiency is much greater than that of optical sectioning in two photon excitation.

5.3 CW STED efficiency with different dump wavelengths

Within the samples there could be a subpopulation of solvation environments producing changes in the spectral properties of the fluorophores (a phenomenon known as solvatochromism [1]), and therefore a possibility that there is a subpopulation of molecules not accessible by the 594/595nm dump wavelengths used in the experiments presented thus far. As the dump wavelength is required to be at the very red edge of the fluorophore emission spectrum a subpopulation undergoing, for example, a small blue shift in emission spectrum could render the 594/595nm dump wavelengths ineffective. STED cross-sections have previously been measured for a range of dump wavelengths in pulsed STED [9, 57], and previous work has also investigated whether the measured efficiency of CW STED depends on the spectral observation window (detected wavelengths) for fluorescent proteins. In this case it was seen that STED efficiency was similar across two distinct observation windows [15]; however, this was only investigated at a dump wavelength of 594nm.

To investigate whether there is any wavelength dependence underlying the low STED efficiencies repeatedly seen in Chapter 4, CW STED was performed at different dump wavelengths for both coumarin 6 and pyridine 2, a dye with a large Stokes shift which has been used in STED microscopy [141, 142].

5.3.1 Methods

The effect of dump wavelength was investigated for 1×10^{-5}M coumarin 6 in ethylene glycol and 1×10^{-5}M pyridine 2 (Exciton Inc.) in ethylene glycol. For both experiments single photon pump was used at a repetition rate of 20MHz. For coumarin 6 the VECSEL laser was used as the dump source as described in Section 4.6.2, but here tuned to 603nm.

The dump source for pyridine 2 was CW output of the Ti:Sapphire laser (which was used in pulsed mode for two photon excitation in Section 5.1). The Ti:Sapphire laser was adjusted to produce a stable high power CW beam and the pulse picker was also set to operate in CW mode (here the pulse picker was not used for any triggering purposes and the 490nm laser was triggered internally as for previous experiments). The dump path followed the same path as the two photon pump shown in Fig. 5.1, with the same beam combiner and major dichroic as used for the two photon pump experiments. Fluorescence transmitted through the major dichroic was filtered to remove residual pump (HQ510LP), passed through the tube lens and 50μm pinhole before being further filtered at Box 2 to remove residual dump (730/10 notch filter, Newport, for 797nm dump or S40-700 bandpass filter, Newport, for 760nm dump) and split into the two SPAD detectors using a cube polariser.

5.3.2 Results

Figure 5.8 shows intensity parameter plots obtained for coumarin 6 in ethylene glycol with single photon pump for both 595nm and 603nm CW dump. The individual fluorescence lifetime components for the two dump wavelengths were within close quantitative agreement for dump powers $<$ 20mW with a slightly greater degree of shortening seen for the 595nm dump at higher powers (Fig. 5.8a); a similar relationship was seen for the k_{STED} rates (Fig. 5.8b). The fractional amplitudes (Fig. 5.8c) were in close quantitative agreement between the two dump wavelengths.

The fractional depletion curves for the two wavelengths (Fig. 5.8d) were also quantitatively similar for dump powers up to $\sim$ 20mW, with the shorter dump wavelength producing slightly larger values of F_d for higher dump powers (F_d with 68mW 595nm dump = 0.496 ± 0.003 compared to F_d with 73mW 603nm dump = 0.476 ± 0.005). However, the F_d curves appeared to saturate similarly for both dump wavelengths suggesting that this saturation is not a peculiarity of the 594/595nm dump wavelength used previously. It is not possible to estimate the expected difference in STED efficiency based on wavelength alone; however STED cross sections (σ_{STED}, as in Eqs. 4.2 and 4.6) for other fluorophores have been seen to mimic the shape of the emission spectrum [9, 57]. Whilst there are no measurements of σ_{STED} for coumarin 6 in the literature, the difference between relative emission values for the two wavelengths is small (relative emission at 595nm = 0.11, relative emission at 603nm = 0.08, Appendix Fig. A.3) and hence in the absence of any spectral sub-

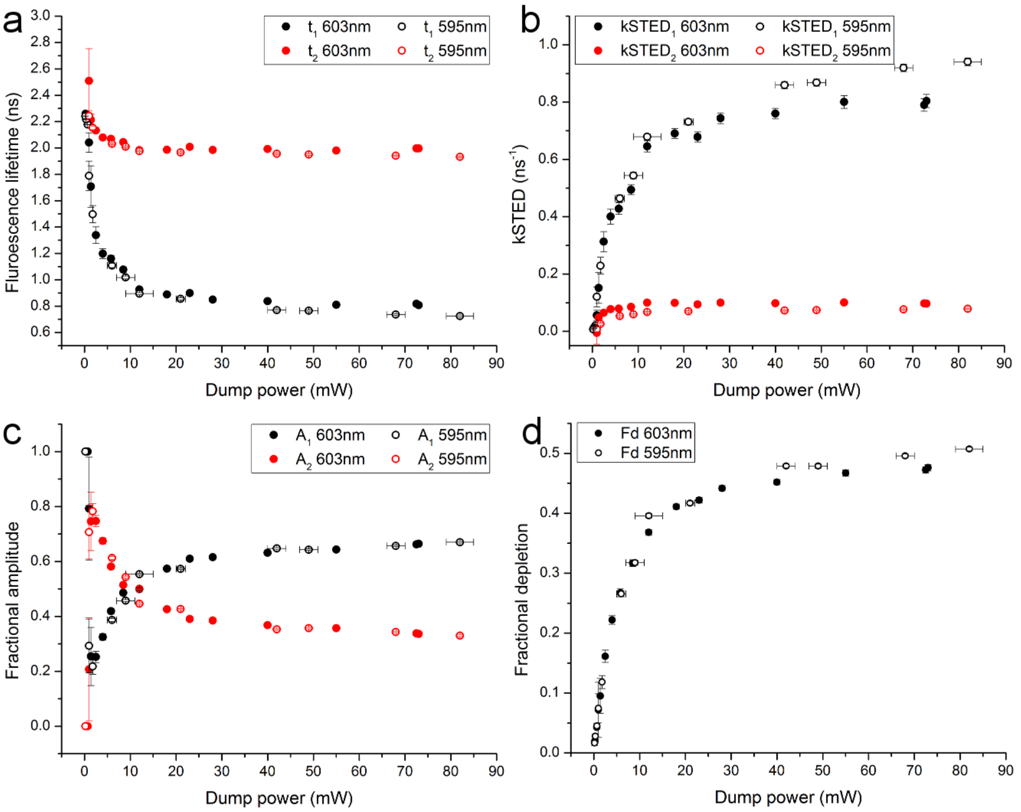

Figure 5.8: Parameters derived from intensity decays of coumarin 6 in ethylene glycol with two different dump wavelengths. Solid circles are data obtained using 603nm CW dump, empty circles are data obtained using 595nm CW dump. a) Fluorescence lifetime components of the biexponential decay. b) Corresponding STED rates for each lifetime component. c) Fractional amplitudes for each lifetime component. d) Fractional depletion.

populations the difference in STED efficiency for 595nm and 603nm is also expected to be small.

A fluorophore possessing a large Stokes shift, pyridine 2 (Appendix Fig. A.4), was also examined with the same single photon pump, but with the dump beam provided by the high power tunable CW output of the Ti:Sapphire laser. Figure 5.9 shows F_d curves for pyridine 2 obtained using two different CW dump wavelengths. A full series of results were obtained for a dump wavelength of 797nm where the CW output of the laser was most stable and powerful. A few data points were also obtained at a dump wavelength of 760nm where the emission of pyridine 2 was substantially larger. However, there was much higher background signal at 760nm compared to 797nm which made fitting and analysis difficult.

The F_d curve measured with 797nm CW dump was still seen to plateau at high dump powers, despite the dump powers measured after the major dichroic being an order of magnitude larger than those produced by the 594nm DPSS dump laser.

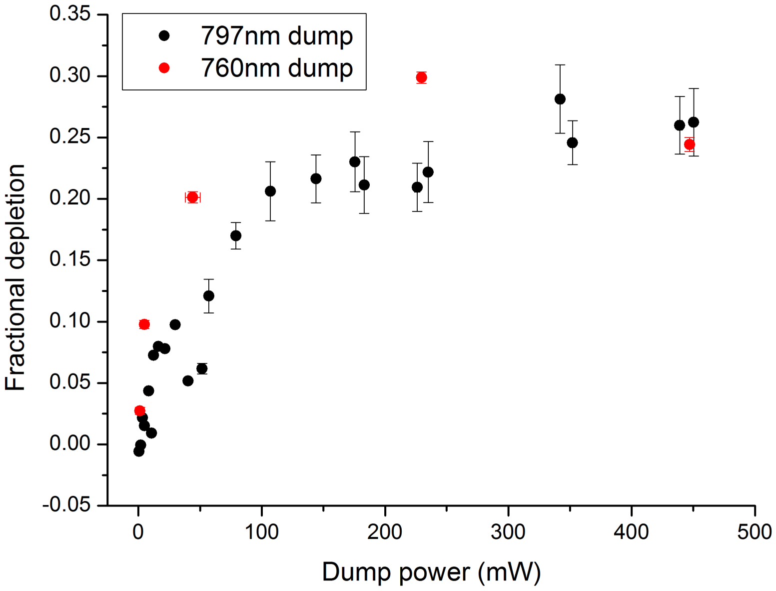

Figure 5.9: Fractional depletion curves for pyridine 2 for single photon pump and near-IR CW dump (black circles 797nm, red circles 760nm).

The F_d values measured with the 760nm dump were larger than those measured with the 797nm dump, although even the small number of data points obtained indicated that the F_d curve was also reaching a plateau at high powers. As seen for coumarin 6 above, a higher STED efficiency reflects the probable larger σ_{STED} for pyridine 2 at 760nm compared to 797nm. The difference between the F_d curves for the two dump wavelengths applied to pyridine 2 (with the exception of the data point obtained at the highest power for 760nm dump) appeared to be greater than the difference between the F_d curves for the two dump wavelengths applied to coumarin 6. Again, this is expected as there is a larger difference between the relative emission values of pyridine 2 (relative emission at 760nm $\sim$ 0.5, relative emission at 797nm $\sim$ 0.2, Appendix Fig. A.4) than there was for coumarin 6.

The other parameters obtained from the intensity decays are not displayed as the short lifetime of pyridine 2 (0.64 ± 0.04ns monoexponential decay, N=8 undumped measurements) led to large errors in the exponential fitting, with a second lifetime component obvious in the measurements taken with high dump powers ($>$ 40mW) but difficult to resolve at the lower dump powers. Similarly this short fluorescence lifetime made the anisotropy decays noisy and difficult to interpret.

5.3.3 Discussion

The results obtained from using a longer dump wavelength for CW STED of coumarin 6 and near-IR dump of pyridine 2 both indicated low, saturating STED efficiencies at high dump powers, as seen in the experiments in Chapter 4. This suggests that the saturation of STED efficiency at high dump powers is not due to a wavelength-dependent phenomenon. For both samples higher F_d values were obtained for the shorter dump wavelengths; this was not unexpected, as there is stronger emission at the shorter dump wavelengths for both fluorophores and hence they will have higher STED cross-sections at these wavelengths [9, 57]. Using the CW output of the Ti:Sapphire laser also allowed for much higher dump powers to be achieved than with the DPSS laser or the VECSEL, although the saturation of F_d with increasing dump power was still evident.

5.4 The effect of pump repetition rate on CW STED efficiency

One cause of the low STED efficiency could be that there is an accumulation of photophysical states over time that cannot be depleted efficiently. Throughout Chapters 4 and 5 of this thesis all experiments have been performed with decreasing dump power - starting at the highest dump power and then measuring at incrementally lower dump powers - with a repeat of the highest dump power measurement once the full range of powers have been measured. It has been consistently seen that the second measurement with the highest dump power produced identical results to the first measurement, with no changes seen across the regularly-measured undumped decays. Whilst this indicates that there is no permanent accumulation of states over the course of a whole experiment, there could still be changes occurring within the sample during individual measurements.

To investigate this, CW STED experiments for fluorescein in water were repeated at a variety of pump repetition rates. The greater the time between successive pump pulses, the more time there is available for fluorophores to re-equilibriate to the state that they were in before pumping (and subsequent STED) occurred. This re-equilibriation could simply consist of diffusion of fresh solution into the focal volume before the arrival of the next pulse or reversing of a conformational change (such as twisting) of the fluorophore which may have occurred in its excited state. Decreasing the repetition rate has similarly been employed as a strategy in STED microscopy to attempt to limit photobleaching [72].

5.4.1 Methods

The single photon pump was set to different repetition rates either by internal triggering (20MHz, 10MHz and 5MHz measurements) or external triggering from the pulse picker as described in Section 5.1 (3.8MHz and 250kHz measurements, two photon beam blocked from entering microscope). For all measurements pump power was adjusted such that count rate was $\sim$1% of the repetition rate ($<$ 1μW measured before the optical fibre at all repetition rates) and the dump source was the 594nm DPSS laser. Filtering was identical to that used throughout for experiments with 490nm pump and 594nm dump. To ensure collection of a sufficient number of

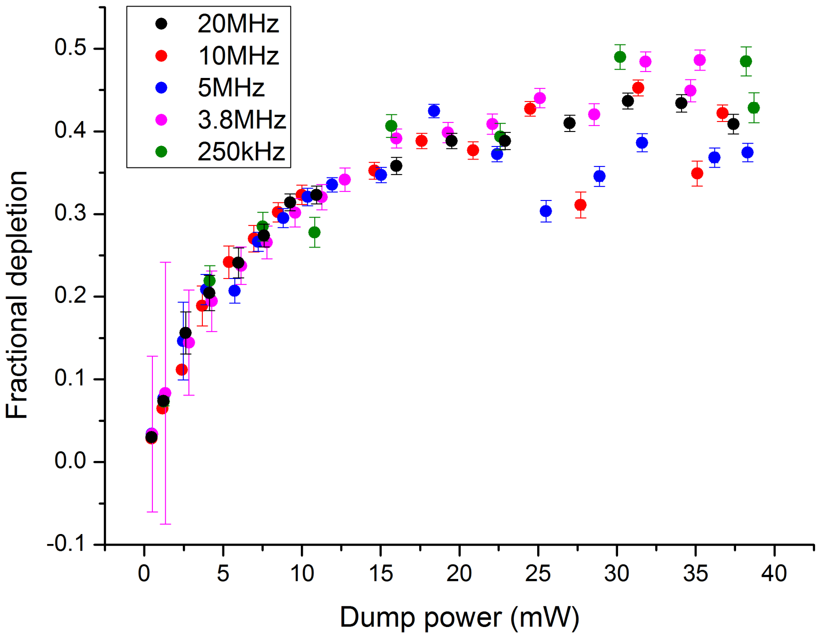

Figure 5.10: Fractional depletion of fluorescein in water measured at different pump repetition rates.

photons for fitting, longer recording times were used for the lower repetition rates as follows: 30s recordings for 20MHz and 10MHz, 45s recordings for 5MHz, 60s recordings for 3.8MHz and 300s recordings for 250kHz. The sample for all measurements was 1×10^{-5}M 2’7’-dichlorofluorescein in water.

5.4.2 Results

Figure 5.10 shows fractional depletion curves obtained at a range of pump repetition rates. The F_d values obtained for the different repetition rates were largely all in agreement up to $\sim$ 13mW dump, and all data sets became noisier for higher dump powers. Whilst the 250kHz repetition rate did yield the largest measured F_d (0.49 ± 0.01), the difference between this and the F_d measured at 20MHz (0.44 ± 0.01) was small considering the 100-fold difference in the repetition rates. Furthermore, there was no clear trend observed between maximum F_d and repetition rate; indeed, the ‘average’ maximum F_d values (average of the three highest F_d values at each repetition rate) agreed within error for all repetition rates except 5MHz, which yielded a lower average maximum F_d.

5.4.3 Discussion

The results shown in Fig. 5.10 suggest that there is no appreciable effect of pump repetition rate on CW STED efficiency. This implies either that there is no build up of STED-insensitive states arising from the repetition rate being too high, or that any photophysical products produced require longer than 4µs (the time between pulses at 250kHz) to be removed from the population. Further investigation of repetition rates lower than 250kHz would be beneficial to confirm the results shown here.

5.5 Investigating CW dump exposure time

Whilst the pump repetition rate was varied in Section 5.4 to allow the system to reach an equilibrium before the next cycle of excitation, the CW dump beam was still present on the sample throughout. The continuous presence of the CW dump beam, rather than the frequent arrival of pump pulses discussed in Section 5.4, could be creating a population of states resistant to depletion, even at the low repetition rates where the pump beam is effectively 'off' for the majority of the acquisition. To investigate this the dump beam was rapidly blocked and unblocked during the course of each measurement such that the sample was exposed alternately to pump only and pump + dump beams to allow for periods of 'recovery' time when the sample was not exposed to the dump beam.

5.5.1 Methods

The basic experimental set-up was as used previously for experiments with 490nm pump and 594nm CW dump. To vary the CW dump beam exposure time, the 594nm dump beam was 'chopped' such that it was alternately intense and blocked. To achieve this a mechanical chopper and electronic controller (SR540, Stanford) were set up in the path of the dump beam before the optical diode and fibre coupling unit. A signal from the chopper controller was sent to the 'count enable' port of the TCSPC router such that detected photons would only be recorded in the lifetime histograms when the CW dump was on the sample in addition to the pulsed pump, and not when the chopper was blocking the dump (where pump, which was not chopped, was still on). The chopper controller was then used to drive the chopper at different frequencies and hence different dump exposure times.

To calibrate the chopper, a photodiode was placed in the path of the chopped laser output and its signal monitored using an oscilloscope. The signal from the chopper controller which indicated whether the beam was blocked or not (which was sent to the count enable port of the TCSPC router during measurements) was also monitored using the oscilloscope. The angle of the chopper as it cut across the dump beam was then finely adjusted until the photodiode signal and chopper signal were exactly in phase.

The pump repetition rate was set to 20MHz for all chopper experiments and pump power was $\sim 1\mu$W before entry into the optical fibre. Samples used were 1×10^{-5}M 2'7'-dichlorofluorescein in water and 1×10^{-5}M 2'7'-dichlorofluorescein in ethylene glycol.

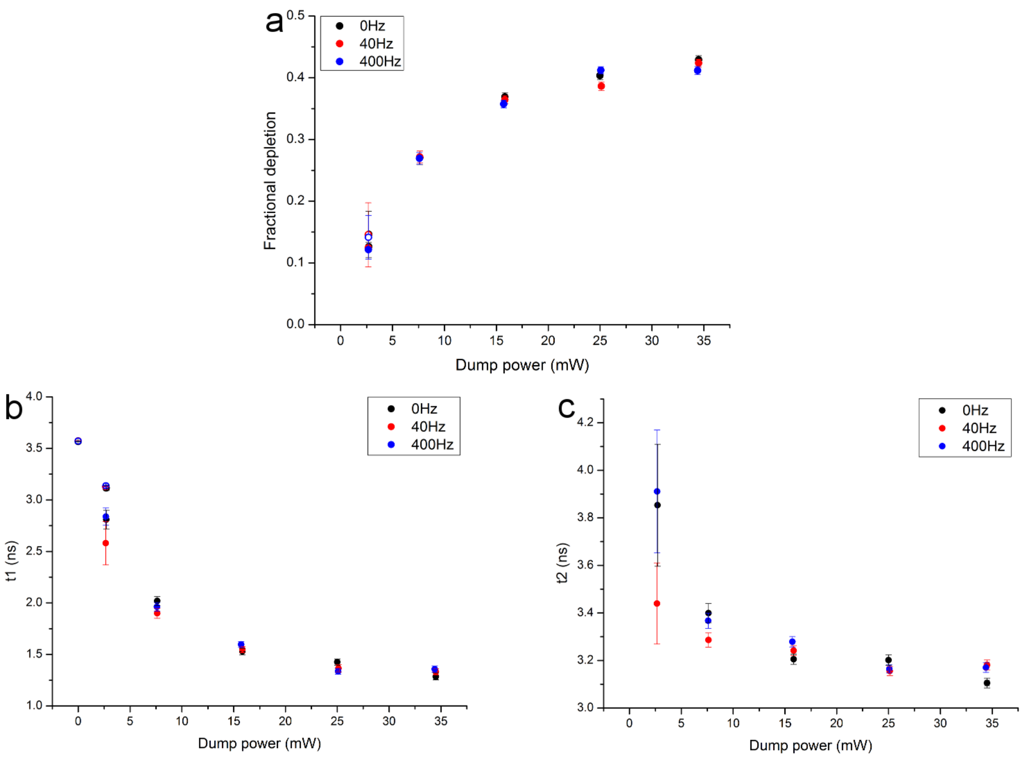

Figure 5.11: The effect of chopping the CW dump beam on depletion of fluorescein in water. 0Hz indicates measurements taken where dump beam was not chopped. Solid circles are data obtained from biexponential fitting, empty circles are data obtained from monoexponential fitting. a) Fractional depletion. b) Short lifetime component τ_1. c) Long lifetime component τ_2. Error bars are fitting errors for each measured intensity decay.

5.5.2 Results

To ascertain whether prolonged exposure of the sample to the CW dump beam was creating photophysical products insensitive to STED, the dump beam was chopped at two different frequencies: 40Hz, where the sample was exposed to the dump beam in 25ms bursts, and 400Hz, where the sample was exposed to the dump beam in 2.5ms bursts.

Figure 5.11 shows the fractional depletion curves and individual lifetime components of fluorescein in water measured at five different dump powers and chopped at 40Hz, 400Hz, and with no chopping. There did not appear to be any difference in the fractional depletion measured at different chopping frequencies (Fig. 5.11a), nor was there any noticeable difference in the measured biexponential lifetime components (Fig. 5.11b,c).

The experiment was repeated using a more viscous solvent, ethylene glycol, to ascertain whether chopping the dump beam affected depletion in a system where translational diffusion was slower. Figure 5.12 shows measurements of fractional depletion and lifetime components for different chopping frequencies. Although the

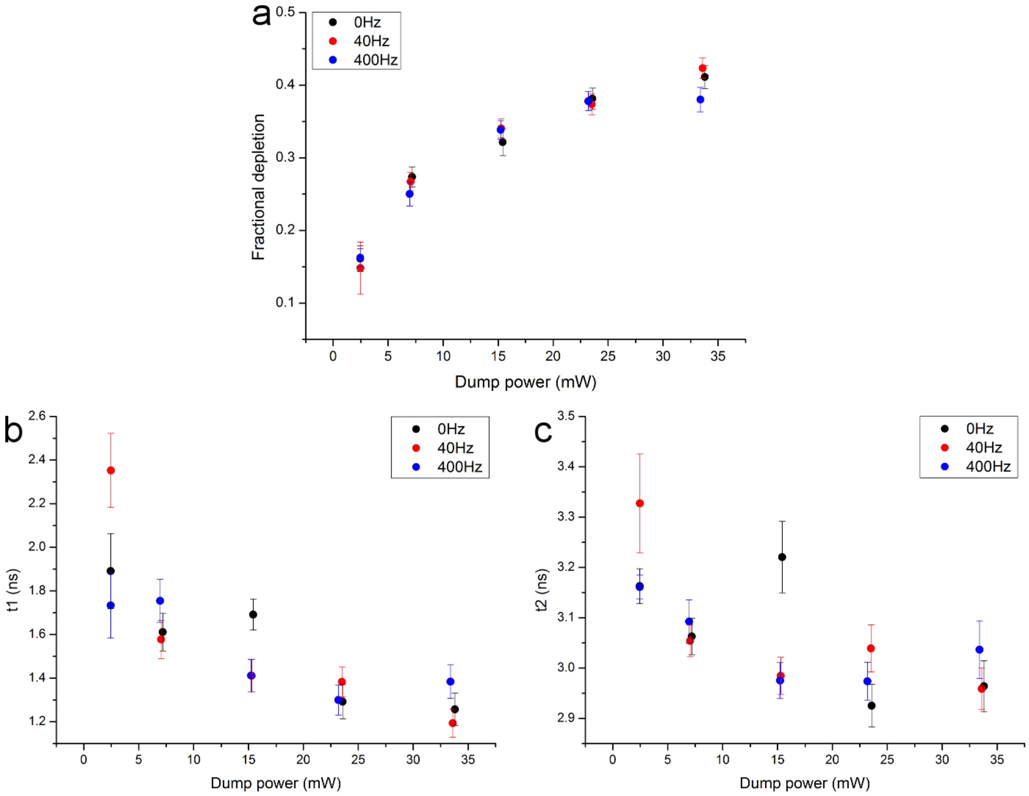

Figure 5.12: The effect of chopping the CW dump beam on depletion of fluorescein in ethylene glycol. 0Hz indicates measurements taken where dump beam was not chopped. a) Fractional depletion. b) Short lifetime component τ_1. c) Long lifetime component τ_2. Error bars are fitting errors for each measured intensity decay.

lifetime data displayed higher variation than the results for fluorescein in water, again there was no difference in the fractional depletion curves measured at different chopper frequencies, and the lifetime components for the different frequencies generally agreed with each other despite a small number of outliers.

5.5.3 Discussion

Whilst the results of varying dump exposure time suggest that the continual exposure of the sample to the dump beam is not the cause of low STED efficiency, more control over the duty cycle of the system is necessary to confirm this. In these experiments, the dump beam is still present for a large number of pump pulses: $\sim 50,000$ pump pulses at 400Hz chopping and $\sim 500,000$ pump pulses at 40Hz chopping. Even reducing the repetition rate to 250kHz would result in the dump chopped at 400Hz coinciding with ~ 750 pump pulses. An ideal experiment would have control over the exact number of pump pulses coinciding with the dump beam (Fig. 5.13), however we do not currently have the capability to modulate the dump intensity at the appropriate frequency for this. One potential method for performing this

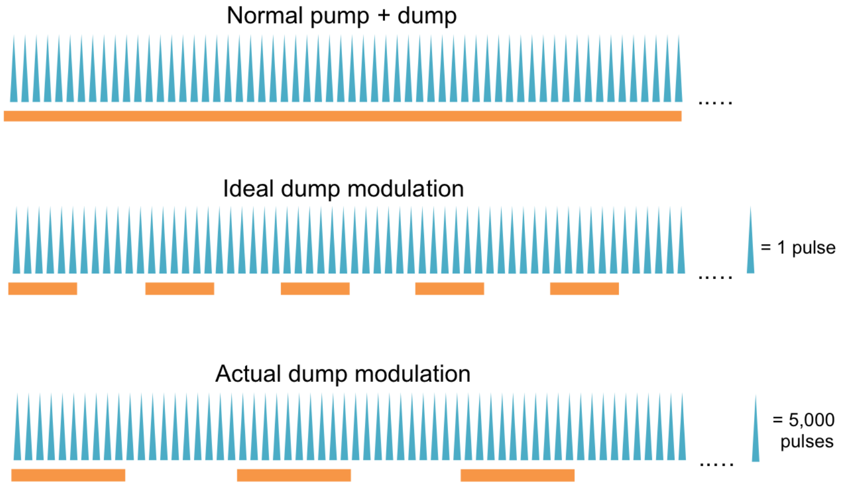

Figure 5.13: Schematic illustrating dump intensity modulation. Normal pump + dump shows pulsed pump (blue triangles) and unmodulated CW dump (orange rectangles) as used for all other CW STED experiments. Ideal dump modulation shows a case where the dump is modulated such that six pulses are dumped, then six are not dumped. Actual dump modulation illustrates the experiment as performed above, with each blue triangle now representing 5,000 pulses.

experiment would be to use a pulsed dump laser with very long (tens to hundreds of nanoseconds) pulses that would coincide with a small number of pump pulses at a time.

An alternative experiment which could be performed in the future would be to set up a pulsed STED experiment where the dump pulse is split such that half of the pulse arrives at the sample at the same time as the pump pulse as is usual, with the other half of the pulse arriving at the sample in the low pump intensity period between two pump pulses. This could yield information on the effect of the dump beam on the sample when it is not being pumped.

5.6 Investigations using fluorescence correlation spectroscopy

Fluorescence correlation spectroscopy (FCS) is a technique used for investigating molecular fluctuations, and information is obtained by fitting models to the autocorrelation of detected fluorescence from low concentration (typically nanomolar) solutions of fluorophores such that approximately one fluorophore is within the focal volume at any given time [143]. Autocorrelated fluorescence provides information on any process with a characteristic timescale in the microseconds to milliseconds range such as diffusion in and out of the focal volume ($\sim 10^{-5}$s for fluorescein in water, this thesis) and molecules entering and leaving the triplet state ($\sim 10^{-6}$s for fluorescein in water, this thesis). The autocorrelated fluorescence is calculated as a function of 'lag time' (time between two observations), and is then fitted to an appropriate model for the phenomenon being investigated.

Here FCS is used to investigate two phenomena: firstly whether the CW dump beam alters the volume from which fluorescence is detected, as measurement of this will help to quantify the results of the pinhole experiments in Section 5.2. Secondly the effect of the powers of the pump and dump beams on the triplet population of the sample, as the triplet state is a long-lived photophysical state which cannot itself fluoresce or undergo STED (Section 1.1.6).

5.6.1 Methods

Fluorescence correlation spectroscopy was performed with single photon pulsed pump and CW dump (where stated). The pump repetition rate in all experiments was 80MHz. For all experiments the same major dichroic was used as for previous single photon experiments, residual pump was filtered from the detection pathway, and a 30μm pinhole was used. For pump only measurements there was no further filtering, whereas when the dump beam was present an additional filter was present (FES550). Detection was not polarisation-resolved here, and instead of the cube polariser used in previous experiments a 50/50 beam splitter was used to split fluorescence into the two SPAD detectors. Measurement times were varied from 2-20 minutes to obtain sufficient photon counts for FCS fitting, depending on the beams present and their powers. A short section of a typical measurement is shown in Fig. 5.14a.

FCS model fitting was performed on a cross correlation of the signal from the two detectors, rather than an autocorrelation, to avoid the dead time of the detectors [144] and to remove the effect of detector afterpulsing. The cross correlation function for signal detected in two detectors is given by [145]

$$G_{ij}(\tau) = \frac{\langle \delta F_i(t) \delta F_j(t+\tau) \rangle}{\langle F_i(t) \rangle \langle F_j(t) \rangle} \tag{5.3}$$

where F_i and F_j are the fluorescence intensities detected in detectors i and j respectively, τ is the lag time and $\delta F_i(t) = F_i(t) - \langle F_i(t) \rangle$. The cross correlated fluorescence intensity was then fitted to a model describing free diffusion of a single fluorescent species as provided in the SymPhoTime analysis software:

$$G_{\text{diff}}(\tau) = \frac{1}{\langle N \rangle} \left(1 + \frac{\tau}{\tau_D}\right)^{-1} \left(1 + \frac{\tau}{\tau_D \kappa^2}\right)^{-\frac{1}{2}} \tag{5.4}$$

where $\langle N \rangle$ is the average number of molecules in the focal volume, τ_D is the diffusion time and $\kappa = z_0/\omega_0$ where z_0 is the axial FWHM of the focal spot and ω_0 is the lateral FWHM. For fitting of pump only measurements ω_0 was set to be 0.25μm, as this was the typical FWHM measured for sub-diffraction limit sized fluorescent beads (Chapter 3). A typical free diffusion model fit is shown in Fig. 5.14b. From

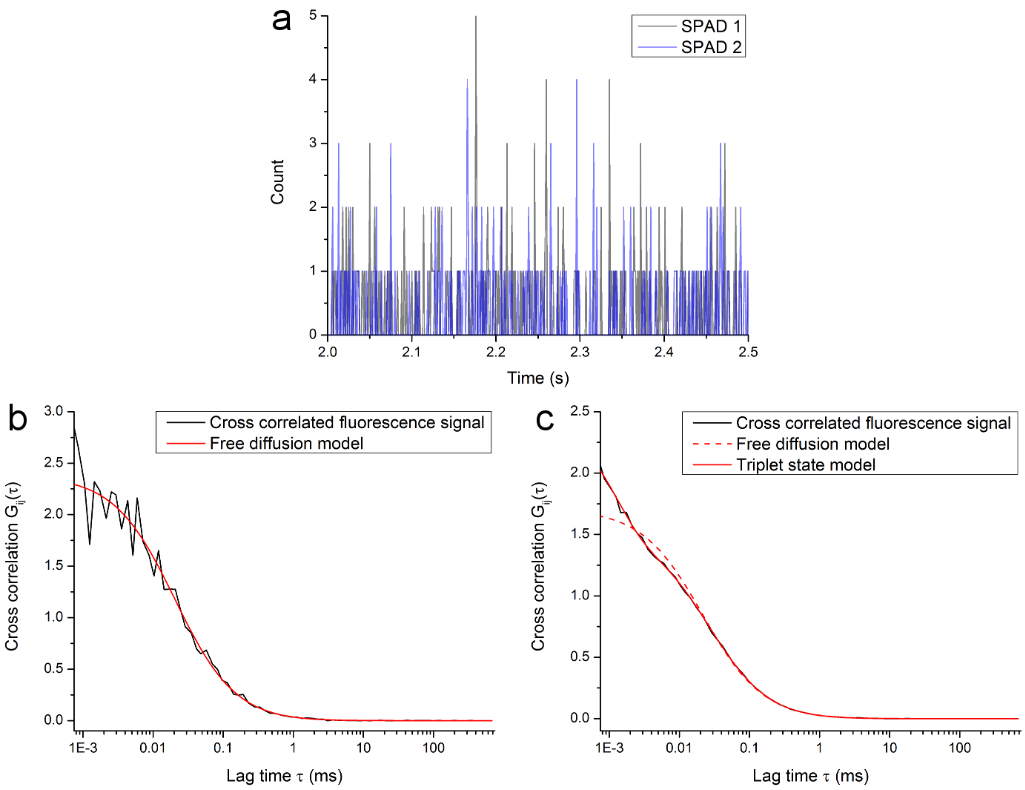

Figure 5.14: Typical data collected and analysed in FCS measurements. a) Portion of raw data used for FCS of fluorescein in water with two detectors. b) Cross correlated fluorescence (black) and fitted free diffusion model (red) for a measurement with negligible triplet formation. c) Cross correlated fluorescence (black) and fitted triplet state model (red) for a measurement with significant triplet formation. An attempt to fit the free diffusion model to the data is also shown (dashed red line).

this model the following parameters can be derived:

- Effective focal volume: $V_{\text{eff}} = \pi^{\frac{3}{2}} \omega_0^2 z_0$
- Average concentration: $\langle C \rangle = \langle N \rangle / V_{\text{eff}}$
- Diffusion coefficient: $D = \omega_0^2 / 4\tau_D$

When this free diffusion model did not fit the data (Fig. 5.14c, dashed red line), a model with a correction for the presence of a triplet state was fitted:

$$G_{\text{trip}}(\tau) = \left[1 - T + T \exp\left(-\frac{\tau}{\tau_T}\right)\right] \frac{G_{\text{diff}}(\tau)}{1 - T} \tag{5.5}$$

where T is the fraction of molecules in the triplet state, referred to as the triplet fraction, and τ_T is the triplet state lifetime. An example of this model fitting is shown in Fig. 5.14c.

Errors in fitting the models were generated using bootstrap error analysis provided in the software. Bootstrap analysis is a re-sampling technique where the data set of N values is re-fitted to a data set of N values consisting of a proportion of the original data set with some values duplicated. Many of these re-sampled data sets were generated (here 10,000) and populations of fitted parameters were then obtained from which errors could be determined. Here the errors were taken from the 68% confidence interval. Errors quoted on average values are combined errors from bootstrap analysis of each individual value and standard deviation of the population of values, as in Section 2.6.6.

The sample used for FCS was 1×10^{-9}M 2’7’-dichlorofluorescein in water. Quoted pump powers were measured prior to entry into the fibre coupling unit.

5.6.2 Results

To evaluate the effect of CW STED on the size of the focal volume, FCS was performed with several different dump powers. The pump power was $50.64 \pm 0.01\mu$W for all dump powers tested, and the average values of FCS parameters for six undumped measurements are shown in Table 5.1 (all fitting using triplet state model $G_{\text{trip}}(\tau)$). The measured value of the concentration was in good agreement with the concentration of the fluorescein solution used and the triplet lifetime was also in agreement with the value of 10^{-6}s quoted in the literature [146]. The diffusion coefficient measured here was larger than the published value of 2’7’-dichlorofluorescein in water, $425 \pm 7\mu\text{m}^2/\text{s}$ [147].

For FCS fitting of undumped data, ω_0 was fixed at 0.25μm. However, as FCS was being used to assess the impact of CW STED on focal volume, this parameter could not be fixed in measurements taken with the dump beam. Therefore the diffusion coefficient D was instead fixed in FCS fitting of the dumped measurements to match

Fitted parameter	Value
Axial FWHM z_0	1.8 ± 0.3 μm
Focal volume V_{eff}	0.6 ± 0.2 fl
Diffusion time τ_D	20 ± 10 μs
Diffusion coefficient D	700 ± 200 μm^2/s
Concentration $\langle C \rangle$	1.9 ± 0.8 nM
Length ratio of focus κ	7 ± 1
Triplet fraction T	0.20 ± 0.07
Triplet lifetime τ_T	1.1 ± 0.7 μs

Table 5.1: FCS parameters from fits to undumped measurements at 50μW pump power for comparison with dumped measurements.

that obtained in the undumped measurements, as STED should not alter the value of the diffusion coefficient.

The relationship between dump power and effective focal volume V_{eff} is shown in Fig. 5.15. Despite the large fitting errors (faint error bars, Fig. 5.15), values obtained for V_{eff} were consistent for similar dump powers, as indicated by their standard deviation (bold error bars, Fig. 5.15). An increase in V_{eff} was seen with increasing dump power (Spearman correlation = 0.85, P< 0.0001) with the maximum focal volumes measured at ∼24.5mW dump ranging from $3 - 4$fl, representative of a $\sim 5 - 7$-fold increase in volume compared with the undumped measurements.

FCS was also used to quantify the effect of pump and dump powers on the triplet state population. Firstly, the effect of pump power was investigated, and undumped measurements were made at a range of pump powers up to the maximum power output of the pump laser. The relationship between pump power and the proportion of fluorophores in triplet state (the triplet fraction T) is shown in Fig. 5.16a. Below 21μW the data fitted well to the free diffusion model (ω_0 fixed at 0.25μm) indicating that the triplet fraction at these powers was negligible, and for powers $\geq$ 21μW T increased approximately linearly with power up to 102μW. The rate at which T increased with pump power then began to slow, with little change in T at the four highest pump powers tested, where the average triplet fraction was 0.72±0.02. There was little variation in the values of the other fitted parameters with pump power, and the average values of these are shown in Table 5.2.

The parameters in Table 5.2 were all in agreement with those measured at a single pump power (50μW) in Table 5.1, with the average value of the diffusion coefficient agreeing within experimental error to the published value for this second data set.

The effect of dump power on the triplet fraction was also investigated: values for the triplet fraction were obtained from the fitting to the dumped data (same data set as used in Fig. 5.15, pump power = 50μW), and these are shown in Fig. 5.16b. The measured triplet fractions varied for individual dump powers, and here the standard deviations of repeated measurements reflected the fitting errors. There

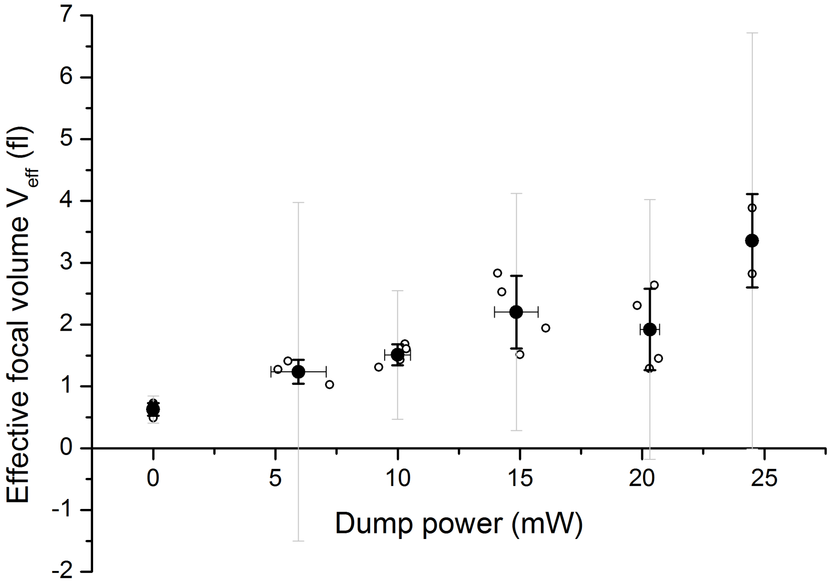

Figure 5.15: Effect of CW dump power on focal volume. Empty circles are individual measurements, solid points are average values for each cluster of powers tested. Bold error bars show the standard deviations of the average values for each cluster of dump powers, faint error bars show the combination of the standard deviation with the fitting error on each point. Fitting errors are not shown for individual points.

Fitted parameter	Value
Axial FWHM z_0	1.6 ± 0.4 µm
Focal volume V_{eff}	0.6 ± 0.1 fl
Diffusion time τ_D	28 ± 9 µs
Diffusion coefficient D	600 ± 200 µm^2/s
Concentration $\langle C \rangle$	1.2 ± 0.6 nM
Length ratio of focus κ	7 ± 2
Triplet lifetime τ_T	1.2 ± 0.7 µs

Table 5.2: FCS parameters from fits to undumped measurements of fluorescein in water at a range of pump powers.

was no significant correlation between dump power and triplet fraction (P=0.10, Spearman's correlation test), and the average triplet fraction for all dump powers other than 24mW agreed with the undumped measurements within both descriptions of error.

5.6.3 Discussion

The increase of the effective focal volume V_{eff} with dump power provides further evidence that CW STED is not just confined to the focal plane of the pump and dump beams. At dump powers of 20-25mW, where the F_d curve of fluorescein in water has been seen to plateau (Section 4.7.2), FCS measurements have confirmed

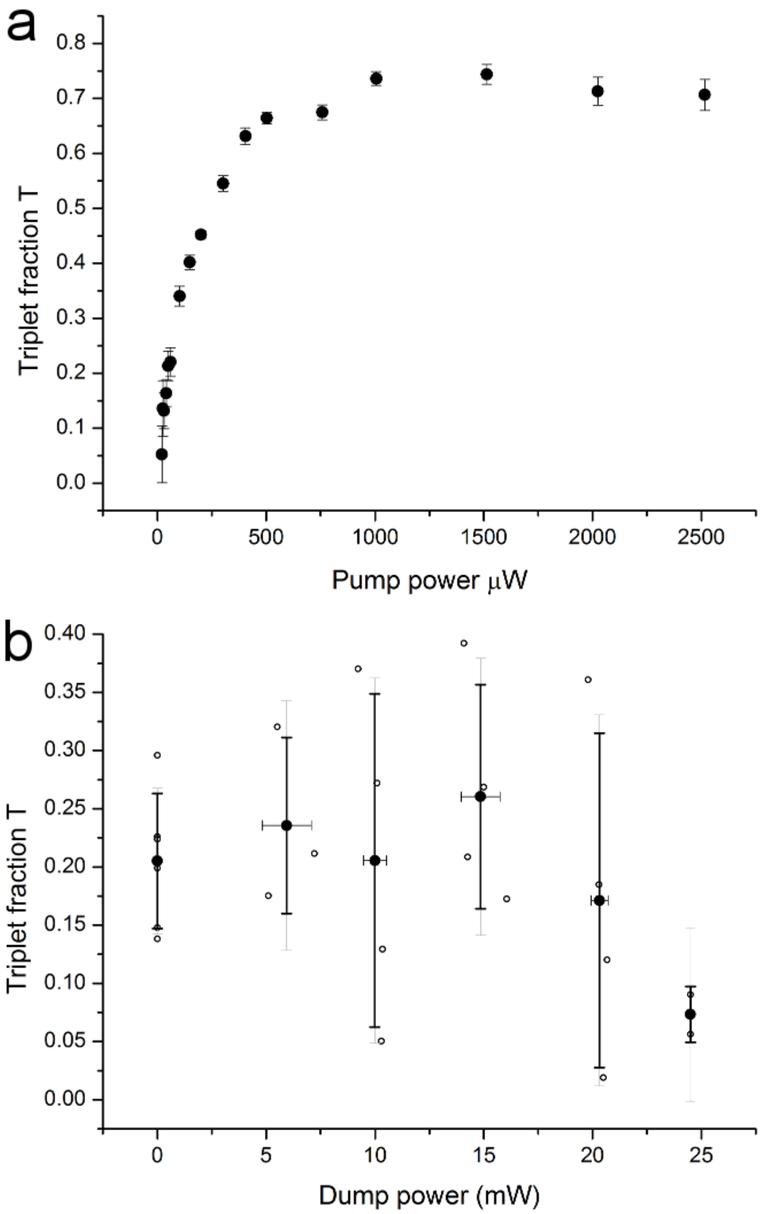

Figure 5.16: Effect of laser power on triplet fraction. a) Triplet fraction measured at a variety of pump powers with no dump. Error bars are fitting errors associated with each individual point. b) Triplet fraction measured at several dump powers with 50μW pump. Bold error bars show the standard deviations of the average values for each cluster of dump powers, faint error bars show the combination of the standard deviation with the fitting error on each point. Fitting errors are not shown for individual points.

that fluorescence detected is from a volume approximately 5 times larger than that of undumped measurements. As discussed in Section 5.2, this larger focal volume will contain a large proportion of molecules which have been depleted less efficiently than molecules at the focus itself. These results, taken together with the results obtained using different sized pinholes, indicate that including contributions of fluorescence from above and below the focal plane in the mathematical modelling of CW STED is necessary. This is undertaken later in this chapter (Section 5.8.1).

That the triplet fraction only became measurable at pump powers above 21μW confirmed that the pump powers used in all other experiments in this thesis thus far are not high enough to be producing a substantial proportion of triplets. The dump beam did not significantly alter the triplet fraction produced with 50μW pump, indicating that the pump power has a greater effect on triplet production than dump power. However, the data obtained for the various dump powers were also very noisy.

A flaw in FCS fitting is the large number of parameters used in the models, and this was particularly problematic for the data obtained using the dump beam, where additional noise was contributed to the already sensitive measurements. Fixing the value of the diffusion coefficient when fitting models to the data with the dump beam was performed as this parameter was assumed to be the least sensitive to STED; however if the presence of the dump beam was changing the diffusion coefficient, for example through sample heating, then this may have introduced some systematic error. The models used here also assume a Gaussian point spread function in all directions, and this is not the case for the effective point spread function when both beams are present which may also be creating systematic errors in the calculation of parameters [62].

5.7 Comparing methods of quantifying STED efficiency

One major difference between the CW STED data presented in this thesis and the pulsed STED and super resolution STED microscopy data presented elsewhere is the method of quantifying STED efficiency (fractional depletion). Whilst elsewhere, including previous pulsed STED work, the STED efficiency is quantified by measurement of fluorescence suppression as deduced from intensity measurements (e.g. pulsed STED measurements in Section 4.8.2), for all CW STED experiments here it has been calculated from lifetime measurements. Therefore to see whether there is an inherent difference between intensity- and lifetime-based measurements of STED efficiency, CW STED experiments were performed where both methods of calculating fractional depletion could be performed and compared. This was performed not just at a range of dump powers, but also at a range of pump powers to investigate the effect of an increased triplet fraction on STED efficiency.

5.7.1 Methods

The experimental set-up for these experiments was as for previous experiments with single photon pump (20MHz repetition rate) and 594nm CW dump. Both pump and dump beams were filtered in the detection pathway following the major dichroic, and the 50µm pinhole was used in all cases. The filtered fluorescence was split into the two SPAD detectors using a cube polariser for polarisation-resolved detection. In the experiments where pump power was investigated, a neutral density wheel was included in the detection pathway after the pinhole, and this was adjusted such that the count rate remained between 100,000 and 200,000 counts per second at each pump power. The G-factor was re-measured after each adjustment of the neutral density wheel to account for any small displacement of the detected fluorescence. Pump powers were measured before the fibre coupling unit.

The following experimental sequence was used to obtain data from which lifetime and intensity measurements could be extracted whose measurement conditions were as faithful to one another as possible. For each dump power, a 30 second recording was taken with both beams together (as for previous experiments), followed immediately by a 30 second recording with sequential blocking and unblocking of the beams such that the sample was exposed to a cycle of: pump only, dump only and then pump + dump together several times (Fig. 5.17). 30 second pump only recordings were taken every four dump powers to monitor undumped lifetime.

Exponential functions were fitted to the intensity decays ($I(t) = I_V(t) + 2I_H(t)$) obtained for the 30 second pump + dump recordings to extract lifetimes as before for calculation of 'lifetime' F_d (here referred to as F_d^{life}). For the recordings with sequential beam blocking the MCS traces produced by the microscope control software (SymPhoTime), which show absolute detected intensity over the recording period, were used to extract fluorescence intensities for the sample subject to pump only, dump only and pump + dump in each detector (Fig. 5.17). These MCS traces were analysed in MATLAB as follows: time periods corresponding to a specific beam condition (e.g. pump only) were selected, and the mean and standard deviation of fluorescence intensity over these time periods were calculated for each detector. The total average intensity for each beam condition was thus calculated as $\overline{I} = \frac{1}{G}\overline{I_V} + 2\overline{I_H}$ where the same G-factor was used as for lifetime measurements, and error on $\overline{I}$ was calculated by appropriately combining the standard deviations. This process was repeated for each beam condition, and hence 'intensity' F_d was calculated for each MCS trace (corresponding to a given dump power) as

$$F_d^{\text{int}} = \frac{\overline{I_P} - (\overline{I_{PD}} - \overline{I_D})}{\overline{I_P}} \tag{5.6}$$

where $\overline{I_P}$ is the total average intensity for pump only, $\overline{I_{PD}}$ is the pump + dump intensity and $\overline{I_D}$ is the dump only intensity. Error on F_d^{int} was then propagated accordingly.

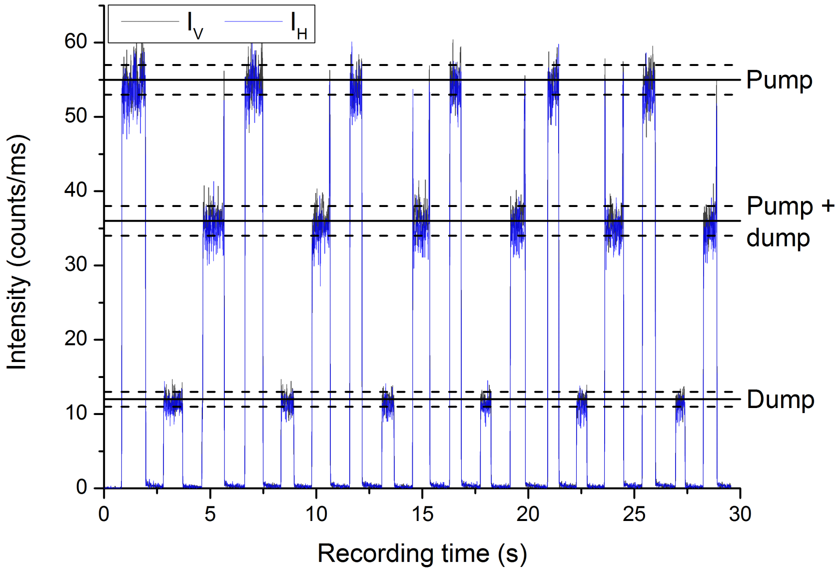

Figure 5.17: Example of an MCS trace used for calculation of intensity F_d. Grey lines are V-polarised intensity (corrected for G-factor) and blue lines are H-polarised intensity. Solid black lines indicate mean values of I_V for this trace and dashed black lines indicate the standard deviation ΔI_V. Mean and standard deviation not shown for I_H, but were calculated similarly.

The samples used were 1×10^{-5}M 2'7'-dichlorofluorescein in water, 1×10^{-5}M 2'7'-dichlorofluorescein in ethylene glycol and 1×10^{-5}M coumarin 6 in ethylene glycol.

5.7.2 Results

Firstly, the quantification of F_d using the lifetime and intensity based measurements was compared over a range of dump powers (Fig. 5.18). CW STED of fluorescein was assessed in both water (Fig. 5.18a) and ethylene glycol (Fig. 5.18b) at a range of different dump powers, but also at two different pump powers, $< 1\mu$W (too small to accurately measure) and $\sim 12\mu$W ($11.98 \pm 0.01\mu$W in water and $12.05 \pm 0.05\mu$W in ethylene glycol). The results from the FCS experiments in Section 5.6.2 indicate that the triplet fraction at 12μW pump should still be negligible.

For fluorescein in water (Fig. 5.18a), the F_d^{int} series did not vary between the two pump powers tested, whereas the F_d^{life} series measured with 12μW pump had slightly lower values than the F_d^{life} series measured with 1μW pump power (maximum F_d^{life} at $< 1\mu\text{W} = 0.44 \pm 0.01$ compared to 0.389 ± 0.006 at 12μW). As has been repeatedly observed, the F_d^{life} curves began to plateau at dump powers > 15mW. The F_d^{int} curves were in agreement with the F_d^{life} curves for dump powers < 11mW, whereafter the F_d^{int} and F_d^{life} curves diverged. Notably, although the rate of increase of F_d^{int} with dump power still slowed for higher dump powers, the curves did not plateau as dramatically as the F_d^{life} curves. The highest F_d^{int} was measured to be

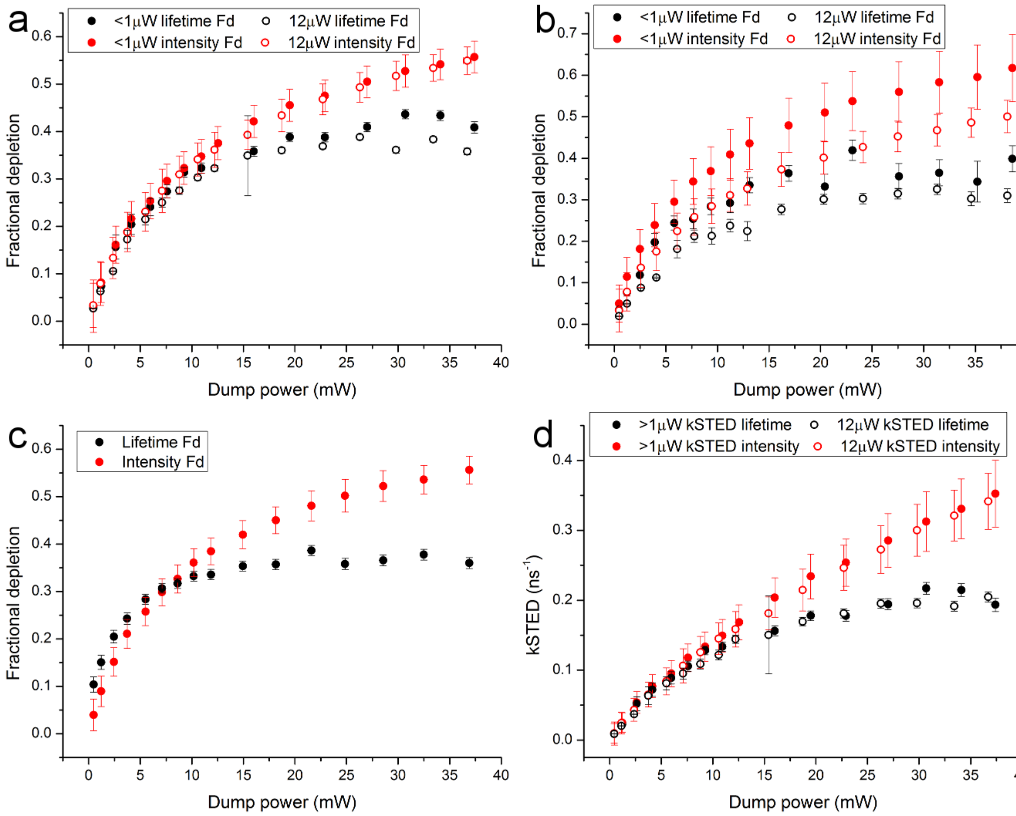

Figure 5.18: Comparison of F_d values calculated from intensity and lifetime data for a range of dump powers. In all plots black points are calculated from fluorescence lifetime histograms (F_d^{life}) and red points are calculated from absolute intensity values (F_d^{int}). Solid points indicate pump power = 1µW, empty circles indicate pump power = 12µW. a) Fluorescein in water at two different pump powers. b) Fluorescein in ethylene glycol at two different pump powers. c) Coumarin 6 in ethylene glycol, pump power = 6.7µW. d) k_{STED} calculated for fluorescein in water.

0.56 ± 0.03 (at 38mW) compared to the highest F_d^{life} of 0.44 ± 0.01 (at 31mW with < 1µW pump).

For fluorescein in ethylene glycol (Fig. 5.18b), fractional depletion varied with pump power for both the F_d^{int} and F_d^{life} curves; for both quantification methods F_d values were larger with < 1µW pump than with 12µW pump. As seen for fluorescein in water, the F_d^{int} curves had larger values that the F_d^{life} curves, and again displayed less dramatic plateauing. Here F_d^{int} and F_d^{life} agreed within experimental error up to $\sim$ 7mW for both pump powers before F_d^{int} reached a maximum value of 0.62 ± 0.08 (dump power $\sim$ 39mW), with F_d^{life} only reaching 0.40 ± 0.03 at the same dump power (both < 1µW pump power).

To ascertain whether this discrepancy between F_d^{int} and F_d^{life} was a unique attribute of fluorescein, the experiment was repeated for coumarin 6 in ethylene glycol at a single pump power of 6.694 ± 0.004µW (Fig. 5.18c). Coumarin 6 behaved similarly to fluorescein, where F_d^{int} continued to increase after F_d^{life} had reached a plateau.

As seen in all previous experiments, fluorescein in water exhibited a biexponential decay in the presence of CW dump which, as discussed in Chapter 4, was unexpected due to fast rotational diffusion. k_{STED} was calculated for the lifetime and intensity data, where for the lifetime data an ‘average’ k_{STED} was calculated for the average dumped fluorescence lifetime at each dump power:

$$k_{\mathrm{STED}} = \frac{1}{\tau_d} - \frac{1}{\tau_f}, \tag{5.7}$$

where τ_d = average dumped fluorescence lifetime (Eq. 4.16). A different approach was used for calculating k_{STED} from the lifetime data: as fractional depletion can be described in terms of the ratio between the rate of fluorescence with and without CW STED by

$$1 - F_d = \frac{k_f}{k_f + k_{\mathrm{STED}}}, \tag{5.8}$$

where $k_f = 1/\tau_f$, k_{STED} can be calculated as

$$k_{\mathrm{STED}} = \frac{1}{\tau_f}\left(\frac{1}{1 - F_d} - 1\right) \tag{5.9}$$

from the F_d^{int} values and undumped lifetime τ_f as determined from the regularly acquired undumped measurements. For the intensity data it should be noted that the nomenclature k_{STED} will not be entirely accurate as this rate will include fluorescence loss mechanisms such as photobleaching which cannot be separated from STED in the intensity data.

The calculated values of ‘average’ k_{STED} for the intensity and lifetime data for fluorescein in water are shown in Fig. 5.18d (same data set as used in Fig. 5.18a). As seen previously, the lifetime k_{STED} plot becomes highly sublinear at high dump powers. The k_{STED} values from the intensity data agree with the lifetime k_{STED} values at dump powers < 13mW, where the relationship between k_{STED} and dump power is approximately linear for both quantification methods, and then this relationship also becomes sublinear (albeit to a lesser extent than the lifetime data).

As pump power had an appreciable effect on the amount of depletion obtained for fluorescein in ethylene glycol, F_d^{int} and F_d^{life} were measured for fluorescein in both water and ethylene glycol for a large range of pump powers (Fig. 5.18). For both samples pump powers ranging from 1 - 350µW were applied in conjunction with the highest dump power available (average values over experiments: 35.2 ± 0.3mW in water, 35.2 ± 0.2mW in ethylene glycol) and the highest dump power at which the F_d^{int} and F_d^{life} values agreed well as judged from the dump series data (average values over experiments: 9.79 ± 0.07mW in water, 6.2 ± 0.2mW in ethylene glycol).

The results of pump power variation on STED efficiency for fluorescein in water

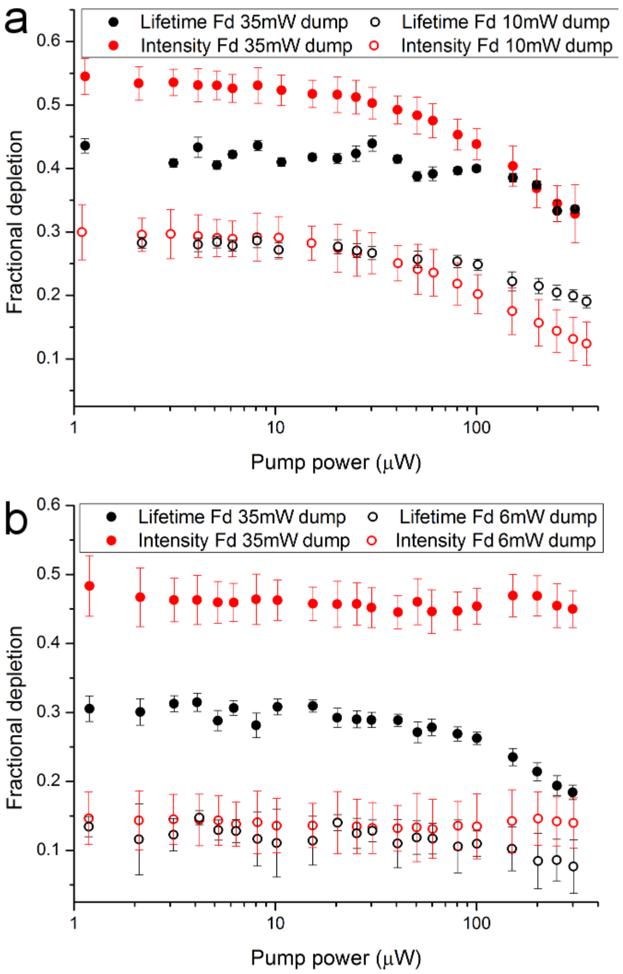

Figure 5.19: Comparison of F_d calculated from intensity and lifetime data for a range of pump powers. In all plots black points are calculated from fluorescence lifetime histograms and red points are calculated from absolute intensity values. Solid points were measured with high dump power and empty points were measured at a lower dump power. a) Fluorescein in water. b) Fluorescein in ethylene glycol.

are shown in Fig. 5.19a. The F_d^{life} values (black points) remained constant at both dump powers for pump powers up to 30μW (average F_d^{life} values: 0.277 ± 0.007 at 10mW, 0.42 ± 0.01 at 35mW) before decreasing at higher pump powers, with the smallest F_d^{life} values measured to be 0.19 ± 0.01 with 10mW dump and 0.33 ± 0.02 at 35mW dump at the highest pump power. This translated into a percentage decrease in F_d^{life} of $31 \pm 4\%$ for 10mW dump compared to $21 \pm 5\%$ for 35mW dump. The F_d^{int} values (red points) behaved similarly, although for both dump powers F_d^{int} only remained constant up to 10μW before decreasing at higher pump powers. The average values of F_d^{int} for pump powers up to 10μW were 0.29 ± 0.01 (10mW dump) and 0.53 ± 0.01 (35mW dump), and these decreased to minimum values of 0.12 ± 0.03 and 0.33 ± 0.05 respectively; the corresponding percentage decreases in F_d^{int} were $60 \pm 10\%$ at 10mW dump and $40 \pm 10\%$ at 35mW dump. These results indicate that for fluorescein in water, increasing pump power has a greater impact on STED efficiency as measured by F_d^{int} than it does for F_d^{life}, and for both measures this effect was greater at the lower of the two dump powers tested.

Figure 5.19b shows the effect of pump power on F_d for fluorescein in ethylene glycol. The F_d^{life} values measured in ethylene glycol behaved similarly to the values measured in water over the range of pump powers, with little change in F_d^{life} for pump powers up to 30μW for both dump powers, followed by a decrease in F_d^{life} at higher pump powers. Here the F_d^{life} averaged over powers up to 30μW was measured as 0.13 ± 0.01 for 6mW dump and 0.30 ± 0.01 for 35mW dump, and the lowest measured values of F_d^{life} were 0.08 ± 0.04 and 0.18 ± 0.01 respectively at 300μW pump. The percentage changes in F_d^{life} for the two dump powers this time agreed within error (6mW: $40 \pm 30\%$, 35mW: $40 \pm 4\%$). The F_d^{int} values, however, did not show the previously observed decrease as seen for F_d^{int} in water and F_d^{life} in both solvents. In ethylene glycol, the measured F_d^{int} values remained constant (within error) across all pump powers for each dump power tested, with a mean value of 0.14 ± 0.01 at 6mW dump and 0.46 ± 0.01 at 35mW dump.

5.7.3 Discussion

The results presented in this section show that there is a clear difference between STED efficiency quantified using lifetime measurements and STED efficiency quantified using intensity measurements. At low dump power (typically < 10mW), the lifetime and intensity measurements generated similar values of F_d. This, combined with the linearity of the F_d plots and k_{STED} plots for fluorescein in water at low dump powers, suggests that our understanding of CW STED is correct in this regime. However at high dump powers, where F_d^{life} values begin to plateau, F_d^{int} values continue to rise, although recalculation of the rate of removal of excited state population (k_{STED}) using intensity data showed that this was still not linear with dump power. It has been stated many times (e.g. Section 4.7.2, Section 5.1) that the non-linearity of k_{STED} in a fast rotation regime should not arise from orientational

	Low dump power	High dump power
Low pump power	$F_d^{\text{int}} = F_d^{\text{life}}$ in both water and ethylene glycol	$F_d^{\text{int}} \gg F_d^{\text{life}}$ in both water and ethylene glycol
High pump power	$F_d^{\text{int}} < F_d^{\text{life}}$ in water, $F_d^{\text{int}} \approx F_d^{\text{life}}$ in ethylene glycol	$F_d^{\text{int}} \approx F_d^{\text{life}}$ in water, $F_d^{\text{int}} \gg F_d^{\text{life}}$ in ethylene glycol

Table 5.3: Summary of CW STED efficiency in four different pump and dump power regimes for fluorescein in water and ethylene glycol. 'Low' pump power corresponds to $< 30\mu$W, high and low dump powers are defined as in the text of Section 5.7.2.

effects. The data presented here also indicates that this non-linearity is unlikely to result from photobleaching, which depends strongly on pump power, as identical k_{STED} series were obtained from the 'intensity' data at two different pump powers (Fig. 5.18d). Thus, these results suggest that there is a dump-dependent mechanism which prevents further lifetime shortening at high dump powers but does not impact upon intensity suppression to the same extent. Furthermore, this mechanism is also non-linear with dump power.

The interplay between pump power and dump power was also examined, and the results obtained are briefly summarised in Table 5.3 for four different regimes. The relationship between pump power and dump power appears to be both complex and solvent dependent. For the results for fluorescein in water, the sensitivity of F_d^{int} (and to a lesser extent F_d^{life}) to increasing pump powers could indicate involvement of the triplet state. This is in contrast to the F_d^{life} values which to be appear largely independent of the pump power (and thus assumed triplet fraction) apart from at the highest pump powers investigated. The F_d^{int} values obtained for fluorescein in ethylene glycol were completely insensitive to pump power, implying that fluorophore environment is important in determining the joint effect of the pump and dump beams.

5.8 Proposals for a mechanism underlying reduced STED efficiency

The combined results of this chapter and Chapter 4 show that our current modelling of CW STED dynamics does not correctly describe the experimentally observed data. In this section, modifications to the model described in Chapter 4 are suggested and potential physical processes previously unaccounted for are discussed.

5.8.1 Spatial averaging

As the FCS experiments in Section 5.6.2 showed that the effective focal volume increases with CW dump power, combined with the pinhole size experiments in Section 5.2.2 where out-of-focus fluorescence decreased the measured STED efficiency, a modification was made to the model to account for the spatial variations in depletion. The model used in Chapter 4 assumed that both excitation and depletion occurred at the focal plane of the sample, with all molecules experiencing the same pump field and dump field regardless of location (but not orientation). The updated model presented below, which was formulated by Dr Richard Marsh and executed in Mathematica, takes into account both the spatial variations within the focal plane (as exploited in Chapters 2 and 3 for LIR-SR) and contributions from out-of-focus fluorescence.

In this model, the simulated fluorescence intensity decay depends on orientation as before, but here also depends on the radial distance r from the centre of the focal plane, where the centre of the beam is at $r = 0$, and the axial distance z from the focal plane, where the focal plane is at $z = 0$. As in Section 2.5 the shape of the focus is assumed to be Gaussian in the lateral direction and Lorentzian in the axial direction. The fixed parameters in the model are wavelength λ and the diameter at the beam waist ω_0; the units of r and z are expressed in terms of the dimensionless quantity ω_0/λ. The probability of exciting a molecule at a given orientation is still given by

$$P_u(\theta, \phi) = \frac{1}{4\pi}\left(1 + \frac{2}{\sqrt{5}}\frac{Y_{20}(\theta, \phi)}{Y_{00}(\theta, \phi)}\right), \tag{5.10}$$

and again it is assumed that the system is cylindrically symmetric and that the absorption and emission dipole moments of the fluorophore are parallel. The spatial profile of detected fluorescence in the absence of depletion is given by

$$N_u(r, z) = \frac{1}{1 + kz^2}\exp\left(-\frac{r^2}{2\omega_0^2}\right) \tag{5.11}$$

where the parameter k describes the ratio of the Rayleigh range (z resolution) to the beam waist ω_0 as

$$k = \left(\frac{\lambda}{\pi\omega_0^2}\right)^2. \tag{5.12}$$

The diameter of the beam at a given axial position z is given by

$$\omega(z) = \omega_0\sqrt{1 + kz^2}, \tag{5.13}$$

which can then be used to describe the spatial profile of the dump field as

$$N_d(r, z) = \sqrt{\frac{2\pi\omega_0^2}{\pi^2\omega_0^4 + \pi^2\lambda^2}}\exp\left(-\frac{r^2}{2\omega(z)^2}\right). \tag{5.14}$$

It should be noted that in Eq. 5.14 the intensity distribution within each focal ‘slice’ (i.e. for each value of z) is normalised.

The resulting probability of depletion is thus given by the product of the combined angular and spatial probability of excitation $P_u(\theta, \phi)N_u(r, z)$ with the expo-

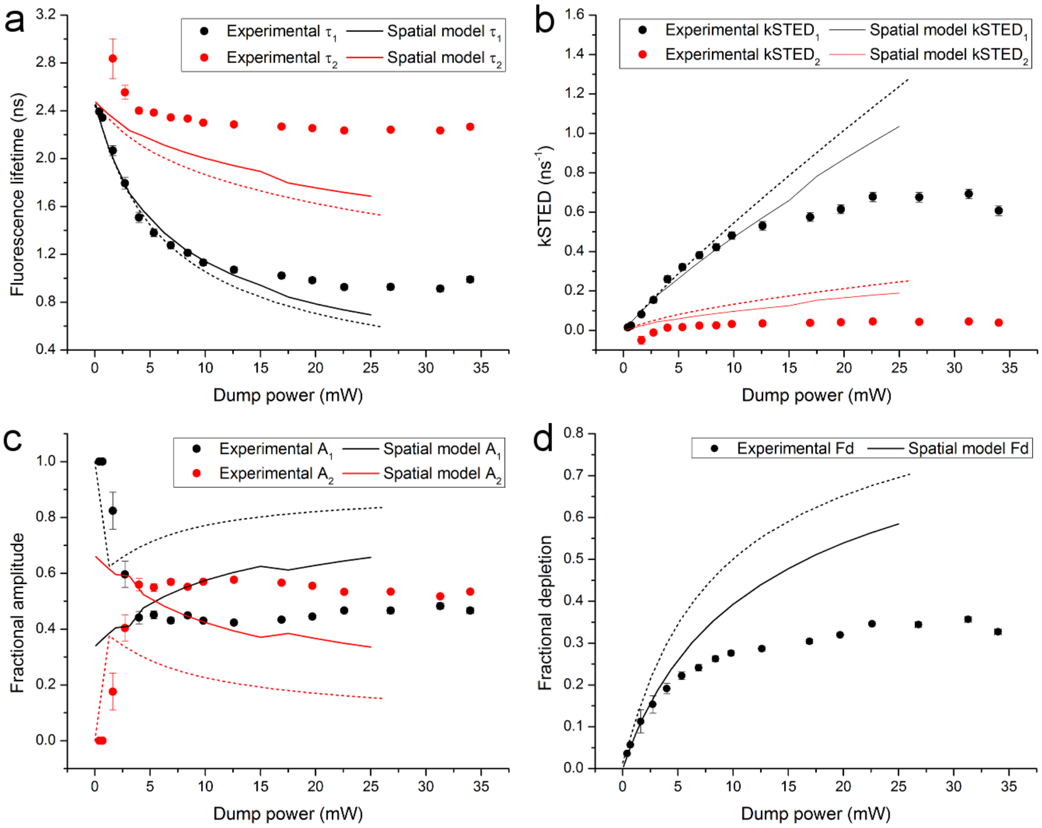

Figure 5.20: Revised model of CW STED with no rotation and spatial averaging based on results for coumarin 6 in glycerol. Experimental data points are those obtained in Chapter 4 with the model simulations used previously depicted as dashed lines. Solid lines represent results of model including spatial averaging effects. a) Lifetime components. b) STED rates. c) Fractional amplitudes. d) Fractional depletion.

nential decay of the excited state population in the presence of the dump beam, which also has angular and spatial dependence, as

$$P_d(\theta,\phi,r,z,t) = P_u(\theta,\phi)N_u(r,z)\exp\left(-(k_f + S'\cos^2\theta N_d(r,z))t\right). \qquad (5.15)$$

The fluorescence intensity decay of the population can then calculated by numerically solving

$$I_d(t) \propto \int_{z=-25}^{z=25}\int_{\psi=0}^{\psi=2\pi}\int_{r=0}^{r=5}\int_{\phi=0}^{\phi=2\pi}\int_{\theta=0}^{\theta=\pi} P_d(\theta,\phi,r,z,t)\sin\theta \mathrm{d}\theta r \mathrm{d}r \mathrm{d}\psi \mathrm{d}\phi \mathrm{d}z \qquad (5.16)$$

over an appropriate time range for several values of S' as discussed previously. The limits of integration for r and z were determined by incrementally reducing the range over which integration was performed from larger limits until further reductions in these limits significantly altered the results. This was done to reduce computation time.

Parameters extracted from fitting the intensity decays generated by the spatial averaging model are plotted in Fig. 5.20 alongside the experimental data for coumarin 6 in glycerol and parameters derived using the previous model where spatial variations were neglected. The spatial averaging model does indeed appear to be an improvement on the orientation-only model, with τ_1, k_{STED1} and F_d agreeing with the experimental data for a slightly larger range of dump powers than seen previously. However, the longer lifetime component and corresponding STED rate (τ_2 and k_{STED2}) still do not quantitatively agree with the spatial averaging model, and whilst the magnitudes of the fractional amplitudes generated with the spatial averaging model were similar to the values obtained experimentally, the two amplitudes appeared again to be the 'wrong way round', with the spatial model A_1 values similar to the experimental A_2 values and vice versa.

The inclusion of spatial averaging in the model of CW STED dynamics in the limit of no rotation had the expected effect of agreeing with the previous model at low dump powers (where our understanding of CW STED already appears to be correct) and deviating from the previous model at higher dump powers, where we now know there to be a progressive error arising from the increasing focal volume. However the spatial averaging model still predicted much higher STED efficiencies than were seen in the experimental results. This suggests that neither orientation nor spatial variations in depletion efficiency are sufficient to explain the measured behaviour.

Therefore the part of the model which is not describing the behaviour of STED correctly could be the time-dependent term describing the dynamics of the two state model of CW depletion. Two assumptions have been made in the formulation of the model: firstly, that the rate of ground state vibrational relaxation is sufficiently fast to prevent the dump beam exciting molecules in the higher vibrational levels of S_0 back up to S_1, and secondly that there are no other photophysical states that impact upon STED efficiency other than the higher vibrational levels of S_0 and the lower vibrational levels of S_1. If either of these assumptions are insufficient, then this could result in the model over-estimating the efficiency of CW STED. The validity of these two assumptions is discussed further below.

5.8.2 Re-pumping with the dump beam

One simple mechanism which could be reducing STED efficiency could be re-pumping by the dump beam, which is accounted for in pulsed STED modelling but not in CW STED modelling. A schematic showing re-pumping of a fluorophore modelled as a four level system is shown in Fig. 5.21a. In the four level system, absorption excites molecules from low vibrational levels of the ground state S_0 to high vibrational levels of the excited state, S_1^*. Rapid vibrational relaxation at rate k_{vib1} then populates the lowest vibrational levels of the excited state, S_1; this is the group of energy levels from which fluorescence and stimulated emission occur at rates k_f and k_{STED} respectively to higher vibrational levels of the ground state S_0^*. The assumption in the two state system is that the sole route away from S_0^* is relaxation to S_0 at rate k_{vib0}, but here a re-pumping pathway has been added which returns molecules from S_0^* to S_1 at a rate $k_{\text{repump}} = k_{\text{STED}}$. The rate equations for the populations of S_0^* (N_0^*) and S_1 (N_1) are thus:

$$\frac{\mathrm{d}N_1}{\mathrm{d}t} = -(k_f + k_{\text{STED}})N_1 + k_{\text{STED}}N_0^* \tag{5.17a}$$

$$\frac{\mathrm{d}N_0^*}{\mathrm{d}t} = (k_f + k_{\text{STED}})N_1 - (k_{\text{vib0}} + k_{\text{STED}})N_0^*. \tag{5.17b}$$

The consequence of re-pumping would be that molecules spend longer in S_1 on average than predicted when there is no re-pumping, and that higher fluorescence intensities would be detected than without re-pumping due to increased cycling between S_1 and S_0^*.

However, re-pumping is unlikely to be the cause of reduced STED efficiency for two main reasons. Firstly, re-pumping would affect measured lifetimes and intensities in similar ways (lengthening τ_d and increasing intensity), and so this does not agree with the observed difference between F_d^{int} and F_d^{life} seen for the experiments in Section 5.7.2. Secondly, and more importantly, the values of the rates involved do not allow for S_0^* to be non-negligibly populated. From CW STED experiments, k_{STED} values are measured on the order of $10^8 - 10^9\text{s}^{-1}$ (i.e. similar to k_f) whereas the measurement of τ_R ($= 1/k_{\text{vib0}}$) from the pulsed STED experiment in Section 4.8.2 estimates k_{vib0} on the order of $10^{12} - 10^{13}\text{s}^{-1}$. As $k_{\text{vib0}} \gg (k_{\text{STED}}, k_f)$ the k_{vib0} term in Eq. 5.17b dominates over all others, and so Eq. 5.17b can be solved as

$$N_0^*(t) \approx \exp(-k_{\text{vib0}}t). \tag{5.18}$$

Hence it can be seen that the population of S_0^* at any given time is negligible due to the rapid rate of ground state vibrational relaxation and so the probability of re-pumping occurring is also negligible.

5.8.3 Triplet state involvement

As the two state model assumed throughout appears to be insufficient for describing CW STED dynamics, a model which includes other energy states of the fluorophore and transitions involving these may be necessary. Therefore an alternative mechanism is proposed where reduced STED efficiency could arise from substantial involvement of the triplet state. Whilst it was seen in the FCS measurements that presence of the dump beam did not appear to increase the fraction of excited state molecules entering the triplet state (Fig. 5.16b), the dump beam may instead be inducing molecular transitions for molecules which have already entered the triplet manifold. A summary of potential transitions which could occur if this were the case is summarised in Fig. 5.21b, and Table 5.4 details relevant rates.

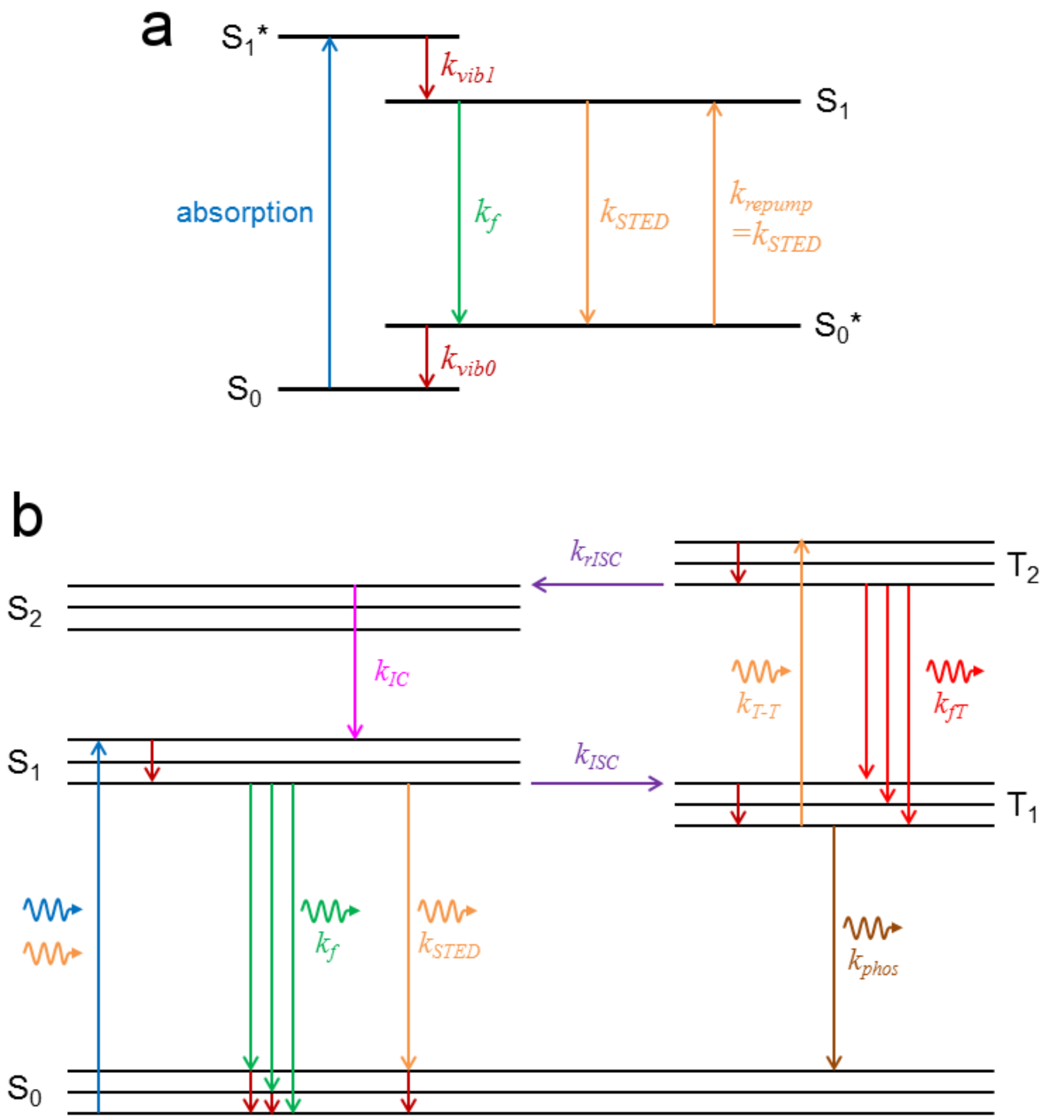

Figure 5.21: Alternative models of CW STED. a) Modification of the two state model to include a repumping rate k_{repump}. k_{vib1} and k_{vib0} are vibrational relaxation rates for S_1 and S_0 respectively. b) Modification of the model to include pathways through the triplet state. Wavy arrowed lines indicate processes involving the absorption/emission of a photon. Rates are given for the following processes: k_{ISC} = intersystem crossing, k_{phos} = phosphorescence, k_{T-T} = triplet-triplet absorption, k_{fT} = spontaneous emission from T_2, k_{rISC} = reverse intersystem crossing, k_{IC} = internal conversion. Unlabelled dark red arrows represent rapid vibrational relaxation.

Rate	Value	Notes
k_f	$(2.803 \pm 0.003) \times 10^8\ \mathrm{s}^{-1}$	Calculated from undumped fluorescence lifetime of fluorescein in water measured in this thesis
k_{STED}	$(2.06 \pm 0.07) \times 10^8\ \mathrm{s}^{-1}$	Maximum STED rate measured using lifetime data in this thesis
k_{ISC}	$6.6 \times 10^6\ \mathrm{s}^{-1}$	Measured for free acid form of fluorescein in water [148]
k_{phos}	$10^0 - 10^1\ \mathrm{s}^{-1}$	Range of rates for halogenated fluorescein derivatives in solution [149] and polymer films [150]
k_{T-T}	$\sim k_{\mathrm{STED}}$	Triplet-triplet excitation transition assumed to be resonant with the dump wavelength and hence occur at rate proportional to STED rate
k_{fT}	$\sim k_f$	Triplet-triplet fluorescence assumed to occur at similar rate to singlet-singlet fluorescence
k_{rISC}	$0.2 \times k_{\mathrm{ISC}}$	Calculated for rhodamine A (another xanthene dye) in aqueous solution [151]
k_{IC}	$\sim 10^{12}\ \mathrm{s}^{-1}$	Taken from [2] as a general order of magnitude
$T + T \rightarrow T + S_0$	$5 \times 10^8\ \mathrm{M}^{-1}\mathrm{s}^{-1}$	Triplet quenching through triplet-triplet collisions, producing triplet and ground state singlet [148]
$T + S_0 \rightarrow S_0 + S_0$	$5 \times 10^7\ \mathrm{M}^{-1}\mathrm{s}^{-1}$	Triplet quenching through triplet-singlet collisions, producing ground state singlet [148]
$T + \mathrm{O}_2 \rightarrow S_0 + \mathrm{O}_2$	$1.56 \times 10^9\ \mathrm{M}^{-1}\mathrm{s}^{-1}$	Physical quenching of the triplet state by molecular oxygen, producing singlet state and oxygen [148]
$T + \mathrm{O}_2 \rightarrow X + \mathrm{O}_2^-$	$1.4 \times 10^8\ \mathrm{M}^{-1}\mathrm{s}^{-1}$	Chemical quenching of the triplet state by molecular oxygen, producing an oxidised product X and superoxide radical [148]

Table 5.4: Rates relevant to Fig. 5.21b for fluorescein derivatives in aqueous solution.

Molecules can cross into the first triplet state T_1 from S_1 (intersystem crossing) at rate k_{ISC}, the value of which should not be affected by either the pump intensity or dump intensity, but is however sensitive to solvation environment and is larger for polar solvents [152]. This is notable as all three solvents (water, ethylene glycol and glycerol) used in this thesis are polar molecules. As k_{ISC} is slow compared to k_f and k_{STED}, the majority of molecules in S_1 are still more likely to return to S_0 via spontaneous or stimulated emission rather than cross into T_1, but the latter is not a negligible process. The triplet state, like the singlet state, has many different electronic energy levels and so it is conceivable that excitation and spontaneous emission can occur between triplet states, here assumed to be T_1 and T_2 for the purpose of demonstration.

Therefore one possibility is that molecules which have crossed into T_1 are excited into T_2 by the dump beam at rate k_{T-T}, which would be dependent on the dump power and thus proportional to k_{STED}. The feasibility of this is confirmed by measurements of the triplet-triplet absorbance of fluorescein which show absorption at wavelengths above 540nm which extends to wavelengths > 594nm (the dump wavelength used here) [148]. Once in T_2 the molecule can radiatively de-excite back to T_1 at rate k_{fT} assumed to be similar to the radiative rate for $S_1 \rightarrow S_0$ (k_f), or alternatively it can undergo reverse intersystem crossing at rate k_{rISC} to a higher singlet state (denoted S_2 for this example). Again, k_{rISC} is slow compared to (the assumed) k_{fT} and so it is possible that there are several cycles of excitation and emission in the triplet manifold before the molecule returns to the singlet manifold. If reverse intersystem crossing did occur then this would be followed by rapid internal conversion back to S_1 at rate k_{IC}, and from there the molecule could then fluoresce or undergo stimulated emission. This proposed cycle would arise from the combined effects of the long triplet state lifetime and continuous presence of the dump beam, and would thus be negligible for STED with short dump pulses. This could contribute to an explanation of why STED efficiency appears to decrease with lengthening dump pulses.

The net effect of a cycle such as this would be that there is refilling of S_1 which overall reduces the rate at which S_1 decays in the presence of CW dump. The two state model of CW STED used throughout this thesis is based on the treatment of the population of S_1 as

$$\frac{\mathrm{d}N_1}{\mathrm{d}t} = -(k_f + k_{\mathrm{STED}})N_1. \tag{5.19}$$

However refilling of S_1 would modify Eq. 5.19 such that

$$\frac{\mathrm{d}N_1}{\mathrm{d}t} = -(k_f + k_{\mathrm{STED}} - k_{\mathrm{refill}})N_1 \tag{5.20}$$

where the rate k_{refill} may have a complicated dependence on dump power and hence k_{STED}. As such the measured dumped lifetime with refilling of S_1 will be longer than one where there is no refilling of S_1, and so this will reduce the value of F_d^{life}.

The proposed modifications to the model should not affect F_d^{int} as it will not necessarily alter the total number of photons spontaneously emitted from S_1, just the length of time before a molecule returns to S_0. However, there are several pathways through which molecules can leave the triplet manifold which are distinct from the transitions shown in Fig. 5.21b (which are listed at the bottom of Table 5.4). For example, collisions with other fluorophores or oxygen molecules can non-radiatively return triplet state molecules to S_0, and in the case of oxygen collisions irreversible photochemical destruction of the fluorescent molecule itself can occur. This loss of excited state population, and hence loss of fluorescence, will appear to be induced by the dump beam when measured by intensity alone (thus contributing to F_d^{int}), especially if any of these collisional reactions are more probable for molecules in higher triplet states ($T_{>1}$).

The addition of spatial averaging to the model of CW STED dynamics was computationally intensive, and so the integration of other factors such as triplet state dynamics into this framework may not be possible. Therefore, a different modelling strategy such as Monte Carlo simulations could be used to gauge whether inclusion of the triplet state in modelling of CW STED results in the plateau in STED efficiency repeatedly observed throughout this thesis. Alternatively, in lieu of formulating a new model experiments could be performed to either to minimise k_{ISC}, which would hypothetically increase agreement with the current model, or to maximise k_{ISC}, which would conversely decrease agreement with the current model if passage through the triplet state does indeed affect STED efficiency. The former could be achieved by using non-polar solvents such as cyclohexane and benzene, whilst the latter could be achieved by introducing heavy atoms into the solvent as these increase spin-orbit coupling and hence the rate of intersystem crossing [1], or performing experiments on fluorophores containing heavy atoms (such as 4’5’-diiodofluorescein [153]).

However, whilst future incorporation of triplet state involvement and spatial averaging into CW STED dynamics may reduce the difference between expected and observed STED efficiency, these are unlikely to be the only mechanisms reducing efficiency. For example fluorescence, stimulated emission and intersystem crossing are not the only possible fates for molecules in S_1. This can be seen in the fluorescence and triplet quantum yields which have values $\Phi_f = 0.92$ [154] and $\Phi_T = 0.02 - 0.05$ [148] for the free acid form of fluorescein; as $\Phi_f + \Phi_T < 1$ there must be alternative de-excitation pathways such as excited state absorption which have not been considered here. Furthermore the low values of F_d^{life} were observed not just for high pump powers, where there is a substantial triplet fraction, but also at low pump powers where the triplet fraction was measured to be negligible (for fluorescein in water).

5.8.4 CW STED dynamics of individual molecules

One feature common to all of the experiments performed in this thesis (with the exception of the FCS experiments) is that the dynamics of fluorophore populations are examined as opposed to the behaviour of individual molecules. The only current method available here to quantify the properties of single molecules undergoing CW STED is FCS, and to perform this successfully a more appropriate FCS model would need to be formulated, as models used here do not account for any STED effects. Therefore the studies in this thesis have been restricted to studying the average behaviour of many molecules, which differs from single molecule behaviour as a result of factors such as orientational dependence and spatial averaging of out-of-focus fluorescence.

However there is one example in the literature where the effects of CW STED on the fluorescence lifetimes of isolated fluorophores have been quantified. Vicidomini et al. (2011) [86] performed STED on individual nitrogen vacancy centres using pulsed pump at 532nm and CW dump at 740nm in an early description of gSTED microscopy, with both beams possessing Gaussian intensity profiles (as used in this thesis). Nitrogen vacancies are an attractive test sample for STED microscopy as they are small ($\sim$ 4nm), have well-characterised energy levels and display a high level of photostability with no bleaching or blinking [155]. Vicidomini et al. appear to have used the nitrogen vacancy for this very purpose in gSTED as there was no discussion regarding the photophysics of CW STED of nitrogen vacancies in this paper.

Figure 5.22a shows the lifetimes of individual nitrogen vacancies measured using TCSPC with different dump powers, taken directly from the Vicidomini et al. paper. Plotted with the experimental data is a predicted relationship between lifetime and dump power (P_{dump}) as given by [86]

$$\tau_D = \frac{1}{k_f + \frac{\sigma_{\text{STED}}\lambda_{\text{STED}}}{Ahc}P_{\text{dump}}} \tag{5.21}$$

where all parameters are as previously discussed. This formula is evidently based on the same two state model as is used here, which can be seen by taking the reciprocal of the dumped fluorescence rate $k_f + \alpha S'$ seen in the time-dependent terms of the modelling, where α takes into account orientational effects and/or spatial averaging (e.g. Eqs. 4.23, 5.15). Comparing Eq. 5.21 with those used in this thesis indicates again that any orientational effects were not taken into account (i.e. the α term is absent). Whilst this relationship appears to fit the data well at low dump powers ($\leq$ 5mW, measured at back aperture of the objective), the data deviates from the predicted relationship at higher dump powers. If this data is converted into F_d^{life} values (Fig. 5.22b), it can be seen that whilst the fractional depletion is higher than for any experiment described in this thesis, it still falls below the predicted values. This is more obvious when the data is replotted in terms of the STED rate

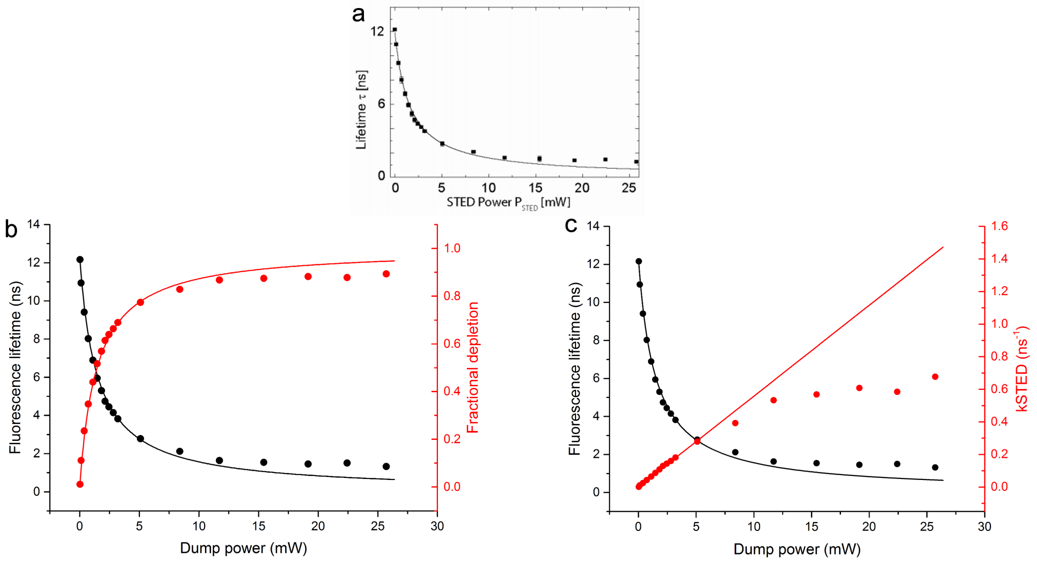

Figure 5.22: CW STED of nitrogen vacancies as measured by Vicidomini et al. [86]. a) Dumped fluorescence lifetime from TCSPC measurements on single nitrogen vacancies, where each point is the average of five measurements for five different nitrogen vacancies. b) Fractional depletion values (red points) calculated from published lifetime data (black dots) with respective model relationships as calculated using Eq. 5.21 and combined with lifetime fractional depletion calculation (Eq. 4.15). c) STED rates (red points) calculated from published lifetime data (black dots) with respective model relationships as calculated using Eq. 5.21 and combined with STED rate calculation in Eq. 5.7.

(Fig. 5.22c). As only single molecules were examined in the case of the nitrogen vacancies, a single exponential lifetime decay would be expected. However, the denominator of the model used by Vicidomini et al. (Eq. 5.21) implies that the STED rate should increase linearly with dump power, yet the data is sublinear and even appears to plateau as seen in the results of this thesis. The STED rate at which the modelling of the nitrogen vacancies appeared to 'break down' was approximately $0.3 - 0.4\text{ns}^{-1}$; this is the same k_{STED} range as where fluorescein, coumarin 6 and pyridine 2 departed from model behaviour in all solvents tested with CW STED in this thesis. The higher F_d values obtained in the nitrogen vacancies could have resulted from the vacancy having a very long fluorescence lifetime (> 12ns) to begin with.

This data is important as nitrogen vacancies do not experience orientational dependence or concentration dependent effects, or suffer from contamination with out-of-focus fluorescence, but still appear to experience lower than expected STED efficiencies. This suggests that CW STED inefficiency is due to intrinsic photophysics rather than a byproduct of population effects.

5.9 Future experimental exploration of CW STED dynamics

Further investigations are necessary to confirm whether involvement of the triplet state is a contributing factor to STED efficiency. One experiment could be to measure triplet-triplet spontaneous emission and its relationship with both pump power and dump power. This radiation is assumed to be longer than the dump beam wavelength, and so is currently filtered from the detection pathway by the 550nm shortpass filter.

Another strategy would be to alter the population of the triplet state. For instance, adding an oxidising agent such as hydrogen peroxide to the fluorophore solution would increase the concentration of molecular oxygen in the sample and drive triplet state molecules to either S_0 or photochemical destruction, thus preventing the triplet state molecule returning to S_1. An alternative way to achieve this could be by increasing fluorophore concentration, as triplet-triplet and triplet-singlet collisional quenching are both concentration-dependent processes (Table 5.4). However this may have the unwanted complication of introducing more collisional quenching of S_1 which would artificially reduce the measured fluorescence lifetime. The STED dynamics of molecules with varying triplet state yields could also be examined; an interesting molecule to investigate would be eosin, a bromonated fluorescein derivative with $\Phi_T = 0.64$ [148] which should have a substantially lower F_d^{life} than expected due to increased cycling through the triplet state.

Mechanical quenching could also be used to physically remove recently formed triplets from the sample, which is a strategy used to minimise absorption losses in

CW dye lasers [156]. An example of such a technique being used to increase the photostability of rhodamine 6G, another xanthene dye, uses a 100µm thick nozzle to flow fluorophore solution through a beam focus of diameter 15µm at a rate of 15ms^{-1}, ensuring that solution only remained at the focus for 1µs [157]. In the experimental set-up used here, a microfluidic device could be used to flow fluorophore solution across the focus of the microscope objective; ideally the rate of flow would be such that the volume at the focus (~ 0.6fl) was replaced more rapidly than the rate of return of triplets to the singlet manifold (microsecond timescale). Such an experiment could also be adapted to remove the effects of out-of-focus fluorescence: for example, if a lower NA objective was used (thus increasing the size of the focus) in conjunction with tubing/jet nozzle of low internal diameter, a situation could be achieved where the pump and dump fields were largely constant across the entire volume of sample flowing across the sample at a given time.

If involvement of the triplet state in CW STED can be confirmed by performing the above experiments on fluorophores in bulk solution, then this knowledge could be used to enhance the performance of CW STED-based microscopy techniques. Whilst in a labelled biological sample fluorophores could not be readily nor rapidly exchanged to remove triplet states (as would be the case in the mechanical quenching experiment suggested), imaging buffers could be used to optimise the fluorophore environment to minimise the rate of intersystem crossing or to chemically remove triplets from the fluorophore population. A more detailed understanding of the involvement of the triplet state in CW STED could also be used to better inform the selection and development of fluorophores for CW STED techniques.

5.10 Summary

In this chapter, potential mechanisms underlying reduced STED efficiency have been experimentally investigated and used to propose altered models of CW STED dynamics. Results obtained from measurements of CW STED following two photon excitation and CW STED with differing focal volumes, along with FCS measurements of the volume of the focus itself with various dump powers, have indicated that out-of-focus fluorescence is contributing to a low observed STED efficiency. This effect has been incorporated into the model of CW STED dynamics; however, whilst this correction reduces the quantitative disagreement between experimental observations and simulated STED efficiencies, this discrepancy is still far larger than can be accounted for by experimental error.

Published results of CW STED on nitrogen vacancies indicate that there may be intrinsic photophysical pathways which prevent high CW STED efficiencies (though not alluded to in the study itself), and results in this chapter also indicate that this may be the case. Increasing the (single photon) pump power resulted in lower STED efficiencies, which here is assumed to be the effect of an increased triplet state population, and discrepancies between quantifying STED efficiency via suppression of fluorescence intensity and lifetime shortening may result from molecules spending extended periods of time in the triplet manifold. An alternative model involving the molecule spending extended durations of time in the triplet manifold has been thus proposed along with potential experiments to verify it.

Chapter 6

Conclusions

The field of super resolution microscopy had been steadily growing over the past decade, with the importance of developing optical microscopy techniques capable of resolving biological structures on the nanometre scale earning three founders of super resolution microscopy the Nobel Prize in Chemistry in 2014.

This thesis has presented the theoretical and experimental basis for a novel super resolution microscopy technique, LIR-SR. The results obtained using LIR-SR are promising, and although the resolution increases were modest compared to established super resolution techniques, the microscope had a simple set-up compared to STED microscopy and the reconstruction of super resolution images was rapid in comparison to PALM and STORM. Furthermore, on-sample laser powers over the course of image acquisition were low compared to established super resolution techniques, making LIR-SR a promising method for live-cell super resolution imaging. Aspects of LIR-SR where there is scope for improvement have been identified and it will be exciting to see how the technique performs in the future with these technical refinements, especially for imaging samples with labelled biological structures as opposed to fluorescent beads.

Detailed investigations into the underlying photophysics of CW STED were undertaken, motivated jointly by the requirement for a more complete understanding of the fundamental physical processes occurring in LIR-SR and previous work in the group which suggested that CW STED may not behave as predicted by modelling of a two state system. The experiments in Chapters 4 and 5 repeatedly showed that CW STED efficiency was much lower than expected for several different fluorophores and solvents, especially at high dump powers, and broadly represented an extrapolation of observations in long pulse STED. Contamination of the detected signal with out-of-focus fluorescence was seen to have a significant effect on the measured STED efficiency, and although incorporation of this contamination into modelling of CW STED dynamics was a significant improvement on the previous model used, which only accounted for the initial excited state orientational distribution function of the fluorophore population, there was still a large discrepancy between the predictions of the model and the measured data. A discrepancy was also observed between quantification of STED efficiency through lifetime and intensity measurements, which was unexpected and implied that there may be some complex mechanism causing longer than expected lifetimes in fluorophore populations subject to CW STED. Indeed, the suggested involvement of the triplet state could also be the root of the deviations from model behaviour for pulsed STED where the dump pulse becomes increasingly long compared to the duration of the excitation pulse, fluorescence lifetime of the fluorophore and the rotational correlation time of the fluorophore. The modelling used in this thesis is more detailed than any published modelling of CW STED, and yet this is still not sufficient to explain why CW STED efficiency is lower than expected.

The recurring theme in the experiments presented in Chapters 4 and 5 is that CW STED behaves as predicated when low pump powers and low dump powers are used, but not when either or both laser powers are high. This is an important finding with regard to LIR-SR, as this low power regime is compatible with LIR-SR given that the fluorophores used to label the sample are sufficiently bright, and super resolution images can be obtained with dump powers corresponding to less than 50% lifetime shortening. The photophysical studies also suggest that this aspect of LIR-SR is behaving as suggested by the modelling belying the technique, and that there are not inefficiencies associated with low power CW STED that are restricting the resolution obtainable with LIR-SR. Rather, future development of LIR-SR should be focused on optimising the computational methods required for time window selection and subsequent image reconstruction.

However, in STED microscopy the dump beam power is required to be at least an order of magnitude larger than is used for LIR-SR, and pump power is also frequently higher than is used here, presumably to maintain an appropriate signal-to-noise ratio in images. For example, if the pump beam used here is assumed to undergo the same relative losses in the optical path as the dump beam, then typical on-sample powers for LIR-SR are in the range of $0.1 - 1\mu\text{W}$, compared to pump powers in gSTED which are an order of magnitude higher [86]. There is also considerable interest in the development of novel fluorophores for STED microscopy (e.g. [79, 80, 158]) and an incomplete understanding of the photophysical pathways taken by fluorophores in the presence of a CW (or long pulsed) dump field may hinder this progress. Therefore the findings of the experiments into CW STED efficiency presented here are relevant not only for verification that LIR-SR operates in a regime where the two state system assumption appears sufficient, but also for the progression of other CW STED-based microscopy techniques.

References

[1] B. Valeur, *Molecular Fluorescence: Principles and Applications*, vol. 8. Weinheim, Germany: Wiley-VCH, 2001.

[2] J. R. Lakowicz, *Principles of Fluorescence Spectroscopy.* New York: Springer Science, third ed., 2006.

[3] P. Atkins and R. Friedman, *Molecular Quantum Mechanics.* New York, US: Oxford University Press, fourth ed., 2005.

[4] J. W. Lichtman and J.-A. Conchello, “Fluorescence microscopy.,” *Nature methods*, vol. 2, pp. 910–9, Dec. 2005.

[5] P. Atkins and J. de Paula, *Physical Chemistry.* New York, US: W.H. Freeman and Company, eighth ed., 2006.

[6] S. Prahl, “PhotoChemCAD Chemicals, http://omlc.org/spectra/ PhotochemCAD/index.html,” 2012.

[7] Jackson ImmunoResearch Laboratories Inc., “Cyanine Dyes (Cy2, Cy3 and Cy5), https://www.jacksonimmuno.com/technical/products/conjugate-selection/cyanine.”

[8] R. C. Hilborn, “Einstein coefficients, cross sections, f values, dipole moments, and all that,” *American Journal of Physics*, vol. 50, p. 982, Nov. 1982.

[9] D. A. Armoogum, *Time resolved excited state photo-engineering.* PhD thesis, UCL, 2004.

[10] T. S. Blacker, R. J. Marsh, M. R. Duchen, and A. J. Bain, “Activated barrier crossing dynamics in the non-radiative decay of NADH and NADPH,” *Chemical Physics*, vol. 422, pp. 184–194, Aug. 2013.

[11] E. Monge, *Single and two photon fluorescence studies of ordered molecular systems.* PhD thesis, UCL, 2003.

[12] G. Lipari and A. Szabo, “Effect of librational motion on fluorescence depolarization and nuclear magnetic resonance relaxation in macromolecules and membranes.,” *Biophysical journal*, vol. 30, pp. 489–506, June 1980.

[13] A. J. Bain, P. Chandna, G. Butcher, and J. Bryant, “Picosecond polarized fluorescence studies of anisotropic fluid media. II. Experimental studies of molecular order and motion in jet aligned rhodamine 6G and resorufin solutions,” *The Journal of Chemical Physics*, vol. 112, p. 10435, June 2000.

[14] A. J. Bain, P. Chandna, and J. Bryant, “Picosecond polarized fluorescence studies of anisotropic fluid media. I. Theory,” *The Journal of Chemical Physics*, vol. 112, p. 10418, June 2000.

[15] E. Bailey, *Polarised Fluorescence and Stimulated Emission Depletion Studies of Excited State Dynamics.* PhD thesis, UCL, 2013.

[16] A. J. Bain, “Multiphoton processes,” in *Handbook of Photonics, Volume 1* (D. L. Andrews, ed.), Wiley (in press), 2015.

[17] T. S. Blacker, Z. F. Mann, J. E. Gale, M. Ziegler, A. J. Bain, G. Szabadkai, and M. R. Duchen, “Separating NADH and NADPH fluorescence in live cells and tissues using FLIM.,” *Nature communications*, vol. 5, p. 3936, Jan. 2014.

[18] M. A. Albota, C. Xu, and W. W. Webb, “Two-Photon Fluorescence Excitation Cross Sections of Biomolecular Probes from 690 to 960 nm,” *Applied Optics*, vol. 37, p. 7352, Nov. 1998.

[19] C. Xu and W. W. Webb, “Measurement of two-photon excitation cross sections of molecular fluorophores with data from 690 to 1050 nm,” *Journal of the Optical Society of America B*, vol. 13, p. 481, Mar. 1996.

[20] Cornell University, “Developmental Resource for Biophysical Imaging Opto-electronics.”

[21] J. R. Lakowicz, “Volume 5: Nonlinear and Two-Photon-Induced Fluorescence,” in *Topics in Fluorescence Spectroscopy*, Kluwer, 2002.

[22] T. Blacker, *Monitoring cell metabolism with NAD(P)H fluorescence lifetime imaging.* PhD thesis, UCL, 2014.

[23] M. A. Bopp, Y. Jia, G. Haran, E. A. Morlino, and R. M. Hochstrasser, “Single-molecule spectroscopy with 27 fs pulses: Time-resolved experiments and direct imaging of orientational distributions,” *Applied Physics Letters*, vol. 73, p. 7, July 1998.

[24] PicoQuant GmbH, “PicoHarp 300 User’s Manual and Technical Data.”

[25] W. Becker, *The bh TCSPC Handbook.* Berlin: Becker & Hickl GmbH, 2nd ed., 2006.

[26] D. Colquhoun and F. J. Sigworth, “Fitting and Statistical Analysis of Single-Channel Records,” in *Single-Channel Recording* (B. Sakmann and E. Neher, eds.), pp. 483–587, Springer US, 1995.

[27] M. Wahl, “Time-Correlated Single Photon Counting (technical note),” 2014. http://www.picoquant.com/images/uploads/page/files/7253/technote_tcspc.pdf.

[28] R. Marsh, D. Armoogum, and A. Bain, “Stimulated emission depletion of two-photon excited states,” *Chemical Physics Letters*, vol. 366, pp. 398–405, Dec. 2002.

[29] C. K. Rosenthal and A. Heinrichs, “Milestones in Light Microscopy,” *Nature Cell Biol.*, vol. 11, pp. S6–S7, 2009.

[30] M. Minsky, “Microscopy apparatus,” Dec. 1961. US Patent Number: US3013467.

[31] T. A. Masters, V. Calleja, D. A. Armoogum, R. J. Marsh, C. J. Applebee, M. Laguerre, A. J. Bain, and B. Larijani, “Regulation of 3-phosphoinositide-dependent protein kinase 1 activity by homodimerization in live cells.,” *Science signaling*, vol. 3, p. ra78, Jan. 2010.

[32] H. Wallrabe and A. Periasamy, “Imaging protein molecules using FRET and FLIM microscopy.,” *Current opinion in biotechnology*, vol. 16, pp. 19–27, Mar. 2005.

[33] M. A. Hink, R. A. Griep, J. W. Borst, A. van Hoek, M. H. Eppink, A. Schots, and A. J. Visser, “Structural dynamics of green fluorescent protein alone and fused with a single chain Fv protein.,” *The Journal of biological chemistry*, vol. 275, pp. 17556–60, June 2000.

[34] M. Reth, “Matching cellular dimensions with molecular sizes.,” *Nature immunology*, vol. 14, pp. 765–7, Aug. 2013.

[35] P. A. Weber, H.-C. Chang, K. E. Spaeth, J. M. Nitsche, and B. J. Nicholson, “The permeability of gap junction channels to probes of different size is dependent on connexin composition and permeant-pore affinities.,” *Biophysical journal*, vol. 87, pp. 958–73, Aug. 2004.

[36] A. H. Coons, H. J. Creech, R. N. Jones, and E. Berliner, “The Demonstration of Pneumococcal Antigen in Tissues by the Use of Fluorescent Antibody,” *The Journal of Immunology*, vol. 45, pp. 159–170, Nov. 1942.

[37] N. Panchuk-Voloshina, R. P. Haugland, J. Bishop-Stewart, M. K. Bhalgat, P. J. Millard, F. Mao, and W.-Y. Leung, “Alexa Dyes, a Series of New Fluorescent Dyes that Yield Exceptionally Bright, Photostable Conjugates,” *Journal of Histochemistry & Cytochemistry*, vol. 47, pp. 1179–1188, Sept. 1999.

[38] R. B. Mujumdar, L. A. Ernst, S. R. Mujumdar, C. J. Lewis, and A. S. Waggoner, “Cyanine dye labeling reagents: Sulfoindocyanine succinimidyl esters,” *Bioconjugate Chemistry*, vol. 4, pp. 105–111, Mar. 1993.

[39] J.-M. Fritschy and W. Härtig, “Indirect Immunofluorescence of Cultured Cells,” in *Encyclopedia of Life Sciences*, Chichester, UK: John Wiley & Sons, Ltd, May 2001.

[40] C. Grienberger and A. Konnerth, “Imaging calcium in neurons.,” *Neuron*, vol. 73, pp. 862–85, Mar. 2012.

[41] M. Chalfie, Y. Tu, G. Euskirchen, W. Ward, and D. Prasher, “Green fluorescent protein as a marker for gene expression,” *Science*, vol. 263, pp. 802–805, Feb. 1994.

[42] R. Y. Tsien, “The green fluorescent protein.,” *Annual review of biochemistry*, vol. 67, pp. 509–44, Jan. 1998.

[43] R. Heim, A. B. Cubitt, and R. Y. Tsien, “Improved green fluorescence.,” *Nature*, vol. 373, pp. 663–4, Feb. 1995.

[44] R. Heim and R. Y. Tsien, “Engineering green fluorescent protein for improved brightness, longer wavelengths and fluorescence resonance energy transfer,” *Current Biology*, vol. 6, pp. 178–182, Feb. 1996.

[45] F. Helmchen and W. Denk, “Deep tissue two-photon microscopy.,” *Nature methods*, vol. 2, pp. 932–40, Dec. 2005.

[46] P.-C. Cheng, “The Contrast Formation in Optical Microscopy,” in *Handbook of Biological Confocal Microscopy* (J. B. Pawley, ed.), ch. 8, pp. 162–206, New York: Springer US, third ed., 2006.

[47] W. Denk, D. W. Piston, and W. W. Webb, “Multi-Photon Molecular Excitation in Laser-Scanning Microscopy,” in *Handbook of Biological Confocal Microscopy* (J. B. Pawley, ed.), ch. 28, pp. 535–549, New York: Springer Science, third ed., 2006.

[48] M. Valko, D. Leibfritz, J. Moncol, M. T. D. Cronin, M. Mazur, and J. Telser, “Free radicals and antioxidants in normal physiological functions and human disease.,” *The international journal of biochemistry & cell biology*, vol. 39, pp. 44–84, Jan. 2007.

[49] R. Dixit and R. Cyr, “Cell damage and reactive oxygen species production induced by fluorescence microscopy: effect on mitosis and guidelines for non-invasive fluorescence microscopy,” *The Plant Journal*, vol. 36, pp. 280–290, Oct. 2003.

[50] K. König, “Cell Damage During Multi-Photon Microscopy,” in *Handbook of Biological Confocal Microscopy* (J. B. Pawley, ed.), ch. 38, pp. 680–689, New York: Springer Science, third ed., 2006.

[51] D. J. Stephens and V. J. Allan, “Light microscopy techniques for live cell imaging.,” *Science (New York, N.Y.)*, vol. 300, pp. 82–6, Apr. 2003.

[52] C. B. Griesinger, C. D. Richards, and J. F. Ashmore, “FM1-43 Reveals Membrane Recycling in Adult Inner Hair Cells of the Mammalian Cochlea,” *J. Neurosci.*, vol. 22, pp. 3939–3952, May 2002.

[53] B. F. Grewe, D. Langer, H. Kasper, B. M. Kampa, and F. Helmchen, “High-speed in vivo calcium imaging reveals neuronal network activity with near-millisecond precision.,” *Nature methods*, vol. 7, pp. 399–405, May 2010.

[54] L. Leybaert, A. de Meyer, C. Mabilde, and M. J. Sanderson, “A simple and practical method to acquire geometrically correct images with resonant scanning-based line scanning in a custom-built video-rate laser scanning microscope.,” *Journal of microscopy*, vol. 219, pp. 133–40, Sept. 2005.

[55] F. L. Pedrotti, L. M. Pedrotti, and L. S. Pedrotti, *Introduction to Optics*. Pearson, 3rd ed., 2007.

[56] D. E. Reisner, R. W. Field, J. L. Kinsey, and H.-L. Dai, “Stimulated emission spectroscopy: A complete set of vibrational constants for X1A1 formaldehyde,” *The Journal of Chemical Physics*, vol. 80, p. 5968, June 1984.

[57] T. A. Masters, *Time-resolved fluorescence studies of Enhanced Green Fluorescent Protein and the molecular dynamics of 3-Phosphoinositide Dependent Protein Kinase 1.* PhD thesis, UCL, 2009.

[58] S. Watanabe, A. Punge, G. Hollopeter, K. I. Willig, R. J. Hobson, M. W. Davis, S. W. Hell, and E. M. Jorgensen, “Protein localization in electron micrographs using fluorescence nanoscopy,” *Nature Methods*, vol. 8, pp. 80–84, Nov. 2011.

[59] M. A. Lauterbach, “Finding, defining and breaking the diffraction barrier in microscopy a historical perspective,” *Optical Nanoscopy*, vol. 1, p. 8, Nov. 2012.

[60] Ram, S and Ward, E S and Ober, R J, “Beyond Rayleigh’s criterion: A resolution measure with application to single-molecule microscopy,” *Proceedings of the National Academy of Sciences of the United States of America*, vol. 103, no. 12, pp. 4457–4462, 2006.

[61] T. Wilson, “Optical sectioning in fluorescence microscopy,” *Journal of Microscopy*, vol. 242, no. 2, pp. 111–116, 2010.

[62] S. T. Hess and W. W. Webb, “Focal volume optics and experimental artifacts in confocal fluorescence correlation spectroscopy.,” *Biophysical journal*, vol. 83, pp. 2300–17, Oct. 2002.

[63] E. Betzig, G. H. Patterson, R. Sougrat, O. W. Lindwasser, S. Olenych, J. S. Bonifacino, M. W. Davidson, J. Lippincott-Schwartz, and H. F. Hess, “Imaging intracellular fluorescent proteins at nanometer resolution.,” *Science*, vol. 313, pp. 1642–5, Sept. 2006.

[64] M. J. Rust, M. Bates, and X. Zhuang, “Sub-diffraction-limit imaging by stochastic optical reconstruction microscopy (STORM).,” *Nature methods*, vol. 3, pp. 793–5, Oct. 2006.

[65] G. T. Dempsey, J. C. Vaughan, K. H. Chen, M. Bates, and X. Zhuang, “Evaluation of fluorophores for optimal performance in localization-based super-resolution imaging,” *Nature Methods*, vol. 12, no. 8, pp. 1027–1036, 2011.

[66] R. Henriques, C. Griffiths, E. Hesper Rego, and M. M. Mhlanga, “PALM and STORM: unlocking live-cell super-resolution.,” *Biopolymers*, vol. 95, pp. 322–31, May 2011.

[67] M. J. Mlodzianoski, J. M. Schreiner, S. P. Callahan, K. Smolková, A. Dlasková, J. Santorová, P. Ježek, and J. Bewersdorf, “Sample drift correction in 3D fluorescence photoactivation localization microscopy.,” *Optics express*, vol. 19, pp. 15009–19, Aug. 2011.

[68] M. G. L. Gustafsson, “Surpassing the lateral resolution limit by a factor of two using structured illumination microscopy.,” *Journal of Microscopy*, vol. 198, pp. 82–87, May 2000.

[69] M. G. L. Gustafsson, “Nonlinear structured-illumination microscopy: wide-field fluorescence imaging with theoretically unlimited resolution.,” *Proceedings of the National Academy of Sciences of the United States of America*, vol. 102, pp. 13081–6, Sept. 2005.

[70] P. Kner, B. B. Chhun, E. R. Griffis, L. Winoto, and M. G. L. Gustafsson, “Super-resolution video microscopy of live cells by structured illumination.,” *Nature methods*, vol. 6, pp. 339–42, May 2009.

[71] S. W. Hell and J. Wichmann, “Breaking the diffraction resolution limit by stimulated emission: stimulated-emission-depletion fluorescence microscopy,” *Optics Letters*, vol. 19, p. 780, June 1994.

[72] G. Donnert, J. Keller, R. Medda, M. A. Andrei, S. O. Rizzoli, R. Lührmann, R. Jahn, C. Eggeling, and S. W. Hell, “Macromolecular-scale resolution in biological fluorescence microscopy.,” *Proceedings of the National Academy of Sciences of the United States of America*, vol. 103, pp. 11440–5, Aug. 2006.

[73] L. E. Helseth, “Smallest focal hole,” *Optics Communications*, vol. 257, no. 1, pp. 1–8, 2006.

[74] X. Hao, C. Kuang, T. Wang, and X. Liu, “Effects of polarization on the de-excitation dark focal spot in STED microscopy,” *Journal of Optics*, vol. 12, p. 115707, 2010.

[75] D. Wildanger, E. Rittweger, L. Kastrup, and S. W. Hell, “STED microscopy with a supercontinuum laser source,” *Optics Express*, vol. 16, no. 13, pp. 9614–9621, 2008.

[76] V. Westphal and S. Hell, “Nanoscale Resolution in the Focal Plane of an Optical Microscope,” *Physical Review Letters*, vol. 94, p. 143903, Apr. 2005.

[77] D. Wildanger, R. Medda, L. Kastrup, and S. W. Hell, “A compact STED microscope providing 3D nanoscale resolution.,” *Journal of microscopy*, vol. 236, pp. 35–43, Oct. 2009.

[78] M. Fernández-Suárez and A. Y. Ting, “Fluorescent probes for super-resolution imaging in living cells,” *Nature Reviews Molecular Cell Biology*, vol. 9, pp. 929–943, 2008.

[79] C. A. Wurm, K. Kolmakov, F. Göttfert, H. Ta, M. Bossi, H. Schill, S. Berning, S. Jakobs, G. Donnert, V. N. Belov, and S. W. Hell, “Novel red fluorophores with superior performance in STED microscopy,” *Optical Nanoscopy*, vol. 1, p. 7, Sept. 2012.

[80] G. Lukinavičius, K. Umezawa, N. Olivier, A. Honigmann, G. Yang, T. Plass, V. Mueller, L. Reymond, I. R. Corrêa, Z.-G. Luo, C. Schultz, E. A. Lemke, P. Heppenstall, C. Eggeling, S. Manley, and K. Johnsson, “A near-infrared fluorophore for live-cell super-resolution microscopy of cellular proteins.,” *Nature chemistry*, vol. 5, pp. 132–9, Feb. 2013.

[81] K. I. Willig, S. O. Rizzoli, V. Westphal, R. Jahn, and S. W. Hell, “STED microscopy reveals that synaptotagmin remains clustered after synaptic vesicle exocytosis.,” *Nature*, vol. 440, pp. 935–9, Apr. 2006.

[82] K. T. Takasaki, J. B. Ding, and B. L. Sabatini, “Live-cell superresolution imaging by pulsed STED two-photon excitation microscopy.,” *Biophysical journal*, vol. 104, pp. 770–7, Feb. 2013.

[83] N. Stafford, “The million dollar microscope,” *Chemistry World*, Mar. 2007.

[84] Leica Microsystems GmbH, “Super-Resolution Microscope Leica TCS STED,” 2014. http://www.leica-microsystems.com/products/confocal-microscopes/details/product/leica-tcs-sted/. Retrieved 08/09/2014.

[85] K. I. Willig, B. Harke, R. Medda, and S. W. Hell, “STED microscopy with continuous wave beams.,” *Nature methods*, vol. 4, pp. 915–8, Nov. 2007.

[86] G. Vicidomini, G. Moneron, K. Y. Han, V. Westphal, H. Ta, M. Reuss, J. Engelhardt, C. Eggeling, and S. W. Hell, “Sharper low-power STED nanoscopy by time gating.,” *Nature methods*, vol. 8, pp. 571–3, July 2011.

[87] B. Hein, K. I. Willig, and S. W. Hell, “Stimulated emission depletion (STED) nanoscopy of a fluorescent protein-labeled organelle inside a living cell.,” *Proceedings of the National Academy of Sciences of the United States of America*, vol. 105, pp. 14271–6, Sept. 2008.

[88] A. J. Bain and R. J. Marsh, “Improvements relating to fluorescence microscopy,” Jan. 2012. European Patent Number: WO2013008033A1.

[89] R. J. Marsh, S. Culley, and A. J. Bain, “Low power super resolution fluorescence microscopy by lifetime modification and image reconstruction,” *Optics Express*, vol. 22, pp. 12327–38, May 2014.

[90] S. A. Self, “Focusing of spherical Gaussian beams,” *Applied Optics*, vol. 22, p. 658, Mar. 1983.

[91] S. Inoue, “Foundations of Confocal Scanned Imaging in Light Microscopy,” in *Handbook of Biological Confocal Microscopy* (J. B. Pawley, ed.), ch. 1, New York, US: Springer Science, third ed., 2006.

[92] B. Huang, W. Wang, M. Bates, and X. Zhuang, “Three-dimensional super-resolution imaging by stochastic optical reconstruction microscopy.,” *Science*, vol. 319, pp. 810–3, Feb. 2008.

[93] L. Schermelleh, R. Heintzmann, and H. Leonhardt, “A guide to super-resolution fluorescence microscopy.,” *The Journal of cell biology*, vol. 190, pp. 165–75, July 2010.

[94] A. Punge, S. O. Rizzoli, R. Jahn, J. D. Wildanger, L. Meyer, A. Schönle, L. Kastrup, and S. W. Hell, “3D reconstruction of high-resolution STED microscope images.,” *Microscopy research and technique*, vol. 71, pp. 644–50, Sept. 2008.

[95] R. Schmidt, C. A. Wurm, S. Jakobs, J. Engelhardt, A. Egner, and S. W. Hell, “Spherical nanosized focal spot unravels the interior of cells.,” *Nature methods*, vol. 5, pp. 539–44, June 2008.

[96] C. Osseforth, J. R. Moffitt, L. Schermelleh, and J. Michaelis, “Simultaneous dual-color 3D STED microscopy.,” *Optics express*, vol. 22, pp. 7028–39, Mar. 2014.

[97] L. Petrak and W. Salmon, “Fluorescent Microsphere Test Speciment Preparations.” https://nic.med.harvard.edu/bead_preparations.

[98] W. Zauner, N. A. Farrow, and A. M. Haines, “In vitro uptake of polystyrene microspheres: effect of particle size, cell line and cell density,” *Journal of Controlled Release*, vol. 71, pp. 39–51, Mar. 2001.

[99] W. Strober, “Trypan blue exclusion test of cell viability.,” *Current protocols in immunology*, vol. Appendix 3, p. Appendix 3B, May 2001.

[100] J. B. Pawley, “Points, Pixels, and Gray Levels: Digitizing Image Data,” in *Handbook of Biological Confocal Microscopy* (J. B. Pawley, ed.), ch. 4, pp. 64–70, New York, US: Springer Science, third ed., 2006.

[101] D. T. Pham and D. Karaboga, *Intelligent Optimisation Techniques: Genetic Algorithms, Tabu Search, Simulated Annealing and Neural Networks*. London: Springer-Verlag, 2000.

[102] A. H. K. Roeder, A. Cunha, M. C. Burl, and E. M. Meyerowitz, “A computational image analysis glossary for biologists.,” *Development*, vol. 139, pp. 3071–80, Sept. 2012.

[103] I. Hughes and T. Hase, *Measurements and Their Uncertainties: A Practical Guide to Modern Error Analysis*. Oxford: Oxford University Press, 2010.

[104] D. Lutz, K. A. Nelson, C. Gochanour, and M. Fayer, “Electronic excited state energy transfer, trapping by dimers and fluorescence quenching in concentrated dye solutions: Picosecond transient grating experiments,” *Chemical Physics*, vol. 58, pp. 325–334, Jan. 1981.

[105] A. Giudice, M. Ghioni, R. Biasi, F. Zappa, S. Cova, P. Maccagnani, and A. Gulinatti, “High-rate photon counting and picosecond timing with silicon-SPAD based compact detector modules,” *Journal of Modern Optics*, vol. 54, pp. 225–237, Jan. 2007.

[106] S. Cova, M. Ghioni, A. Lacaita, C. Samori, and F. Zappa, “Avalanche photodiodes and quenching circuits for single-photon detection.,” *Applied optics*, vol. 35, pp. 1956–76, Apr. 1996.

[107] S. Cova, A. Lacaita, and G. Ripamonti, “Trapping phenomena in avalanche photodiodes on nanosecond scale,” *IEEE Electron Device Letters*, vol. 12, pp. 685–687, Dec. 1991.

[108] G. Anzivino, H. Arnaudon, P. Baillon, P. Benetti, L. Boskma, P. Burger, A. Contin, R. DeSalvo, P. Gorodetzky, D. Grassi, W. Hao, H. He, L. Liu, M. Lundin, M. Mondardini, S. Paolucci, M. Rossella, J. Santiard, R. Schomaker, K. You, K. Wang, Y. Wang, X. Xia, C. Xu, C. Yang, and M. Zhao, “Review of the hybrid photo diode tube (HPD) an advanced light detector for physics,” *Nuclear Instruments and Methods in Physics Research Section A: Accelerators, Spectrometers, Detectors and Associated Equipment*, vol. 365, pp. 76–82, Nov. 1995.

[109] Becker & Hickl GmbH, “The HPM-100-40 Hybrid Detector.”

[110] G. Vicidomini, A. Schönle, H. Ta, K. Y. Han, G. Moneron, C. Eggeling, and S. W. Hell, “STED nanoscopy with time-gated detection: theoretical and experimental aspects.,” *PloS one*, vol. 8, p. e54421, Jan. 2013.

[111] S. Culley, “Super Resolution Fluorescence Microscopy Using Stimulated Emission Depletion,” 2011. UCL Master’s Project.

[112] K. Y. Han, K. I. Willig, E. Rittweger, F. Jelezko, C. Eggeling, and S. W. Hell, “Three-dimensional stimulated emission depletion microscopy of nitrogen-vacancy centers in diamond using continuous-wave light.,” *Nano letters*, vol. 9, pp. 3323–9, Sept. 2009.

[113] G. Moneron, R. Medda, B. Hein, A. Giske, V. Westphal, and S. W. Hell, "Fast STED microscopy with continuous wave fiber lasers.," *Optics express*, vol. 18, pp. 1302–9, Jan. 2010.

[114] A. Diaspro, F. Federici, and M. Robello, "Influence of refractive-index mismatch in high-resolution three-dimensional confocal microscopy," *Applied Optics*, vol. 41, no. 4, pp. 685–690, 2002.

[115] J. C. Spall, *Introduction to Stochastic Search and Optimization: Estimation, Simulation and Control.* Hoboken, USA: John Wiley & Sons, Ltd, 2003.

[116] J. Canny, "A Computational Approach to Edge Detection," *IEEE Transactions on Pattern Analysis and Machine Intelligence*, vol. PAMI-8, pp. 679–698, Nov. 1986.

[117] G. Vicidomini, G. Moneron, C. Eggeling, E. Rittweger, and S. W. Hell, "STED with wavelengths closer to the emission maximum.," *Optics express*, vol. 20, pp. 5225–36, Feb. 2012.

[118] v. Bálint, I. Verdeny Vilanova, A. Sandoval Álvarez, and M. Lakadamyali, "Correlative live-cell and superresolution microscopy reveals cargo transport dynamics at microtubule intersections.," *Proceedings of the National Academy of Sciences of the United States of America*, vol. 110, pp. 3375–80, Mar. 2013.

[119] J. F. Ashmore, S. Culley, J. Boutet de Monvel, C. Petit, and S. Safieddine, "Two Photon Imaging of Calcium Signalling at the Mouse Inner Hair Cell Ribbon Synapse," *Biophysical Journal*, vol. 98, p. 508a, Jan. 2010.

[120] S. P. Poland, N. Krstajić, R. D. Knight, R. K. Henderson, and S. M. Ameer-Beg, "Development of a doubly weighted Gerchberg-Saxton algorithm for use in multibeam imaging applications.," *Optics letters*, vol. 39, pp. 2431–4, Apr. 2014.

[121] R. McGorty, D. Kamiyama, and B. Huang, "Active Microscope Stabilization in Three Dimensions Using Image Correlation.," *Optical nanoscopy*, vol. 2, p. 3, Apr. 2013.

[122] R. Marsh, N. Leonczek, D. Armoogum, L. Porres, O. Mongin, M. Blanchard-Desce, and A. Bain, "Stimulated emission depletion dynamics in push-push polyenes," in *Proceedings of the Society of Photo-optical Instrumentation Engineers (SPIE)*, pp. 117–128, 2004.

[123] D. A. Armoogum, R. J. Marsh, N. Nicolaou, O. Mongin, M. Blanchard-Desce, and A. J. Bain, "Stimulated Emission Depletion and Fluorescence Correlation Spectroscopy of a Branched Quadrupolar Chromophore," in *Proceedings of the Society of Photo-optical Instrumentation Engineers (SPIE)*, p. S300, 2008.

[124] B. R. Rankin, G. Moneron, C. A. Wurm, J. C. Nelson, A. Walter, D. Schwarzer, J. Schroeder, D. A. Colón-Ramos, and S. W. Hell, "Nanoscopy in a living multicellular organism expressing GFP.," *Biophysical journal*, vol. 100, pp. L63–5, June 2011.

[125] G. Vicidomini, I. C. Hernández, M. D'Amora, F. C. Zanacchi, P. Bianchini, and A. Diaspro, "Gated CW-STED microscopy: a versatile tool for biological nanometer scale investigation.," *Methods*, vol. 66, pp. 124–30, Mar. 2014.

[126] B. Harke, J. Keller, C. K. Ullal, V. Westphal, A. Schönle, and S. W. Hell, "Resolution scaling in STED microscopy," *Optics Express*, vol. 16, p. 4154, Mar. 2008.

[127] P. Dedecker, B. Muls, J. Hoefkens, J. Enderlein, and J.-i. Hotta, "Orientational effects in the excitation and de-excitation of single molecules interacting with donut-mode laser beams," *Optics Express*, vol. 12, pp. 3372–3383, Mar. 2007.

[128] M. Leutenegger, C. Eggeling, and S. W. Hell, "Analytical description of STED microscopy performance.," *Optics express*, vol. 18, pp. 26417–29, Dec. 2010.

[129] E. Kantola, T. Leinonen, S. Ranta, M. Tavast, and M. Guina, "High-efficiency 20W yellow VECSEL.," *Optics express*, vol. 22, pp. 6372–80, Mar. 2014.

[130] D. T. Westwick and R. E. Kearney, *Identification of Nonlinear Physiological Systems*. Piscataway, NJ, USA: Wiley, 2003.

[131] J. Wodarczyk and B. Kierdaszuk, "Interpretation of fluorescence decays using a power-like model.," *Biophysical journal*, vol. 85, pp. 589–98, July 2003.

[132] N.-S. Cheng, "Formula for the Viscosity of a Glycerol-Water Mixture," *Industrial & Engineering Chemistry Research*, vol. 47, pp. 3285–3288, May 2008.

[133] J. R. Janesick, "Photon Transfer Noise Sources," in *Photon Transfer: DN $-->$ lambda*, ch. 3, Washington, USA: SPIE, 2007.

[134] Microelectronics Heat Transfer Laboratory, "Fluid Properties Calculator," 1997. http://www.mhtl.uwaterloo.ca/old/onlinetools/airprop/airprop.html.

[135] H. Kang, B. Jia, and M. Gu, "Polarization characterization in the focal volume of high numerical aperture objectives.," *Optics express*, vol. 18, pp. 10813–21, May 2010.

[136] K. C. B. Lee, J. Siegel, S. E. D. Webb, S. Lévêque-Fort, M. J. Cole, R. Jones, K. Dowling, M. J. Lever, and P. M. W. French, "Application of the stretched exponential function to fluorescence lifetime imaging," *Biophysical Journal*, vol. 81, no. 3, pp. 1265–1274, 2001.

[137] P. R. Barber, S. M. Ameer-Beg, S. Pathmananthan, M. Rowley, and A. C. C. Coolen, "A Bayesian methods for single molecule, fluorescence burst analysis," *Biomedical Optics Express*, vol. 1, no. 4, pp. 1148–1158, 2010.

[138] M. Rowley, P. R. Barber, A. C. C. Coolen, and B. Vojnovic, "Bayesian analysis of fluorescence lifetime imaging data," *SPIE Proceedings*, vol. 7903, p. 790325, 2011.

[139] H. E. Keller, "Objective Lenses For Confocal Microscopy," in *Handbook of Biological Confocal Microscopy* (J. B. Pawley, ed.), ch. 7, New York: Springer Science, third ed., 2006.

[140] W. R. Zipfel, R. M. Williams, and W. W. Webb, "Nonlinear magic: multiphoton microscopy in the biosciences," *Nature Biotechnology*, vol. 21, pp. 1369–1377, Nov. 2003.

[141] M. Dyba and S. Hell, "Focal Spots of Size $\lambda/23$ Open Up Far-Field Florescence Microscopy at 33 nm Axial Resolution," *Physical Review Letters*, vol. 88, p. 163901, Apr. 2002.

[142] M. Dyba, J. Keller, and S. W. Hell, "Phase filter enhanced STED-4Pi fluorescence microscopy: theory and experiment," *New Journal of Physics*, vol. 7, pp. 134–134, May 2005.

[143] O. Krichevsky and G. Bonnet, "Fluorescence correlation spectroscopy: the technique and its applications," *Reports on Progress in Physics*, vol. 65, pp. 251–297, Feb. 2002.

[144] J. Widengren, R. Rigler, and U. Mets, "Triplet-state monitoring by fluorescence correlation spectroscopy.," *Journal of fluorescence*, vol. 4, pp. 255–8, Sept. 1994.

[145] P. Schwille, F. J. Meyer-Almes, and R. Rigler, "Dual-color fluorescence cross-correlation spectroscopy for multicomponent diffusional analysis in solution.," *Biophysical journal*, vol. 72, pp. 1878–86, Apr. 1997.

[146] R. Y. Tsien, L. A. Ernst, and A. S. Waggoner, "Fluorophores for confocal microscopy: photophysics and photochemistry," in *Handbook of Biological Confocal Microscopy* (J. B. Pawley, ed.), ch. 16, New York, US: Springer Science, third ed., 2006.

[147] C. Culbertson, "Diffusion coefficient measurements in microfluidic devices," *Talanta*, vol. 56, pp. 365–373, Feb. 2002.

[148] L. Song, C. A. Varma, J. W. Verhoeven, and H. J. Tanke, "Influence of the triplet excited state on the photobleaching kinetics of fluorescein in microscopy.," *Biophysical journal*, vol. 70, pp. 2959–68, June 1996.

[149] L. S. Forster and D. Dudley, "The luminescence of fluorescein dyes," *The Journal of Physical Chemistry*, vol. 66, pp. 838–840, May 1962.

[150] M. P. Lettinga, H. Zuilhof, and M. A. M. J. van Zandvoort, "Phosphorescence and fluorescence characterization of fluorescein derivatives immobilized in various polymer matrices," *Physical Chemistry Chemical Physics*, vol. 2, no. 16, pp. 3697–3707, 2000.

[151] C. M. Marian, M. Etinski, and V. Rai-Constapel, "Reverse intersystem crossing in rhodamines by near-infrared laser excitation.," *The journal of physical chemistry. A*, vol. 118, pp. 6985–90, Aug. 2014.

[152] G. R. Fleming, A. W. E. Knight, J. M. Morris, R. J. S. Morrison, and S. W. Robinson, "Picosecond fluorescence studies of xanthene dyes," *Journal of the American Chemical Society*, vol. 99, no. 13, pp. 4306–4311, 1977.

[153] X.-F. Zhang, J. Zhang, and L. Liu, "Fluorescence properties of twenty fluorescein derivatives: lifetime, quantum yield, absorption and emission spectra.," *Journal of fluorescence*, vol. 24, pp. 819–26, May 2014.

[154] P. G. Bowers and G. Porter, "Triplet State Quantum Yields for Some Aromatic Hydrocarbons and Xanthene Dyes in Dilute Solution," *Proceedings of the Royal Society A: Mathematical, Physical and Engineering Sciences*, vol. 299, pp. 348–353, July 1967.

[155] R. Schirhagl, K. Chang, M. Loretz, and C. L. Degen, “Nitrogen-vacancy centers in diamond: nanoscale sensors for physics and biology.,” *Annual review of physical chemistry*, vol. 65, pp. 83–105, Jan. 2014.

[156] W. Demtroder, *Laser Spectroscopy Volume 1: Basic Principles.* Springer, fourth ed., 2008.

[157] M. Heupel, I. Gregor, and E. Becker, St. andThiel, “Photophysical and photochemical properties of electronically excited fluorescent dyes: a new type of time-resolved laser-scanning spectroscopy,” *International Journal of Photoenergy*, vol. 1, no. 3, pp. 165–172, 1999.

[158] G. Lukinavičius, L. Reymond, E. D’Este, A. Masharina, F. Göttfert, H. Ta, A. Güther, M. Fournier, S. Rizzo, H. Waldmann, C. Blaukopf, C. Sommer, D. W. Gerlich, H.-D. Arndt, S. W. Hell, and K. Johnsson, “Fluorogenic probes for live-cell imaging of the cytoskeleton.,” *Nature methods*, vol. 11, pp. 731–3, July 2014.

Appendix A

Spectra of fluorophores

The figures below show the absorption and emission structure of the fluorophores used in this thesis along with the chemical structures provided on the material data sheets (where available). The light blue lines show the single photon pump wavelength used from excitation (490nm, two photon pump not shown), and the orange and red lines show the dump wavelength(s) used.

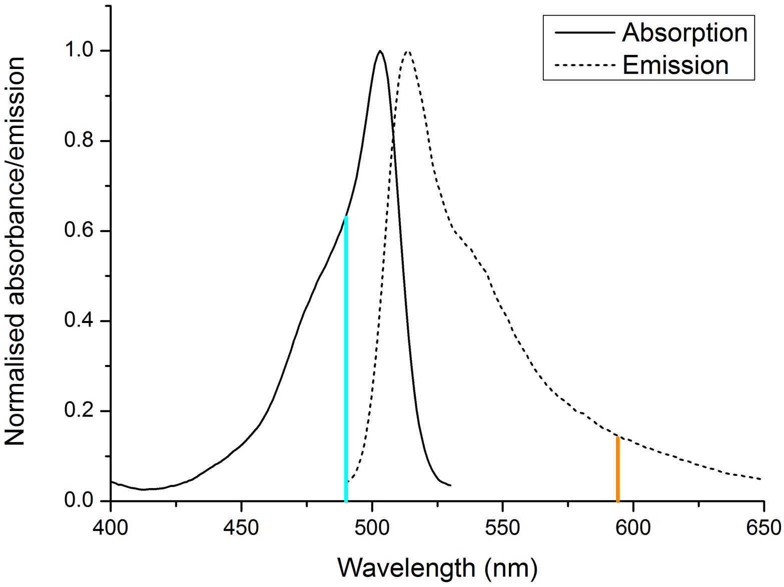

Figure A.1: Absorption and emission spectra of yellow-green fluospheres provided by the manufacturer (Invitrogen Inc.)

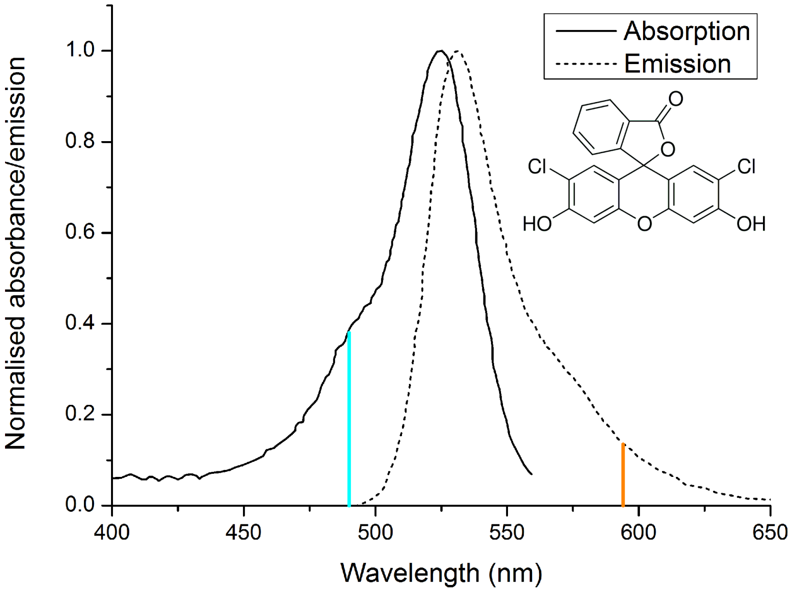

Figure A.2: Absorption and emission spectra of 2',7'-dichlorofluorescein in water. Taken from X. Zhang et al. “Fluorescence properties of twenty fluorescein derivatives: lifetime, quantum yield, absorption and emission spectra,” *Journal of Fluorescence*, vol. 24, pg. 816-26, 2014.

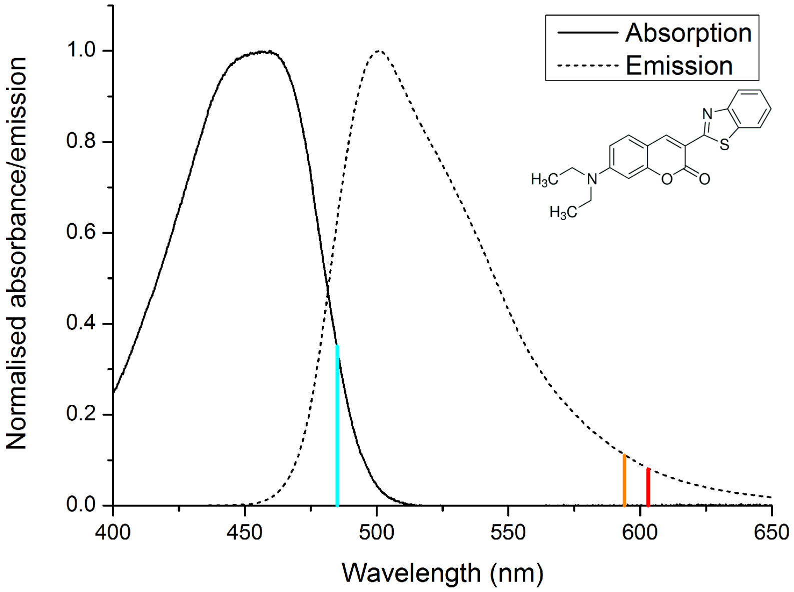

Figure A.3: Absorption and emission spectra of coumarin 6 in ethanol. Taken from S. Prahl “Coumarin 6,” URL: http://omlc.org/spectra/PhotochemCAD/html/013.html, March 2012.

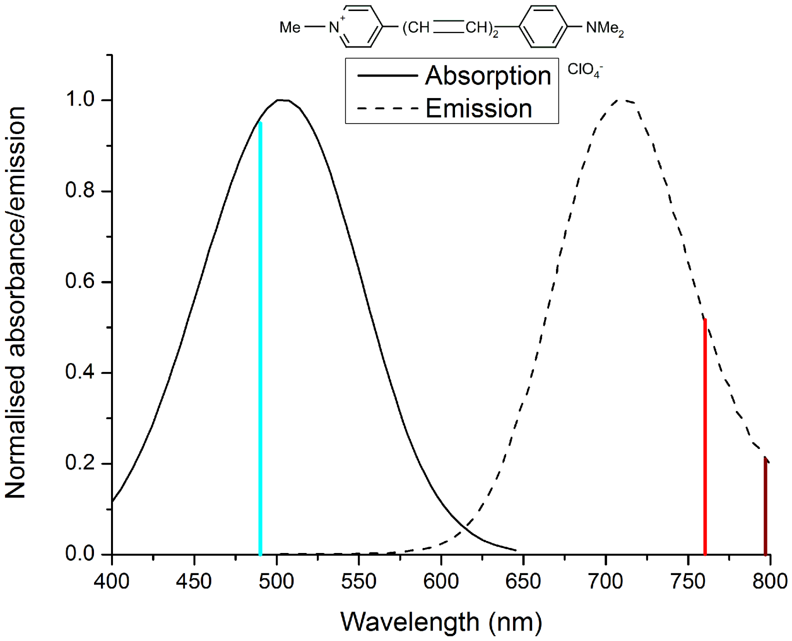

Figure A.4: Absorption and emission spectra of pyridine 2 (LDS 722) in water. Taken from V. Martínez-Martínez et al. "Distribution and orientation study of dyes intercalated into single sepiolite fibers. A confocal fluorescence microscopy approach," *Journal of Materials Chemistry*, vol. 21, pg. 269, 2011.

Appendix B

Custom-written MATLAB code

B.1 FluoEvolution

```
%% FluoEvolution: code to generate temporally evolving
    fluorescence images

% Read in structure to 'image'
pic = imread('image.png');
pic = im2double(pic);

% Set imaging parameters
lambda = 550;
NA = 1.2;

FWHM = lambda/(2*NA);
PXsize = 40;
FWHM_PX = FWHM/PXsize;

% Calculate omega
wD = FWHM_PX/(2*sqrt(2*log(2)));

% Create two-dimensional depletion intensity distribution
     kernel (Eq. 2.17)
Id = zeros(21,21);

for y = 1:21,
    for x = 1:21,
        Id(y,x) = exp(-((((y-11)^2)/(2*wD^2))+(((x-11)^2)
           /(2*wD^2))));
    end
end

% Convolve depletion intensity kernel Id with imported
    image to generate
% confocal image for reference (Eq. 2.2)
confocal = zeros(95,95);
blank = zeros(95,95);
```

```

for y = 1:75,
    for x = 1:75,
        blank = zeros(95,95);
        blank(y:y+20,x:x+20) = 500*pic(y,x)*Id;
        confocal = confocal+blank;
    end
end

% Set lifetime parameters
Fd = 0.5;
tf = 3;

% Generate two-dimensional lifetime kernel td (Eq. 2.20)
td = zeros(21,21);

for i = 1:(21*21),
    td(i) = ((1-Fd)*tf)/(1+(Id(i)-1)*Fd);
end

% Create time stack of 200 images Intot(x,y,t) simulated at 0.1ns intervals
Intot = zeros(75,75,201);

for t = 1:201,

    expfun = zeros(21,21);
    for i=1:(21*21),
        expfun(i)=expfun(i)+exp(-(0.1*(t-1))/td(i));
    end

    product = zeros(21,21);
    for i = 1:(21*21),
        product(i) = Id(i).*expfun(i);
    end

    Tpic = zeros(95,95);
    for y = 1:75,
        for x = 1:75,
            Tint = zeros(95,95);
            Tint(y:y+20,x:x+20) = 500*pic(y,x)*product;
            Tpic = Tpic+Tint;
        end
    end

    Intot(:,:,t) = Tpic(11:85,11:85);

end

```

```
% Example of 5 time windows produced by adding narrow
    time points
TW1im = Intot(:,:,1:10);
TW1im = sum(TW1im,3);

TW2im = Intot(:,:,11:30);
TW2im = sum(TW2im,3);

TW3im = Intot(:,:,31:60);
TW3im = sum(TW3im,3);

TW4im = Intot(:,:,61:100);
TW4im = sum(TW4im,3);

TW5im = Intot(:,:,101:140);
TW5im = sum(TW5im,3);
```

B.2 SimEqRecon

```
%% SimEqRecon: code to reconstruction super resolution
    images from
%% simulated data using simultaneous equations

function SimEqRecon

%% Same code as in FluoEvolution to generate Intot(x,y,t)
     and 5 time
%% window images (TW1im, TW2im...TW5im), omitted to avoid
     repetition

% Selection of line profiles from time window images
TW1 = TW1im(:,38);
TW2 = TW2im(:,38);
TW3 = TW3im(:,38);
TW4 = TW4im(:,38);
TW5 = TW5im(:,38);

% Generate random starting point for coefficients
c0 = [randi([-5 5]) randi([-10 10]) randi([-25 25]) randi
    ([-50 50])]

% Choose fitting algorithm
options = optimset('Algorithm', 'levenberg-marquardt');

% Call matlab simultaneous equation solving function
[c,fval] = fsolve(@sumfun,c0,options);

% Generate reconstructed line profile using generated
    coefficients
```

```
Y = TW1 + c(1)*TW2 + c(2)*TW3 + c(3)*TW4 + c(4)*TW5;
Y = Y';
X = 0:74;
X = X';

% Define Gaussian fitting function
f = fittype('a*exp(-((x-b)/c)^2)+d');

% Fit reconstructed line profile to Gaussian distribution
[Yfit Ygof] = fit(X, Y', f, 'Start', [max(Y) 11 3 mean(Y(1:3))]);
Ycoeffs = coeffvalues(Yfit);

% Calculate FWHM of fitted Gaussian (in terms of pixel number) as a
% measure of resolution
YFWHM = Ycoeffs(3)*sqrt(2*log(2))

% R-squared goodness of fit to Gaussian distribution
r2 = Ygof.rsquare

% Generate reconstructed image from time window images
FinIm = TW1im + c(1)*TW2im + c(2)*TW3im + c(3)*TW4im + c(4)*TW5im;

% Equations to solve
function F = sumfun(c)

    % 5 simultaneous equations for the 5 time windows attempting to
    % set 5 pixels equal to zero adjacent to point source (Eq. 2.26)
    F = [TW1(29)+c(1)*TW2(29)+c(2)*TW3(29)+c(3)*TW4(29)+c(4)*TW5(29);
      TW1(30)+c(1)*TW2(30)+c(2)*TW3(30)+c(3)*TW4(30)+c(4)*TW5(30);
      TW1(31)+c(1)*TW2(31)+c(2)*TW3(31)+c(3)*TW4(31)+c(4)*TW5(31);
      TW1(32)+c(1)*TW2(32)+c(2)*TW3(32)+c(3)*TW4(32)+c(4)*TW5(32);
      TW1(33)+c(1)*TW2(33)+c(2)*TW3(33)+c(3)*TW4(33)+c(4)*TW5(33)];

  end
end
```

B.3 AxialEvolution

```
%% AxialEvolution: code to generate temporally evolving
   fluorescence images
%% in the xz plane

% Read in structure to 'image'
pic = imread('image.png');
pic = im2double(pic);

% Set imaging parameters
lambda = 550;
NA = 1.2;

FWHM_x = lambda/(2*NA);
PXsize = 20;
FWHM_PX_x = FWHM_x/PXsize;

FWHM_z=(2*lambda*1.33)/(NA^2);
FWHM_PX_z=FWHM_z/PXsize;

% Calculate omega
wD = FWHM_PX_x/(2*sqrt(2*log(2)));

% Calculate two-dimensional depletion intensity
   distribution in xz
Id = zeros(115,115);

for z = 1:115,
    for x = 1:115,
        Id(z,x) = exp(-((((x-58)^2)/(2*wD^2))))*...
            (0.25*FWHM_PX_z^2)/((z-58)^2+(0.5*FWHM_PX_z)
               ^2);
    end
end

% Set lifetime parameters
Fd = 0.5;
tf = 3;

% Generate two-dimensional lifetime kernel td (Eq. 2.20)
td = zeros(115,115);

for i = 1:(115*115),
    td(i) = ((1-Fd)*tf)/(1+(Id(i)-1)*Fd);
end

% Create time stack of 200 images Intot(z,x,t) simulated
   at 0.1ns intervals
Intot = zeros(115, 115, 201);
```

```

for i = 1:115,
    for j = 1:115,
        for T = 1:201,
            t = 0.1*(T-1);
            Intot(i,j,T) = 1000*Id(i,j)*exp(-t/td(i,j));
        end
    end
end

% Example of 5 time windows produced by adding narrow
   time points
TW1im = Intot(:,:,1:10);
TW1im = sum(TW1im,3);

TW2im = Intot(:,:,11:30);
TW2im = sum(TW2im,3);

TW3im = Intot(:,:,31:60);
TW3im = sum(TW3im,3);

TW4im = Intot(:,:,61:100);
TW4im = sum(TW4im,3);

TW5im = Intot(:,:,101:140);
TW5im = sum(TW5im,3);
```

B.4 GetImages and TWSelect

```
%% GetImages: code to read data from .bin files produced
   by microscope

% Select data file
[filename pathname]=uigetfile('*.bin', 'Pre-histogrammed
   data:');
fid=fopen([pathname filename]);

% Read header information
fseek(fid,0,'bof');
PixX = fread(fid, 1, 'int32');

fseek(fid,4,'bof');
PixY = fread(fid, 1, 'int32');

fseek(fid,8,'bof');
PixResol = fread(fid, 1, 'float32');

fseek(fid,12,'bof');
TCSPCChannels = fread(fid, 1, 'int32');
```

```

fseek(fid,16,'bof');
TimeResol = fread(fid, 1, 'float32');

% Read data from file and convert into lifetime histogram
fseek(fid,20,'bof');
Data = fread(fid,inf,'int32');

Hist = zeros(TCSPCChannels,1);

for i=1:(PixX*PixY)
    Hist=Hist+Data(((TCSPCChannels*(i-1))+1:(
       TCSPCChannels*i));
end

% Free up memory
clear Data
TWclose = 0;

% Pass relevant information into time window selection
   program
h=TWSelect(Hist, TimeResol, fid, TCSPCChannels, PixX,
   PixY, PixResol);

waitfor(h)
```

```
%% TWSelect: a GUI for interactively choosing time window
    images from a
%% fluorescence decay and plotting intensity profiles for
    obtained images

function h = TWSelect(Hist, TimeResol, fid, TCSPCChannels
   , PixX, PixY, ...
    PixResol)

%% Initialization tasks

scrsz = get(0,'ScreenSize');
scrwidth = scrsz(3);
scrheight = scrsz(4);

lh = [];
S.TW = zeros(PixY, PixX, 5);
S.Tf = [];

TWclose = 0;

%% Components of the GUI - omitted here as just setting
   up graphics

```

```
%% Plot lifetime histogram
semilogy(S.Hist, Hist)
axis tight
axes(S.Hist)
xlabel('Channel number')
ylabel('Intensity (counts)')

%% Callback functions for GUI components

    % Trim lifetime histogram
    function ExpTrim(~,~)

        uiwait(msgbox('Select end of decay to trim'));

        set(S.fh, 'CurrentAxes', S.Hist);

        Trim = floor(ginput(1));
        Trim = Trim(1);

        HistT = Hist(1:Trim);

        semilogy(HistT)
        axis tight
        xlabel('Channel number')
        ylabel('Intensity (counts)')

    end

    % Fit biexponential decay to lifetime histogram
    function ExpFitting(~,~)

        uiwait(msgbox('Select start point for exponential
            fitting'));

        ExpStart = floor(ginput(1));

        YFitData = Hist(ExpStart:length(Hist));
        XFitData = (ExpStart:length(Hist))*TimeResol;

        ExpFit = fit(XFitData',YFitData,'exp2');

        ExpCoeffs = coeffvalues(ExpFit);

        Tf = ((ExpCoeffs(1)*(-1/ExpCoeffs(2)))+ ...
            (ExpCoeffs(3)*(-1/ExpCoeffs(4))))/(ExpCoeffs
               (1)+ExpCoeffs(3));

        TfChan = round(Tf/TimeResol);

```

```
        line([ExpStart(1) ExpStart(1)], [min(Hist) max(Hist)], ...
            'Color', 'b', 'LineWidth', 0.5)
        line([TfChan+ExpStart(1) TfChan+ExpStart(1)], ...
            [min(Hist) max(Hist)], 'Color', 'r', 'LineWidth',1.5)

        sth = uicontrol(S.Fitted, 'Style', 'text', 'Units', ...
            'normalized', 'Position', [0.05, 0.7, 0.9, 0.2], 'String', ...
            ['Fitting start point at channel ' num2str(ExpStart(1))]);

        sth = uicontrol(S.Fitted, 'Style', 'text', 'Units', ...
            'normalized', 'Position', [0.05, 0.3, 0.9, 0.4], 'String', ...
            ['I = ' num2str(ExpCoeffs(1),3)...
            'exp(-t/' num2str(abs(1/ExpCoeffs(2)),3) ...
            ') + ' num2str(ExpCoeffs(3),3)...
            'exp(-t/' num2str(abs(1/ExpCoeffs(4)),3) ...
            ')']);

        sth1 = uicontrol(S.Fitted, 'Style', 'text', 'Units', ...
            'normalized','Position', [0.05, 0.05, 0.9, 0.15], 'String', ...
            ['Fluorescence lifetime = ' num2str(Tf,3)...
            'ns (channel no. ' num2str(TfChan+ExpStart(1),3) ')']);

        S.Tf = Tf;
        assignin('base', 'TfDumped', S.Tf);

    end

    % Reset histogram
    function Reset(~,~)

        set(S.fh, 'CurrentAxes', S.Hist);
        plot(Hist)
        axis tight
        xlabel('Channel number')

        sth = uicontrol(S.Fitted, 'Style', 'text', 'Units', ...
            'normalized', 'Position', [0.05, 0.5, 0.9, 0.4], 'String', '');

```

```
        sth1 = uicontrol(S.Fitted, 'Style', 'text', 'Units', ...
            'normalized','Position', [0.05, 0.05, 0.9, 0.4], 'String', '');
    end

    % Plot time window image
    function [] = TWPlot(varargin)

        X = ginput(2);

        if X(1)<X(2),
            WinStart = floor(X(1));
            WinStop = floor(X(2));
        else WinStart = floor(X(2));
            WinStop = floor(X(1));
        end

        TWOut = zeros(PixX*PixY,1);

        hWait = waitbar(0, ['Plotting from channel ' num2str(WinStart) ...
            ' to channel ' num2str(WinStop) '...']);
        steps = WinStop-WinStart;

        for i = WinStart:WinStop,

            fseek(fid,20+(i-1)*4,'bof');
            im = fread(fid,inf,'int32',(TCSPCChannels-1)*4);
            TWOut = TWOut+im;

            step = i-(WinStart-1);
            waitbar(step/steps)

        end

        close(hWait)

        TWOut = reshape(TWOut,PixY,PixX)';

        clear im

        h = varargin{1};

        N = find(S.pbh==h);

        set(S.fh,'CurrentAxes',S.ax(N));
        imagesc(TWOut)
```

```
        colormap hot; colorbar('Location','SouthOutside');...
            axis image; axis off
        set(S.edStart(N),'String',num2str(WinStart));
        set(S.edStop(N),'String',num2str(WinStop));

        S.TW(:,:,N) = TWOut;

    end

    % Plot updated time window image
    function [] = TWUpdate(varargin)

        TWOut = zeros(PixY*PixX,1);

        h = varargin{1};

        N = find(S.pbhR==h);

        WinStart = str2double(get(S.edStart(N), 'String'));
        WinStop = str2double(get(S.edStop(N), 'String'));

        hWait = waitbar(0, 'Updating image...');
        steps = WinStop - WinStart;

        for i = WinStart:WinStop,

            fseek(fid,20+(i-1)*4,'bof');
            im = fread(fid,inf,'int32',(TCSPCChannels-1)*4);
            TWOut = TWOut+im;

            step = i-(WinStart-1);
            waitbar(step/steps)

        end

        close(hWait)

        TWOut = reshape(TWOut,PixY,PixX)';

        clear im

        set(S.fh,'CurrentAxes',S.ax(N))
        imagesc(TWOut)
        colormap hot; colorbar('Location','SouthOutside');...
            axis image; axis off
        S.TW(:,:,N) = TWOut;
```

```

    end

    % Close program and assign variables into base
       workspace
    function [] = TWClose(varargin)

        assignin('base', 'TW1', S.TW(:,:,1));
        assignin('base', 'TW2', S.TW(:,:,2));
        assignin('base', 'TW3', S.TW(:,:,3));
        assignin('base', 'TW4', S.TW(:,:,4));
        assignin('base', 'TW5', S.TW(:,:,5));

        assignin('base', 'TWclose', 1);

        close(S.fh)

    end

end
```

B.5 NoisyEvolution

```
%% NoisyEvolution: code for noisy evolution of simulated
   data

%% Same code as FluoEvolution up to line 49.

% Generate noiseless image Intot(x,y,t) and noisy image
   noiseImage(x,y,t)
Intot = zeros(75,75,201);
noiseImage = zeros(75,75,201);

for t = 1:201,

    expfun = zeros(21,21);
    for i = 1:(21*21),
        expfun(i)=expfun(i)+exp(-(0.1*t)/td(i));
    end

    product = zeros(21,21);
    for i = 1:(21*21),
        product(i) = Id(i).*expfun(i);
    end

    Tpic = zeros(95,95);
    for y = 1:75,
        for x = 1:75,
            Tint = zeros(95,95);
```

```
            Tint(y:y+20,x:x+20) = 500*pic(y,x)*product;
            Tpic = Tpic+Tint;
        end
    end

    Intot(:,:,t) = Tpic(11:85,11:85);
    Tpic = Tpic(11:85,11:85);

    noisePic = zeros(75,75);

    % Poisson noise generation: noise is added to each pixel as a random
    % number from normal distribution with mean = 0 and
    % stdev = sqrt(intensity). If a negative pixel value is produced,
    % noise generation is repeated until a non-negative value is produced.
    for y = 1:75,
        for x = 1:75,
            noisePic(y,x) = Tpic(y,x) + normrnd(0,sqrt(Tpic(y,x)));
            while noisePic(y,x)<0,
                noisePic(y,x) = Tpic(y,x) + normrnd(0,sqrt(Tpic(y,x)));
            end
        end
    end

    noiseImage(:,:,t) = noisePic;

end
```

B.6 GARecon

```
%% GARecon: code to reconstruct super resolution images using genetic
%% algorithm from five time window images
function h = GA_recon(im1, im2, im3, im4, im5)

%% Initialization tasks
global S im1Rsq xRange yRange X im1Prof f base
global FWHMguess
global idealProf
global gamma
global coeffSet xOpt

scrsz = get(0,'ScreenSize');
scrwidth = scrsz(3);
scrheight = scrsz(4);
```

```

PixX = size(im1,1);

S.xRanges = zeros(PixX,3);
S.yRanges = zeros(PixX,3);
S.idealProfs = zeros(PixX,3);
S.residualVectors = zeros(PixX,3);

coeffSet = zeros(1,6);

%% Components of the GUI - omitted here as just setting
   up graphics

%% Display TW1 image
set(S.fh, 'CurrentAxes', S.imView);
imagesc(im1);
colormap hot;

%% Callback functions

    % Get value for target resolution
    function getGamma(varargin)
        items = get(S.gamMenu,'String');
        index_selected = get(S.gamMenu,'Value');
        item_selected = items{index_selected};
        gamma = str2double(item_selected);
    end

    % Clip negative values in reconstructed image to zero
    function cmapEdit(varargin)
        set(S.fh, 'CurrentAxes',S.imFinal)
        CLim = get(S.imFinal,'CLim');
        CMax = CLim(2);
        set(S.imFinal, 'CLim', [0 CMax]);
    end

    % Select profiles from TW1 image
    function selectProf(hObject,eventdata)

        clear xRange yRange im1Prof idealProf
           residualVector idealProfNorm

        h=hObject;
        eventdata

        if find(S.profRedraw==h)>0,
            N = find(S.profRedraw==h);
        else
            N = find(S.profSel==h);
        end
```

```

        N = find(S.profSel==h);

        S.xRanges(:,N) = zeros(PixX,1);
        S.yRanges(:,N) = zeros(PixX,1);
        S.idealProfs(:,N) = zeros(PixX,1);
        S.residualVectors(:,N) = zeros(PixX,1);

        str = (['S.tb(' num2str(N) ')'])

        if exist(str)==1,
            delete(S.tb(N));
        end

        figure(S.fh)
        set(S.fh, 'CurrentAxes', S.imView);
        [xVals yVals]=ginput(2);

        A = [xVals(1) 1; xVals(2) 1];
        B = [yVals(1); yVals(2)];

        linCoeffs = A\B;

        % Mark profile on TW1 image
        S.lh(N) = line([xVals(1) xVals(2)], [yVals(1) yVals(2)], ...
            'Color', 'w', 'LineWidth',1.5);
        S.tb(N) = text(xVals(2), yVals(2), num2str(N), 'Color', 'w',...
            'FontSize',16);

        im1Prof = [];

        % Extract TW1 values from profile
        if round(max(yVals))==round(min(yVals)),
            xRange = round(min(xVals)):round(max(xVals));
            yRange = zeros(1,length(xRange));
            yRange = yRange + round(max(yVals));
            im1Prof = im1(round(max(yVals)), xRange);
        elseif round(max(xVals))==round(min(xVals)),
            yRange = round(min(yVals)):round(max(yVals));
            xRange = zeros(length(yRange),1);
            xRange = xRange + round(max(xVals));
            im1Prof = im1(yRange, round(max(xVals)));
        else,
            if (max(yVals) - min(yVals)) > (max(xVals) - min(xVals)),
                yRange = round(min(yVals)):round(max(yVals));
```

```
                xRange = (yRange - linCoeffs(2))./linCoeffs(1);
                xRange = round(xRange);
            else,
                xRange = round(min(xVals)):round(max(xVals));
                yRange = linCoeffs(1).*xRange + linCoeffs(2);
                yRange = round(yRange);
            end
            for pos = 1:length(xRange),
                im1Prof(pos) = im1(yRange(pos),xRange(pos));
            end
        end


        X = 0:length(xRange)-1;

        f = fittype('a*exp(-((x-b)^2/(2*(c^2))))+d');
        [val, ind] = max(im1Prof);
        FWHMguess = 5;
        base = round(length(im1Prof)/4);

        % Fit profile to Gaussian
        [im1Fit im1Gof] = fit(X', im1Prof', f, ...
            'Start', [val ind FWHMguess mean(im1Prof(1:base))]);
        coeffs = coeffvalues(im1Fit);

        clear idealProf

        getGamma

        % Generate target profile
        for i = 0:length(xRange)-1,
            idealProf(i+1) = coeffs(1)*...
                exp(-((i-coeffs(2))^2/(2*((coeffs(3)/gamma)^2))))+...
                coeffs(4);
        end

        % Plot original and target profiles, choice to accept or redraw
        S.profh(N) = figure('Name', ['Profile ' num2str(N)], ...
            'NumberTitle', 'off', 'Position', ...
            [0.13*scrwidth 0.2*scrheight 0.35*scrwidth 0.6*scrheight], ...
            'MenuBar', 'none');
```

```

        S.imProf = axes('Parent', S.profh(N), 'Units', 'normalized', ...
            'Position', [0.1 0.25 0.85 0.7]);

        set(S.profh(N),'CurrentAxes',S.imProf);
        plot(X,im1Prof,X,idealProf)
        title(['Profile ' num2str(N)])
        axis tight
        xlabel('Size(nm)')
        ylabel('Intensity(a.u.)')

        S.profAccept = uicontrol(S.profh(N), 'Style', 'pushbutton', ...
            'String', 'Accept profile', 'FontSize', 12, ...
            'Units', 'normalized', 'Position', [0.08 0.05 0.4 0.1]);

        set(S.profAccept,'callback',@acceptProf);

        function acceptProf(varargin)
            close
        end

        S.profRedraw(N) = uicontrol(S.profh(N), 'Style', 'pushbutton', ...
            'String', 'Redraw profile', 'FontSize', 12, ...
            'Units', 'normalized', 'Position', [0.53 0.05 0.4 0.1]);

        set(S.profRedraw(N),'callback',@selectProf);


        % Creation of weights for residual calculation, here all weights
        % are equal to 1 for all points
        residualVector = zeros(length(idealProf),1);
        residualVector = residualVector + 1;
        idealProfNorm = idealProf/max(idealProf);
        residualVector(idealProfNorm<0.25) = 1;

        S.xRanges(1:length(xRange),N) = xRange;
        S.yRanges(1:length(yRange),N) = yRange;
        S.idealProfs(1:length(idealProf),N) = idealProf;
        S.residualVectors(1:length(residualVector),N) = residualVector;

    end
```

```

    % Define objective function for genetic algorithm
    function G = objectiveFunction(c, TW1, TW2, TW3, TW4, TW5, ideal,...
            xVals, yVals, resVect)

        image = c(5)*(TW1 + c(1)*TW2 + c(2)*TW3 + c(3)*TW4 + c(4)*TW5);

        for i = 1:length(xVals)
            imageProfile(i) = image(yVals(i),xVals(i));
        end

        % Calculating sum of squares difference between reconstructed and
        % target concatenated profile
        residual = imageProfile(:).^resVect(:) - ideal(:);
        G = residual'*residual;

    end

    % Run genetic algorithm
    function doMinimization(varargin)

        clear TW1aProfile totalidealProf finalProfile totalResidualVector

        % Concatenated x coordinates
        xRange1 = S.xRanges(:,1);
        xRange1(xRange1==0) = [];

        xRange2 = S.xRanges(:,2);
        xRange2(xRange2==0) = [];

        xRange3 = S.xRanges(:,3);
        xRange3(xRange3==0) = [];

        xRangecat = vertcat(xRange1,xRange2,xRange3);

        % Concatenated y coordinates
        yRange1 = S.yRanges(:,1);
        yRange1(yRange1==0) = [];

        yRange2 = S.yRanges(:,2);
        yRange2(yRange2==0) = [];

        yRange3 = S.yRanges(:,3);
        yRange3(yRange3==0) = [];

```

```
        yRangecat = vertcat(yRange1,yRange2,yRange3);

        % Concatenated ideal profile
        idealProf1 = S.idealProfs(:,1);
        idealProf1 = idealProf1(1:length(xRange1));

        idealProf2 = S.idealProfs(:,2);
        idealProf2 = idealProf2(1:length(xRange2));

        idealProf3 = S.idealProfs(:,3);
        idealProf3 = idealProf3(1:length(xRange3));

        totalidealProf = vertcat(idealProf1,idealProf2,idealProf3);

        % Concatenated residual weighting (all weighting equal here)
        residualVector1 = S.residualVectors(:,1);
        residualVector1 = residualVector1(1:length(xRange1));

        residualVector2 = S.residualVectors(:,2);
        residualVector2 = residualVector2(1:length(xRange2));

        residualVector3 = S.residualVectors(:,3);
        residualVector3 = residualVector3(1:length(xRange3));

        totalResidualVector= vertcat(residualVector1,...
            residualVector2,residualVector3);

        figure(S.fh)
        set(S.fh,'CurrentAxes',S.profGraph)
        plot(totalidealProf)

        % Set options for genetic algorithm
        options = gaoptimset('Generations', 1000, ...
            'InitialPopulation', randn(1,5),'FitnessLimit',0,...
            'CrossoverFraction',0.8);

        tic

        % Call genetic algorithm
        [xOpt, fVal] = ga(@(c)objectiveFunction(c,im1,im2,im3,im4,im5,...
            totalidealProf, xRangecat, yRangecat, totalResidualVector),...
            5, [], [], [], [], [], [], [], options)
```

```

        toc

        % Generate reconstructed image
        answer = xOpt(5)*...
            (im1 + xOpt(1)*im2 + xOpt(2)*im3 + xOpt(3)*
               im4 + xOpt(4)*im5);

        % Plot reconstructed image
        figure(S.fh)
        set(S.fh,'CurrentAxes',S.imFinal)
        imagesc(answer)
        axis image
        colormap hot
        colorbar

        % Get concatenated reconstructed profile
        for i = 1:length(xRangecat)
            finalProfile(i) = answer(yRangecat(i),
               xRangecat(i));
        end

        % Get concatenated TW1 profile
        for i = 1:length(xRangecat)
            TW1aProfile(i) = im1(yRangecat(i),xRangecat(i
               ));
        end

        % Plot various profiles
        figure(S.fh)
        set(S.fh,'CurrentAxes',S.profGraph)
        plot(1:length(xRangecat), TW1aProfile/max(
           TW1aProfile), '.-', ...
            1:length(xRangecat),totalidealProf/max(
               totalidealProf),'.-',...
            1:length(xRangecat), finalProfile/max(
               finalProfile), '.-')
        legend('Confocal', 'Target', 'Minimised',...
            'Location', 'NorthEastOutside')
        axis tight

        assignin('base','xOpt',xOpt)
        assignin('base','fVal',fVal)

    end

    % Assign coefficients into workspace
    function assignCoeffs(varargin)
        if coeffSet == [0 0 0 0 0 0],
            coeffSet = [xOpt gamma];
```

```
        else
            coeffSet = [coeffSet; xOpt gamma];
        end
    end

end
```

Appendix C

Published paper: Low power super resolution fluorescence microscopy by lifetime modification and image reconstruction